# A Loosely-Coupled Passive Dynamics and Finite Element-based Model for Minimising Biomechanically Driven Unhealthy Joint Loads during Walking in Transtibial Amputees

Swansea University
Prifysgol Abertawe

**Turki Khalid AlQemlas**

College of Engineering

Swansea University

Submitted to Swansea University in Fulfilment of the Requirements for the Degree of

**Doctor of Philosophy, Ph.D**

2020

# Abstract


## A Loosely-Coupled Passive Dynamics and Finite Element-based Model for Minimising Biomechanically Driven Unhealthy Joint Loads during Walking in Transtibial Amputees

The primary objective of a prosthetic foot is to improve the quality of life for amputees by enabling them to walk in a similar way to healthy individuals. Amputees suffer from health risks including joint pain, back pain and joint inflammation. The aim of this thesis is to develop a new computational approach to reduce the likelihood of biomechanically driven joint pain in transtibial amputees resulting from sustained exposure to Unhealthy Loads (ULs) during walking. This is achieved by developing a computational methodology to achieve a customisable stiffness design solution for prosthetic feet so that the occurrence of unhealthy joint loads during walking is minimised.

It is assumed that the healthy population is able to spend energy most optimally during walking at all walking speeds. During walking, the force exerted by the body on the ground is measured by the ground reaction force (GRF). The GRF value is normalised with the body weight defining a dimensionless parameter $G_r$. The $G_r$ values are similar for both legs in healthy populations but are different for the sound and affected leg for amputees. A new hypothesis has been proposed in this thesis that walking is comfortable for an amputee when the difference between $G_r$ values is minimal between the amputee and an equivalent healthy population. The $G_r$ values for healthy adults, as well as amputees, follow a finite number of patterns. The pattern of the $G_r$ values (or the GRF curve) depends on the walking speed of an individual, categorised as slow, fast or free walking. However, it is observed in the literature that free walking speed (FWS) varies over a wide range for healthy individuals (e.g. 1.1 m/s to 1.5 m/s). As a result,

it was difficult to establish a relationship between walking speed and GRF pattern. A novel parametrised description of GRF curves for a healthy population and amputees is proposed so that a new dimensionless velocity ratio parameter and the corresponding value of the FWS can be predicted by observing the GRF pattern of a healthy adult or an amputee. A new classification approach based on the parametrised description of GRF curves, along with the dimensionless velocity ratio parameter, has been recommended for categorising very slow, slow, free, fast and very fast walking. The GRF result predictions are validated on healthy adults in an experiment conducted in a gait lab. A group of candidates who walk a lot in their daily life were specially selected for this experiment. This classification approach is used to develop a new measure of ULs based on the parametrised GRF description for healthy population and amputees. An innovative computational methodology is proposed to design an optimal stiffness response of a prosthetic foot that minimises the occurrence of ULs. This is achieved by transferring the roll-over shape (ROS) information of the prosthetic foot and the corresponding $G_r$ information for a given velocity ratio across a passive walking dynamic (PWD) and a finite element model via a newly defined form of loose coupling. A theoretical case study is presented in which an amputee walks in a gait lab with a representative C-shaped prosthetic foot. The thesis explains how the proposed novel computational methodology is able to redesign the prosthetic foot in a way that is better suited to minimising ULs. The redesign process of the prosthetic foot has led to the development of an innovative 3D printable double keel and double heel design. With the advancement of carbon reinforced polymers and additive manufacturing technology, the stiffness customisation methodology proposed in this thesis has the potential to create a new generation of energy-efficient prosthetic feet.

# Declaration and Statements

**DECLARATION**

This work has not previously been accepted in substance for any degree and is not being concurrently submitted in candidature for any degree.

Signed ..... Turki Kh. AlQemlas .....

Date ..... 14/10/2020 .....

**STATEMENT 1**

This thesis is the result of my own investigations, except where otherwise stated. Other sources are acknowledged by footnotes giving explicit references. A bibliography is appended.

Signed ..... Turki Kh. AlQemlas .....

Date ..... 14/10/2020 .....

**STATEMENT 2**

I hereby give consent for my thesis, if accepted, to be available for photocopying and for inter-library loan, and for the title and summary to be made available to outside organisations.

Signed ..... Turki Kh. AlQemlas .....

Date ..... 14/10/2020 .....

Turki Khalid AlQemlas

$14^{th}$ October 2020

# Acknowledgements

Foremost, I would like to express my sincere gratitude to my supervisor Dr. Rajesh Ransing for the continuous support of my Ph.D. study and research, for his patience, motivation, enthusiasm, and immense knowledge. His guidance helped me in all the time of research and writing of this thesis. I could not have imagined having a better advisor and mentor for my Ph.D. study.

Besides my advisor, I would like to thank my mother and say: 'everything I am you helped me to be'. Moreover, I would like to thank my family for their endless support during my journey toward success. They always motivate me and provide me with their help.

My sincere thanks also goes to my friends specially, Dr. Meshari Al-Ebrahim, who helped me a lot in finalising this project within the limited time frame. I also would like to thank Dr. Nick Owen for his support while performing the experiment in the gait laboratory. Also, a special thanks for my second supervisor Dr. Igor Sazonov.

Finally, special thanks goes to my colleague, Ben Morgan, for his help during my thesis period. I don't know how to show my gratitude for helping me with the APDL script. Your ideas and insights made it much easier to proceed in the right direction and complete the thesis successfully.

# Contents

# List of Figures

# List of Tables

# Nomenclature

| | |
|---|---|
| UL | Unhealthy Load |
| A/P | Anterior/Posterior |
| ALM | Additive Layer Manufacturing |
| ES | Early Stance |
| FA | Forward-Facing Ankle |
| M/L | Medial/Lateral |
| PS | Pre-Swing |
| RA | Reverse-Facing Ankle |
| SA | Solid Ankle |
| SS | Single Support |
| SW | Swing |
| TF | Transfemoral |
| TT | Transtibial |
| ROS | Roll-Over Shape |

DK Double Keel

BW Body Weight

SACH Solid Ankle Cushion Heel

APDL ANSYS Parametric Design Language

vGRF Vertical Ground Reaction Force

COM Centre of Mass

COP Centre of Pressure

GRF Ground Reaction Force

PWD Passive Walker Dynamics

FEA Finite Element Analysis

FEM Finite Element Modelling

FWS Free Walking Speed

$f$ Percentage reduction

$Fz1$ First peak of vGRF curve

$Fz1_h$ First peak of healthy vGRF curve

$Fz1_s$ First peak of sound vGRF curve

$Fz2$ Trough of vGRF curve

$Fz3$ Second peak of vGRF curve

$Fz3_h$ Second peak of healthy vGRF curve

$Fz3_p$ Second peak of prosthetic vGRF curve

$G_r$ vGRF ratio (GRF/BW)

$Gra$ vGRF ratio for affected

$Grs$ vGRF ratio for sound

$t$ Gait cycle percentage

$UL_{erroneous}$ The PWD unhealthy load

$UL_{predicted}$ The PWD predicted unhealthy load

$V_r$ Velocity Ratio

# Chapter 1

# Introduction

Prosthetics improve the quality of life among amputees by enabling them to walk in an efficient and cosmetically normative way [1]. Loss of limbs affects individuals' ability to move autonomously, as changes in gait hinder their effective movement. The walking process involves asymmetrical movements, since both legs work together but perform separate tasks: one leg performs the role of assisting and supporting, while the other leads. The body exerts pressure on the prosthetics to compensate for the loss of weight. Prosthetics are significantly lighter than physiological body parts. Currently available equipment forces people with prosthetics to expend more energy than healthy individuals, as the muscles respond to the inadequate support offered by the walking aid. Hence, a prosthetic foot (for example) can play a significant role in safe standing, and its influence on the entire pattern of movement can be observed when the users are walking.

In this chapter, the main topics and challenges of the dissertation are introduced and addressed. In Section 1.1, the background of the problem is defined, while the aims and objectives of the study are outlined in Section 1.2. In Section 1.3, publishable results for potential journal papers are mentioned and discussed. Finally, Section 1.4 presents the dissertation's layout.

## 1.1 Background and Rationale

The NHS has recorded an increase in the number of amputations in the UK over the years. For instance, Scotland has seen a steady increase in amputation numbers since the 1980s, with a significant increase since 2006 [2,3]. These statistics are common across the UK and are believed to have been caused by the increased prevalence of diabetes in the older population. This is projected to rise by 3.9 million over the next fifteen years [4]. England had 25,883 amputations between 2003 and 2008 and has recorded similar trends in recent times [5]. Subsequently, 24,181 amputations occurred between 2012 and 2015, while 27,456 took place between 2015 and 2018 [6], as shown in Figure 1.1.

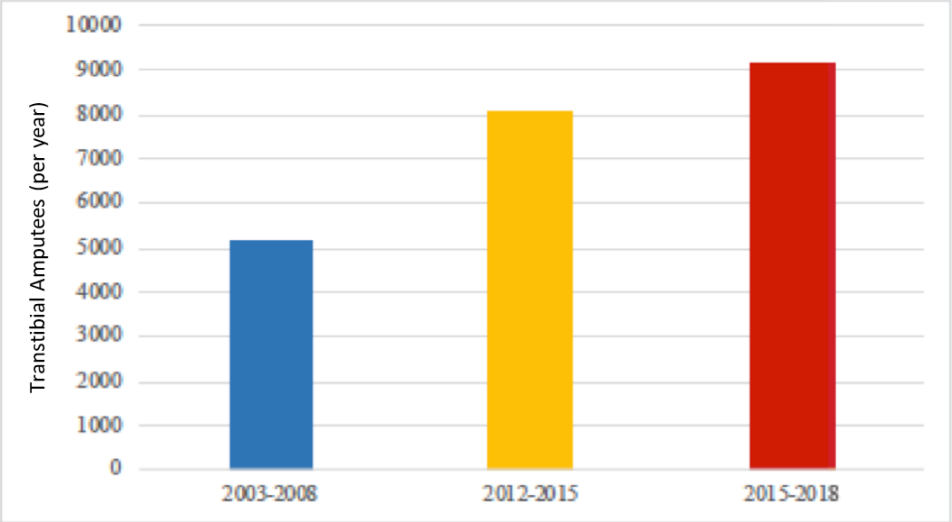


Figure 1.1: England's average number of transtibial amputees per year, based on the last two decades [5, 6].

The relationship between the prevalence of diabetes in the ageing population and cases of amputations is demonstrated by the occurrence of diabetes among amputees (there has been a 19% increase in some incidents) [7], and the age distribution is inclined towards older patients (see Figure 1.2).

The primary objective of a prosthetic foot is to improve amputees' quality of life by enabling them to walk in a similar way to healthy individuals. Loss of limbs affects individuals' capacity for autonomous movement, as changes in gait hinder their effective movement [3].

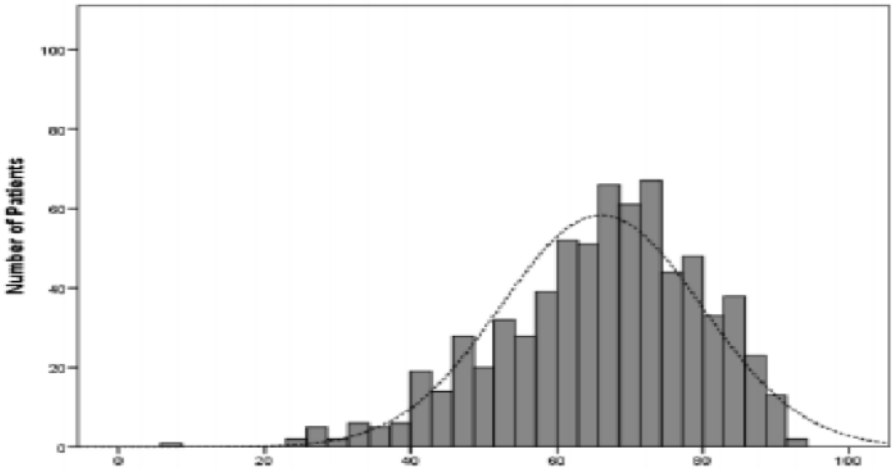


Figure 1.2: Amputees' age distribution [3].

The walking process involves asymmetrical movements, as both legs work together but perform separate tasks: one leg performs the role of assisting and supporting, while the other leads [8]. The body exerts pressure on the prosthetic foot to compensate for the loss of weight. The human body considers prosthetic feet to be dead weight (not supported by muscles) that it needs to carry. As a result, prosthetic feet are required to be significantly lighter in weight than the corresponding physiological body parts. This biomechanically driven imbalance leads to additional loads on joints, which are referred to as 'Unhealthy Loads (ULs)' in this thesis. Low-activity patients, who are predominantly elderly diabetic patients, are more likely to be overweight and have strained joints due to carrying additional loads over the years; prosthetics are expected to worsen this situation by exposing joints to further ULs. These patients are less likely to run and more likely to walk fast for their daily exercise and well-being. Reducing ULs during the walking transition is thus a critical area of research. It follows that Figures 1.1 and

1.2 are pivotal, as they have helped define elderly patients with low activity levels as both the target market and direct beneficiaries of the research outcome of this thesis.

The magnitude of ULs, along with the resulting discomfort, is person-specific and not directly quantifiable. Indirect measures, such as deviation from symmetric walking or limping [9], variation in oxygen consumption [10], variation in walking speed [11], step length [12] and subjective assessment of discomfort as experienced and communicated by an amputee [13], have been used in the literature to quantify the effect on a person of using prosthetic feet.

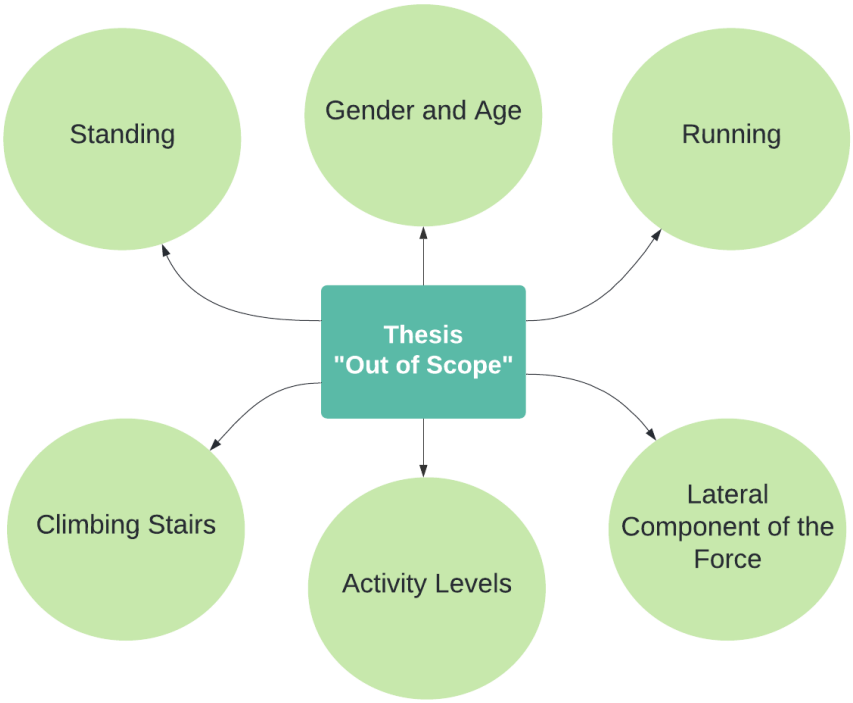


Figure 1.3: Excluded points of the thesis scope

According to Newton's third law of motion, the pressure exerted by legs on the ground during walking results in an equal and opposite reaction force from the ground. This is referred to as the ground reaction force (GRF), and is generally a three-dimensional vector. The vertical ground reaction force (vGRF) is the most dominant component of the force vector, while the horizontal component of the frictional resistance offered by the ground during braking and the

forward movement of walking. The side way or lateral motion is balanced by the remaining component of the GRF. The effect of this lateral component of the force, as well as the loads generated during standing, running, climbing stairs etc. (see Figure 1.3), are excluded from the scope of the work in this thesis; the effect of gender, age and activity levels of an individual is also not considered. This thesis considers only the effect of walking speed on vGRF and its contribution to the ULs. The measurement and the factors affecting variation in the vGRF are reviewed in Chapter Two.

A new set of formulae based on the variation observed in the vGRF component with respect to the walking speeds for both an amputee's legs, along with the corresponding vGRF components for a representative healthy adult population, has been proposed in this thesis to quantify Unhealthy Loads (Chapter Four, Section 4.5.4). A theoretical computational framework has also been proposed in this thesis that uses this newly proposed vGRF metric to design prosthetic feet in order to minimise the estimated occurrence of resulting Unhealthy Loads.

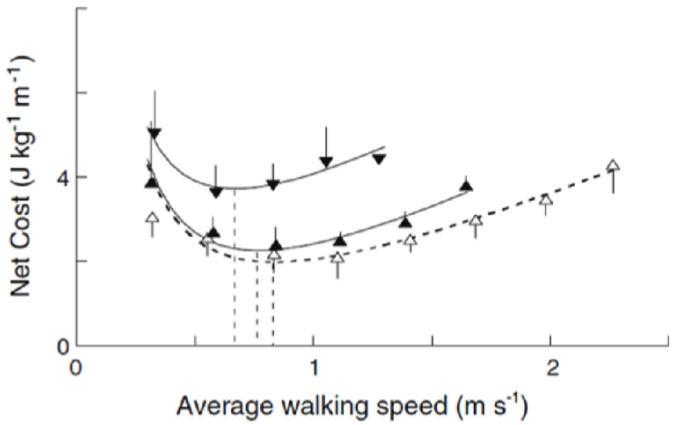


Figure 1.4: Metabolic cost of locomotion and stability among lower limb amputees, along with cost of transport with walking speed. The figure from [10] represents the cost of transport (net cost ($Jkg^{-1}m^{-1}$) versus walking speed ($ms^{-1}$) for able-bodied, transtibial and transfemoral participants; (open upward triangles), (bold upward triangles) and (bold downward triangles), respectively [14].

Individuals with prosthetic feet tend to expend more energy than healthy individuals, as their muscles respond to the inadequate support offered by the walking aid. Moreover, they also tend to walk more slowly despite their relatively high energy use (see Figure 1.4). Prostheses have a limited range of movement when compared to anatomical limbs. Amputees with transtibial amputation pay at least 20% more in metabolic costs when walking than their able-bodied counterparts do [15].

Amputees also experience different health complications due to their unstable gait. Those with lower limb prosthetics experience poor stability and experience a higher incidence of falls. Sheehan et al. [16] report that over 50% of lower-limb amputees fall at least once a year, while Silverman and Neptune [17] firther contend that below-knee amputees have an increased risk of falling due to differences in their whole-body angular momentum when compared to non-amputees [2]. The difficulties in regulating angular momentum during walking exposes amputees to higher rates of falls, while the functional loss of ankle muscles also lowers their stability. The design of the prosthetic leg should thus address the metabolic cost of locomotion and stability among lower limb amputees, as shown in Figure 1.4.

This increased risk of falling may led to physical harm, broken bones and internal bleeding; consequences of falling include hospitalisations and other comorbid issues. Moreover, a heightened fear of falling may led to the disuse of prosthetics, meaning that these individuals may experience a decreased quality of life. Additionally, asymmetric walking leads to imbalances in leg muscles and joints [17], and amputees may experience chronic back pain and joint problems [18] and long-term secondary complications throughout their lifetimes. Thirdly, amputees also experience mobility limitations. Their lack of stability increases their chances of injury and falling. Amputees require more energy to move, and move more slowly than healthy individuals. Moreover, individuals who rely on their physiological limbs over prosthetics may

develop osteoarthritis. Prosthetics should therefore be designed to alleviate health implications for amputees.

Several studies on this topic [10, 14–17] indicate that amputees can compensate for the cost of metabolism by reducing inertia in the prosthetic leg. However, it is challenging to maintain a symmetrical gait with a prosthesis due to the different mechanisms of the anatomical leg and the artificial limb. The asymmetrical load, or the UL, affects the joints and exacerbates back pain.

One of the most economical and widely used prosthetic feet on the market is probably the one known as the 'Jaipur foot' [19]. These feet are freely distributed from donations received. However, they are not efficient as commercially available prosthetic feet. Powered (active) bionic prosthetic feet are at the upper end of the market [20], while the most popular and commercially successful feet on the market are passive carbon-fibre-based energy storage and return models. The design and development efforts of all of these prosthetic feet are targeted at achieving the same goal: namely, minimising the occurrence of ULs in order to reduce the resulting discomfort for an amputee at an affordable cost.

Optimising the stiffness response of a prosthetic foot is one of the options for minimising the occurrence of ULs. The stiffness of prosthetic feet affects both the gait characteristics and locomotion of amputees. Walking mechanics determine the distribution of the energy stored during walking. Currently available prosthetic feet only release a fraction of the energy they absorb (i.e. high values of negative net mechanical work), which contributes further to asymmetrical walking. Prosthetic feet rely on their stiffness to provide the range of motion required for different surfaces [21]. Hedrick et al. [11] found that during walking in healthy adults, the foot-ankle-knee-hip structure of both legs compresses and recoils along the longitudinal axis of the leg and performs near-zero, or slightly negative, net mechanical work from Free to Fast transition in walking speeds. This indicates that the mechanical work production is similar to

an ideal spring in the Free–Fast walking speed range. Moreover, ULs increase significantly as walking speed increases from free to fast walking, and are low at slow walking speeds [17, 22].

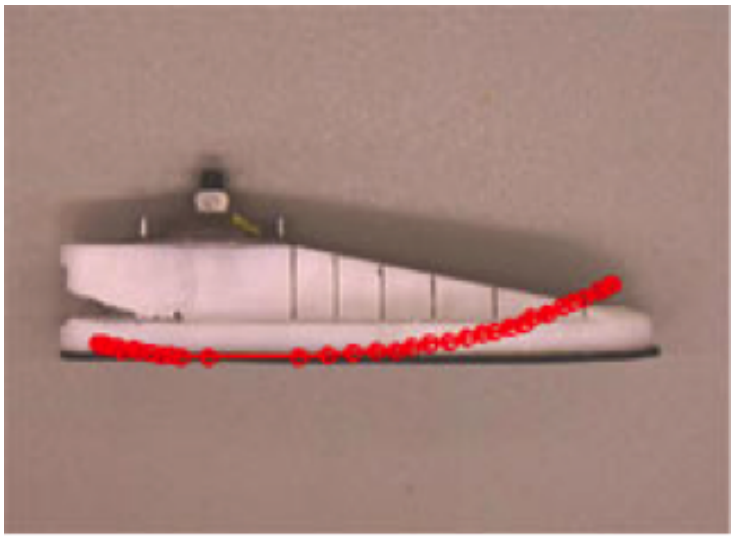

Figure 1.5: Shape and Roll Foot [21].

Over the past decade, the use of polymer-based prosthetic feet has been explored in an attempt to achieve a desirable stiffness response. A stiffness-optimised, polymer-based foot (Figure 1.5) [23] was designed as an effective rocker that closely matched the physiological ankle-foot-roll-over shape [21].

However, this foot was later withdrawn from the market when reports of premature failure arose during field testing [24]. Recent advances in additive manufacturing technologies have included manufacturing wear-resistant products [25, 26], innovations in materials such as reinforced polymers [27] and advanced computer modelling techniques; these have all enabled the digitisation of processes in relation to the design and manufacturing of prosthetic feet. The digitisation of these processes has opened the way to new research challenges, including commercially exploitable opportunities for realising patient-specific customisations and stiffness optimisation of prosthetic feet [28]. This approach is being trialled not only in Western countries, but also in the UAE [29].

Passive walking is an uncontrolled process that does not use any actuators. Traditionally, passive walking dynamics (PWDs) has been used to design minimum controls for a walking biped robot [30]. However, as reviewed in Chapter Three, the current research on walking dynamics has progressed into developing complex multi-link-powered or active walking models that present head, hands, upper body, legs, ankles, knees and feet with muscles and rotation at various joints [15] compared to simple two-link passive walking models in which each link represents a leg without a knee or ankle. Complex models generate many unknown variables that require person-specific experimental data for calibration [15]. In a recent study, Zaytsev et al. [31] used a very simple point mass model to study the effect of step length and step time on walkers' ability to fall and then discover stability regions for bipedal walking. Ruina [30] has further argued that powered walking need not be visualised as passive walking with minimum control, but rather as a highly controlled process optimised for minimum actuator use.

In the present thesis, the decision to use a simple two-link passive model to determine ULs is consistent with the approach adopted by Zaytsev et al. [31]. If Zaytsev et al's [31] underlying point mass walking model is enhanced to sufficient complexity to enable it to model prosthetic foot designs (e.g. by replacing its point contact formulation with a rolling contact, introducing massless linear springs for both legs, and incorporating point masses for both legs with a double support phase) while retaining its inherent simplicity of using a two-link model, then it can be argued that the approach can be extended to design the next generation of energy-efficient actuators for powered (active) bionic prosthetic feet. This requirement supports the choice to use a PWD model, as proposed by Charles [15] in this thesis (see Figure 3.9 in Section 3.3.2).

## 1.2 Aims and Objectives

Existing approaches either use the finite element method (FEM) or walking dynamics algorithms, independently of each other, to design a prosthetic foot. The boundary conditions used in the current FEM-based models are unable to account for swing leg dynamics. Moreover, the walking dynamics models based on modelling kinematics and kinetics are either based on simple two-link point mass models for forward dynamics simulation or on complex multi-link models that rely on inverse dynamics to initialise many unknowns from the experimental data. These complex models lose their generalisation ability.

The aim of this thesis is to reduce the likelihood of biomechanically driven joint pain in transtibial amputees resulting from sustained exposure to ULs during walking. The goal of the thesis is thus defined as developing a computational methodology to achieve a customisable stiffness design solution for prosthetic feet, so that the occurrence of ULs during walking is minimised. The supporting objectives can be outlined as follows:

1. Develop a model to quantify Unhealthy Loads in order to minimise its value with a parametrised description of ground reaction force (GRF) curves for the healthy population and amputees at a given walking speed.

2. Develop a methodology to transfer information associated with walking speed and stiffness values among measurements from experiments, walking dynamics models and FEM-based simulation results.

3. Develop a coupled walking-dynamics and finite-element-based approach with sufficient complexity to reduce Unhealthy Loads, while retaining the necessary simplicity of models so that they can still be used for the stability analysis.

4. Undertake computational verification of the results from the proposed models when compared to the published state-of-the-art research outputs.

The present thesis proposes two innovative techniques to optimise stiffness in prosthetic feet in order to enhance their effectiveness at various walking speeds. The first is a proposed dimensionless equation used to estimate GRFs for the healthy population, in addition to both the sound and affected legs of amputees, at various walking speeds. The second is the development of a non-linear mapping function to transfer stiffness and velocity values among walking dynamics and FEMs, as well as in experiments. The discovery of these novel and innovative techniques has enabled the development of a new coupled approach for minimising the occurrence of ULs driven by unbalanced mass, length and stiffness ratios at different walking speeds. The PWD approach is based on the PhD research undertaken by two previous students at Swansea University – Mahmoodi [32] and Charles [15]. In more detail, Mahmoodi [32] utilised a kinematic model to study the effects of unbalanced mass and length ratios on roll-over shapes. An independent optimisation analysis of roll-over shape was also recommended for the stiffness optimisation of prosthetic feet. A non-energy-conserving multiple contact point was used to define roll-over shapes (ROS); with the assumption of rigid legs, the resulting GRF curve was not M-shaped (a shape typically observed for GRF curves). Charles [15] further proposed a spring-legged PWD model with rolling contact to produce M-shaped GRF curves, and also investigated the effect of unbalanced mass and varying length ratios. However, the model was stable over a narrow range of walking speeds and spring stiffness values; it is only able to simulate the M-shaped GRF curve for free walking.

## 1.3 Publishable Results for Potential Journal Papers

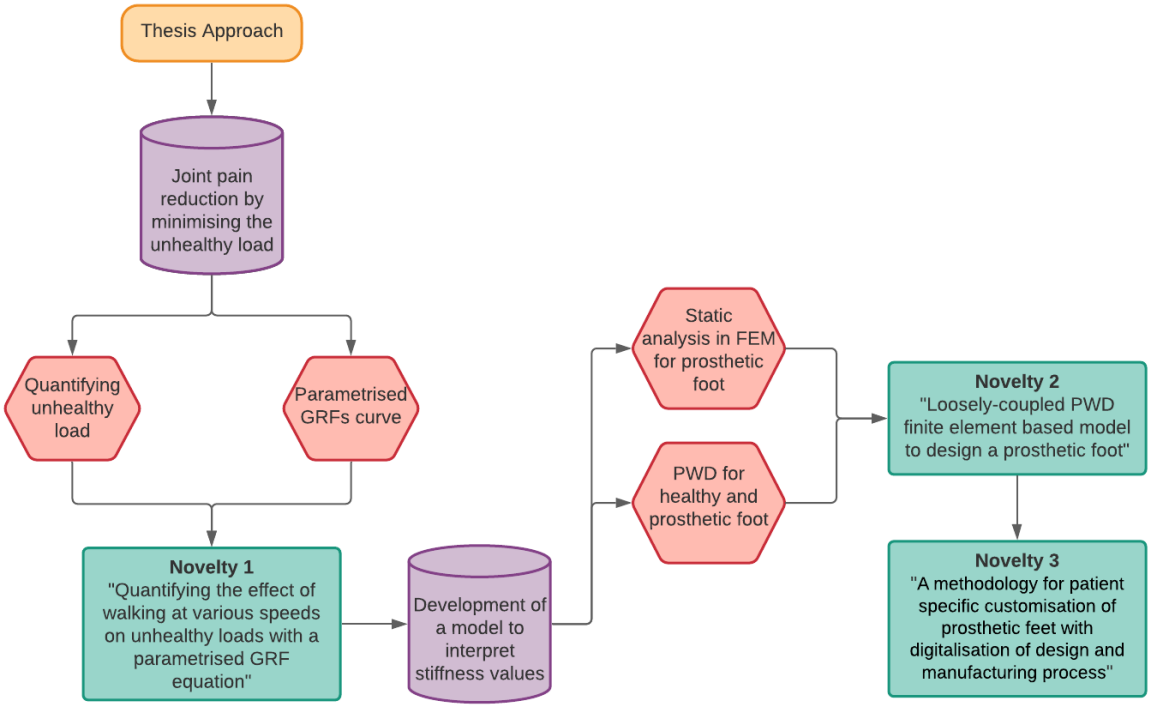


Figure 1.6: Thesis Flow

The present thesis has achieved all of its objectives. The publishable results regarding the novelties identified in this research will be included in different journal papers. The novelty approach flowchart is presented in Figure 1.6. The proposed titles of articles for good-quality journals are as follows:

1. **Novelty 1**: Quantifying the effect of walking at various speeds on Unhealthy Loads with a parametrised GRF equation.

2. **Novelty 2**: A novel, loosely-coupled PWD and finite element-based model to design a prosthetic foot.

3. **Novelty 3**: A 3D printable double-keel prosthetic foot design to enhance stiffness variation ability.

## 1.4 Thesis Layout

In this section, the thesis layout is introduced to provide a brief summary of all chapters included. Figure 1.7 illustrates the thesis layout diagrammatically. The present thesis is based on three pillars (research directions) that are normally pursued independently in the research community: experimental gait analysis, finite element simulation and PWD models. The literature review associated with these directions is split into two chapters to improve readability. The objective of this review is to facilitate an understanding of the published literature in order to propose design criteria for the stiffness optimisation of prosthetic feet that satisfy the aims and objectives defined in this thesis. The structure of this thesis is outlined below.

- **Chapter 2 - A Vertical Ground Reaction Force (vGRF)-based Objective Function for Stiffness Optimisation 'A Review':** This chapter explains the limitations of using kinematic data measured from motion capture systems and explains how kinetic data based on individual measurements from force platforms can be reliably generalised for population-based predictions (and vice versa). It focuses on why optimisation is necessary in enhancing the efficiency of prosthetic feet across different walking speeds. The variation in GRFs with respect to walking speed is studied for both amputees and the healthy population. The chapter identifies the need to develop a parameterised equation for vGRF so that it can be used as part of an objective function for the subsequent stiffness optimisation problem.

- **Chapter 3 - The Roll-Over Shape (ROS) as a Design Variable for Stiffness Optimisation 'A Review':** This chapter presents a literature review on the significance of optimising prosthetic feet and their limitations. The use of ROSs in linking experimental gait data, PWD and FEM-based simulation models is explored, and the performance of

walking dynamics models with varying complexities is critically evaluated, along with the use of FEM techniques in the stiffness design of prosthetic feet.

- **Chapter 4 - A Set of Dimensionless Equations for GRF Estimation:** The GRF curves and the equation proposed in the ISO 22675 standard [33] represent the characteristic M-shaped curve for FWS. From the literature, it can be observed that the value of free (or self-selected) walking speed in $m/s$ ranges from $1m/s$ to $1.5m/s$, with $1.3m/s$ being the most frequently reported. This chapter reviews the GRF variation in detail. A number of characteristic M-shaped curves for the very slow to very fast walking range are identified for both healthy adults and amputees. The GRF data is then transformed in a dimensionless format so that it can be compared across published results. A group of healthy male university students who walk extensively in their daily lives were selected, and these students were asked to walk at self-selected speeds in a gait lab. It was discovered that the students walked at an average speed that was fast or very fast ($1.855m/s$), but all exhibited the characteristic M-shaped curve of free-walking GRF. The insights from this experiment helped in developing an appreciation of the variability in published results, while a set of dimensionless equations for GRF estimation are proposed for healthy adults and amputees.

- **Chapter 5 - A Loosely-Coupled Model:** The range of stiffness values from a PWDs model with linear elastic springs was juxtaposed with the viscoelastic springs results published in the literature, along with the stiffness values used in FEM; these were measured in gait experiments in order to develop a mapping function capable of transferring information across models. Following extensive simulations, and using the set of dimensionless equations proposed in Chapter Four, the stiffness values were mapped indirectly via the

GRFs and roll-over shapes across dynamic walking models, FEMs and experiments. A loosely coupled algorithm is proposed to realise the patient-specific stiffness customisation of prosthetic feet. Results are discussed in the context of a sample C-shaped prosthetic foot with heel that mimics a real-life scenario.

- **Chapter 6 - A 3D-Printable Double-Keel Prosthetic Foot Design to Enhance Stiffness Variation Ability:**The digitalisation of the design and manufacturing processes for producing prosthetic feet has created new opportunities for patient-specific stiffness customisation opportunities. Inspired by a recently launched Mecuris prosthetic foot design [28], this chapter proposes a methodology for patient-specific stiffness customisation of prosthetic feet to reduce the occurrence of ULs using the novel algorithms proposed in Chapters Four and Five. A newly proposed double-keel prosthetic foot design is analysed to demonstrate the stiffness variation ability of the C-shaped prosthetic foot with heel.

- **Chapter 7 - Conclusion and Future Work:** This chapter concludes the work by describing how the objectives set out at the beginning of the research are met, including a discussion of the limitations of the proposed methodology. Recommendations for future work include techniques to improve or adapt the proposed model in enhancing the effectiveness of prosthetic foot design. The chapter also discusses the importance of future human trials that will aid in advancing the design of prosthetic feet. The need to include human-based trials is relatively obvious, as an effective experimental design will be required in order to calibrate the model accurately. In addition to redesigning passive prosthetic feet with the proposed algorithms, it will also be interesting to explore the embedding of Ruina's approach [31] within the models proposed in this thesis in order to design the next generation of energy- efficient actuators for bionic feet. Once the proposed

model has been benchmarked with gait experiments on amputees, future work can progress to redesign the foot with variable stiffness that is currently being proposed by Morgan [34] at Swansea University. It is expected that this future work will be achieved by taking advantage of the productivity improvement and patient-specific customisation opportunities offered by the digitisation of the associated design and manufacturing processes.

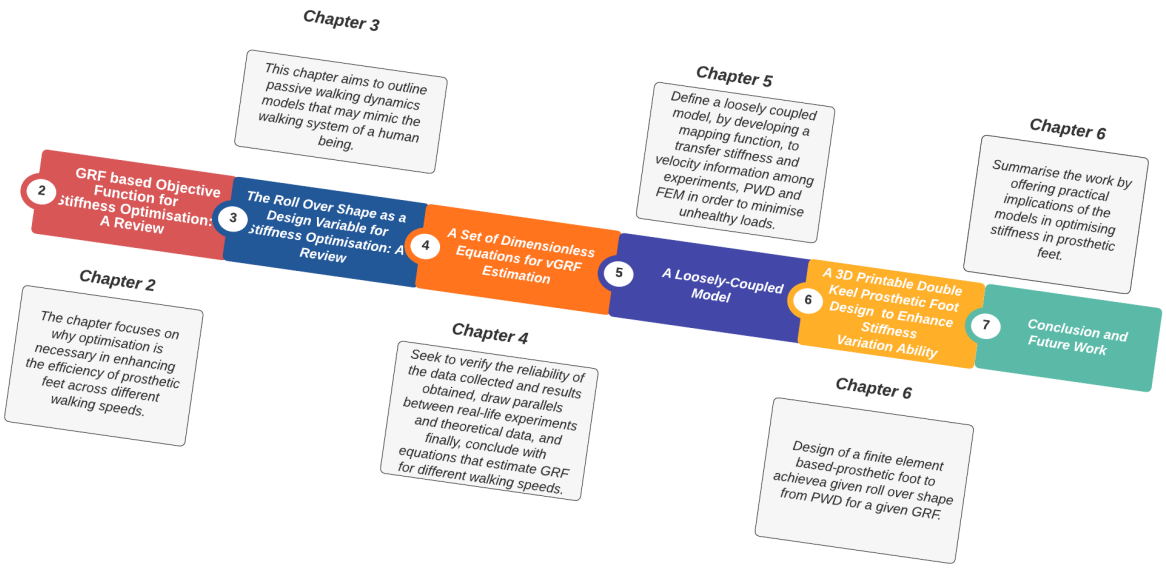


Figure 1.7: Thesis layout

# Chapter 2

# A vGRF-based Objective Function for Stiffness Optimisation: A Review

## 2.1 Introduction

The evolution of bipedal gait, otherwise known as 'walking', is an effect of a sophisticated engagement that involves several anatomical parts: specifically, muscles, bones and joints, the brain, and the spinal cord [1]. Studies on human gait have proven to be valuable in multiple applications; for instance, augmenting knowledge of disease progression or treatment efficacy [35]. Bipedal gait is evidently a multiplex affair that, for all intents and purposes, has still not been sufficiently discerned; the experiences of gait efficiencies are the evident culmination of evolution and self-learning. Defining the typical dynamics of walking is also challenging. Gait dynamics can be differentiated to a greater extent among certain humans [36], and it is concluded that these humans exert asymmetrical muscle action for progression and support [37]. Counterintuitively, gait optimisation in patients is not always a result of the minimisation of energy consumption; instead, they may choose to use additional energy to sustain

their kinematic paradigm [38]. Although, interestingly, the causes of this remain shrouded in mystery, they are more often than not linked to an attempt to diminish discomfort, joint pain, or gait asymmetry (for aesthetic reasons) [39]. One possible way of mastering the biomechanics of walking is to unravel the innate manifold of walking through analysis of a simple model of said biomechanics [39, 40]. The next part explores the mannerisms of what is deemed as normal walking and the methodologies habitually used for the collection of data during human experiments. Invariably, gaits are variegated and include running and sprinting, jogging, skipping, and walking. These distinct styles of gait have patterns that are cyclical in nature, and each activated extremity finishes a cycle within a similar length of time. Bipedal gait (or walking) is the most familiar gait form, with the prototypical 'man in the street' taking 10,000 steps per day [41]. Notably, there is a double-support phase evident in the process of walking as each step takes place, i.e. when both feet are touching the ground. Typically, humans choose a person-specific speed at which they prefer to walk; this speed is referred to as 'self-selected' or 'free walking' speed. Each person chooses this speed to reduce the use of metabolic energy and ensure that a comfortable gait pattern can be maintained for long periods [42].

The chapter begins with a description of bipedal gait in the context of a healthy gait. It goes on to highlight the insights gained from human experimentation, then outlines the distinct methods of gait analysis and the reasons for their performance. As is evident, if normal gait patterns are understood, then variation in the amputee gait can be better explained, meaning that corrective actions can be taken to improve the gait. Moreover, the chapter goes on to describe walking asymmetries (where normal walking is profoundly asymmetrical), which contradict and negate many assumptions. Larger asymmetries in the gait dynamic analysis suggest that their cause may be the result of an incredible disparity between the two legs; for example, orthoses, prosthetic feet, or exoskeletons. The ensuing effects will be examined with particular emphasis

given to the recalibration of proper gait. The variation in GRFs for gait walking is also described in detail.

The chapter outline can be described as follows. Section 2.2 describes the mechanics of bipedal gait. This section reviews the state-of-the-art literature on bipedal gait and introduces the commonly used M-shaped pattern for GRF curves. The changes to GRF pattern resulting from walking speed variation are also discussed. Section 2.3 outlines the effect of walking asymmetries resulting from amputation and the subsequent use of a prosthetic foot. The chapter concludes in Section 2.4 by discussing the effect of activity levels on prosthetic foot design, along with the need to parametrise GRF curve variations so that they can be used effectively as part of an objective function for optimising the stiffness response for prosthetic feet.

## 2.2 Fundamentals of Bipedal Gait

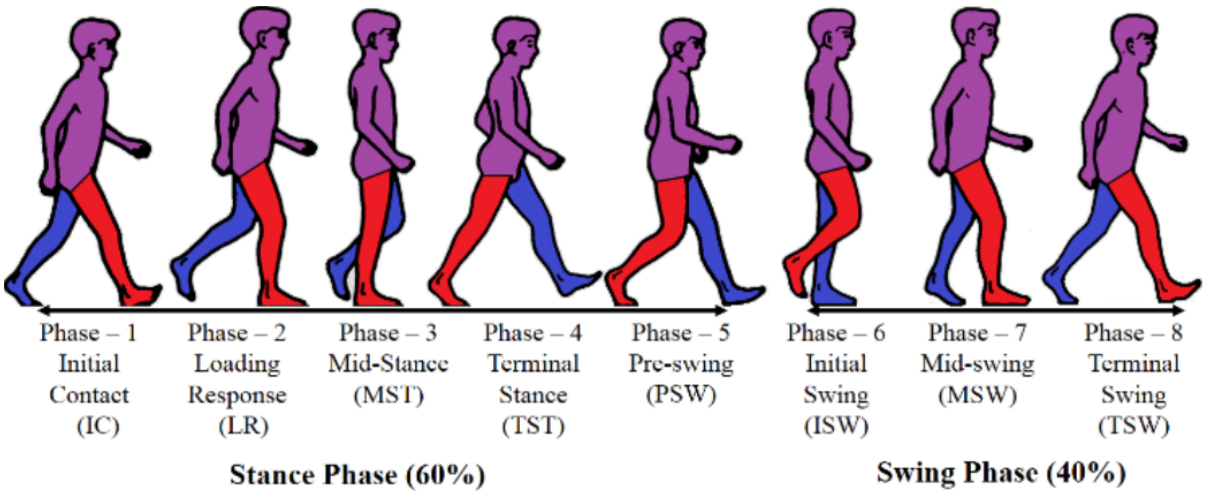


Figure 2.1: Distinct step phases during a gait cycle, where the right leg (red colour) is considered as the reference leg [43].

Gait analysis refers to a methodology for identifying and assessing the dysfunctions of the lower extremities in dynamic movement and loading. In a lab setting, motion capture markers are attached to patients at conventional anatomical landmarks to act as references. As such, biomechanical information can be acquired that is not limited to joint velocities, GRF, and joint positions.

Guidance from biomechanics specialists is a prerequisite in standard gait analysis due to the amount of complexity involved, which sometimes makes it difficult to uncover insights from gait experiments. Gait analyses require well-calibrated equipment; this process can take a long time, which may impact a patient's recovery period, particularly when such analysis is required for diagnostic purposes [1]. The GRF is measured by a force platform [35] and also monitors the movement of the centre of pressure (COP) of the foot for the duration of the gait cycle.

Table 2.1: The timing of the stride [1, 44].

| **Phase** | **Steps** | **Percentage** |
|---|---|---|
| **Stance Phase** | First Contact | 0 % |
| | Loading Reaction | 0 - 10% |
| | Mid Stance | 10 - 30 % |
| | Terminal Stance | 30 - 50 % |
| | Pre Swing | 50 - 60 % |
| **Swing Phase** | Initial Swing | 60 - 70 % |
| | Mid Swing | 73 - 87 % |
| | Terminal Swing | 87 - 100 % |

The gait cycle is demarcated through distinct activities, as listed in Table 2.1. Principally, the typical timing of the aforesaid activities that distinguish the gait cycle – that is, the heel-to-toe

contact – is hereby expressed as a percentage of said complete cycle of gait [1, 44]. The timing of both the stance and swing phases are presented in Table 2.1.

The gait phase is a periodic paradigm comprising deliberate steps and aesthetic strides. A typical stride along with the approximate phase percentage associated with each step is presented in Table 2.1. Moreover, the definition of a full cycle of gait rests on the time at which the starter leg hits the ground again. The double-support phase is roughly 10% of each step. The stance phase is 60% of the gait cycle (when the foot is grounded). The other foot, which swings forward in the air, is described as being part of the swing phase of gait. The study of the relative motion between adjacent joints (joint kinematics) and the forces that instigate this motion (joint kinetics) is thus essential. More specifically, kinematics focuses on the relationships among displacement, velocity, and time, while kinetics studies gravity, torque, and friction.

Most research efforts that use a motion capture system for prosthetic and gait analysis employ computational methods based on inverse dynamics and kinematic data to estimate gait parameters. Nonetheless, there are inherent drawbacks to this approach that influence the accuracy of results. For instance, errors in readings can be caused by markers placed on the body to signify joint centres [45]. The malleolus can be located easily, as it protrudes at the ankle; however, the lateral femoral condyle is hard to locate, as it is found deep in the muscle. Furthermore, the skin is a form of tissue that stretches and moves easily, changing the original position of the marker [45]. This inaccuracy impacts models due to the resulting generalisation estimations for the population. Major errors have been found in results when the orientation and joint position do not represent the patient [21]. These issues result in considerably high uncertainties, estimated at between 6% and 232% for torque estimates in the case of the 13-segment linkage model. The values increase from the distal ankle to the proximal hip joint, which exposes the error propagation intrinsic to inverse dynamic calculations [46]. By contrast,

the GRF measurement technique using a force platform is not exposed to these limitations; in other words, it is a reliable and repeatable technique that yields accurate and precise results. Accordingly, emphasis has been placed in this thesis on understanding the variation of GRFs in order to define ULs and the resulting stiffness design methodology for prosthetic feet.

### 2.2.1 The vertical Ground Reaction Force (vGRF) Curve

Force plates are used to collect GRF data; this means a patient is required to stand, walk or run on top of the force plate to measure the load response. Usually, these plates measure forces in three dimensions and can be incorporated into treadmills [47]. Existing approaches to measuring GRFs and body kinematics generally comprise optical motion capture systems combined with floor-mounted Kistler force plates [35]. However, these methods have some limitations; for example, observing a limited number of strides cannot adequately represent the variations that occur during standard gait cycles. Moreover, the force plates employed can only facilitate measurement of the GRF acting on a single foot as well as occurring only on a limited area, which may not accurately reflect the normal gait characteristics.

The direct measurement of ground reactions has been shown to yield the most accurate gait analysis results. One of the most common approaches utilised in gait analysis is the M-shaped GRF plot for the stance foot and its association with the breakdown of the actions during gait, as shown in Figure 2.2. The first two peaks produce very similar values at self-selected or free walking speeds. At lower walking speeds, these peaks are less discernible than at higher speeds.

Different approaches can be applied to obtain this data, and the methods used are dependent on the associated costs and evaluation purpose. First, the videotape examination method enables an accurate time-base and cheap definitions of each event and phase; as a result, it is commonly applied in clinical settings [48, 49]. Nevertheless, this does not offer accurate data relating to

weight distributions, as these are best determined using the force plates that are below the stance foot. Coordinating the accurate momentary pressure profiles and phase definition with data on joint rotation from potentiometers and strain gauges is pivotal [50]. A plot of the vGRF found in the sagittal plane can be established in relation to the stance phase percentage and the seven stages of the gait cycle. This curve is critical to prosthetics due to its variation between individuals, which shows how the mechanics and kinematics are unique to each patient. It is affected by elements including the gait abnormalities, gait speed, and anatomy of the individual, which underscores the need for prostheses to be used for different functions [51]. Secondly, an understanding of a healthy foot's functioning can be used to optimise the prostheses to a patient's natural behaviour. Judging from this characteristic profile of a healthy gait, the collective transient forces and the joint and muscle anatomical response can be used to conduct a detailed evaluation and optimisation of the correct stiffness profile for an unreceptive prosthesis.

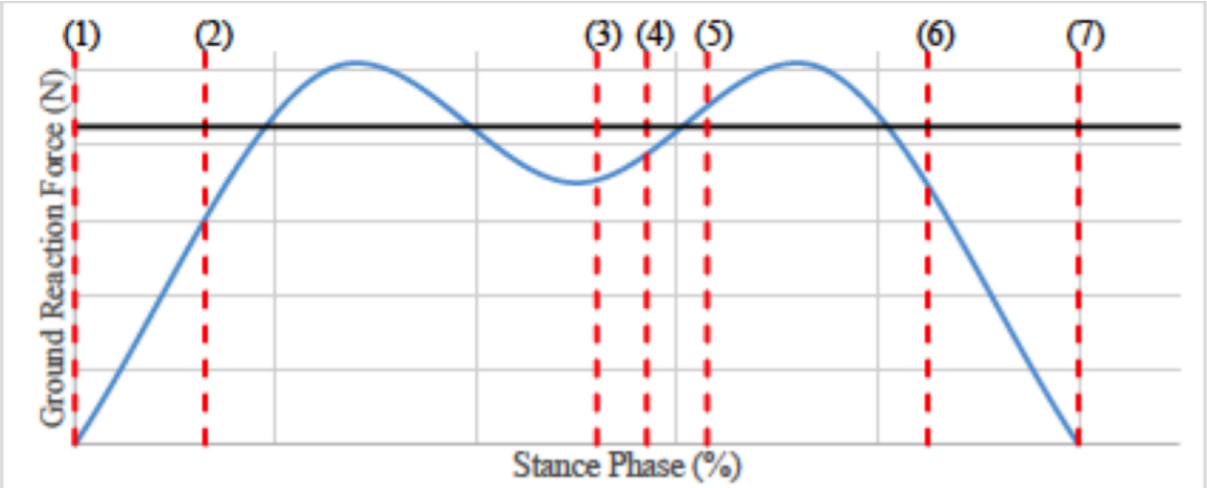


Figure 2.2: The gait cycle stages of GRF with stance phase; here, the horizontal black line represents the subject's body weight.

The initial peak is a collective response of the momentum change in the initial body contact (Figure 2.2, label (1)) and the vigorous reaction of the opposite limb that provides forward

momentum upwards until the opposite toe lifts off for the case in question (Figure 2.2, label (2)). Together, these forces cause a GRF that rapidly peaks above the body weight (generally 200%-300% while running and 120% while walking). This means that the prosthetic foot should be designed to withstand the pressure of heavy loads while also absorbing the impact to shield the remaining limb [52, 53]. To attain this profile, the stiffness of the prosthesis can be designed using a high level of accuracy based on individuals [54]. The testing approaches stipulated in ISO 22675 [33] are founded on this typical profile, along with varying patient weights, which are input into a computer model to ascertain the structural integrity of the proposed designs.

The trunk then enters a controlled fall where the core muscles and those below them provide active support to the stance leg. Following this, the GRF gradually falls below the body weight until the feet are adjacent (Figure 2.2, label (3)). At this point, the prosthesis has replicated various functions including joint rotation, shock absorption and the movement into one support at mid stance (Figure 2.2, label (2-4)). Figure 2.2 (label (5-7)) represents the toe-off stage. This explains the significance of variable stiffness, which is a critical facet of competitive patient-designed prostheses. The other approach that can be utilised to ascertain the significance of variable stiffness is the use of a Pedotti diagram (see Figure 2.3), which illustrates the resulting ground reaction vector force found in the sagittal plane in relation to foot progression from left to right [1]. The magnitude associated with those seen in the typical GRF profile are described above. However, this plot offers valuable information concerning force direction. Despite the fact that the magnitudes have been replicated accurately, the prostheses may be inefficient in copying biological movements. This further emphasises the problem of the prosthesis' ability to imitate the behaviour of a healthy foot being directly associated with the variable stiffness profile, which dictates energy use where accurate profiles are related to pathological conditions [21].

The last facet of the stance phase entails the stance foot acting to move the body forward

using an active muscular reaction at heel rise [5], which can be attributed to the second peak above body weight. The second peak presents various design issues for passive prosthetics, as they can emit the level of kinetic energy that they can absorb. The Pedotti diagram demonstrates the directional importance of the resultant force, where the energy brought back should be effectively managed to transmit momentum through the body in order to push the body forward and upward.

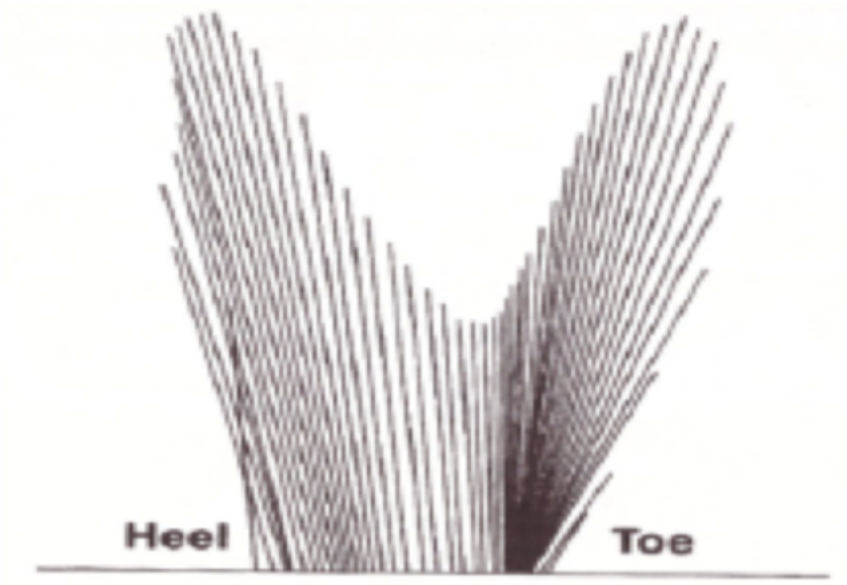


Figure 2.3: Pedotti diagram [50]

The European Standard EN ISO22675 [33] is applied for all tests that involve investigating the fatigue, proof, and ultimate strengths of prosthetic ankle-foot devices and foot units. This standard provides the conditions that the parameters employed in the test equipment must satisfy and can be tested under [55]. The pulsating force $F_c$ is applied as a synchronised function of time $F_c(t)$. According to the standard, $F_c(t)$ is defined by the following: $Fz1$, which is the maximum test force exerted at the quarter percentile of the loading period; $Fz2$, which is the minimum test force applied at the half percentile of the loading period; and $Fz3$, which occurs

at the three-quarter percentile of the loading period. In this case, the loading period is taken as the average time taken to execute a stance phase during a normal cycle of one second in length. It is assumed that the swing phase after the stance phase takes $400ms$ to complete. Taking this into consideration, the equation of $F_c(t)$ expressed as a sixth-degree polynomial becomes:

$$F_c(t) = Fz1 \times 10^{-3} \times 5.12306842296552 \times 10^{-12}t^6 - 9.2037374110419 \times 10^{-9}t^5 + 5.98882225167948 \times 10^{-6}t^3 + 1.64651497111425 \times 10^{-1}t^2 + 3.62495690883228t \quad (2.1)$$

However, this equation is limited by the fact that it applies to free walking speeds (FWSs). The pulsating test force $F_c(t)$ and tilting angle $\gamma$(t) in a standard cyclic test when plotted as a function of time are shown in the figure below. The loading period used is $600ms$.

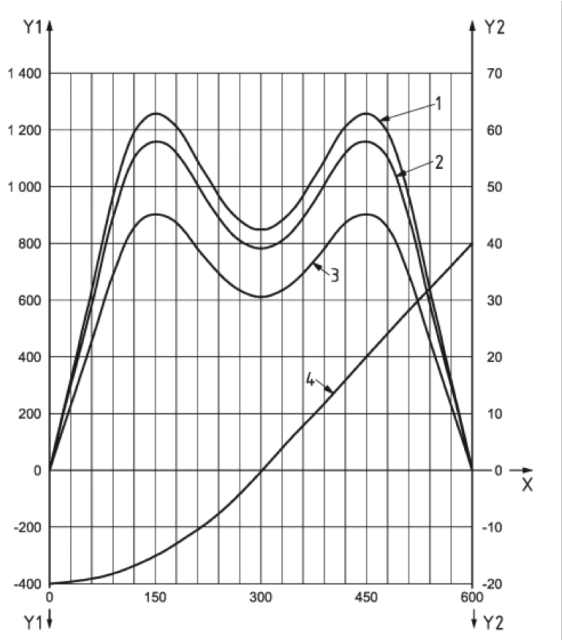


Figure 2.4: Graph showing $F_c(t)$ and $\gamma$(t) plotted as functions of time to determine the cyclic loading conditions in the revised ISO22675 [33].

In Figure 2.4, the loads P3, P2 and P1 correspond to loading weights (mass) of $60kg$, $80kg$ and $100kg$, respectively. Moreover, it is evident that the force $Y1$ increases up to the $25^{th}$

percentile of the loading period, drops up to the $50^{th}$ percentile of the loading period, and rises again up to the $75^{th}$ percentile of the loading period.

### 2.2.2 The Relationship Between Different Walking Speeds and GRFs

Understanding how walking speed variation impacts vertical ground forces is essential, as this knowledge can be useful when synthesising musculoskeletal models for various purposes. Additionally, it can also greatly aid in the diagnosis and treatment of injuries that afflict runners, as well as enabling assessment of their performance. Changes in walking speeds lead to varying impacts of vGRF on the gait (as shown in Figure 2.5) and stability of an amputee. The surface contact of prosthetics differs from that of anatomical limbs. Prosthetic alignments manipulate the GRF due to their lower extremity. The propulsive force derived from prosthesis differs from that of natural legs. A person's body weight, acceleration, and vertical force influence their walking speed. The design of prosthetic legs should thus consider the changes in walking and ambulation due to the loss of limbs.

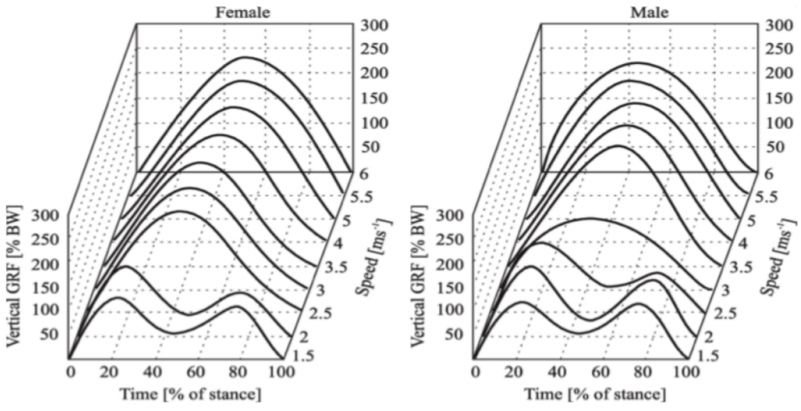


Figure 2.5: Relationship between three parameters such as vGRF, speed, and time (%stance) for both male and female [56].

## 2.3 Walking Asymmetries Due to Amputation

There are many causes that may lead to asymmetric walking mechanics, such as injury, stroke, and neuromuscular and joint disorders, among others. Prosthetic feet exhibit shorter stance times, while contralateral intact extremities exhibit higher peak forces. It is important to note that amputees should not focus solely on achieving a symmetric gait during rehabilitation; they can also settle for a temporal asymmetric gait, which is acceptable in a prosthetic situation [57]. Moreover, as suggested by researchers such as Singh [8], healthy gait is not purely symmetric: one leg propels the body, while the other one pivots it to the ground. An investigation of the correlation between limb dominance and symmetry in healthy gait was carried out by Sadeghi et al. [37,58], who found a healthy gait to be asymmetrical due to the varying action of different limbs: one offers support, while the other aids in propulsion [58]. These observations have also been confirmed by Herzog et al. [59], who contend that rehabilitation experts should bear in mind that regular walking is not symmetric and should thus guide patients recovering from musculoskeletal or neuromuscular conditions accordingly. Furthermore, disregarding the asymmetries of gait may be beneficial in some instances for three key reasons: it makes modelling easier, produces a more convenient model, and yields a better predictive model.

A distinction is made in this thesis between kinematic and kinetic asymmetry. The reason for the asymmetry is the mass imbalance between both legs and a lack of muscle and ankle support for the prosthetic foot. Kinematic asymmetry measured by gait asymmetry (i.e. asymmetric step lengths) is not considered important in terms of its contribution to ULs. By contrast, kinetic asymmetry (i.e. asymmetry in the resulting GRFs between each leg) contributes directly to ULs; hence, it is important to minimise this asymmetry.

### 2.3.1 Computing Gait in People with Amputated Limbs

A large body of research exists concerning amputee gait behaviours. Vanicek [60] acknowledge that amputees are far more prone to fall-related injuries while walking around. Miller et al. [61] point out that most amputee patients are over the age of 55, and that these persons tend to exhibit an asymmetrical gait. Unfortunately for them, they may therefore develop musculoskeletal degenerative changes in the future according to [18, 62–64]. Prosthetic feet, although important in helping amputees to ambulate, have reduced coordination and stability, which makes the user prone to falls because of their unstable walking patterns with varying velocities. They also struggle to adapt to different walking velocities. Notably, as per [65–68], a normal leg has a longer stance time than a prosthetic one; although the results are uncertain, this is generally attributed to discomfort experienced in the residual leg, lack of feedback regarding foot position, and a problematic socket. Additionally, decrements in strength on the prosthetic side and a reduction of confidence in supporting the body weight with this leg may also affect the stance time [67]. The intact leg compensates for the deficits of the prosthetic leg, such as ankle push-off or absent knee extensions, according to Schaarschmidt et al. [69]. The intact leg also shoulders the load bearing while the prosthetic leg drives propulsion through its altered touch-down angle. An experiment was conducted by Snyder et al. [70] to test the gait and load impacts of the residual extremity of five dissimilar prosthetic feet. These authors found that, during loading, the residual limb is prone to heightened vertical forces, notwithstanding a minimised walking velocity. These observations were congruent with those of other researchers [64, 69, 71]. However, the flex-foot was the only one that exhibited different characteristics: it has a large arc of dorsiflection motion and a flexible lengthy heel. Even though amputees exhibit an asymmetrical gait compared to non-amputees, they do not necessarily generate greater forces across the joints of the contralateral

extremity of an amputee compared to a non-amputee, as noted by Hurely et al. [72]. Concurring sentiments have been made suggesting that transtibial amputees undergo a higher GRF peak on their sound leg than in their prosthetic [73]. The same observation, albeit negligible, has also been made for transfemoral amputees.

### 2.3.2 The Mass Imbalances Associated with Prosthetics

As Mattes et al. [67] noted, prosthetic feet designers prefer to use lightweight materials to more accurately reflect the weight of a physiological foot. There have been suggestions that prosthetic asymmetries stem from the use of these lightweight materials. Despite this weight change, it incurs more energy costs when loaded identically to the sound leg [74]. Notably, the metabolic energy costs vary with the type of prosthetics used, with distally positioned prosthesis masses exhibiting more efficiency than proximally positioned masses [75–77]. Another method of increasing the energy cost and achieving greater asymmetry, as reported by Mattes et al. [67], is equating the moments of inertia for the sound leg with that of the prosthetic leg, thus confirming the theory that equating the inertial traits of the legs does not necessarily yield a symmetrical gait. Research has also been conducted on the effects of varying the perturbations of a dissimilar prosthetic weight in the walking cycle. In particular, the area of concern is to determine whether the kinetics and kinematics would be affected. The obtained results imply several outcomes. First, transtibial amputees possess the ability to adapt to mass perturbations. However, their joint kinematics remain unaltered; only the torque at the joints changes [38]. Put simply, an amputee spends more energy trying to preserve the same joint angles in the walking cycle. Although it is clear that the minimisation of energy cost is insignificant, it remains unclear why the aforementioned strategy is used. It has been speculated that amputees may desire to walk in the same manner as non-amputees; that is, by matching the contralateral leg and the prosthetic

leg kinematics. In order to become accustomed to asymmetrical changes in the lower limb inertial characteristics, a five-minute walk is recommended by Smith and Martin [74, 78].

### 2.3.3 Asymmetry in vGRFs for Sound and Affected Legs

The vGRF value varies between able-bodied people and amputees. Numerous investigations have been conducted with the aim of elucidating the correlation between gait speed and GRFs for non-disabled and disabled persons. Human gait is optimised based on morphology and preference; this is achieved by minimising energy expenditure. Following an amputation, patients must adapt to the stiffness and morphology of the prosthetic, while at the same time attempting to optimise energy efficiency. The change is harder for the elderly because they tend to place unhealthy weight on the sound limb; this is both uncomfortable and may cause injury. This means that the sense of discomfort and other adverse impacts of prosthetics can be linked to the dissimilarity between residual and sound limbs.

Controlling the adverse impacts of prosthetics calls for a stiffness that is optimised according to the patient's lifestyle, anatomy and gait. These issues are amplified by the fact that most transtibial amputees are elderly diabetes patients. Consequently, these patients are at risk when carrying heavy loads due to their weak musculoskeletal tissue and brittle joints; therefore, it is critical to come up with a solution. Figure 2.6 compares GRF plots for the residual limb and sound leg, depicting the asymmetry of gait after amputation. The GRF plot of the residual limbs depends on the prosthetic energy transfer and storage during gait. The energy transfer is linked to the stiffness profile, and eventually, the prosthetic geometry. Therefore, the prosthetic foot geometry can be optimised to alter the stiffness profile in order to obtain the desired GRF plots, consequently reducing discomfort and ULs for the patient.

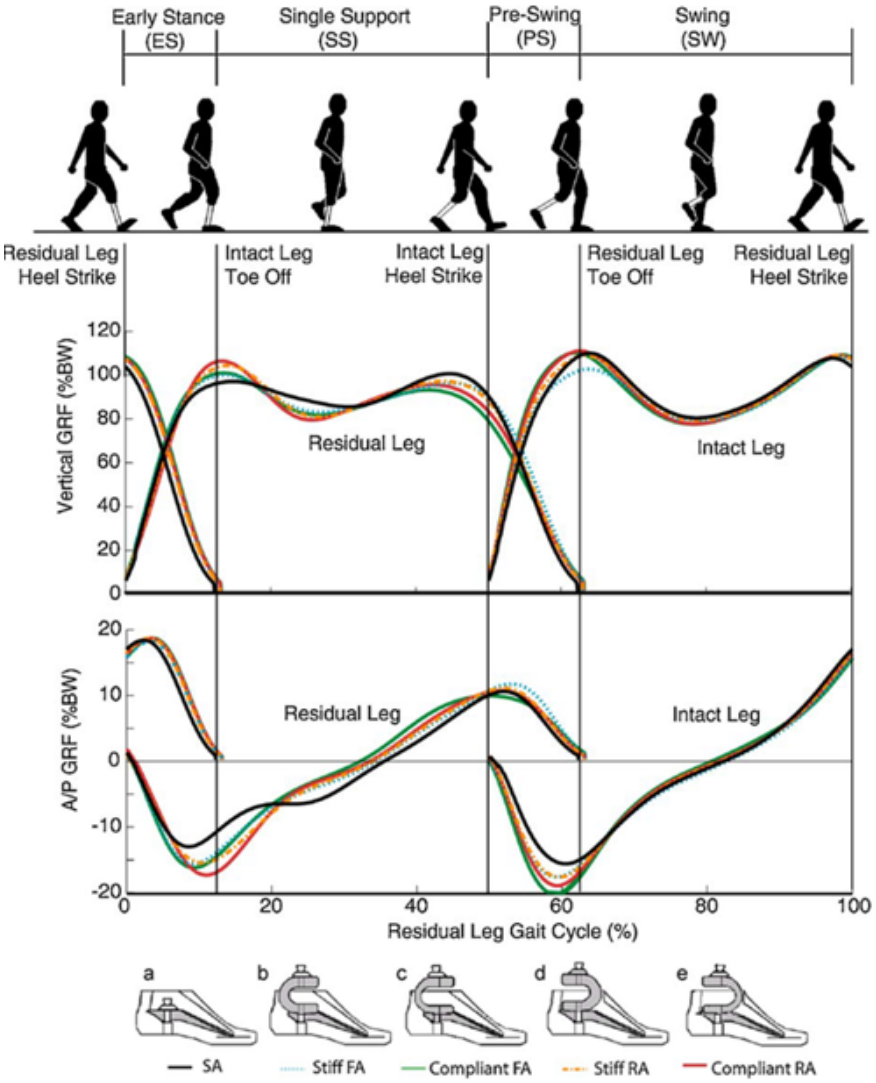


Figure 2.6: The vertical GRF variation. Regions of the residual leg gait cycle and corresponding vertical and anterior/posterior (A/P) GRFs of the intact and residual legs. Early stance (ES) is defined as being from residual leg heel strike to intact leg toe-off; single support (SS) follows until intact leg heel-strike; pre-swing (PS) follows until residual leg toe- off, and swing (SW) follows until residual leg heel-strike. Ankle conditions: (a) solid ankle (SA); (b) stiff forward-facing ankle (FA); (c) compliant FA; (d) stiff reverse-facing ankle (RA); (e) compliant RA. The effect of prosthetic ankle energy storage and return properties on muscle activity in below-knee amputee walking is outlined in [79]

Keller et al. [56] investigated the behaviour of the vertical GRFs over varying walking speeds of non-disabled persons (specifically, fast walking and jogging). These authors observed that the GRFs varied consistently as the gait speed increased; there was also a linear correlation between the vertical thrust maximum and speed increments, albeit only up to a velocity of $4m/s$ (beyond this limit, this force remained constant). A similar linear relationship between the varying walking speeds and gait of children was observed by Schwartz et al. [80]. Importantly, there is a substantial difference between running while maintaining an upright posture and leaning forward: the latter reduces the centre of gravity and downward velocity of the runner's body, which lowers the magnitude of the GRFs; likewise, slow jogging produces more forces than walking, as it demands a higher centre of gravity, which in turn increases the downward velocity of the body and consequently the magnitude of the GRF [56].

Chiu et al. [81] also studied whether there were any significant contributions made by speed and gender in the magnitude of vGRFs. Their findings demonstrated that the vGRFs varied at different speeds. For instance, the scope of the force generated at speeds of 4 and $5km/hr$ exceeded that generated at speeds of $3km/hr$. However, this was seen during the loading response phase; the inverse was observed during the mid-stance phase. Thus, as walking speed increases, the peak force in the loading (heel strike) phase increases, while the vertical reaction force reduces as the speed increases in the mid-stance phase. Gender-wise, females exhibited more vertical ground forces in the loading and toe-off stages, since they walk faster by increasing step length compared to males (who vary their cadence). Chung and Wang [82] supported these findings in a study conducted to investigate the behaviour of gait parameters at different walking speeds, which exhibited similar results. The researchers found that walking speeds greatly affected the resultant vertical GRFs. Notably, increasing the speed resulted in an increased vGRF in the heel strike phase and a decreased vGRF in the flat-foot phase. The higher vGRF

during the heel strike stems from the fact that the lower-extremity muscles are forced to work more to reverse the downward momentum. Conversely, the decrements observed in the vGRF at mid-stance as walking speed increases can be attributed to the deceleration of the centre of gravity's vertical lift at higher speeds. Moreover, the vertical oscillation of the person's COM is more significant as walking speed increases. Nolan et al. [73] studied trans-tibial and trans-femoral amputees to learn the adjustments made to their gait symmetry and, in particular, the effect of varying walking speeds on the magnitude of vGRFs. Their findings corresponded to those of other studies finding that the vGRF increased as the walking speed increased, albeit more on the intact limb than the prosthetic limb. The same effect was noted on trans-femoral amputees; the loading on the limbs increased as the walking speeds slowly transitioned [73].

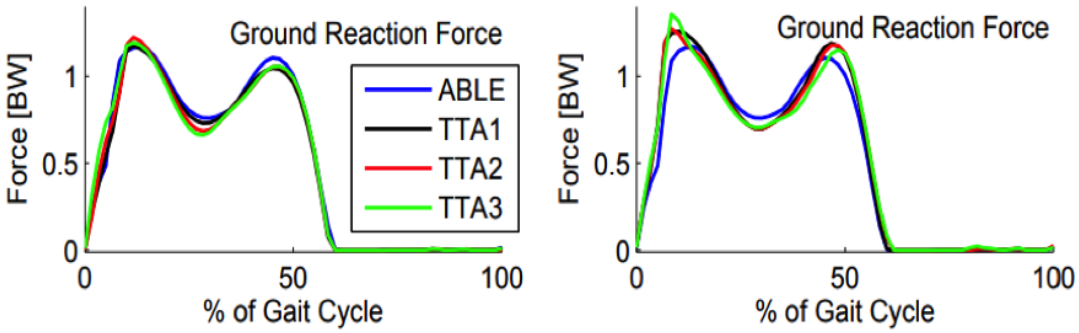


Figure 2.7: GRFs for the sound (right) and affected (left) legs for solutions TTA1, TTA2, TTA3, and ABLE [83].

Predictive simulations have been employed by prosthesis designers to predict how the gait of trans-tibial (TT) amputees is affected. Using this approach, TT amputees were investigated by Koelewijn [83] to facilitate understanding of the joint moment asymmetry that occurs in the hips and knees. Also observed were the GRFs on both the sound and affected sides. The experiment used three solutions – TTA1, TTA2, and TTA3, each with varying weight parameters (0, 0.3,

and 10) – to vary the effort exerted on the feet. The findings indicated that less effort was exerted in an asymmetric gait; however, a slight increase in the amount of effort amplified the joint moment symmetry and decreased the joint reaction forces. The predictive simulations also showed that the peak GRF on the sound limb was highest for solution TTA3 (see Figure 2.7).

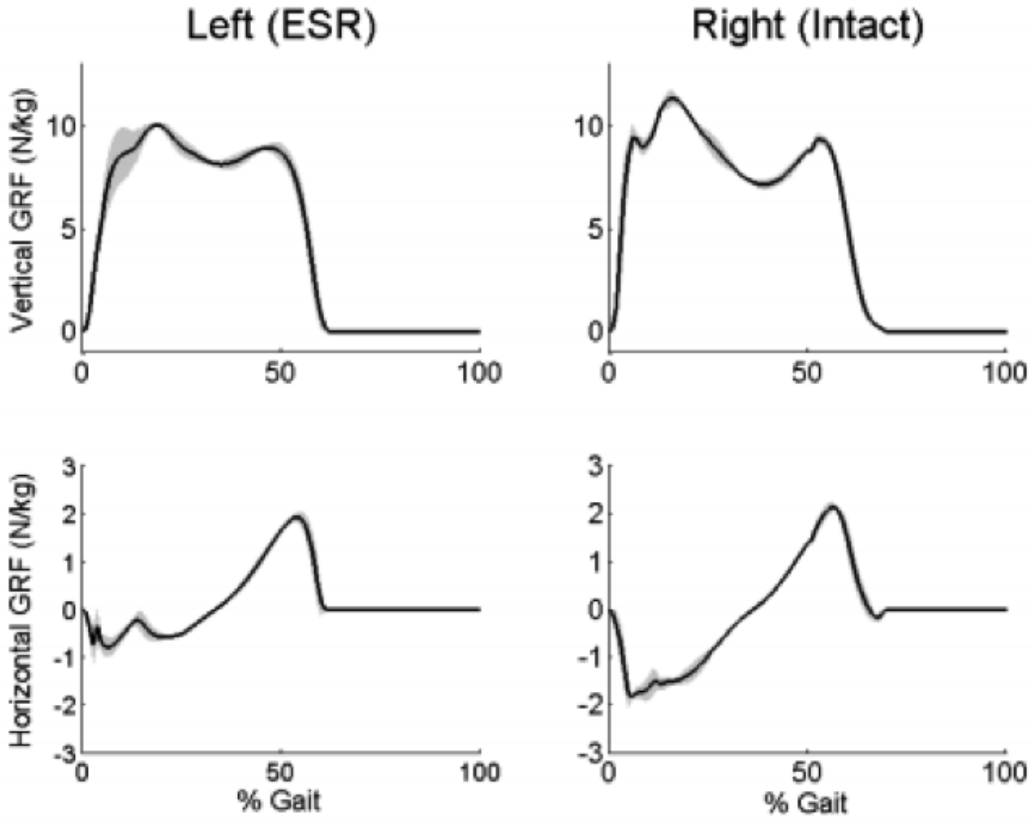


Figure 2.8: Graphs plotting the average GRFs (vertical and horizontal) for the affected and sound limbs. The affected limb is fitted with an ESAR foot prosthesis [84].

The presence of stronger forces on the side with the sound leg indicates that the muscles perform more work on this side than on the side with the affected limb. The vertical GRF for all solutions on the side with the affected limb was identical, as shown in Figure 2.7. Similar observations were made by LaPre [84], who analysed the average reaction of nominalised GRFs on the affected and sound limbs (see Figure 2.8). In this case, the affected limb was fitted with an

energy storage and return (ESAR) foot. The study revealed that the vertical and horizontal GRFs were higher on the sound side than on the prosthetic side. Notably, the recorded horizontal GRFs affirmed that, during initial loading, a slight oscillation occurs in the three rotational coordinates: this is attributed to the absence of any significant reaction moment for the subject to stabilise against as they balance on the unactuated residuum-socket joint.

Amputees have also been shown to exhibit varying ranges of angular momentum at varying walking speeds. This phenomenon stems from the symmetry between foot placement and GRFs [17]. This knowledge is useful for understanding why amputees are more susceptible to falling compared to non-amputees. Silverman and Neptune [17] experimented with both amputees and non-amputees to determine the variances in whole-body angular momentum across different walking velocities. These authors noted that, as the velocity increased, the range of the three measured angular momentum components decreased for both non-amputees and amputees. Also noted were interaction effects in the GRFs between the two groups as walking speeds varied.

The same phenomenon was noted by Nolan et al. [73]. Conclusively, the GRFs affect the time rate of change for the angular momentum. The results from amputees also revealed an increased positive time rate of change of angular momentum, attributed to the considerably smaller second intact vertical GRF peak. Remarkably, the frontal plane angular momentum for the same quantity exhibited a negative correlation at walking speeds of 0.9 and $1.5m/s$. Further observations showed a reduced residual vGRF in the second half of the residual gait cycle; consequently, the angular momentum exhibited a more negative time rate of change. Compared to non-amputees, this quantity was smaller for all measured speeds. Furthermore, a negative correlation with the range of angular momentum at velocities of 1.2 and $1.5m/s$ was evident. The decreased intact and residual vertical GRF during the first and second half of the

residual gait cycles respectively caused a broader range of frontal-plane angular momentum for the amputees (see Figure 2.9).

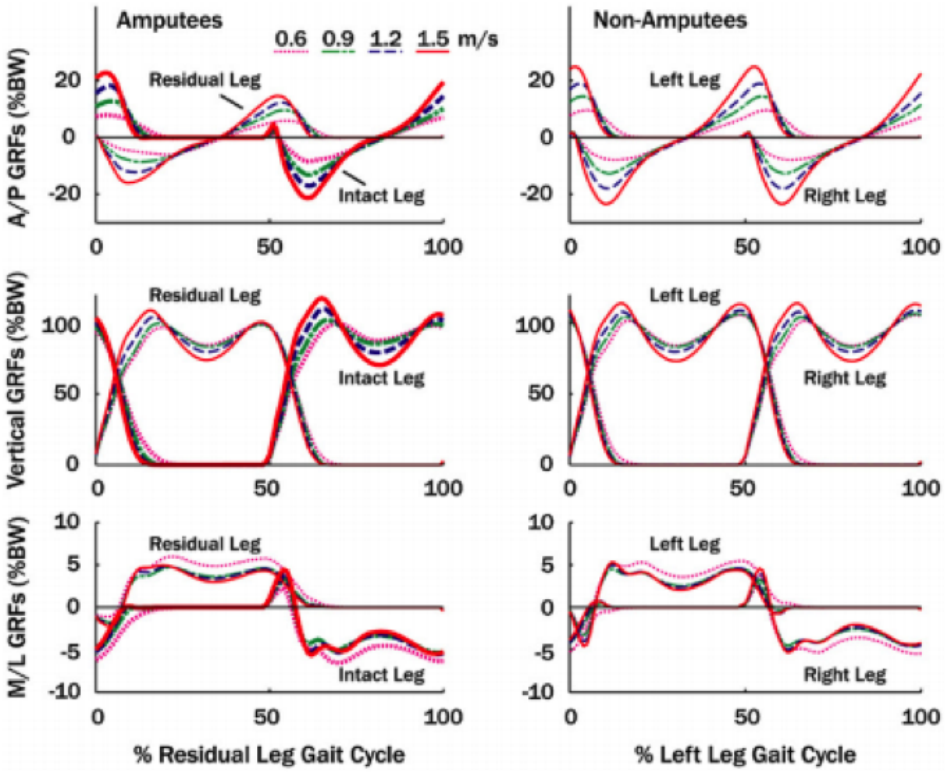


Figure 2.9: Simulation graphs plotting the average GRFs for non-amputees and amputees at measured velocities. The GRFs have been normalised to the gait cycles of the left (non-amputees) and residual (amputees) limbs. A/P denote Anterior/Posterior; M/L denote Medial/Lateral [17].

The position of the residual and intact legs relative to the body's centre of mass (COM) during the residual gait cycle affects the body's external moments. A reduction in the residual braking force decreases the negative external moment on the body. Consequently, the time rate of change for angular momentum is positively increased. In comparison, amputees showed a lower residual peak braking than non-amputees at all walking speeds, which can be attributed to the range of sagittal-plane angular momentum at the measured peak velocities. Additionally,

the COM's negative external moment would be reduced by the posterior X-moment arm and the decreased intact vGRF. By contrast, a negative correlation between the angular momentum's range at the measured top velocities and the reduced intact second vGRF was observed. These observations inform the conclusion that residual braking contributes significantly to a broader range of sagittal-plane angular momentum in the first half of amputees' gait cycle compared to the contributions of the intact second vGRF.

In the second half of the residual gait cycle, the range of sagittal plane angular momentum was lowest for amputees. Since the residual leg provided both the propulsion and the intact leg braking, the peak propulsive GRF on the residual side was smaller for the amputees. This causes a negative effect on the positive external momentum and angular momentum's rate of change. Moreover, the effect of the reduced residual propulsion on the angular momentum was opposed by the smaller residual posterior $X$-moment. At the same time, a negative correlation was observed between the larger intact $Y$-moment arm and the range of angular momentum for all walking speeds. However, this correlation was not as strong as the one with the residual propulsive GRF. In addition, the transition of the anterior/posterior GRF from braking to propulsion yielded the maximum Y-moment, as well as a small external moment. The prosthetic foot employed affects the magnitude of both the GRFs and that of the external moment arms, which influences the overall angular momentum trajectory of the body. Overall, the first and second residual gait cycles have a reduced intact vertical and residual GRF, respectively, which correlates with the higher range of angular momentum observed in amputees. It is important to note that the study that produced the above results did not factor in the contribution of specific muscles (such as the arms) to angular momentum; future studies should focus on this.

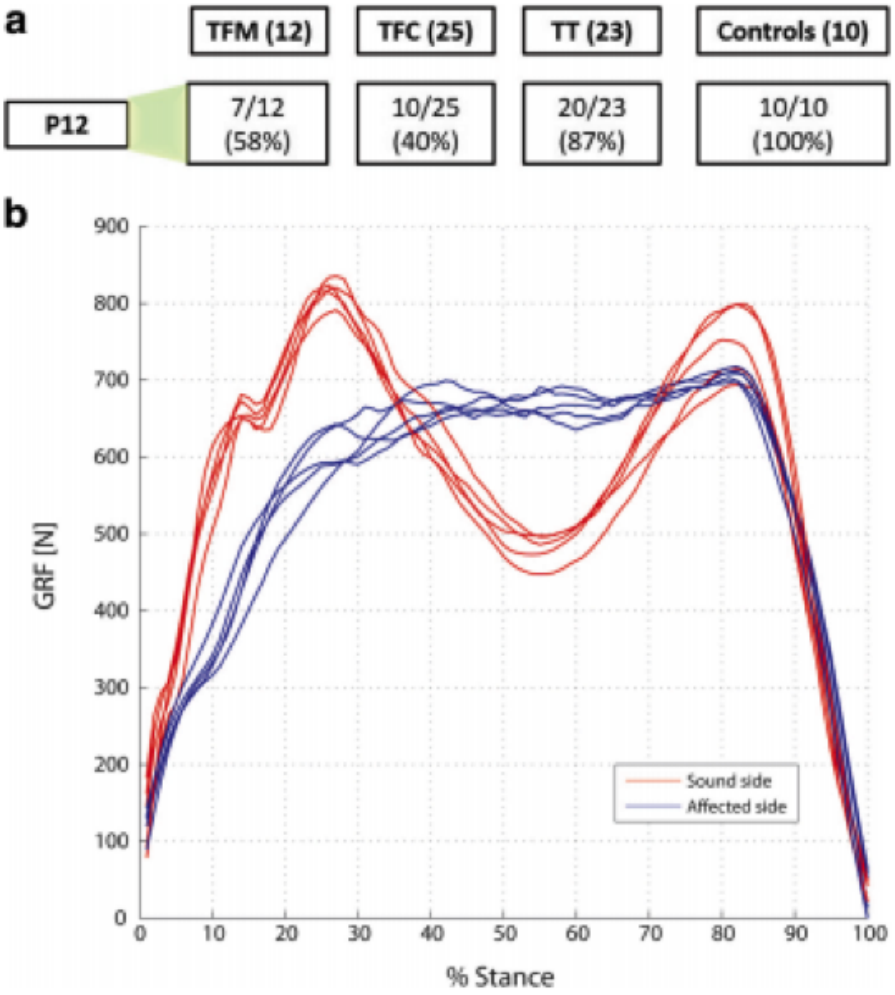


Figure 2.10: Simulation graph plotting the typical patterns of vertical GRFs that are characteristic of Transfemoral (TFM), Transtibial (TT), Transfemoral using the C-leg (TFC) and Healthy control subjects (control) [85].

Understanding the loading symmetry and gait temporal of lower-limb amputees is crucial; it can help to improve the design of prosthetic feet in order to achieve a more improved roll-over shape and push-off, as well as an enhanced range of motion to decrease the initial peak at loading response. Cutti et al. [85] experimented with several subjects with different levels of amputations in order to obtain more insight about whether the type of prosthetics used and the amputation performed affected the classical levels of loading and temporal symmetry. Their

investigations concluded that the amputation level greatly influences the impulse, stance, and first peak symmetries for TF and TT amputees. TT amputees, in particular, experience the lowest impulse, but a higher first peak at loading response on the side with the sound limb (see Figure 2.10). The type of prosthetic components used also affect the loading response and temporal symmetry: the more advanced the prosthetic, the more positive the effect. For example, using an ESAR foot enhanced all symmetry indexes for TT amputees compared to using a solid ankle cushion heel (SACH) foot. TT amputees also overload the sound side with increased peak GRF.

## 2.4 Concluding Remarks

Innovative prosthetic designs address the activity levels of the intended uses. Amputees expend a wide range of energy depending on their walking speeds. However, many designs fail to consider their gait asymmetries. The stiffness of the prosthetics is dependent on the activity level of the individual. Currently, four major levels are used to classify patients' needs showing their level of mobility: these vary from $K1$ to $K4$, with $K1$ depicting limited mobility. A $K$-scale is defined to categorise functional mobility of amputees in five groups, i.e. $K0$-$K4$. More specifically, the $K0$ category is for amputees with no mobility, $K1$ indicates very limited mobility, $K2$ is limited mobility, $K3$ denotes average mobility, and category $K4$ corresponds to the most mobile amputees [86]. Previous evidence has shown that most amputees are either diabetic or ageing and have existing damage to their musculoskeletal tissue and joints, which reduces their level of motion. Therefore, the focus is on differentiation between $K1$ to $K3$ activity levels, as they make up most of the patients and thus translate into the largest market share. Most of the prosthetics are accordingly tailored to meet the needs of those within this range.

The walking profile is more intricate, while the running profile has one peak (as shown in Figure 2.5). For the running gait cycle, the prosthetic should effectively function like a spring, as one tends to bounce while running. On the other hand, walking gait is different, as it requires a diverse stiffness profile to comfortably and effectively transmit the heel strike to the toe. For example, activity level 2 users require softer springs to benefit from the prosthetics; transtibial and transfemoral amputees are required to set the foot one spring lower [87]. Activity level 4 users require either softer or stiffer springs depending on their weight. Hence, the activity level influences the stiffness response required from the prosthetic foot.

Walking speeds also exert a significant impact on the gait of lower limb amputees. However, the expected vGRF varies depending on the walking speed. The prosthetic materials' rate-dependent stiffness and elastic hysteresis properties affect their responses to changes in speed. There are differences in vGRF between FWS and slow, fast, and very fast walking. The velocity generated depends on a person's speed (both healthy people and amputees); an increase in speed leads to an increase in vGRF. The centre of mass is higher and less fixed when a person is running. However, limb support affects the ground force due to the alignment of muscles. Amputees have a single-limb support, which contributes to a decrease in vGRF. As a result, the proposed computational methodology for prosthetic foot design needs to consider the effect of changes in walking speed among lower-limb amputees. This is further discussed in Chapter Four, in which a novel set of GRF equations is proposed for use in the objective function in order to minimise ULs during the stiffness optimisation process of prosthetic feet.

# Chapter 3

# The Roll-Over Shape as a Design Variable for Stiffness Optimisation: A Review

## 3.1 Introduction

Since the commercial introduction of the ESAR prosthetic foot in 1985 [88], amputees and prosthetic users have been able to choose ever more specific and potentially suitable feet for any given application. These feet are referred to as 'energy storing and returning' feet because they store energy at the amputee's heel strike. This potential energy is returned at the toe-off stage. The optimal stiffness response of a prosthetic foot is expected to enhance a person's stability during locomotion. Below-knee amputees have unique gait characteristics due to the functional loss of their leg muscles. The stiffness of the prosthetic foot is designed to enable the foot to assist forward propulsion and offer body support. Both gait analysis and kinematic modelling form integral parts of the stiffness optimisation process. It is true that a great deal of information has been derived from human experimentation; however, grasping the fundamental principles of biomechanics in operation can be quite problematic [89].

There is only so much that experiments can reveal to us, and developing a gold standard definition of what amounts to healthy walking is not an easy process to attempt. For example, there are times when muscles may malfunction, either due to injury or a congenital weakness. In such cases, using cognate computational models can help to elucidate the peculiarities observed in the locomotion of the human body [39].

This chapter aims to outline PWD models that may mimic the walking system of a human being. Existing models that anticipate facets of human walking are evaluated. Additionally, this chapter also elaborates on the main elements of the biomechanics of walking, which grant utility to the field of robotics or general gait rehabilitation. The above-mentioned models come in different forms, from simplified ones like the inverted pendulum to more intricate ones involving musculoskeletal anatomical models [90,91]. Simulations of musculoskeletal-multibody systems amount to depictions of muscles, bones, ligaments, and other structures. Muscles generate joint moments, which can be computed to survey the effects of the geometrical shifting of the musculoskeletal system and other criteria of the model. The inverted pendulum model is one example of a simple model of this kind [91, 92]. Its complexity can however be enhanced by incorporating an additional swinging leg, motor elements or compliant links, and knee or ankle joints between the joints (see Section 3.3). The spring-loaded inverted pendulum model [91] for simulating human gait is also briefly discussed. Most of the focus is targeted at passive walking. These models are aimed at the simplification of gait processes and grant a deeper comprehension of locomotive dynamics of humans. During walking, a non-disabled walker's foot mimics a rolling contact, which exhibits dynamics almost identical to that of a rocker-based inverted pendulum. An inverted pendulum has its centre of mass above its pivot point (Figure 3.7); thus, it is unstable and falls over without additional help. During walking, the stance leg's point of contact with the ground is assumed to be the pivot point around which that hip mass

moves. The swing leg pivots around the hip mass. The motion of equations for walking, as the point of contact rolls along the ROS for the stance leg, follow an inverted double-pendulum model. A mathematical model used to solve these equations for rolling contact is proposed by Mahmoodi [32] and Charles [15], and is used in this thesis.

### A Patient-Specific Prosthetic Foot Design Scenario

This project aims to improve the quality of transtibial prosthetic feet by implementing customisable stiffness, providing patient-specific designs. These designs improve quality by reducing the total number and magnitude of ULs imparted on patient joints, while also increasing push-off power without increasing the weight of the prosthetic; this is enabled by the power efficiency and customisability of the design to individual patients. It is envisaged that future prosthetic feet will be built via additive manufacturing processes, which will broaden the material selection and enhance design specificity via complex geometry. This is in contrast to conventional prosthetic customisation methods that require an experienced prosthesis to tweak generic designs specifically to patients. This process is expensive, requiring one-to-one consultation and a process of trial and error with the patient. The digitalisation of the design and manufacturing process has the potential to reduce lead times for manufacturing patient-specific prosthetics; this is enhanced by installing manufacturing printers in hospitals, digitising the design process, and refining and manufacturing tailored prosthetics. The design is further empowered by mathematical models that predict the required stiffness profiles for the patient, potentially consolidated and improved by conventional testing to corroborate and incrementally improve the models. Furthermore, Finite Element-based ANSYS models of the gait cycle force patterns being applied to the design (in accordance with international standards) are being developed to maximise push-off power and strength-to-weight ratio [93].

One company that has engaged in a similar re-evaluation of the process for designing prosthetic feet is Mecuris [28]. This company employs digitalisation in its design and manufacturing process. The applicability of the digitalisation process suggested in this thesis is further investigated in Chapter Six with a novel double-keel shaped foot, along with the criteria discussed in this and the second chapter. In order to develop the digital design methodology, this chapter further reviews literature to suggest suitable design variables to improve the stiffness performance of prosthetic feet.

The remainder of this chapter is constructed as follows. Section 3.2 discusses the ROS and its use in the finite element-based optimisation method. The current methods for solving swing leg and passive walking dynamics, along with associated problems, are reviewed in Section 3.3 along with the PhD research recently completed at Swansea University that formed a starting point for this thesis. The design criteria and the choice of design variables is discussed in Section 3.4. The chapter is finally concluded in Section 3.5 with the identification of the research task addressed in the following chapters.

## 3.2 The Roll-Over Shape (ROS)

During walking, the knee-ankle-foot and ankle-foot systems produce suitable rockers over which the body can roll in a stable and efficient manner. Rockers have proven useful in unravelling the dynamics of walking, with some authors stating that the foot creates three rockers in one motion [94]. As such, in order to better understand walking, the standard pendulum has been upgraded to incorporate a rocker at the base, which causes it to mimic the forward motion of the COP during walking. Moreover, it also helps in estimating the vertical excursions of the body's COM. Calculating the ROS involves taking the COP of the GRF during the first half of

the gait cycle from a coordinate system in the lab (global) and transforming it into body-based coordinate systems (local); see Figure 3.1 and Appendix E for ROS calculations.

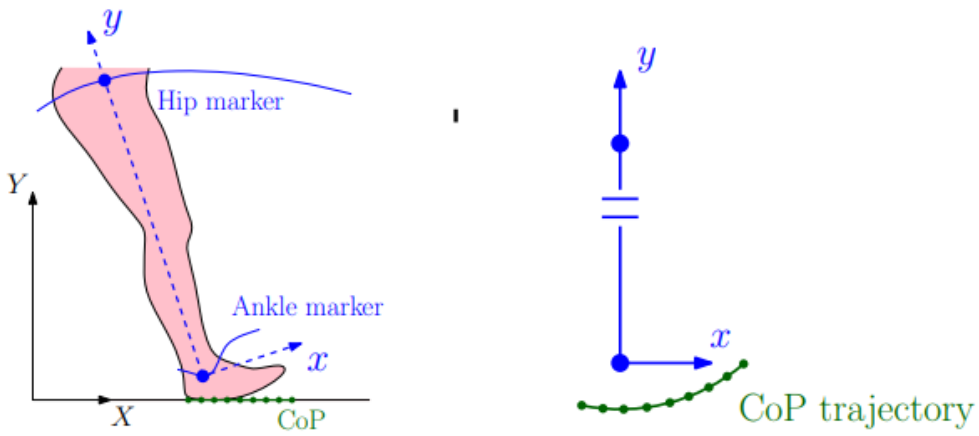


(a) Global coordinate system. (b) Local coordinate system.

Figure 3.1: Motion capture data demonstrating the ROS, which comprises a stance phase's efficient rocker. (a) Hip and ankle directions are represented by markers, and COP locations is obtained using force plates; (b) COP arc is plotted in a 2D plane, in the same way as the stance leg alignment [15].

Investigative findings reveal that walking speed does not profoundly impact the ROS of normal lower-extremities systems [95], the height of the shoe heel [96], during the carrying of more weight [97], and while walking on surfaces that are inclined [98]. The ROS is a modest instrument used to evaluate the gait of an individual, and also for assessing and designing the prosthesis of the lower extremities [99].

Metabolic consumption can be effectively reduced through the use of a rocker radius that is about a third of the length of the leg [100]. Smoother collisional scenarios could be achieved by increasing the arc radii. Wang and Hansen [101] devised experiments in which they made people walk while wearing rocker shoes with contrasting radii. Their experiments confirmed

that the ankle reacted to modifications in the radii of the rocker shoes, along with the speed of walking, to sustain a compatible ankle-foot ROS. Moreover, the most significant kinematic changes seemed to take place at the ankle joint rather than the hip or knee exions or pelvic obliquity. Consequently, this study implies that consistent ankle kinematics do not necessarily result in similar ankle-foot roll-over forms for walking. The particular rationale for these consistent ROSs remains moderately unfamiliar; nevertheless, this peculiarity may serve as a guide that helps to grasp walking biomechanics. Moreover, passive models can be disentangled using a consistent ROS.

According to Curtze et al. [99], the most significant difficulty faced during prosthetic foot design is that of supplanting the behaviour of biological feet as closely as possible via the auspices of a passive dynamic tool. According to Adamczyk et al. [100], the type of foot determines the energy cost involved; for example, the cost is lower for a curved foot than for a flat one. Reportedly, optimal metabolic costs can be obtained when the foot curvature is about a third of the leg length. Curtze et al. [99] determine the roll-over traits of a vast array of prosthetic feet, including the effect of shoe soles.

Prosthetic feet mimic the natural behaviour of ankles by creating a deflection in order to yield a constant ROS. Regardless of the variations and discrepancies in these parameters, there are various studies that define the variation of the ROS as being negligible in patients on level ground while walking at various speeds and carrying different loads [94]. This is because this approach captures movement regardless of conditions, such as weight and walking speed; accordingly, it is mostly used as a criterion to optimise prostheses [102, 103]. This covers the geometry effect and stiffness profiles with measures such as effective foot length, which are easily defined through evaluation using ISO16955 [104]. This means that ROS is a valuable performance indicator that is constant across individuals.

### 3.2.1 The Finite Element Modelling and Roll-Over Shapes

Finite element evaluation offers a novel numerical approach to determining the ROS of prosthetic feet. Smith used the finite modelling analysis model to determine the ROS among amputees over four angles: $-15°$, $0°$, $10°$ and $20°$ [105].

The shank coordinate system was used to calculate the radius of the ROS. Smith's study assumed that the centre of the ROS should be anteriorly placed at $7.6cm$ from the tibia [105]; hence, the design of a prosthesis should determine the GRF of an amputee based on their COP. The geometrical analysis of the foot was conducted using a new setup, including an extended arm and variable loading [12]. The coordinates of the COP were obtained from the force platforms. Figure 3.2 plots the results obtained from this study during numerical and experimental evaluation. Mahmoodi et al.'s [106] study evaluated the impact of the ROS on the design of prosthetic feet (see Figure 3.3). Figure 3.2 presents the ROS of SACH from experimental and numerical data using FEA.

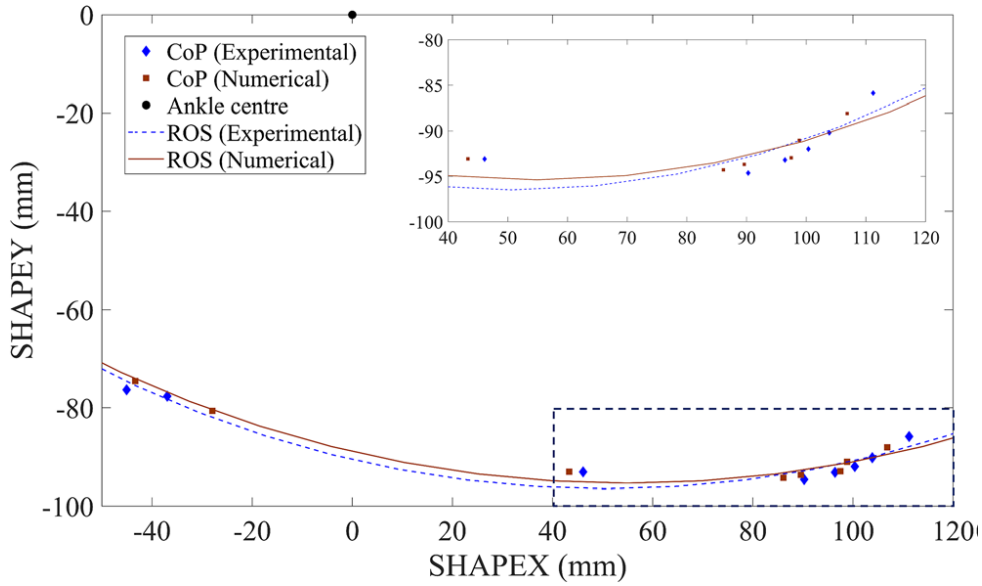


Figure 3.2: Plot of the ROS from the prosthetic feet [12].

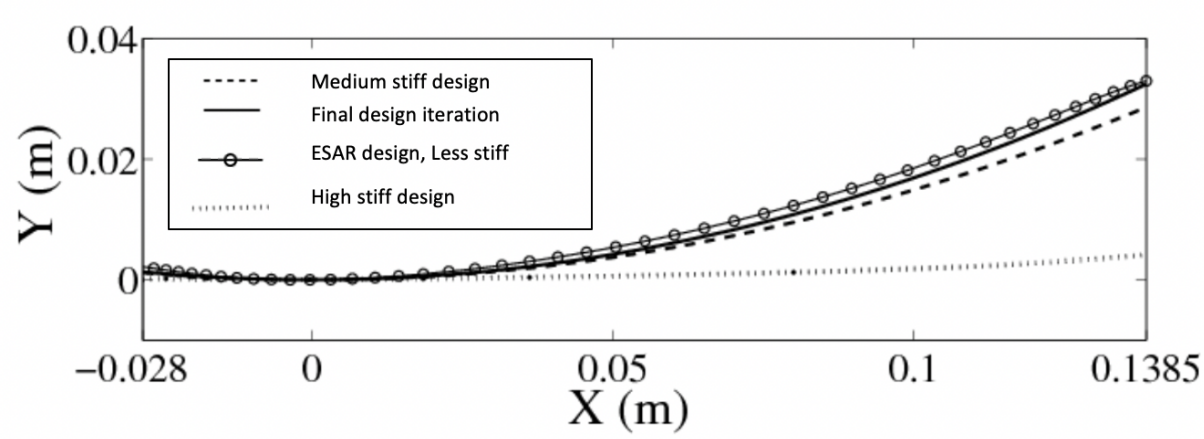


Figure 3.3: The ESAR ROS [32].

According to Strike and Hillery [107], the design of prosthetic feet appears to have been carried out on a trial and error basis. Olesnavage studied the idea of employing a Bezier curve for standardisation [108]. This concept quantifies how C-spring geometry is linked to its stiffness profile from the heel strike to toe push-off. The author devised a curve designed with an $x$-coordinate and $y$-coordinate that has a thickness yielding 12 variables. The research provides a proof of concept that has been used as inspiration for our design, which also employs the Bezier curve. Olesnavage optimised the curve through the minimisation of the lower leg trajectory error [109]. For their part, Tryggvason et al. [110] investigated the stiffness elements of a prosthetic foot. They used ANSYS to construct a prosthetic foot model in order to test dissimilar material characteristics for the purpose of enhancing the prosthetic design. The finite element model is ideal for this purpose because it allows the usage of various spring dampener and stiffness elements that characterise different foot designs. The ANSYS software was used to model a finite model element in 3D (see Figure 3.4).

This simulation depicts carbon blades as elastic surface bodies. It allocates layer elements that designate the accumulation of carbon layers, including their angles, thickness, and constituent materials.

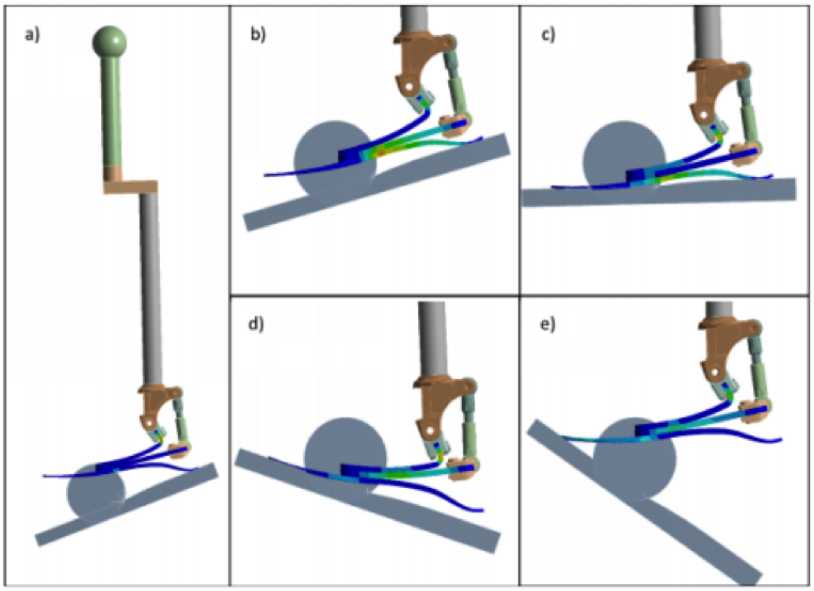


Figure 3.4: FE Simulation using an ANSYS workbench showing different heel strikes and toe-offs [110].

The orientation of the carbon layers is illustrated using orientation elements. For simplification, the model showcases only four foot parts: the two blade clamps, the mechanical link, and the main body. The constituent materials are steel and aluminium alloys, which are used to avert any deformations. At each joint of the mechanical link, a rotational degree of freedom occurs at the axis amid the three joints of the bodies as well as at the fulcrum link of the upper blade and the central body. The linkages between the clamp's joint of the upper and middle blade and the three elastic surface bodies contain contact elements. Contact stiffness is particularly high around the contact areas, making them the most important parts of the model; these allow the impact of the stiffness of the modelled foot to be observed. The mechanical link's reaction force transitions from compression to tension, moving from the heel strike to when the toe lifts off the ground. At this point, the mechanical link exhibits a tension three times that of the GRF acting maximally on the forefoot; thus, any changes to the link's function triggers an effect that influences the gait. It is important to note here that the impact on the mechanical link is high at

mid-stance compared to during the heel strike. However, the limitation of this approach is that the finite element analysis is presumed to be static analysis, so the effect of the swing leg is not considered.

## 3.3 Swing Leg Dynamics with PWD Models

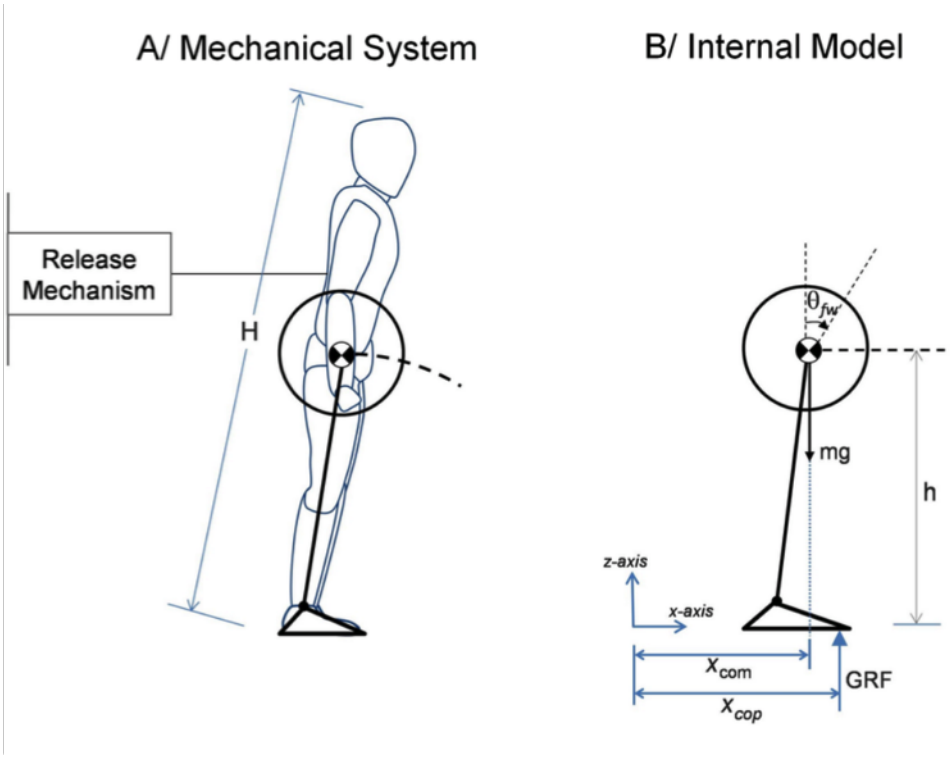


Figure 3.5: The model of an inverted pendulum displaying the resultant arc produced by COM's trajectory while walking in the single-support stance. Both figures illustrate the representations of the human body employed in this context. Left: Mechanical system; Right: simple inverted pendulum and fly-wheel model [111].

An inverted pendulum can help in envisioning the stance phase of a gait. This is depicted clearly in Figure 3.5; here, the leg represents a rigid link, the COM is at the hip, and the leg is pivoted on the ground [90–92]. In this representation, the body rotates about the stance foot, signifying an

inverted pendulum. On the other hand, the swing leg acts from the hip, mimicking an ordinary pendulum. The concept of the inverted pendulum is crucial to an understanding of walking mechanics, as it shows how the mechanical energy and the energy expended during the double support phase remains consistent. Consequently, the COM's trajectory is redirected between each stance phase.

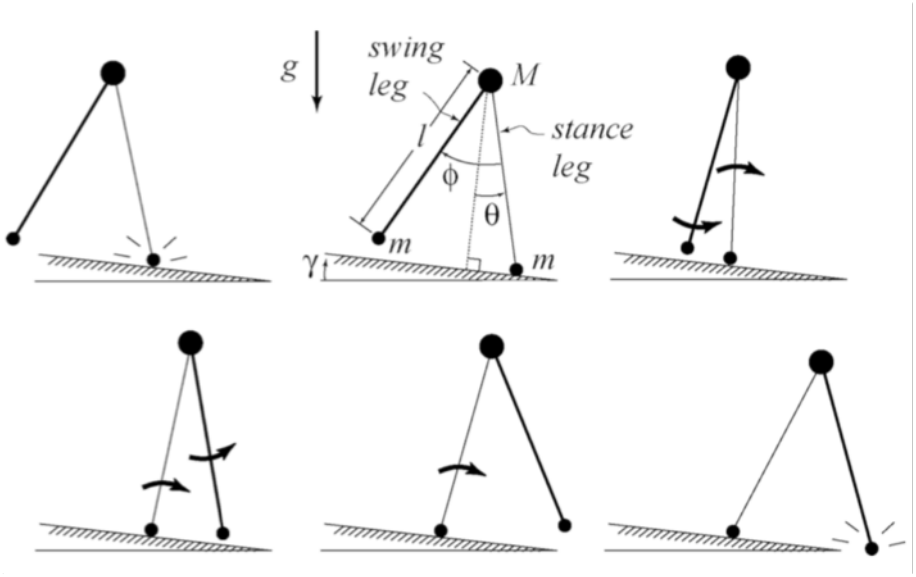


Figure 3.6: Point masses applied to the hip and each leg in a passive dynamic walking model. The model will walk steadily when released on a slope, illustrating a symmetric gait. This helps to show the potential energy obtained from the incline, as well as the energy expenditure incurred by collisional losses during the heel strike. The swing leg (heavier line) swings until the next heel-strike (bottom right picture). The top-centre picture provides a description of the variables and parameters that we use [112].

An experiment designed to study the passive dynamics of walking was conducted by McGeer [113]. He built a walking mechanism that leveraged inertia and gravity to automatically propel itself downhill, as shown in Figure 3.6. The purpose of this mechanism was to demonstrate the human gait. Raised platforms were applied to counter foot friction during leg swing.

This experiment revealed that energy is normally lost while walking downhill, mainly from the collision of the foot with the ground. In order to maintain a steady symmetric gait, it is important to balance the collision energy rate of loss with the gain of the potential energy. An inverted pendulum, despite being popularly used to predict gait, has one limitation; specifically, its inability to predict the GRF, precisely due to the rigid support [114].

### 3.3.1 A Spring-Loaded Inverted Pendulum (SLIP) PWD Model

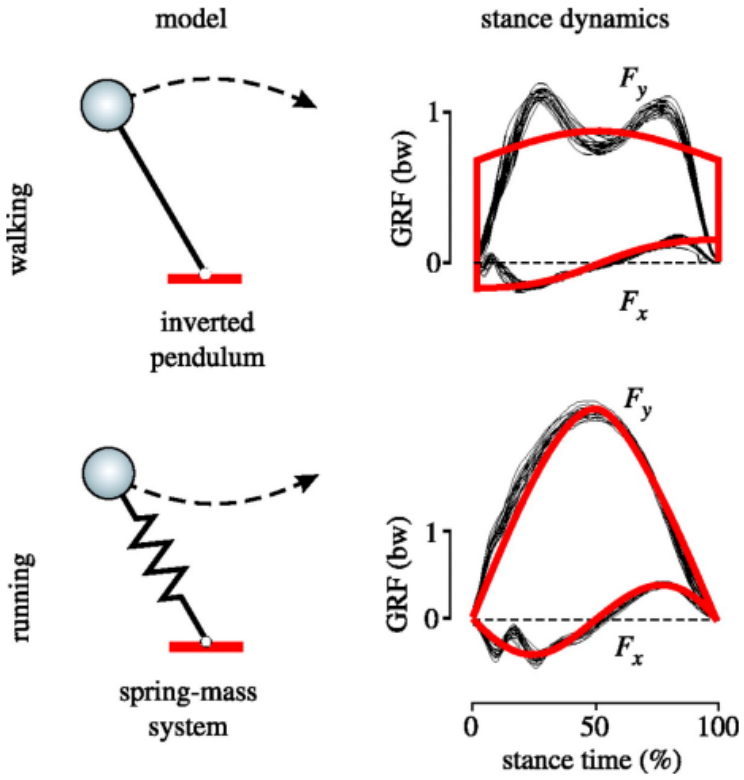


Figure 3.7: The standard models for simulating running and walking cycles have been accepted as the spring-mass system and inverted pendulum, respectively. The red lines represent the predicted stance dynamics, which only accept trial data; these are depicted by the black lines for the running model [114].

Application-wise, the spring-loaded inverted pendulum is applied to simulate running gaits. Remarkably, it can also be useful in appropriately matching the reaction forces from the ground. Researchers have used an inverted pendulum to study walking dynamics and the SLIP to study running dynamics. Figure 3.7 illustrates the limitations of the inverted pendulum in failing to pair the GRFs properly; the same inverted pendulum modified with a spring mass is instead used to model running dynamics. Notably, there is a slight variation at the onset of the step between the wiggle and the horizontal GRF $F_X$. This wiggle is attributed to the effects that are not simulated in the spring mass model, such as the impacts of the heel's contact with the floor prior to the ball of the foot or force plate vibrations [115–117]. The compliant leg plays an imperative role in obtaining the basic mechanics and the GRF movements of human walking, as observed by Geyer et al. [114].

The mass-spring model and the human system can be contrasted using experimental data. The spring's stiffness and initial rest length can be calculated by applying the Hooke's law equation, i.e. $F = kx$. The distance between the COP and the COM represents $x$, while the GRFs represent $F$. The spring mass model was used by Lipfert et al. [118,119] to simulate walking and running. These authors measured the model parameters, such as effective leg stiffness, leg rest length, and weight. Surprisingly, the results accurately matched typical walking speeds. Despite this, not all walking speeds can be simulated using the linear spring-like model. One of the reasons for this discovered during the experiment was that at slow or fast walking speeds, the force length curve signified a nonlinear relationship.

Yang et al. propose a three-dimensional bipedal walking model that adopts damping leg behaviour as the optimal method of modelling pedestrian-induced forces [120]. This model is based on the assumption that the pedestrian's body is a lumped mass with two legs that have equal length and strength. Consequently, the completed step can be easily divided into two,

where the support phase is divided into single and double variables. As a result, when the left or right leg is leading, elastic forces, inertial forces, damping forces, and gravitational forces all act on the pedestrian [120]. Analysis of the equations from the left and the right leg indicate that the three-dimensional bipedal walking model entails the following: a lateral distance between the initial systems energy and the feet, leg stiffness, the length of the resting leg, the legs' damping ratio, angle of attack, and body mass, all of which are independent parameters [120]. More specifically, the leg stiffness and angle of attack are the most important and impactful elements of a pedestrian's walking behaviour. In more detail, Yang et al.'s model [120] can simulate synchronised walking when provided with a specific speed accompanied by the attack angle and leg stiffness. For instance, the step length, frequency, total energy, and average walking speed are prompted to increase by the leg's stiffness [120]. Notably, these results are consistent with previous studies; this is also a general observation when energy is a factor under consideration. However, this model cannot be used with unbalanced mass and different length ratios to predict the walking gait for amputees.

### 3.3.2 Review of Previous Work on PWD Models at Swansea University.

Walking models can accurately predict gait characteristics [15]. As discussed above, an asymmetric gait can lead to long-term health issues; therefore, gait analysis provides insight into rehabilitating gait deformities. In particular, gait alterations can be challenging to study due to the adaptation of kinematic and kinetic gait patterns. Even though commercial prosthetics are heavier than average legs, the human body attains balance in energy exertion, thereby eliminating walking asymmetry [32]. The use of the compass walking model provides an exciting insight into gait dynamics, whereby the asymmetric touchdown affects step length. Charles [15] proposes a 'two link passive walking kinematic model, with realistic masses for prosthetic,

physiological legs and upper body' in order to study the gait pattern. The research supporting Charles's proposed model further reiterates the importance of integrating the correct stiffness and an efficient energy release mechanism into the design of prosthetic feet. Conversely, Mahmoodi [32] proposed a comparison between simpler prosthetic foot designs and dynamic models that make use of mechanics to further promote the optimisation of energy manipulation, and in doing so, create greater comfort and ease of use for the patient.

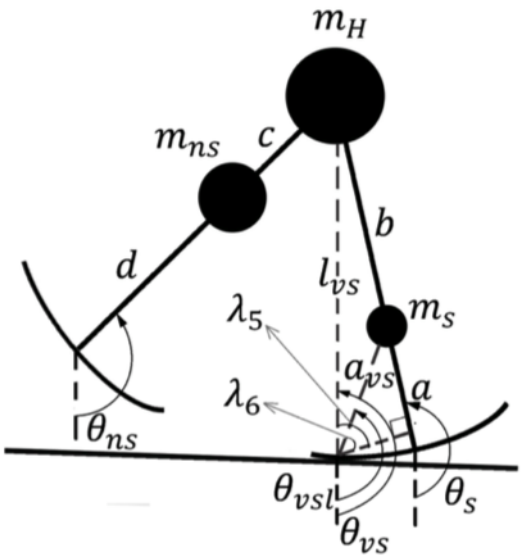


Figure 3.8: A schematic representation of Mahmoodi's model [32], which is a two-linked model with different masses and different positions of the corresponding centre of masses rolling down a shallow The dashed lines represent the virtual stance leg and the virtual stance lower leg [32].

Mahmoodi's [32] study used kinematic modelling to measure GRF among below-knee amputees. Studying the gait pattern on bodies with a commercial prosthetic, using ROS modelling and bifurcation diagrams, reveals the impact of ROS on natural gait in amputees. The study [32] focuses on the energy release and stiffness of prosthetic feet. The stability analysis of bipedal

walking is necessary to design light-weight prosthetic feet that aim to match amputees' normal gait. The study concludes that these gait studies can be integral to selecting materials and designing prosthetic feet. The researcher further notes that the body exerts more energy to overcome the walking asymmetry caused by the mass imbalance of people who use prosthetics. In this case, the foot was modelled using a ROS to improve the gait pattern. A multiple-contact point model was proposed based on the discretised description of the curve, as shown in Figure 3.8. The roll-over contact model was used to determine the motion of the stance leg during motion. The prosthetic leg used the roll-over concept to improve both an amputee's gait and symmetries in leg kinematics. However, there are a number of limitations to this model, as follows:

- The model failed to predict the M-shaped pattern of the GRF, as it assumed rigid legs.
- For FEM, the effect of swing leg dynamics was neglected. The finite element analysis was also conducted independent of PWD models.

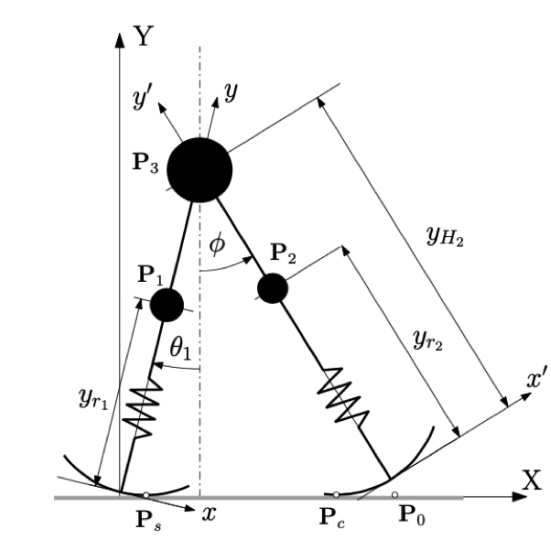


Figure 3.9: Modified model for roll-over contact [15].

Charles' [15] study adopted a simple spring-mass walking model to determine whether leg stiffness affects gait. Amputees experience asymmetrical gait dynamics due to their unbalanced

body mass. This study modified Mahmoodi's [32] work and suggested that the smooth rolling contact model (as shown in Figure 3.9 with spring legs) can be used to predict M-shaped GRF.

Force-length curves and motion data can be used to measure leg stiffness. A hybrid model [15] that emulates human leg reactions is consistent with the previous research [32] on the role played by trailing leg push-off in propelling the body compared to body mass. Notably, the prosthetic leg leads to more joint forces, extended step length, and a lengthier stance period. The robustness of particular gait dynamics and the time needed to recover normal gait during rehabilitation can potentially be explored in future research. However, there are a number of limitations of this study, as follows:

- The research used the PWD model alone to determine the stiffness of the prosthetic leg. The stiffness value was dependent on the underlying model used.
- The model was limited to a very narrow range around FWS. An increase in speed among amputees using a prosthetic foot exhibited unrealistic variation in the GRF curve.

Mahmoodi et al. [106, 121] investigated the gait characteristics of asymmetric masses using a passive walker model. Charles et al. [122] applied a spring-loaded passive walker to explore all gait characteristics. Stable asymmetric walking behaviours were identified on PWD models by Honeycutt et al. [123]; these behaviours occurred after varying the knee and mass locations as well as the mass itself, as well as a distinct leg length. Elsewhere, asymmetric legs and elongated PWD models were used to contrast their unstable boundaries, average velocity of motion, and stable periodic intervals [124]. These results exhibited more sensitivity to mass ratio changes in asymmetric passive walkers.

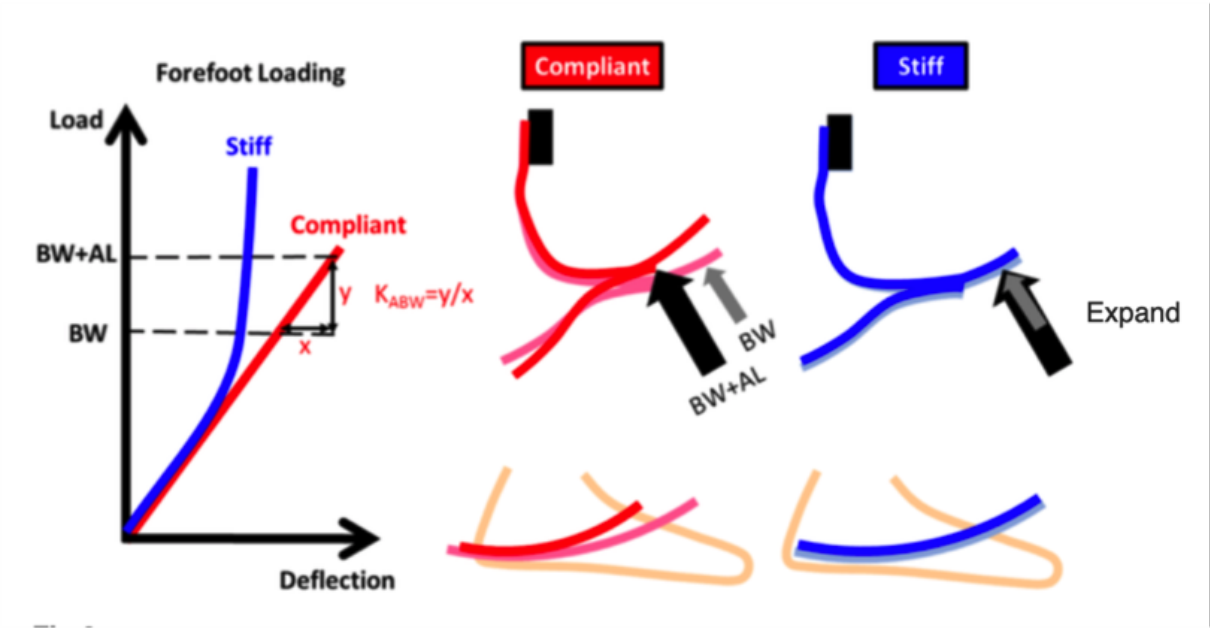


Figure 3.10: Prosthetic feet with stiffness forefoot keel structures should conform to more consistent ROSs when walking with added loads compared to feet with compliant forefoot keel structures [113].

A significant increase in ULs was observed as walking speed increase from free to fast walking speed [11]. During this speed range, a linear spring stiffness response was measured for healthy adults [11]. The visco-elastic model employed produced a similar M-shaped GRF curve for healthy adults, while the walking speed range was also small [120]. Moreover, the stiffness value range is different for Charles (10.8-19$kN/m$) [15], Yang et al. (18-28$kN/m$) [120], ANSYS (forefoot 10-50$kN/m$) [110], and experimental gait (20-36$kN/m$) [118]. As a result, the present research has adopted the spring-loaded passive walker model proposed by Charles [15], in line with the concept of the ROS and anthropological data proposed by Mahmoodi [32]. This is further discussed in Chapter Five, in which a loosely coupled model is proposed.

As shown in Figure 3.10, the hindfoot or forefoot can be made either softer or stiffer; this will change the values for ground force reactions that affect the gait and energy required to

sustain a stable gait. The current finite element-based simulation designs also fail to incorporate the swing leg dynamics calculated by walking dynamics models. This observation motivates the research direction adopted in this thesis, which suggests using combined information from finite element models, experimentally determined GRFs and walking dynamics models. This is discussed in detail in more Chapter Five, in which a novel loosely coupled model is proposed.

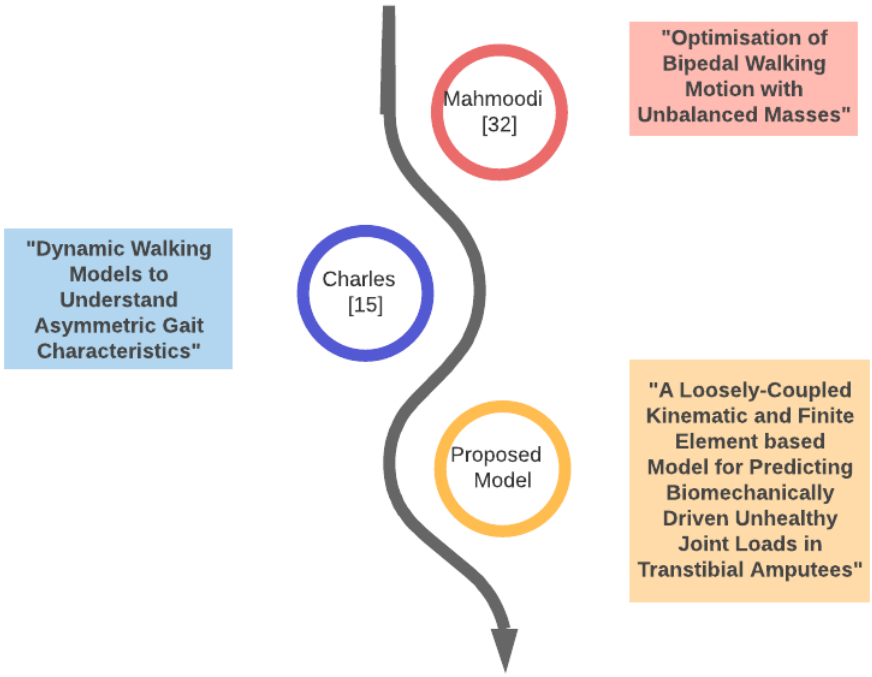


Figure 3.11: Swansea university contribution roadmap

The research roadmap for the biomechanics research developed at Swansea university is shown in Figure 3.11. This research was begun in [32] with a restricted model. Charles [15] developed the passive walker to enhance the GRF pattern. Finally, the proposed model is developed to further enhance the previous model [15], as well as to optimise the stiffness of the prosthetic foot to minimise the UL.

## 3.4 Design Criteria and Design Variables for the Stiffness Optimisation of ESAR Feet

The lower limb prosthetic foot design is based on four different criteria, as listed in the below table.

Table 3.1: Design criteria of lower limb prosthetic foot

| Criteria | Type | Explanation |
|---|---|---|
| **One** | Strength | The prosthetic foot must always endure above body weight while impacting on the ground and load cycling with regards to daily activities. |
| **Two** | Balance | To ensure stability in all day activities. |
| **Three** | Mobility | Allow no restriction to the movement ability. |
| **Four** | Energy storage and return | The prosthetic foot must allow an adequate amount of kinetic energy to ensure that both limb and trunk move in the correct direction. |

This study investigated the current quality requirements and mechanisms of prosthetic foot designs. While providing suitable criteria for these designs, attention was given to a group of sample designs (see Figure 3.12). The ROS of a C-shaped foot is estimated using the finite element simulation outlined in Chapter Five. In order to implement an optimal ROS discovered from the passive dynamics models, the C-shaped foot geometry may need to be redesigned rather than simply changing its material thickness or properties [121]. The design philosophy is used to evaluate existing variations on the traditional C-shaped foot design, as well as to identify features that either need improvement or can be reused as-is.

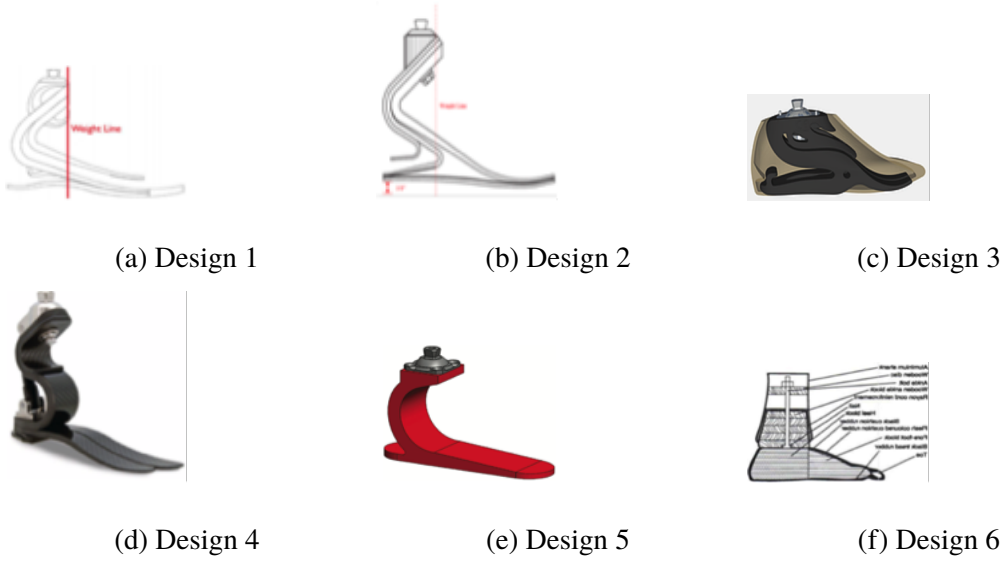

(a) Design 1 (b) Design 2 (c) Design 3

(d) Design 4 (e) Design 5 (f) Design 6

Figure 3.12: Design comparison [19, 28, 109]

The sample designs 1-6 are evaluated in terms of positive aspects and potential areas of further improvements below.

- **Design 1**

  The mass of the design is about 634$g$ (see Figure 3.12a). A novel feature of this design is its double keel. The upper keel is designed to make contact with the lower keel at the mid-stance position, while the design is expected to provide additional spring-back at the toe-off stage so that more energy is returned. The length and stiffness of the upper keel is a design parameter that will control the additional spring-back action. It is envisaged that this double-keel feature may influence the resulting ROS of the foot. However, the manufacturing process offers a narrow choice of materials; thus, this aspect can be further improved.

- **Design 2**

  The mass of this design is about 675$g$ (see Figure 3.12b). This design has a double heel to enhance the foot's ability to absorb shock at the heel strike. It is noted that the double

heel has not created an additional mount joint; it is attached at the top at the same point. This design also offers a narrow materials range of materials (just like design 1 in Figure 3.12a) and offers thus has scope for further improvement.

- **Design 3**

  The mass of this design is about 623$g$ (see Figure 3.12c). This design has a different double keel feature in comparison to design 1 and has an extended cantilever toe. The design has the potential to change section thickness, the dimensions of a double-keel and a cantilever toe to achieve stiffness variability, with the resulting changes to a ROS of the foot. This design, however, may have stress concentration areas at sharp geometrical changes.

- **Design 4**

  The mass of this design is about 493$g$ (see Figure 3.12d). The S-shaped toe design is likely to enhance the foot's ability to absorb shock at the heel strike. The multi-axial rotational ability also offers better stiffness variability. However, this design has only one keel, and it is difficult to change its geometry (e.g. thickness variation). This may constrain its ability to achieve the desired ROSs. The connection points in the S shape do pose a reliability risk and the design is still susceptible to a narrow materials range.

- **Design 5**

  The mass of this design is about 460$g$ (see Figure 3.12e). This is a traditional C-shaped spring design. This foot has scope to change the thickness of the keel. The shape of the foot can be modelled with Bezier curves [108, 109] and its effect is studied on realising a desired ROS for the foot. However, in comparison to the previous designs (Figures 3.12a - 3.12d), this foot has a stiffer heel design.

- **Design 6**

  The design has an unknown mass (see Figure 3.12f). This is a low-cost design that uses a broad range of commonly available materials (rubber, wood, polyurethane etc) and still allows the user to accomplish activities such as squatting, swimming and climbing. The foot is based on a SACH foot design concept, which is unlike the energy return foot designs (Figures 3.12a - 3.12e). This foot design is mostly used in developing countries due to its low cost and can be used as a benchmark for comparing both costs and the gait performance for foot designs.

From several design studies, it was observed that effective and efficient prosthetic feet can withstand more than $650N$ compared to the heel strike of individuals weighing less than $112kg$ [125, 126]. Dorsiflexion oversees the transfer of momentum from the heel-strike to the toe-off, and the 'C-spring' is one of the keel designs needed for good vertical absorption (see designs 1, 2, and 5). The 'L-spring' is formed using an 'S-spring' (design 4) and 'C-spring' (design 3) to reduce the stress of the residual stump and improve vertical absorption. However, during this heel-strike, the energy efficiency is decreased and the toe-off forward momentum is reduced. The real human foot dissipates 17-45% of the energy returned to the ground [127, 128]. For better absorption and transfer of force from a heel-strike, the 'C-spring' is preferable; it returns energy with a forward momentum during toe-off, making it suitable for passive feet. A SACH foot is unable to return energy as efficiently as modern energy return prosthetic feet. Hsu et al. [129] reported experimental results on gait efficiency for physically active participants. Gait efficiency is defined here as energy expenditure relative to distance travelled and is derived from the ratio of the oxygen consumption divided by the walking speed. The variation in the GRFs is not reported however, the study found that the physically active amputees have the ability to adapt to any prosthetic foot (SACH or energy return foot) without showing statistically

significant increase in oxygen consumption. For example, the study showed only a 10% increase in metabolic energy consumption as the walking speed increased up to 1.8 m/s [129]. The paper observed that people with sedentary and physically active lifestyles are likely to demonstrate different values for gait efficiency and energy consumption.

### 3.4.1 ROS as a Design Variable to Satisfy Balance, Mobility and ESAR Criteria

The ROS places applied loads and stiffness into a single curve. Being invariant to velocity, body weight, and slope of the walking surface [130], ROS is essential in terms of subjective preference, gait symmetry, and efficiency of metabolism [131]. The heel-strike increases gait economy and stride length when a curved foot base is employed (design 3). Designs 1 and 4 successfully determine the limits of a curved foot base for the geometry preceding optimisation. While it optimises the foot base geometry, the curved foot base establishes the association between performance indicators and the location of the curve. Nevertheless, the ROS has been found to generate insufficient data on the lower leg orientation (see design 5); this explains why additional testing is necessary, as well as the provision of errors associated with the lower leg trajectory.

### 3.4.2 vGRF as Part of an Objective Function to Satisfy Balance, Mobility and ESAR Criteria

The ISO22523 [132] outlines standards on the safety and strength of prosthetic feet; however, patient-specific factors such as gait speed and anatomy are out of scope. To counter this inadequacy, the prosthetic feet constantly change their structural properties to increase efficiency and

comfort. One way to achieve this is through the use of optimisation software that synchronises the gait cycles and GRF profile of each limb given the individual stiffness characteristics. The stiffness profile is applicable in the mid-foot for toe-off and can also use a broad range of materials (see design 6). Although the stiffness response of a prosthetic foot is optimised, it is also shown in Chapter Five that, unlike vGRF and ROS values, the stiffness values are not shared among computational models (finite element and PWD model) and experimentally determined gait data. Consequently, vGRF is considered as an optimisation function for defining ULs in this thesis, while the stiffness information is kept local to the model. This is discussed further in the next chapter.

### 3.4.3 Prosthetic Foot Mass as a Design Variable to Satisfy the Mobility Criterion

Prosthetic feet can provide smooth and comfortable gait, especially under condition of low mass. Van Jaarsveld et al. [133] supports this view and compares it with the mean mass of competitors at 546 grams. For competitive energy expenditure and low mass, the mass of designs can employ minimalistic geometry (design 4 and 5) or nylon with a density of $0.85 g/cm^3$ as in design 5 [134]. Better performance can be achieved using a 'C-spring' and double keel, as well as designs with thicker sections (design 3). Optimal designs may be required to moderate the number of extra design features. Care is required to ensure that the optimal designs do not increase the mass and step length of the patient.

### 3.4.4 Material Properties as a Design Variable to Satisfy all Criteria

Prosthetic limbs are designed to achieve high levels of success and reliability; thus, the probabil-

ity of failure is assessed and the risks associated with a sharp change in geometry and fasteners are mitigated. For example, the Mecuris foot (design 3) minimises the use of fasteners, but experiences sharp changes in geometry. The selection of materials for prosthetic foot design depends on innovations and advancement in materials engineering research. The current manufacturing process has been improved to utilise a broad range of materials. This expanded range of materials is already being used in the additive layer manufacturing (ALM) process (design 3) as part of the innovations. Designs 3 and 5 allow for variations in material density and lattice-infill geometry and gives designers more freedom to choose materials. Proper material selection is vital if designers are to vary stiffness and easily achieve infill geometry and density. Even so, future developments in prosthetic limbs will be achieved through a precise and accurate stiffness profile.

### Computer Specifications

The simulation results presented in this thesis for each case studies was found on a personal computer 'laptop'. Table 3.2 presents the computer specifications.

Table 3.2: Personal computer specifications

| System Component | Specifications |
|---|---|
| **Operating System** | Windows 10 Home |
| **Processor** | Intel(R) Core(TM) CPU at 1.30$GHz$, 1.50$GHz$ |
| **Installed RAM** | 16.0$GB$ |
| **System Type** | 64-bit operating system, x64-based processor |

## 3.5 Conclusion

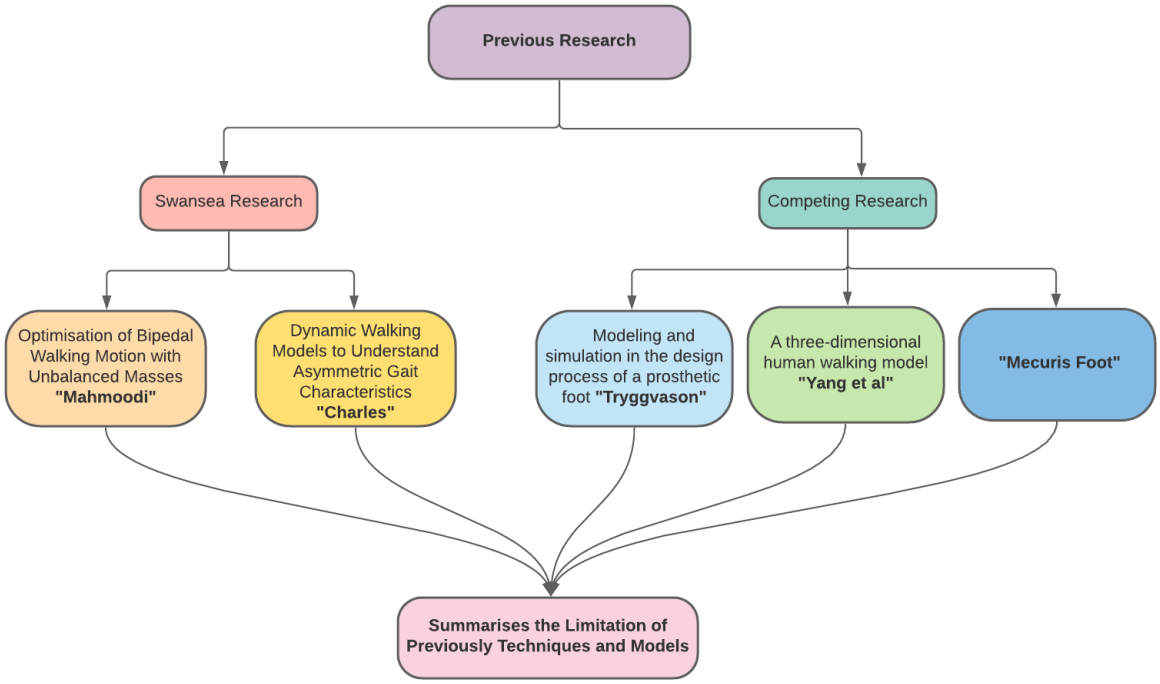


Figure 3.13: The highlights of previous work

The main work that formed the starting point of this thesis is summarised in Figure 3.13. FEM is an integral part of designing the stiffness response of prosthetic feet. The design of assistive devices should consider the mechanical principles of walking dynamics. The current ISO standard does not require the prosthetic foot response to be calibrated with reference to changes in the walking speeds of amputees. The different walking speeds affect the efficacy of prosthetic feet among amputees. As can be concluded from the literature provided in this and the second chapter, the following points cannot be ignored during the stiffness optimisation process of prosthetic feet:

1. The effect of swing leg dynamics.

2. The effect of changes in the GRF pattern for various walking speeds.

3. An ability to quantify the ULs for a given walking speed.

4. The optimisation of the prosthetic foot's stiffness response based on the GRF's shape characteristics.

5. A need to use a multi-physics approach to optimise the prosthetic foot in order to reduce the UL.

6. A requirement to develop a mapping function between PWD, FEM, and gait experiments.

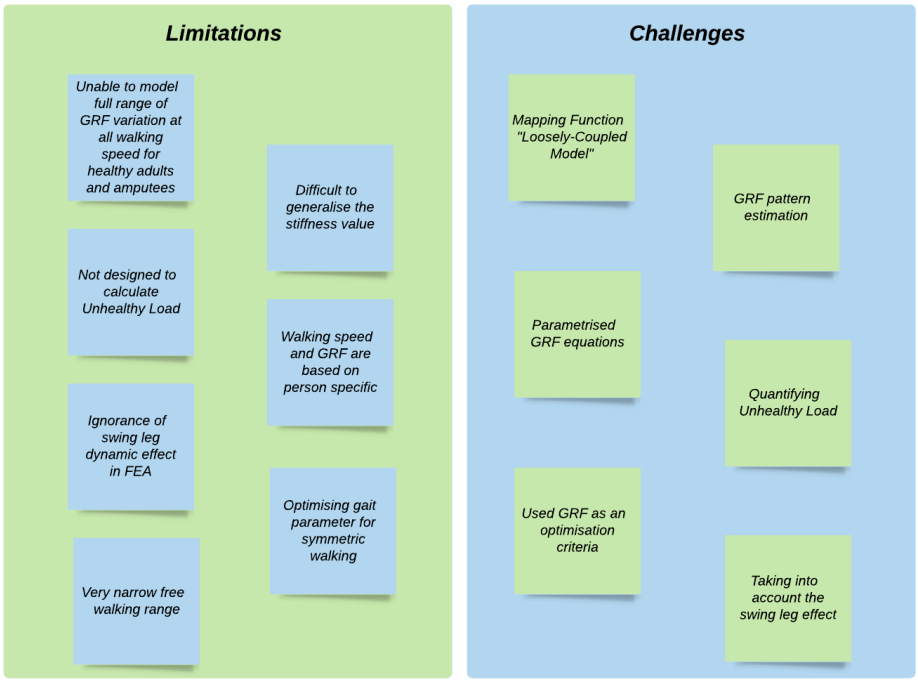


Figure 3.14: Challenges and limitations

Figure 3.14 summarises the challenges and limitations addressed in this thesis. In order to achieve the aim of the present research, a parametrised GRF estimation equation based on various walking speeds was developed to predict the pattern of the GRFs for the healthy population and amputees (see Chapter Four). Moreover, a loosely coupled kinematic and finite element-based model is established to reduce ULs.

## 3.6 Summary

The above literature review has evaluated the various approaches employed by researchers to examine human gait for rehabilitation purposes. Moreover, it has also focused on how different biomechanical models can help to inform research on muscular and gait dynamics. While it is challenging to forecast how an individual's control mechanisms will change after a neuromuscular ailment or injury, performing multibody musculoskeletal simulations can lend great insight to the understanding of muscle and joint biomechanics and movement. The research revealed that normal walking is asymmetric even though the asymmetries are not as amplified as in the gait of an injured person, a person wearing prosthetics, or someone with a neuromuscular condition. Notably, Hof et al. [134] caution against symmetrising the gait behaviour of amputees during rehabilitation. The weight difference between a prosthetic and a real foot is responsible for the difference observed in the swing and stance dynamics of the individual's gait. As a prosthetic leg cannot precisely match the action of a contralateral muscle, a healthy contralateral foot has to work differently when a prosthetic is involved, which can exacerbate existing health issues. Dynamic models can help to improve the understanding of gait mechanics. Merker et al.'s [135] experiment with bipedal spring mass model demonstrated that the variations witnessed in contralateral legs can be permitted; in some instances, they even enhance the system's sturdiness. Hong et al. [40] modelled a spring-loaded inverted pendulum to examine the undulation of the COM relative to the forces of reaction that occur during human walking behaviour. Rasouli et al. [124] investigated the dynamics of the passive walker with asymmetric leg mass positions, concluding that these were more sensitive to mass ratio changes. Tryggvason et al. [110] simulated the stiffness of a prosthetic leg model using the ANSYS software. Various gait rehabilitation hypotheses were also investigated by Honeycutt et

al. [123], who altered several parameters of the passive model, including knee location, mass location, mass, and the leg length of one side. There is a notable lack of adequate research in the field of asymmetric gait; nonetheless, the available research has adequately demonstrated that a linear relationship exists between walking speed and the resultant vGRF, with the latter being substantially impacted by varying gait speeds. More specifically, the vGRF increases as the walking speed changes from slow to fast and decreases as the person transitions from fast walking to slow jogging. The research also demonstrated that the symmetry between foot placement and GRFs affects the angular momentum of the amputee's body for all walking speeds. There is a reduced intact vertical and residual GRF in the first and second residual gait cycles, respectively, which enables parallels to be drawn with the higher range of angular momentum seen in amputees. Moreover, the type of prosthesis used also affects the resultant peak GRFs for different amputees; for example, the vertical and horizontal GRFs are higher on the side with the sound limb than on the one with the prosthetic limb. It would be possible to gain more knowledge of this area if the GRFs associated with asymmetric walking were studied more profoundly. Currently, the PWD used do not accurately model human behaviour like double GRF, while mass-spring systems are yet to be used to simulate asymmetric leg inertia and single leg masses. This thesis accordingly presents the study of ROSs as design variables and vGRFs as an optimisation criterion for the stiffness design of prosthetic feet to minimise UL.

# Chapter 4

# A Set of Dimensionless Equations for vGRF Estimation

## 4.1 Introduction

This chapter, by building on chapter two, primarily seeks to enhance the usability of the data collected and the results obtained by drawing parallels between real-life experiments and theoretical data. It concludes with a set of equations that estimate the vGRF values for given walking speeds for both the healthy population (HP) and amputees (affected) in order to quantify the ULs. A group of healthy adults with an active lifestyle involving considerable walking in their daily routine was selected, and participants were asked to walk at self-selected or FWS in the gait lab. This experiment helped to reinforce the discovery of the variation in the absolute values of FWSs among individuals along with the variance of the vGRF curve with respect to the relative values of very slow, slow, free walking, fast and very fast walking speeds. The results and data were gathered with the help of a web-based digitisation software programme and compared with the results of the present study. The $x$-axis of the plot was selected to represent

the gait cycle percentage, while the $y$-axis was chosen to represent the dimensionless quantity GRF/BW ($G_r$). Another relevant term in the calculation of the GRFs curves is the velocity ratio ($V_r$); this is defined as the ratio of an individual's walking speed to the average FWS for the corresponding population group to which the individual belongs. The data and equations are used to find the vGRF values for different velocity ratios ($V_r$), categorised into 'Very Slow', 'Slow', 'Free', 'Fast', and 'Very Fast' walking speed groups.

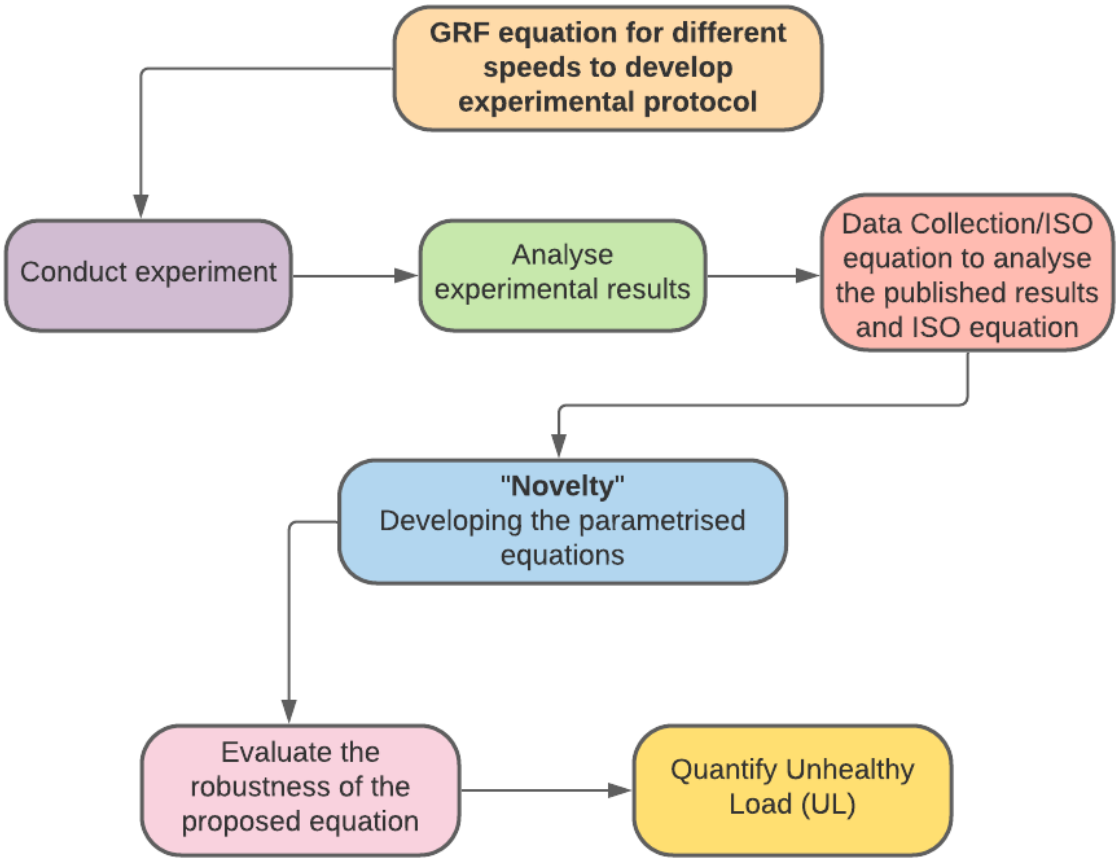


Figure 4.1: The chapter layout explained in a flowchart.

The remainder of this chapter is divided into the following sections. Section 4.2 provides a brief background of the theory behind the premise of the experiment. Section 4.3 discusses the determination of vGRF values using the experimental study, and is broken down into four

subsections, as follows: protocol-motion capture, participants, procedure, and experimental GRF results. In Section 4.4, a set of new parametrised vGRF equations is proposed for both the healthy population and amputees. The results are then discussed in Section 4.5, while an expression is also suggested for quantifying biomechanically driven ULs due to amputation. Finally, Section 4.6 concludes this chapter and summarises the relevant information. Figure 4.1 illustrates the structure of this chapter as a flowchart.

## 4.2 Background

Walking is a simple and basic action that most people can perform easily every day. However, physical limitations can impede the normal performance of this simple movement for some people. Amputees rely on prosthetic limbs in order to walk and lead normal lives; however, the high cost of these prostheses make them economically infeasible for most amputees, and further increase their walking costs by 20 to 30% over able-bodied people [76, 136]. Amputees using prosthetic limbs may also suffer from joint degeneration due to asymmetric loading, and consequently, unintended problems such as lower back pain. Additionally, as pointed out by Vickers et al. [137], prosthetic legs have poor stability, especially when walking on inclined surfaces; this is caused by low GRFs.

Unlike biological legs, prosthetic limbs are unable to easily adapt to different walking terrains. Biological feet can recognise a number of different parameters that are usually monitored by the body, such as velocity, weights, and heights, among others [138]. Thus, conducting a real-life walking experiment involving participants with biological legs is essential to monitoring their movements and understanding how these parameters function. The resultant knowledge can accordingly facilitate the design of the prosthetic limb to simplify the motion and eliminate the

walking challenges experienced by people with artificial feet. Andrysek [139] considers it a challenge to design a prosthetic foot that can function optimally in the same way as a biological foot. Despite the increasingly advanced technology available for the design and development of artificial legs for amputees, poor stability and comfort remain major challenges that inhibit the optimal design of these limbs. Experimental work in this field aims to determine the GRFs and basic foot parameters, such as velocity, displacement, and acceleration. The obtained results can be used to optimise the stiffness of the prosthetic foot [32].

## 4.3 Determination of vGRF Values using a Gait Lab Experiment

This section describes the experimental protocol employed and the setup used to measure vGRF values for a group of healthy and active male adults aged around 22 years. As discussed in Chapter 4, gait parameters can differ between people with sedentary and physically active lifestyles. For example, Hsu et al. [129] noted that physically active amputees may demonstrate different results compared to what is reported in the literature; however, their study did not report the variation in GRFs. As highlighted in Chapter Two, GRFs vary significantly with respect to walking speeds; however, the reported range for walking speeds perceived as FWS is also very wide (1-1.3$m/s$). As a result, a specially chosen group of healthy and physically active male adults aged around 22 years was selected as a sample for out experiment, and the GRFs for FWS were measured. In order to ensure repeatability, each reading was taken five times. The standard deviation for five observations for each recorded reading is low as shown in Table 4.3. The results of this experiment will be plotted on graphs and analysed to both evaluate the parameters for healthy people and estimate the resultant GRF. These results will then be

compared to those from other studies. Subsequently, the final equations for different walking speeds will be deduced and discussed in the next section.

### 4.3.1 Protocol-Motion Capture

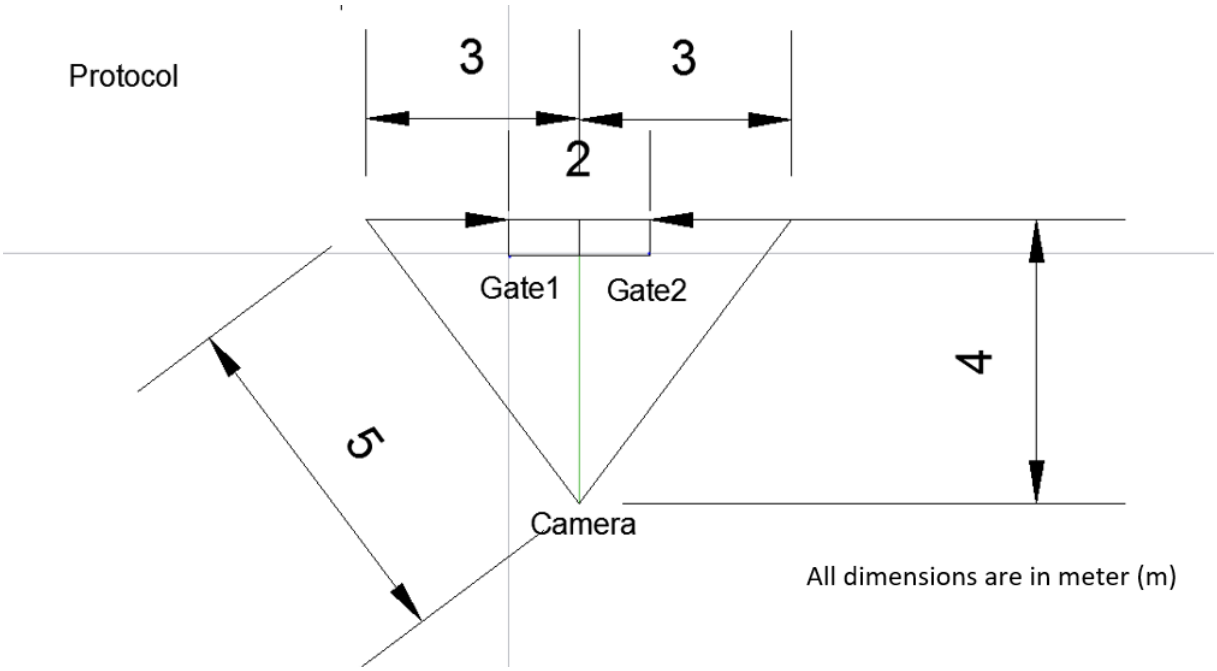


Figure 4.2: CAD drawing explaining the experimental protocol and setup.

An actual experiment was conducted in the gait laboratory at Swansea University. To begin the experimental protocol of this test, the following items were required (and are outlined in Figure 4.2):

- Two force plates.
- Five to six wooden platforms (1m in length and the same height as the force platforms).
- Two pairs of timing gates.
- HD camera with high-speed recording setting (120 FPS minimum[1]) and adjustable tripod.

[1]To ensure that the camera is detecting the marker place accurately.

- High-powered LED lights with adjustable tripod.
- 6$m$ (minimum) measuring tape.
- Tape and marker pen.

The above experimental setup required a large space to accommodate the equipment. Additionally, the camera setup was placed at least 4$m$ perpendicularly from the centre of the walkway for force plates, which span out 6$m$ in length.

### 4.3.2 Participants

The experiment used six participants with varying characteristics, such as weight and height, to guarantee diversity and examine the effects and changes introduced by the different features. Data for the subjects was recorded as indicated in the tables below (Tables 4.1 and 4.2), with each individual undertaking five trials. The use of six participants with different attributes was key to introducing variation and avoiding bias. Each participant was monitored separately as they performed the experiment to ensure that none of them influenced another by imitating movements or walking abnormally. Moreover, the selected group members were active and considered to be athletes; this assisted in justifying the hypothesis of this chapter, which aims to extract data from real-life experiments and use it in conjunction with other previous studies to identify a way of calculating the GRFs and the corresponding FWS (a new categorisation for the estimation of FWS). Participants agreed to the required code of ethics used at Swansea University before performing the experiment, as presented in Appendix A.

Table 4.1: Experimental subjects' information.

| Subject | Height(m) | Weight (kg) |
|---|---|---|
| **Participant 1** | 1.78 | 76.3 |
| **Participant 2** | 1.82 | 87.3 |
| **Participant 3** | 1.80 | 75.5 |
| **Participant 4** | 1.91 | 97.8 |
| **Participant 5** | 1.85 | 85.5 |
| **Participant 6** | 1.68 | 59.1 |

Table 4.2: Participants' statistical information, including the average and standard deviation for age, height, and mass.

| Statistics | Average | Standard Deviation (SD) | Average ±SD |
|---|---|---|---|
| **Age** | 22.5 | 1.87 | 22.5 ±1.87 |
| **Height (m)** | 1.81 | 0.047187 | 1.81 ±0.047187 |
| **Mass (kg)** | 80.25 | 13.19 | 80.25 ±13.19 |

### 4.3.3 Experimental Protocol

As can be seen in Figure 4.2 , the experimental setup began by selecting the appropriate location to place the recording camera. A walkway 6m in length was then measured and a centre point marked at the 3$m$ point. Beginning from the same centre point, a 4$m$ distance was measured perpendicularly from the walkway; this could be used to measure the distance between this mark and the mark used to check the readings. If this distance was found to be 5m, then the subsequent steps were applied; if not, the process was repeated until all the correct lengths were

achieved. The $4m$ line was then extended further to intersect with the $5m$ line, although it was also essential to keep it straight and perpendicular. The end of this extension served as the placement point for the centre of the camera's tripod (see Figure 4.3).

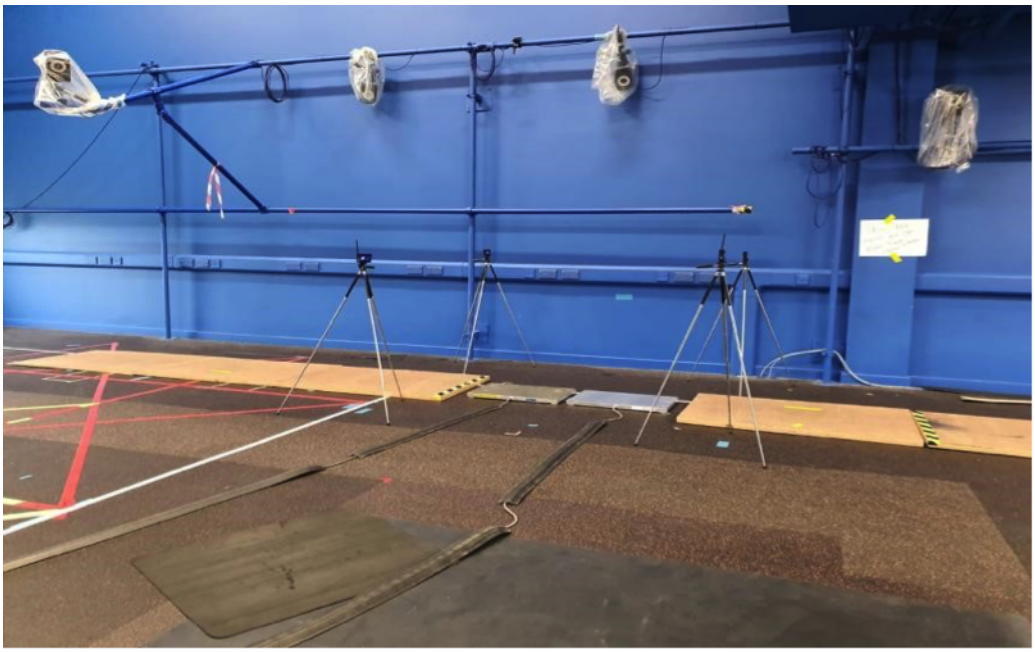

Figure 4.3: Experimental setup, ready to start collecting data.

The team began by fixing the force plates lengthwise on the marked positions. Wooden platforms were placed down in front of the force plates (three on the first force plate and two or three others on the second force plate). The height from the floor to the centre of the camera lens was then measured, after which the centre on the opposing wall was marked and the height from the floor to this point was measured. Subsequently, the camera was focused on the mark on the wall, after which the height, pan and tilt were measured from the tripod to the centre of the camera frame on the wall marking. The camera's focus was then zoomed out to reveal both force plates and capture the lower half of the subject's torso. Once the camera setup was deemed to be ready, the light setup was started: this involved fixing the LED light behind the camera to illuminate the area under its focus. From the centre mark of the force plate and running

parallel to the walkway length, a distance of 1m was measured and marked on both the left and right sides. After the force plates and distances were prepared, timing gate pairs were placed on each of the previously defined marks. Their heights were raised to match the mid-torso of the subjects; the distance between gates [2] was approximately $2m$. The next step was to fix the light: the trigger light was set in a position from which it was viewable in the frame of the camera.

The experiment commenced by connecting the data acquisition box. Six participants were then asked separately to practice the test protocol so that they found the right starting position on the walkway; this would ensure that they hit the first force plate with the closest leg to the camera. To establish this starting point, two methods were proposed: the first was to have them stand on the first force plate and walk backward, using the leg furthest from the camera as the lead leg; the second was to have them walk from a random point and adjust it until a clean foot-strike condition was achieved. Subsequently, the subjects would be checked to verify that they were hitting the other force plate with the leading foot. After setting the starting position, the next step involved placing markers at different locations on the side of the subjects closest to the camera (such as the lateral condyle of the femur, the greater trochanter of the hip, the lateral malleolus, the lateral condyle of the tibia, and the fifth metatarsal head).

The completion of this series of steps signified that the experimental setup was in place and ready to collect data. First, the subjects were instructed to stand on the starting point along the walkway. The lab lights were then turned off while the LED spotlight remained on. The force plate was set to collect data for 10 seconds at $1000Hz$ before commencing the camera recording. Next, the subjects were requested to start walking as the force plates began the data collection process. The recording was ended at the exact moment that they reached the end of the platforms.

[2]Gates 1 and 2 are the time sensors

During the experimental procedure, some critical points were considered, such as the camera setup placement, which was done to ensure that any prospective distortion was minimised. Another consideration concerned the lighting in the room; the lights were switched off to make the room as dark as possible. The subjects also wore tight outfits to reduce kinematic data noise from the marker displacement, and walked barefoot during the process.

### 4.3.4 Experimental vGRF Results

This group of participants were male university students with an above-average amount of walking activity built into their daily routine. A closer observation of the graphs in Figure 4.4 suggests that Participant 2 appears to have different values from the rest of the group; these curves were plotted using participants' data extracted from the experiment. Figure 4.4 plots 20-100 data points measured from experiments for each participant. As seen in Table 4.3, this participant's average walking velocity is $1.59m/s$, which is much lower than the average speed for the rest of the group. However, the first peak value ($Fz1$) for the $G_r$ curve is 1.147, which is the highest among the group. The average $G_r$ variation for the other participants was plotted and compared, with the average $G_r$ variation recorded in the literature for FWSs (Figure 4.9a; curve labelled as AlQemlas $1.855m/s$). Participant 2's $G_r$ curve matched with the $G_r$ variation recorded for Fast walking average (Figure 4.9a, curve labelled as AlQemlas $1.59m/s$). All participants were asked to walk at FWS. This observation supports the view being developed in this thesis, namely that characterisation of Slow, Fast and Free walking speed depends on the shape of the vGRF curve rather than the value of the walking speed.

Table 4.3: Experimental results for all participants

| **Participant** | **Avg Velocity** | **Velocity SD** | $Fz1$ ± **SD** | $Fz2$ ± **SD** | $Fz3$ ± **SD** |
|---|---|---|---|---|---|
| 1 | 1.924 m/s | 0.024 | 1.055 ± 0.089 | 0.862 ± 0.011 | 1.066 ± 0.059 |
| 2 | 1.59 m/s | 0.02 | 1.147 ± 0.094 | 0.818 ± 0.025 | 1.172 ± 0.012 |
| 3 | 1.93 m/s | 0.08 | 1.092 ± 0.075 | 0.806 ± 0.012 | 1.143 ± 0.016 |
| 4 | 1.76 m/s | 0.05 | 1.107 ± 0.050 | 0.8 ± 0.013 | 1.121 ± 0.016 |
| 5 | 1.722 m/s | 0.03 | 1.008 ± 0.018 | 0.811 ± 0.012 | 1.11 ± 0.025 |
| 6 | 1.94 m/s | 0.04 | 1.091 ± 0.047 | 0.815 ± 0.027 | 1.151 ± 0.031 |

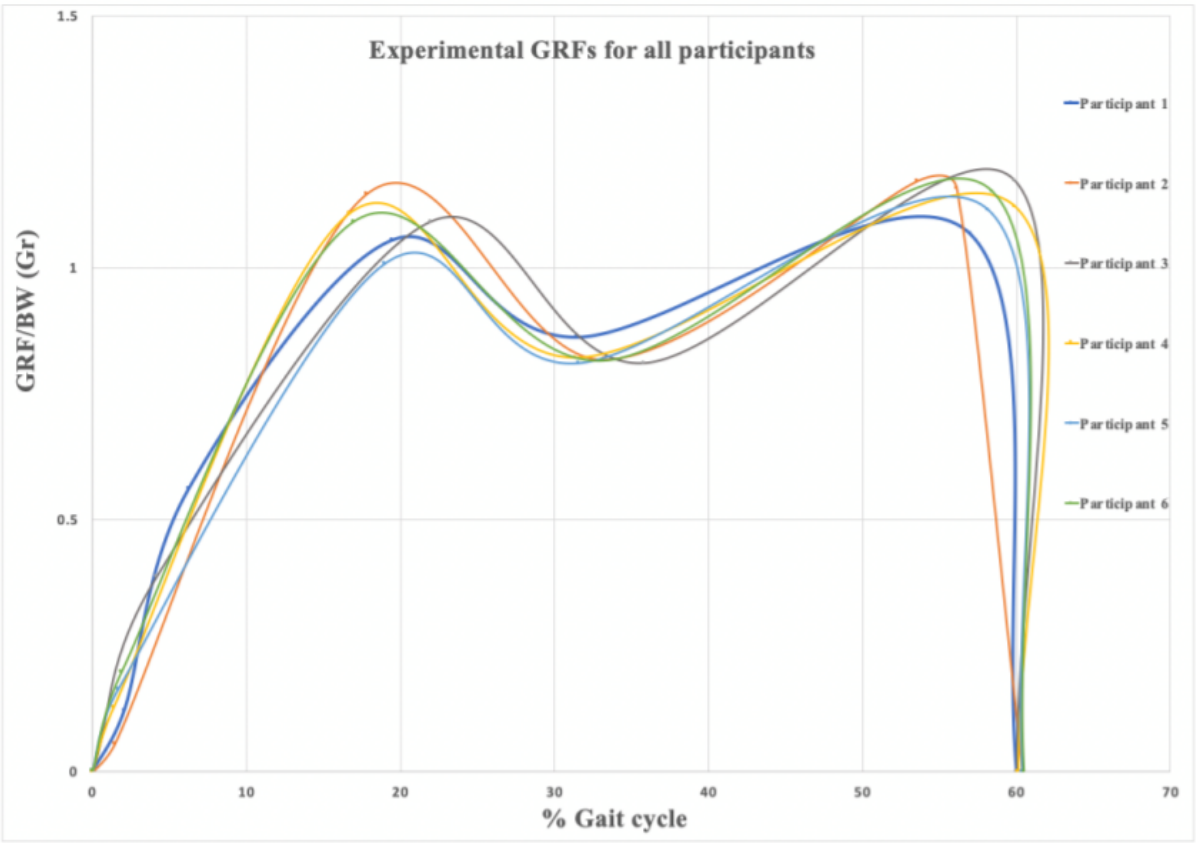


Figure 4.4: GRF results for the first feet for all participants (shown in different colours).

Participants performed the experiment as described above, and results were as shown in Table 4.3. Average velocity, standard deviation, and the most important vGRF values (two peaks and a trough) were summarised in order to check the walking speed of each participant Section 4.5.3, Table 4.10. A new computational method is proposed in Section 4.5.3 to categorise participant walking velocities as shown in Table 4.3 into free, fast or very fast walk speeds.

## 4.4 A Parametric GRF Equation Based on Published Results

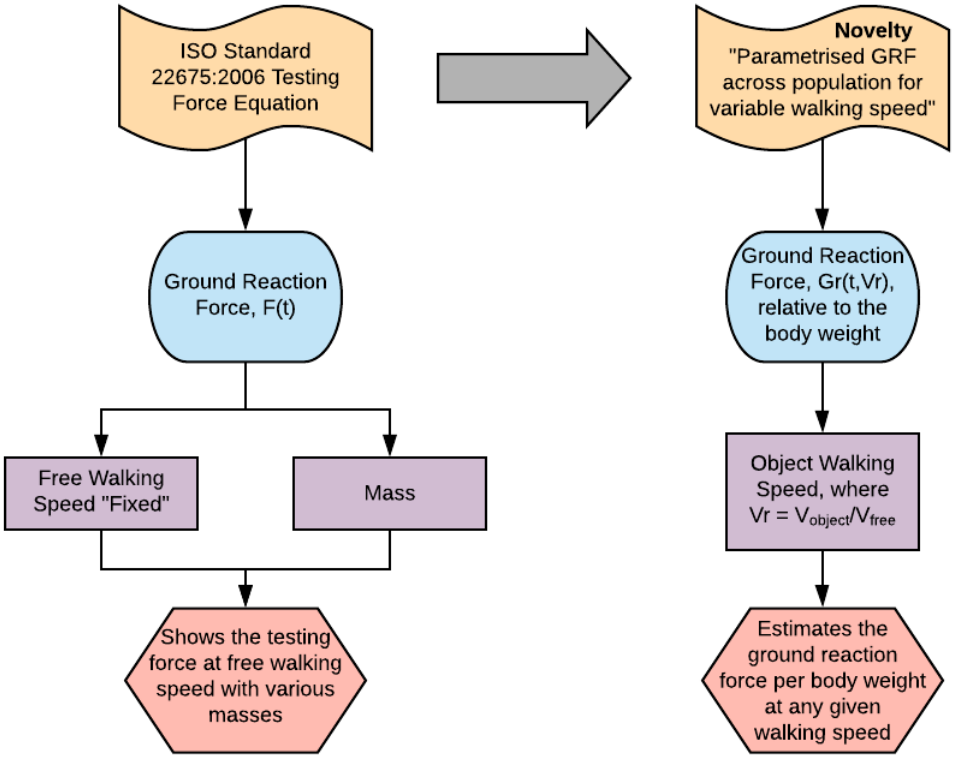


Figure 4.5: Flowchart illustrating the novel approach based on the ISO standard.

This section outlines the development of the GRF estimation equation for the healthy leg, amputees' affected leg, and amputees' sound leg. As expected, the experiment discussed in the previous section has provided a clear idea regarding the characteristics of the GRF curves.

Notably, all previous studies have concentrated on conducting experiments to evaluate the GRFs for various walking speeds. By contrast, this section determines the equation that will be used to calculate $G_r$ for varying walking speeds (one of the novelties of the present research) as shown in Figure 4.5. This section describes the technique used to realise these equations for different speeds, as indicated in Figure 4.5.

### 4.4.1 Analysis of Published Results

This section comprises two parts. The first part discusses a digitisation step used in processing the data, while the second describes the results reported in previous studies.

#### Methodology and Data Collection

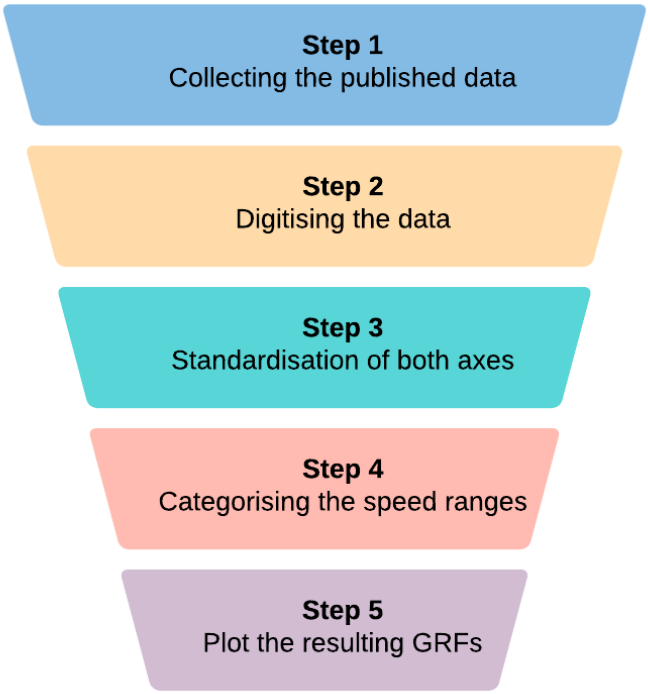


Figure 4.6: Summary of data collection steps.

Following a comprehensive literature review focused on gait, an extensive body of knowledge has been identified pertaining to the role of muscles in the scope of vGRFs and stable walking as applied to healthy persons. In this context, a particular focus was placed on articles evaluating vGRF, which were selected for a consequent examination. To accommodate the digitisation process, relevant vGRF graphs have been extracted from the collected research articles [56, 80, 140–144]. The summarised steps for data collection are shown in Figure 4.6.

Relying on the Web-Plot-Digitizer v3.5 [145] software package, the digitisation process involved the extraction of data from vGRFs articles for the purpose of performing the digitisation of individual images. After the original imagery was uploaded into the tool, the process consisted of defining the axes and using digital elements to accurately designate points along the curve. As both the size and resolution of the visual component correlate positively with points digitised per graph, the average number ranged from 20 to 100 points. Taking into account that the graphs obtained included standard 2D plots, 3D plots and vector format, this stage proved to be particularly time-consuming. Notably, visual issues such as inadequate quality (as observed in Keller's graph [56]) prompted the manual redistribution of the axes prior to digitisation. In this context, the standardisation of the axes emerged as one of the key steps following data extraction. For the purposes of the present research, the $x$-axis is chosen to represent the percentage gait cycle, with the $y$-axis representing vGRF per unit of body weight (vGRF/BW).

While the source material provides different units of speed, the majority of researchers rely on metres per second for recording natural walking speed. More specifically, the article by Stansfield [143] refers to normalised values, as the authors employed the following formula:

$$Velocity \times \frac{1}{\sqrt{height \times leg_{length}}} \tag{4.1}$$

From another perspective, Schwartz et al.'s study [80] avoids dimensionalising the walking speed, as these authors applied the following approach:

$$\frac{Velocity}{\sqrt{gravity \times leg_{length}}} \tag{4.2}$$

The conversion of non-conventional values to the unit of velocity was necessary to standardise walking speed values for the purposes of the research. As Schwartz et al. [80] did not include detailed leg measurements in their data, the leg length was assumed to be equal to the average estimation of 52% of a participant's total height. According to the inquiry into morphology and the mass distribution of military staff conducted by Armstrong [146], 52% of the total height is a reasonable predictor for an individual's leg length. Although Armstrong's study does not indicate valid estimations that can be applied to child subjects, a different approach was selected for standardising leg measurements for underage participants in the research of Schwartz et al. Based on the previously described assumption that leg length typically equals 52% of total height, the measurements for child participants presumed a reduction of 0.5% for each decrease of 10$cm$ in a subject's height.

In the literature, the categorisation of walking speed allowed for distribution of the analysed data into the following five categories: Very Slow, Slow, Free, Fast, and Very Fast. Considering that all researchers recorded FWS, it emerges as a baseline for calculating the remaining four categories. In this context, speeds below 42% of the observed FWS were categorised as Very Slow, while the Slow category corresponds to a 43-80% decrease in relation to FWS; moreover, Fast walking speed is considered to be between 120-140% of it. Finally, all walking speed records exceeding 140% of the observed FWS were regarded as being Very Fast (see Table 4.4 below).

Table 4.4: Walking speed categorisation as reported in the literature.

| **Range** | **Absolute Velocity (m/s)** | **Velocity Category** |
|---|---|---|
| Less than 42% | Less than 0.54 | Very Slow walking |
| 43% - 80% | Between 0.55 to 1 | Slow walking |
| FWS | 1.278 | FWS |
| 120% - 140% | 1.52 - 1.79 | Fast walking |
| More than 140% | Above 1.79 | Very Fast walking |

As can be seen from Figures (4.8 - 4.10), the obtained data were visualised with the help of graphs representing five walking speed categories. Consequently, the analysis of the graphs allowed for the recording of trough points and peak values on each respective curve. With reference to the precedent provided by Andriacchi et al. [141], the following signs were assigned to the values: $Fz1$ for the first peak; $Fz2$ for the trough point; and $Fz3$ for the second peak. The following step involved the examination of the $x$ and $y$ values associated with $Fz1$, $Fz2$, and $Fz3$ for the five walking speed categories. Accordingly, the calculation of the range values and the mean was based on the recordings for every curve of $Fz1$, $Fz2$ and $Fz3$, as illustrated in Appendix B. Regarding the $y$ values for $Fz1$, $Fz2$ and $Fz3$ in the four categories excluding FWS, the former were represented as a percentage of the corresponding figures for FWS. The final stage of the digitisation process involved the generation of individual curves for five speed categories based on the data obtained from the graphs presented in Figures (4.8 - 4.10). Moreover, the average figures of $x$ and $y$ values with regard to $Fz1$, $Fz2$, and $Fz3$ for the five categories are represented by the curves, while Figure 4.11 additionally displays the predicted average vGRFs for different walking speed categories.

**Published Experimental Results**

Figure 4.8a plots the vGRF obtained by different researchers regarding the results for Very Slow walking speed. The colour red denotes the results of Liu [140], results who defined Very Slow speed as $0.54m/s$; on the other hand, blue shows Schwartz's [80] findings, defining a Very Slow speed as $0.44m/s$. Moreover, Figure 4.8b shows the vGRF results for four researchers (Liu [140], Schwartz [80], Masani [142], and Stolwijik [144]), who defined Slow speeds as 0.75, 0.81, 0.83, and $1.0m/s$, respectively. Liu's [140] results are shown in blue, Schwartz's [80] in red, Masani's [142] in orange, and Stolwijik's [144] in green.

Six studies are reviewed to estimate the FWS vGRF results (see Figure 4.9a), Schwartz's [80] results yield a speed of $1.23m/s$, shown in blue, while Stolwijik's [144] results are shown in red with a FWS of $1.39m/s$. In addition, Stansfield [143] measured vGRF at a speed of $1.24m/s$, as shown by the dotted green line, and Andriacchi's [141] findings are shown in purple for a walking speed of $1.5m/s$. Liu [140] defines FWS as $1.15m/s$, which is plotted in cyan. The sixth researcher was Masani [142], shown in orange for a FWS of $1.38m/s$. The average vGRF curve represents the current experimental data for a FWS of $1.855m/s$.

Regarding fast walking speed (see Figure 4.9b), five different researchers defined values for vGRF. First, Schwartz [80] defined the speed as 1.6 m/s; these results are shown in dark blue. Stolwijik's [144] results for $1.78m/s$ walking speed are shown in red, while Liu's [140] for $1.56m/s$ are shown in green. Keller [56] split his Fast speed into two lines, one for women ($1.5m/s$) and one for men ($1.5m/s$); female results are indicated by a dotted purple line, while the male results are plotted using a cyan dotted line. The final average vGRF curve results of participant 2 for the current research with a speed of $1.59m/s$ are also shown in Figure 4.9b.

Very Fast walking speed was defined by three researchers, each of which defined this speed

differently. Schwartz [80] defined Very Fast speed as $1.95m/s$, and the vGRF is shown in blue; next was Masani [142], who defined this speed as $2.22m/s$, with the vGRF results shown in red. The last researcher was Keller [56], who defined three different speeds for Very Fast walking: one for women ($2.0m/s$), indicated by the dotted green line; one for men ($2.0m/s$), represented by the dotted purple line; and a final one that is also for men, but at a different speed ($2.5m/s$). This last one is shown in orange (see Figure 4.10). As can be seen from Figure 4.11, the average results for each researcher whose work were analysed have been plotted for all defined walking speeds. The values were calculated by finding the average of ($Fz1$), ($Fz2$), and ($Fz3$) for each researcher, after which the averages were plotted as shown in Figure 4.11 to summarise the data. The walking speed categories are presented in Figure 4.7.

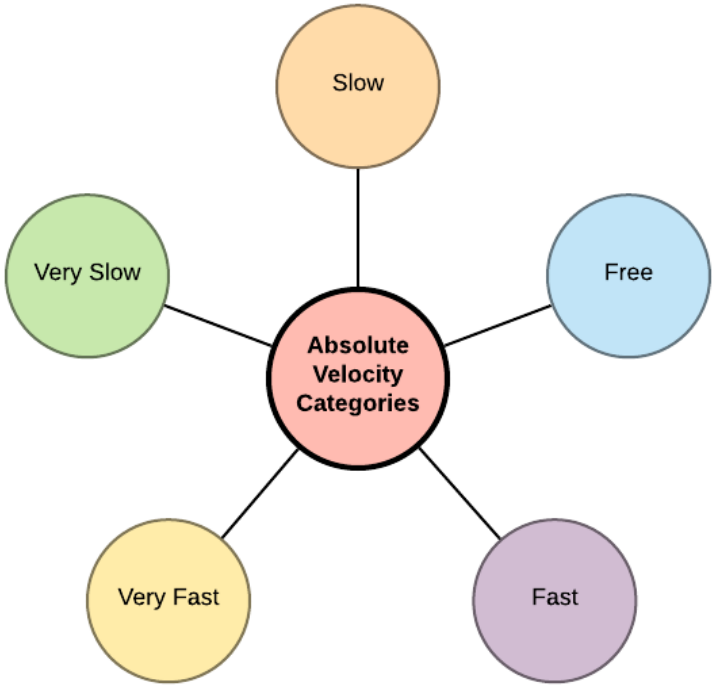


Figure 4.7: Walking Speed Categories

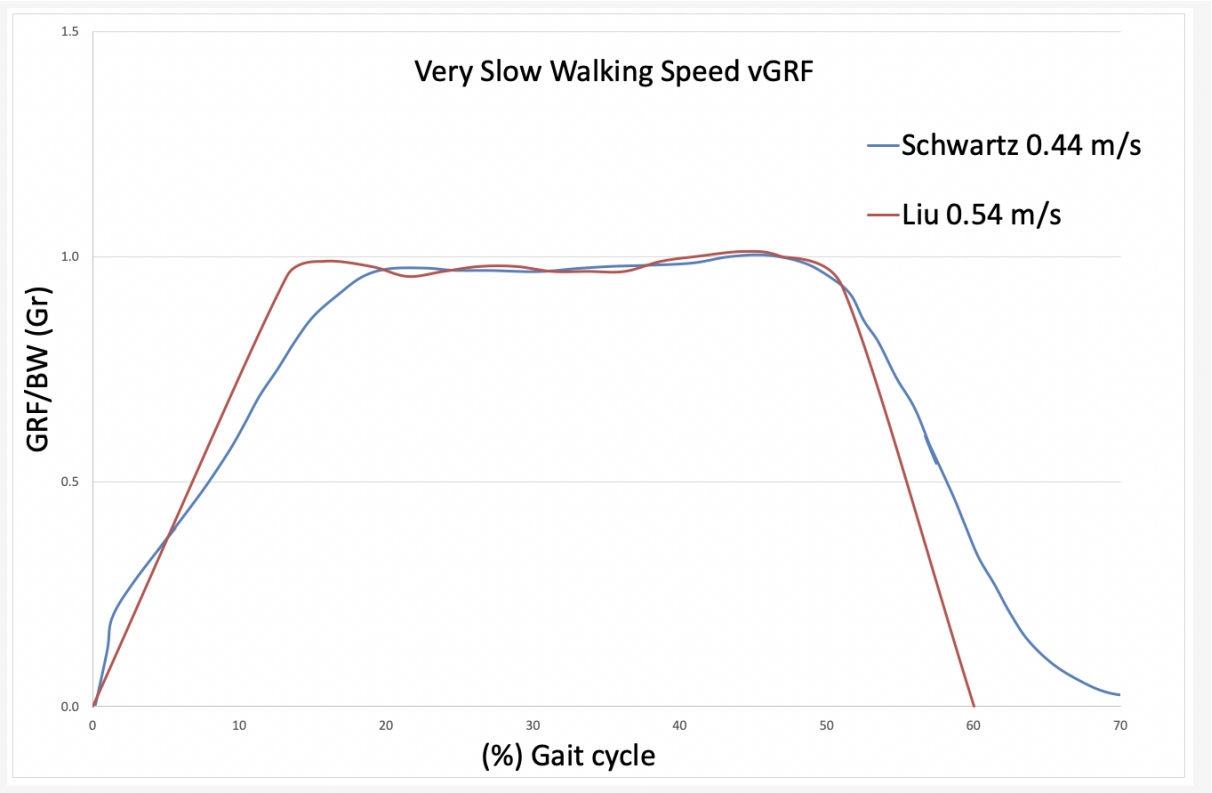


(a) Very Slow walking speed vGRF

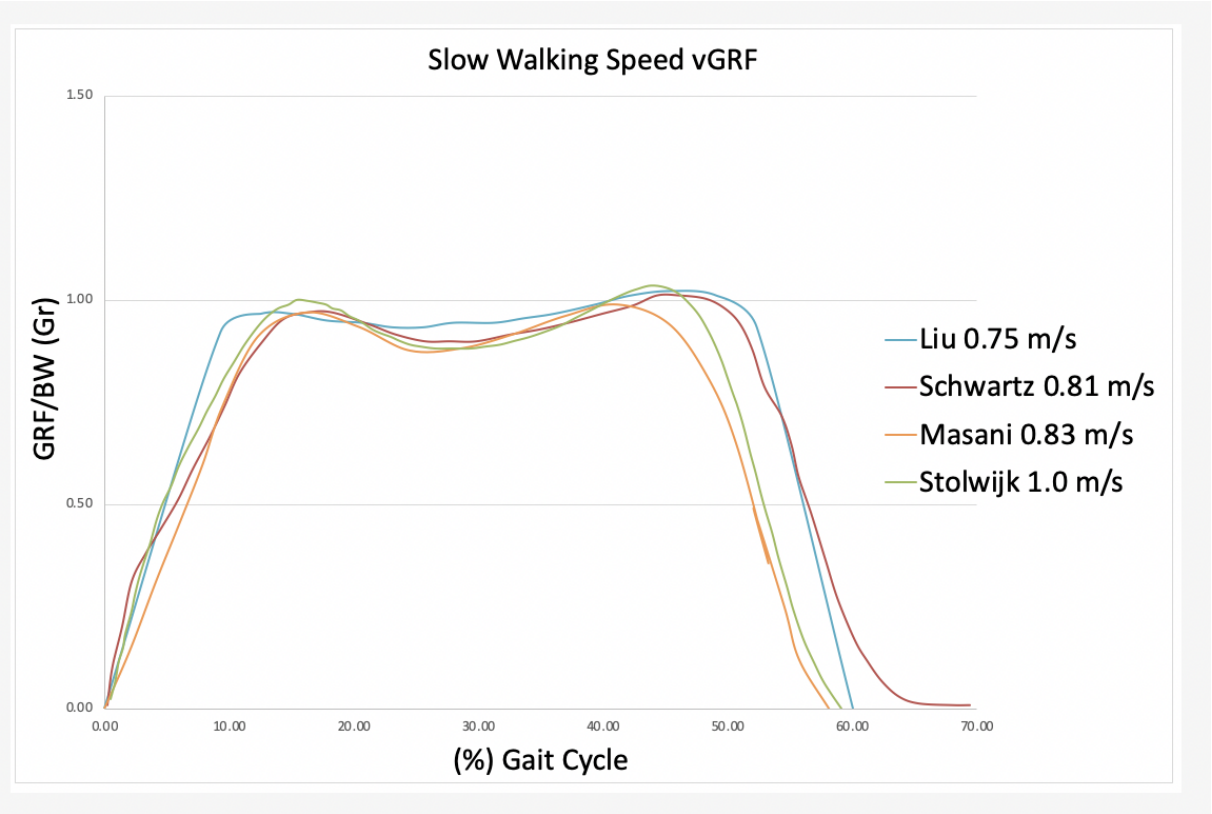


(b) Slow walking speed vGRF

Figure 4.8: Results of Very Slow and Slow speeds from different researchers.

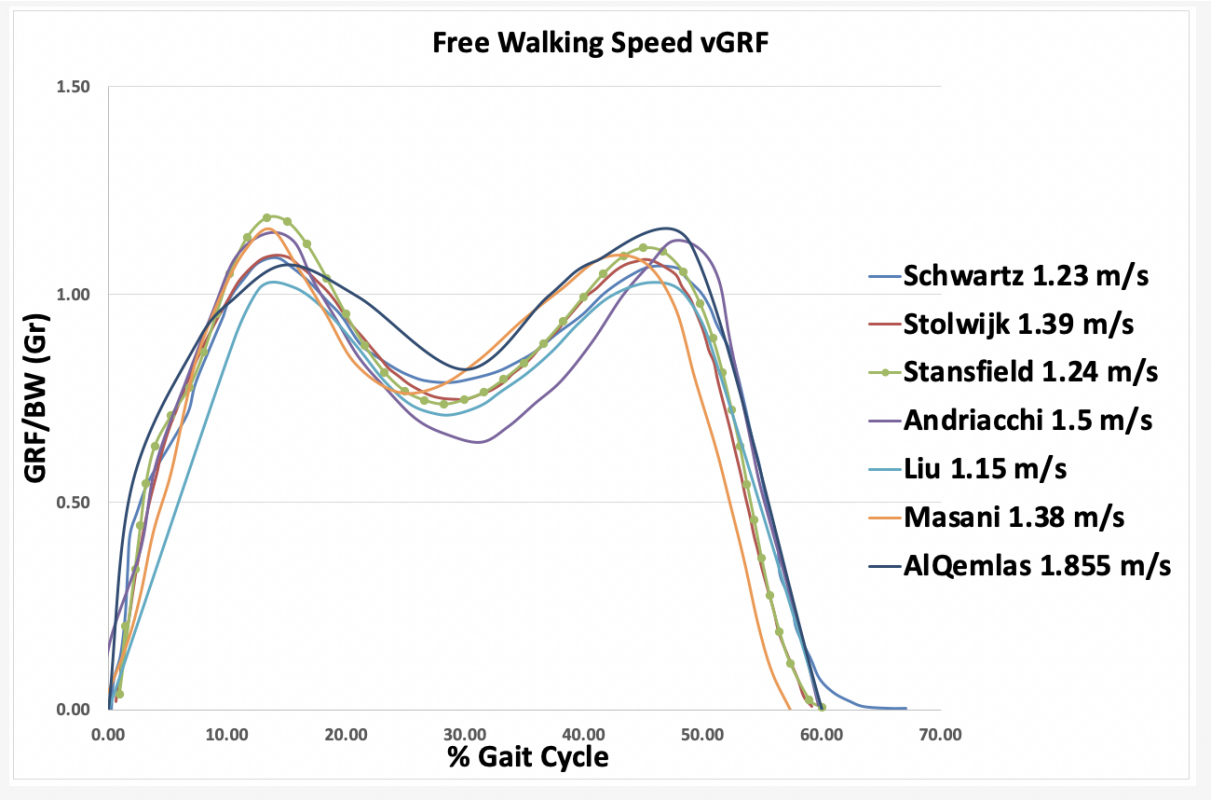


(a) Free Walking speed vGRF

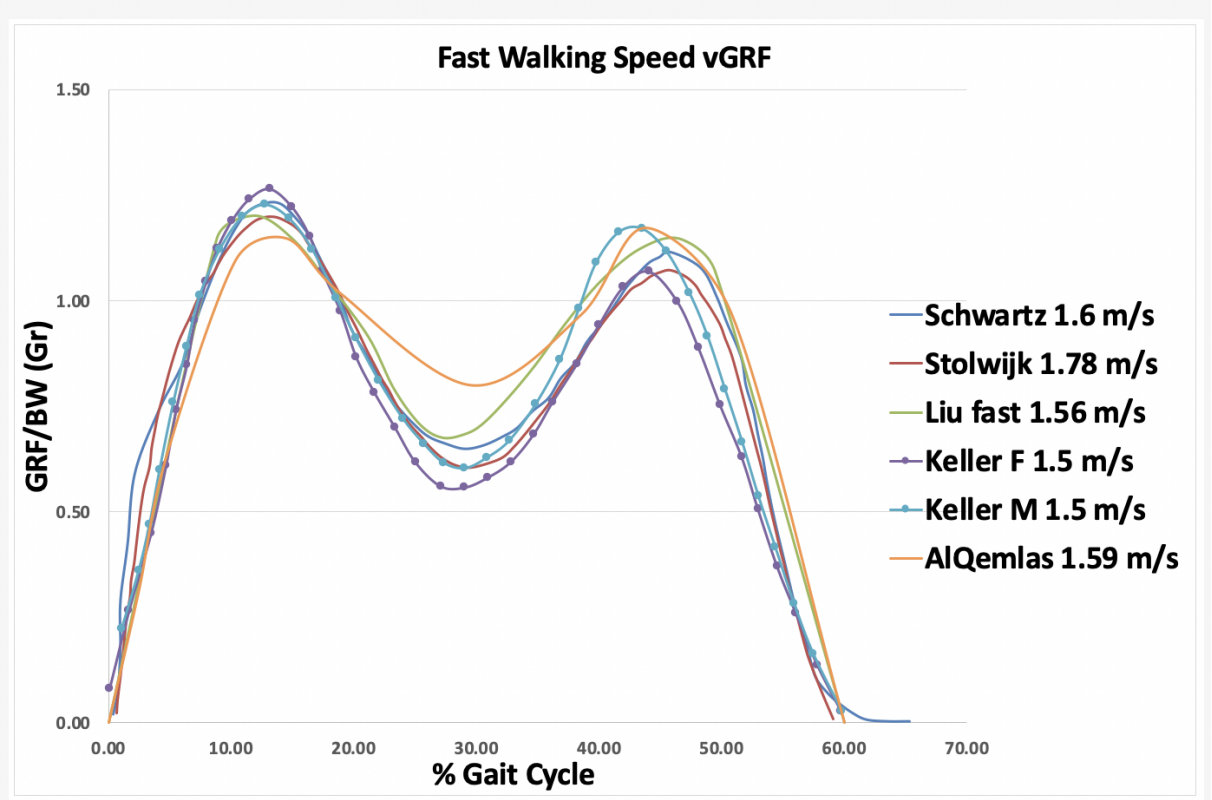


(b) Fast walking speed vGRF

Figure 4.9: Results of Free and Fast speeds from different researchers.

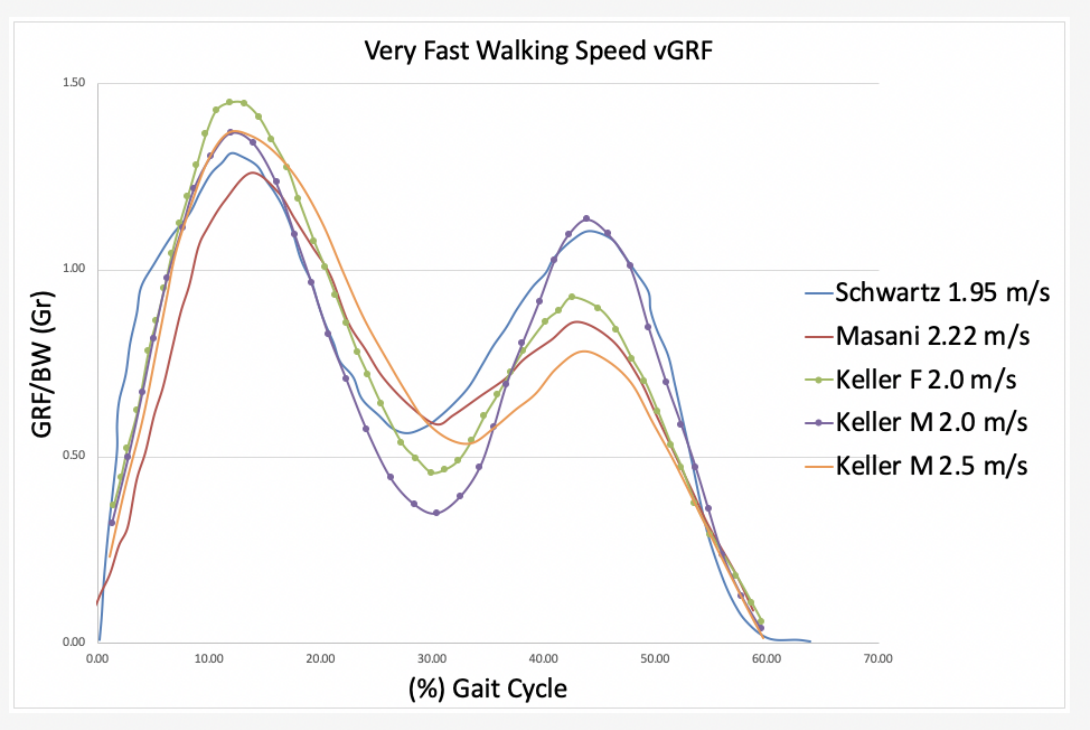


Figure 4.10: Very Fast walking speed vGRF

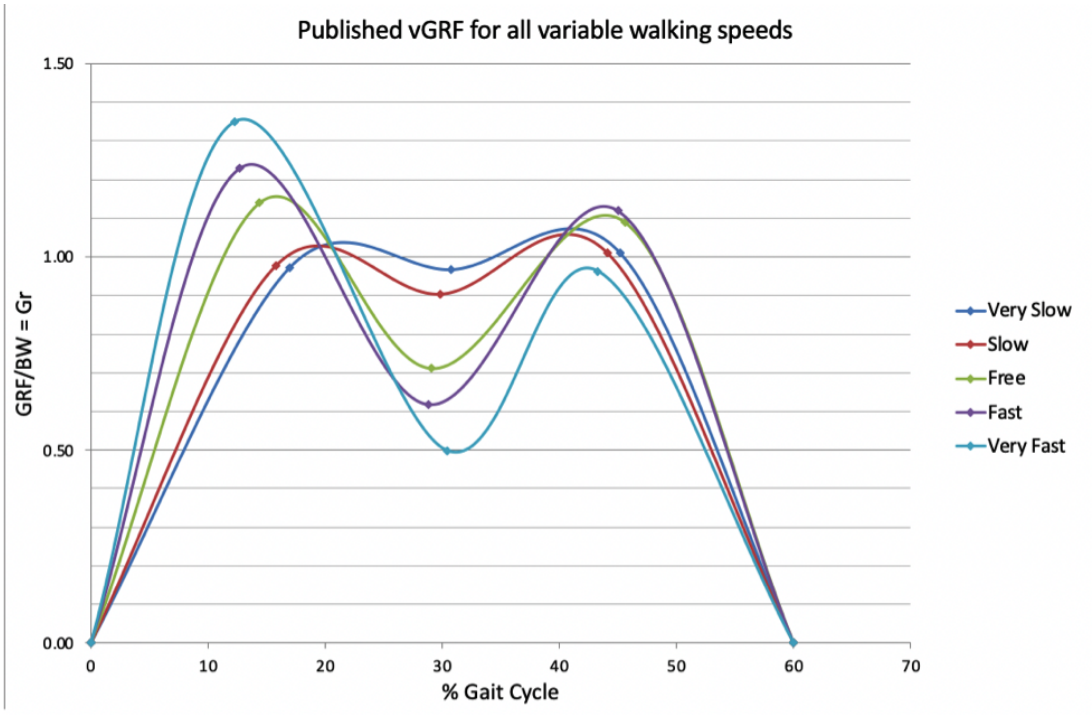


Figure 4.11: Average results for published studies recorded for different speeds: Very Slow, Slow, Free, Fast, and Very Fast.

### 4.4.2 Parametrised GRFs for Healthy Population and Amputees

To achieve the aim of this chapter and introduce the novel elements of this research, the first step was to extract data from previous studies and convert them to the same scale. The next section will discuss the approach to deriving the $G_r$ equations.

#### The Novel Approach

Applying the novel approach requires a well-designed procedure. To devise equations capable of estimating $G_r$ for different walking speeds and various limb situations, the following approach was adopted (this approach is later explained in more detail in Figure 4.12):

- From the previous study (Section 4.4.1), five different velocity ranges from other researchers' studies (Very Slow, Slow, Free, Fast, and Very Fast) were introduced.
- Based on the MATLAB curve fitting software (as shown in Appendix I), a Slow and Very Slow fit line were obtained and observed to be fourth-order polynomial functions (GRF/BW as a function of gait cycle (t)).

$$G_r(t) = at^4 + bt^3 + ct^2 + dt + e \tag{4.3}$$

At this point, the author obtained the GRF/BW ($G_r(t)$) as a function of the gait cycle, for Very Slow (VS) and Slow (S) walking speeds, in order to alter the function of a single variable to a function of multiple variables $G_r(t, V_r)$. The following steps (example for VS and S) are describing how to connect the velocity ratio as a variable of $G_r$.

- First, the velocity ratio ($V_r$) is defined as the ratio between the examined velocities by average of FWS from published data.

- From Equation 4.3 for Very Slow and Slow, the best-fitting curve (obtained from MATLAB curve fitting software [3]) between the coefficient of each term versus the velocity ratio is found. As an example, for Very Slow and Slow GRF equations, the coefficient function is expressed in the form of an exponential function: $a_1 \times e^{a_2 \times V_r}$ (see Figure I-1).

- By substituting each coefficient function with its corresponding coefficient from $G_r(t)$, the parametrised $G_r$ equation is obtained.

- Repeat the previous steps to obtain the remaining parametrised $G_r$ equations for healthy adults and amputees.


Figure 4.12: Mind-map for parametrised GRF

[3] see Appendix I

**Parametrised Equation for Healthy Leg, Prosthetic and Intact Leg**

Applying the approach discussed in the previous section and the results of other published studies discussed earlier in the chapter, the estimated $G_r$ equations can be derived in order to estimate the value for different walking speeds. Obtaining the healthy leg parametrised equation will help in understanding its movement and predicting its corresponding vGRF at various walking speeds, which can help in designing the optimised prosthetic foot that can perform in the exact same manner as a healthy foot. Using the curve fitting method contained in the MATLAB software, the equation for the healthy foot was found (Equation 4.4) to be a piecewise function (Very Slow and Slow) of the fourth-order polynomial, with exponential coefficients of $V_r$ ranging between 0.42 and 0.8. The second equation (Free, Fast, and Very Fast) describes the sixth-order polynomial with a linear-sinusoidal coefficients function (see Figure I-2) and $V_r$ ranging between 0.84 and 1.69 for the same piecewise function. However, a transition region exists between these two equations in the range of 0.81-0.83; this region is not frequently used. Note that Tables 4.5 and 4.6 contain the value of the coefficients for Equation 4.4.

$$G_r(t, V_r) \begin{cases} \left(a_1 \times e^{(a_2 \times V_r)}\right) \times t^4 + \left(b_1 \times e^{(b_2 \times V_r)}\right) \times t^3 + \left(c_1 \times e^{(c_2 \times V_r)}\right) \times t^2 + \\ \left(d_1 \times e^{(d_2 \times V_r)}\right) \times t + \left(e_1 \times e^{(e_2 \times V_r)}\right), \text{ if } (0.42 \leq V_r \leq 0.8) \\ \left(a_1 \times \sin(V_r - \pi) + a_2 \times (V_r - 10)^2 + a_3\right) t^6 + (b_1 \times \sin(V_r - \pi) + b_2 \times \\ (V_r - 10)^2 + b_3) t^5 + \left(c_1 \times \sin(V_r - \pi) + c_2 \times (V_r - 10)^2 + c_3\right) t^4 + (d_1 \times \sin(V_r - \pi) + \\ d_2 \times (V_r - 10)^2 + d_3) t^3 + \left(e_1 \times \sin(V_r - \pi) + e_2 \times (V_r - 10)^2 + e_3\right) t^2 + (f_1 \times \sin(V_r - \pi) + \\ f_2 \times (V_r - 10)^2 + f_3\right) t + \left(g_1 \times \sin(V_r - \pi) + g_2 \times (V_r - 10)^2 + g_3\right) \\ \text{if } (0.84 < V_r \leq 1.69) \end{cases} \tag{4.4}$$

Table 4.5: First form of Equation 4.4 coefficients for healthy leg equations for Very Slow (VS) and Slow (S) walking speeds.

| **Coefficient (VS, S)** | **Value** | **Coefficient (VS, S)** | **Value** |
|---|---|---|---|
| $a_1$ | $-1.828 \times 10^{-6}$ | $c_2$ | -0.07847 |
| $a_2$ | -0.04054 | $d_1$ | 0.1645 |
| $b_1$ | 0.0002184 | $d_2$ | -0.1111 |
| $b_2$ | -0.05367 | $e_1$ | -0.01842 |
| $c_1$ | -0.009255 | $e_2$ | -1.869 |

Table 4.6: Second form of Equation 4.4 coefficients for healthy leg equations for Free, Fast (F) and Very Fast (VF) walking speeds.

| **Coefficient (Free, F, VF)** | **Value** | **Coefficient (Free, F, VF)** | **Value** |
|---|---|---|---|
| $a_1$ | $-2.476 \times 10^{-8}$ | $d_3$ | 0.01602 |
| $a_2$ | $8.46 \times 10^{-11}$ | $e_1$ | -0.1232 |
| $a_3$ | $-2.543 \times 10^{-8}$ | $e_2$ | 0.002074 |
| $b_1$ | $4.542 \times 10^{-6}$ | $e_3$ | -0.2745 |
| $b_2$ | $-2.458 \times 10^{-8}$ | $f_1$ | 0.5655 |
| $b_3$ | $5.418 \times 10^{-6}$ | $f_2$ | -0.01507 |
| $c_1$ | -0.000308 | $f_3$ | 1.847 |
| $c_2$ | $2.426 \times 10^{-6}$ | $g_1$ | -1.017 |
| $c_3$ | 0.0004326 | $g_2$ | 0.01252 |
| $d_1$ | 0.0009383 | $g_3$ | -1.844 |
| $d_2$ | -0.0001058 | | |

According to various studies, the sound leg is defined as the leg that is biologically intact. Eshraghi et al. [147] note that this limb offers support to the prosthetic leg, which in turn increases the pressure on it due to the increased load. As explained in Chapter Two [17], data was extracted from graphs using web-based digitisation, as shown in Figure 2.9. Moreover, more data related to the sound leg was extracted from other published studies; this data has been tabulated in Appendix C [22]. Similarly, identical sources were used for the prosthetic foot. Equation 4.5 represents the estimated $G_r$ for the intact leg, and Table 4.7 contains the values of its coefficients.

$$G_r(t,V_r)\begin{cases} Gr(t,Vr) = \big(a_1(\sin(Vr-\pi)) + a_2(Vr-10)^2 + a_3\big)\times t^6 + (b_1(\sin(Vr-\pi))+ \\ b_2(Vr-10)^2 + b_3\big)\times t^5 + \big(c_1(\sin(Vr-\pi)) + c_2(Vr-10)^2 + c_3\big)\times t^4 + (d_1(\sin(Vr-\pi))+ \\ d_2(Vr-10)^2 + d_3\big)\times t^3 + \big(e_1(\sin(Vr-\pi)) + e_2(Vr-10)^2 + e_3\big)\times t^2 + (f_1(\sin(Vr-\pi))+ \\ f_2(Vr-10)^2 + f_3\big)\times t + \big(g_1(\sin(Vr-\pi)) + g_2(Vr-10)^2 + g_3\big) \end{cases} \tag{4.5}$$

Table 4.7: Equation 4.5 coefficient values.

| Coefficient | Value | Coefficient | Value | Coefficient | Value |
|---|---|---|---|---|---|
| $a_1$ | $-5.729\times10^{-9}$ | $c_2$ | $-6.943\times10^{-7}$ | $e_3$ | 0.07902 |
| $a_2$ | $-3.228\times10^{-11}$ | $c_3$ | $6.481\times10^{-5}$ | $f_1$ | -0.2883 |
| $a_3$ | $2.055\times10^{-9}$ | $d_1$ | 0.0005907 | $f_2$ | 0.005835 |
| $b_1$ | $9.204\times10^{-7}$ | $d_2$ | $3.227\times10^{-5}$ | $f_3$ | -0.6057 |
| $b_2$ | $7.436\times10^{-9}$ | $d_3$ | 0.0003361 | $g_1$ | -0.02692 |
| $b_3$ | $-5.909\times10^{-7}$ | $e_1$ | 0.01503 | $g_2$ | 0.0007578 |
| $c_1$ | $-4.734\times10^{-5}$ | $e_2$ | -0.000719 | $g_3$ | -0.09085 |

The vGRFs should be calculated for different speeds in order to guarantee stability. The $G_r$ for the prosthetic leg can be calculated for a specific range of walking speeds (due to lack of published experimental data) using Equation 4.6. The coefficient values of this equation are shown in Table 4.8.

$$\begin{aligned} Gr_a(t,Vr) = (\ & a_1(\sin(Vr-\pi)) + a_2(Vr-10)^2 + a_3\Big) \times t^6 \\ & + \Big(b_1(\sin(Vr-\pi)) + b_2(Vr-10)^2 + b_3\Big) \times t^5 \\ & + \Big(c_1(\sin(Vr-\pi)) + c_2(Vr-10)^2 + c_3\Big) \times t^4 \\ & + \Big(d_1(\sin(Vr-\pi)) + d_2(Vr-10)^2 + d_3\Big) \times t^3 \\ & + \Big(e_1(\sin(Vr-\pi)) + e_2(Vr-10)^2 + e_3\Big) \times t^2 \\ & + \Big(f_1(\sin(Vr-\pi)) + f_2(Vr-10)^2 + f_3\Big) \times t \\ & + \Big(g_1(\sin(Vr-\pi)) + g_2(Vr-10)^2 + g_3\Big) \end{aligned} \tag{4.6}$$

Table 4.8: Values of prosthetic leg coefficient for the estimated Equation 4.6.

| **Coefficient** | **Value** | **Coefficient** | **Value** | **Coefficient** | **Value** |
|---|---|---|---|---|---|
| $a_1$ | $1.86 \times 10^{-9}$ | $c_2$ | $6.422 \times 10^{-7}$ | $e_3$ | -0.2741 |
| $a_2$ | $-2.408 \times 10^{-10}$ | $c_3$ | $5.548 \times 10^{-5}$ | $f_1$ | 0.4976 |
| $a_3$ | $2.55 \times 10^{-8}$ | $d_1$ | 0.003411 | $f_2$ | -0.02244 |
| $b_1$ | $2.355 \times 10^{-7}$ | $d_2$ | $-9.467 \times 10^{-5}$ | $f_3$ | 2.334 |
| $b_2$ | $1.918 \times 10^{-8}$ | $d_3$ | 0.009383 | $g_1$ | 0.3023 |
| $b_3$ | $-2.118 \times 10^{-6}$ | $e_1$ | -0.07379 | $g_2$ | -0.00626 |
| $c_1$ | $-5.938 \times 10^{-5}$ | $e_2$ | 0.002709 | $g_3$ | 0.7745 |

## 4.5 Results and Discussion

In this section, the GRF results based on the experimental study are discussed. The validation of the results is also deployed.

### 4.5.1 Discussion of GRF Results from the Gait Lab Experiment

Box plots were created for the $Fz1$ (non-dimensional) results for all participants (five trials per participant), as shown in Figure 4.13. The results confirmed the high variability in the participants' $Fz1$ during the experiment, which can be attributed to differences in factors such as body mass. The box plots also revealed other variations that may have been caused by human error and/or the length of time it took some participants to adjust and comprehend the experimental goals. For example, the box plot for Participant 5 exhibits symmetry, and the median is centred; this signifies normality. Notably, the range between the data is low, which means that the variation from this participant is also low – that is, that the values are close to each other. On the other hand, Participant 6's box plot exhibits high variation in the data due to the influence of the various factors mentioned above. It is also evident that the median value is skewed towards the first quartile.

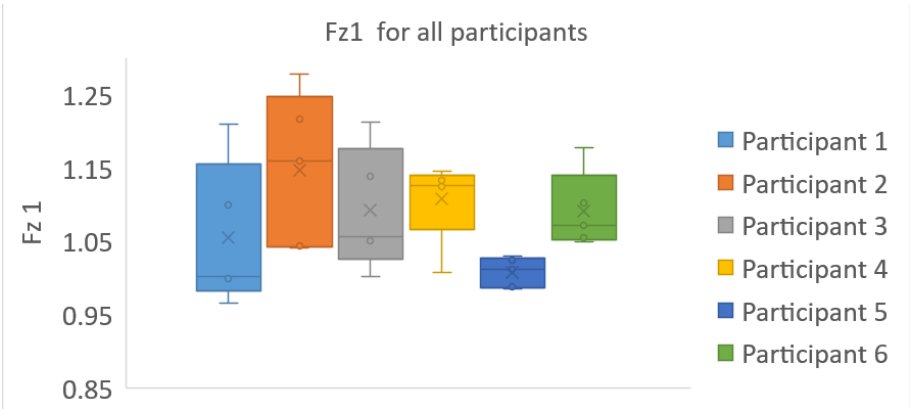


Figure 4.13: Box plots for all participants in the gait lab experiment.

As seen in Figure 4.13, the plot for Participant 1 shows that the median is skewed towards the first quartile and has high variation. Participant 2 also exhibits high variation, while Participant 3 has smaller variation than 1 and 2. The median here is also skewed towards the first quartile. Moreover, Participant 4's variation is small; however, the median is seen to skew towards the third quartile.

### 4.5.2 Verification of the Parametrised Equations with Published Experimental Data

As explained in the previous section, the equations for healthy, sound (intact), and prosthetic (affected) legs were developed to calculate $G_r$ at different walking speeds. Initially, the healthy parametrised equation for GRF was tested for different $V_r$, as illustrated in Figures 4.15 - 4.17. The equation for HP yielded a robust solution while changing the velocity ratio, which provides us with an insight into the characteristics of the curve while changing the velocity ratio. The results are in a dimensionless plane, meaning that the $x$ and $y$-axis are unitless. This dimensionless approach made it possible to extend the results to any body weight. In order to, check the robustness of the equation, the experimental published data has been plotted versus the estimated values under the same conditions ($V_r = V_e/V_{free}$) as shown in Figure 4.14. The equation yielded a visually acceptable match in predicting the pattern of the GRF for Very Slow and Slow walking speeds. On the other hand, when checking the equation using the Free, Fast, and Very Fast speed ranges, the estimated $G_r$ was found to exhibit similar performance in predicting the first peak value. The equation is unable to predict the second peak with appropriate accuracy (approximately 10% error). Figure 4.18 plots the comparison between the parametrised equation and other published data. The results suggest that changes in GRFs are

strongly related with the velocity ratio. Moreover, the GRF curve at the unit velocity ratio can be used as a basis for predicting the GRF curves associated with the walking speed categories. As deviations in the values of $Fz1$, $Fz2$ and $Fz3$ points tend to alter the structure of the GRF curve, the relative location of these three points is interpreted as being indicative of the expected changes (see Figure 4.18). In the case of Very Slow speed, there are almost no changes to the curve between $Fz1$ and $Fz3$. Moreover, as walking speed increases from Slow to Very Fast, the curve attains a wave-shaped character with significant changes to its amplitude. Finally, the points $Fz1$ and $Fz3$ on the GRF curve are typically equal at $V_r = 1$. The validation steps corresponding to the GRF are shown in Figure 4.14. However, predicting the second peak of the curve was not possible due to the limited number of papers from which the estimated equations were extracted; in addition; the current publications showed greater variability in the second peak value at walking speeds, age, type of prosthetic foot used and mobility of amputees.

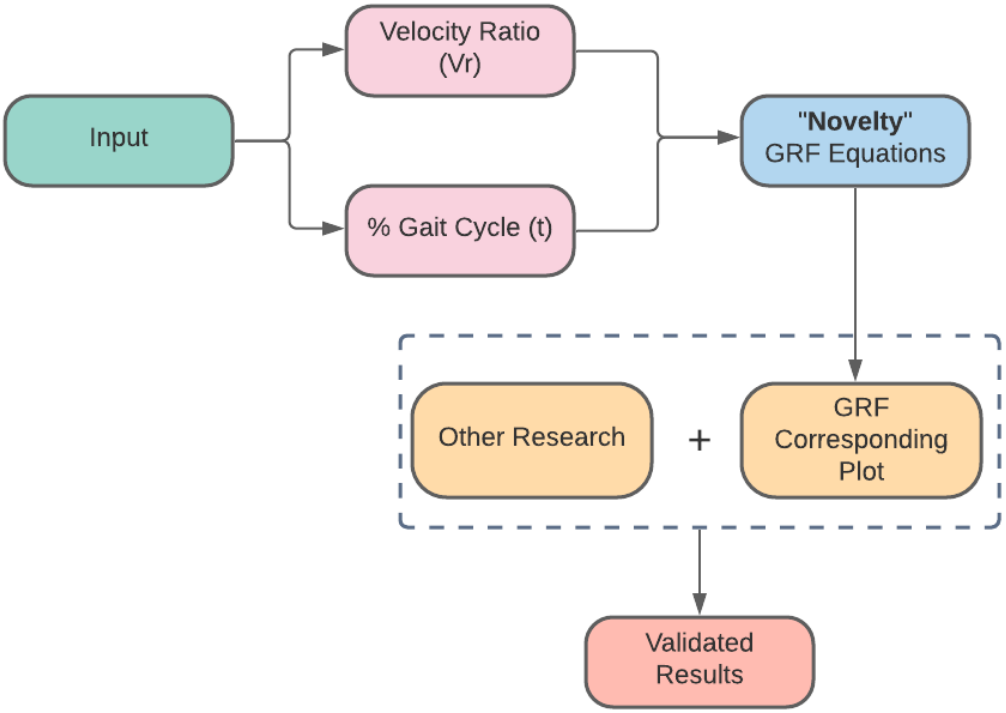


Figure 4.14: A process for verifying GRF results

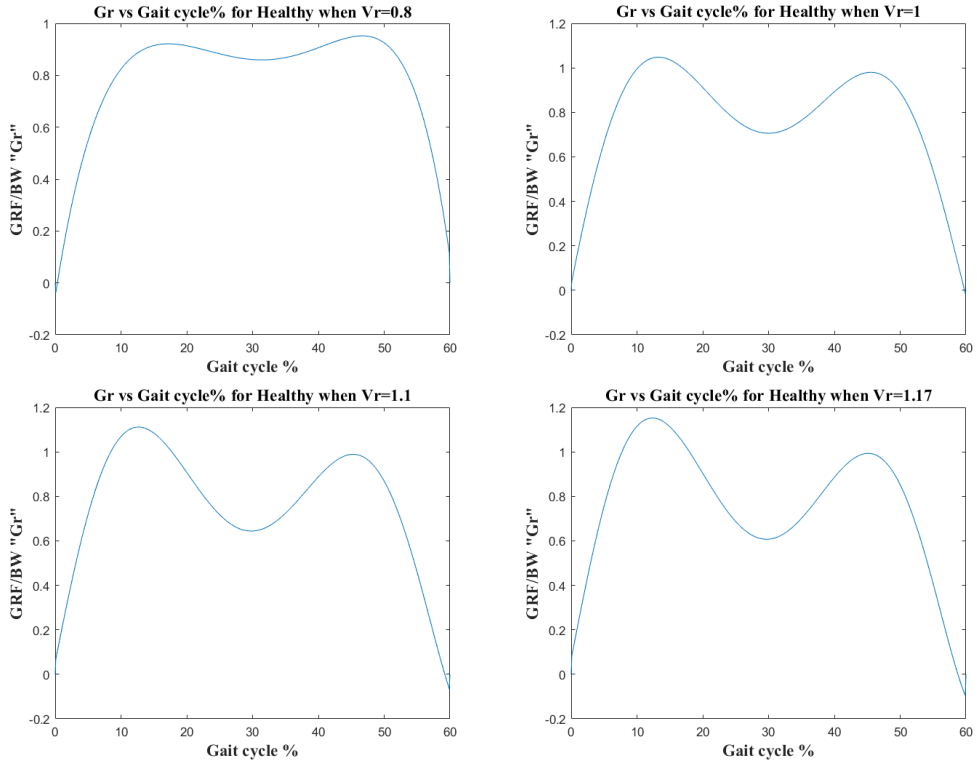


Figure 4.15: $G_r$ vs. Gait cycle% plots for Velocity Ratio ($V_r$) of 0.8, 1, 1.1, 1.17.

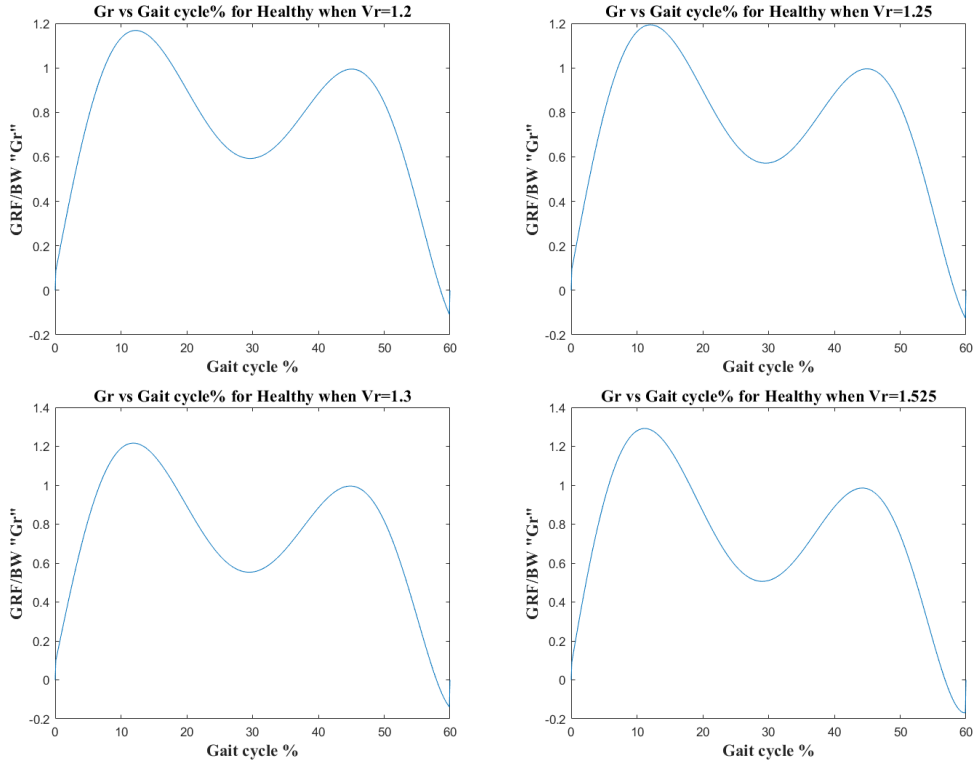


Figure 4.16: $G_r$ vs. Gait cycle% plots for Velocity Ratio ($V_r$) values of 1.2, 1.25, 1.3, 1.525.

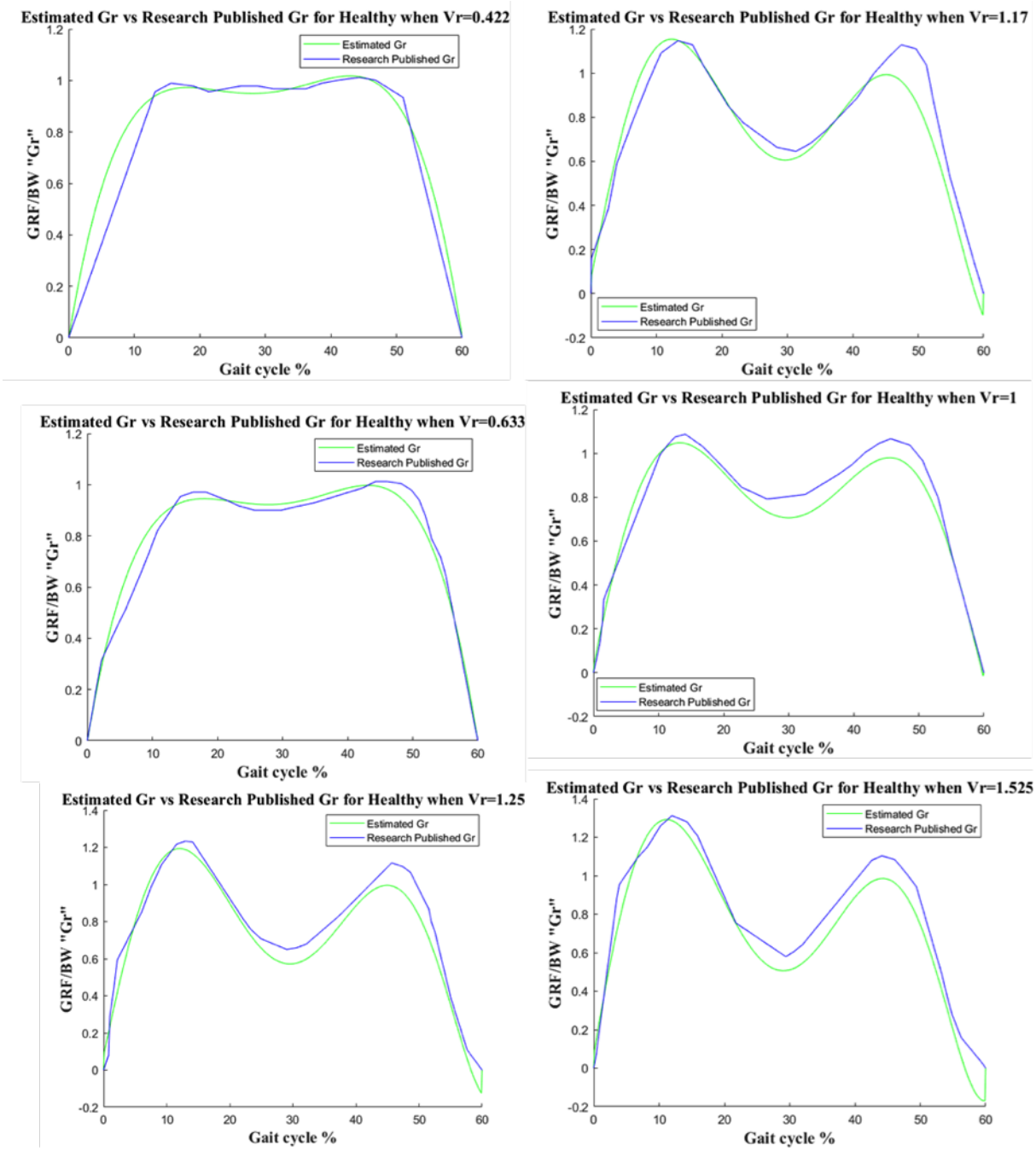


Figure 4.17: $G_r$ estimation results compared with those of Silverman and Neptune [17] for the healthy leg.

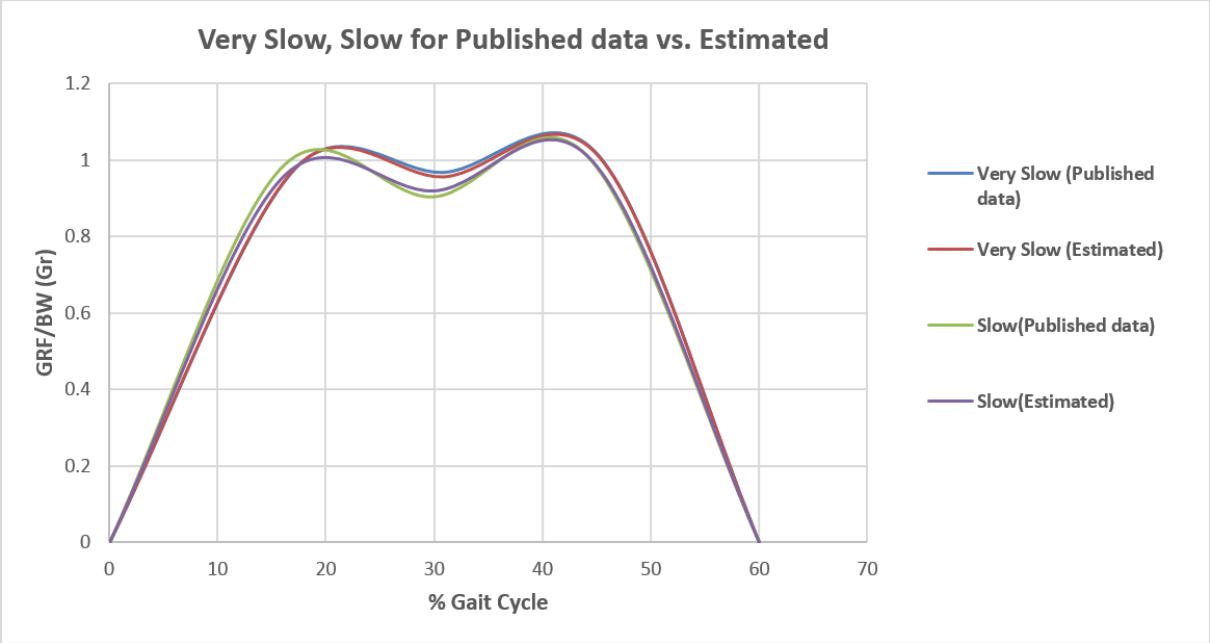


(a) Very Slow (VS), Slow(S) (vGRF) for published data vs. estimated at $V_r$ = 0.4 and 0.63

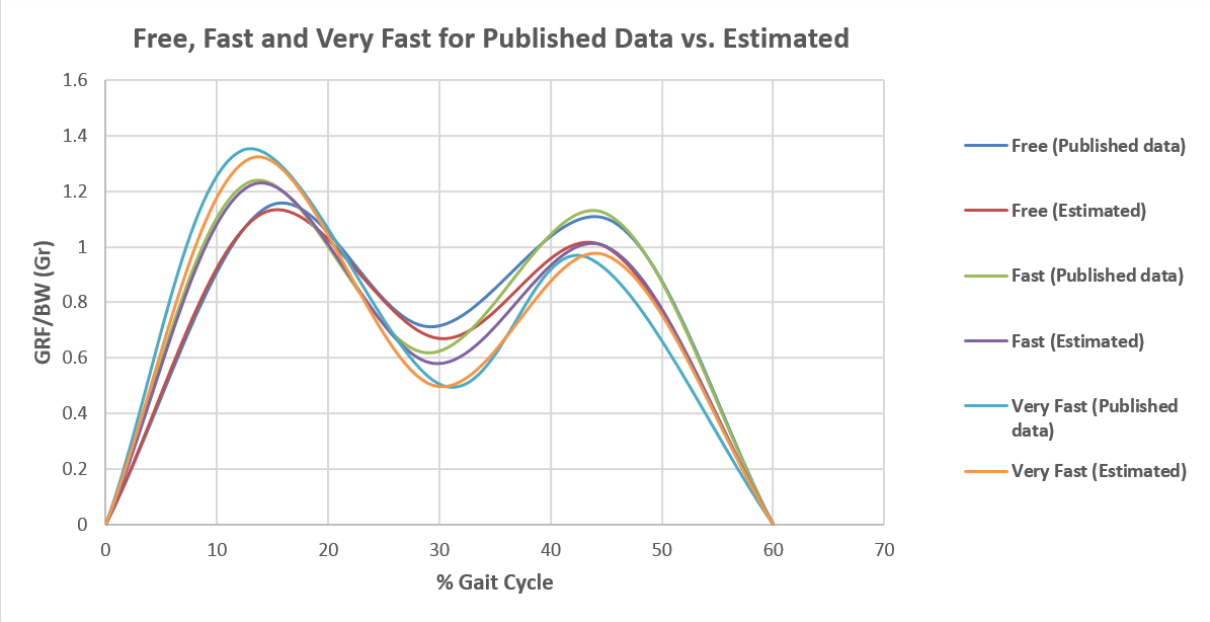


(b) Free, Fast (F) and Very Fast (VF) (vGRF) for published data vs. estimated at $V_r$ = 1.09, 1.29 and 1.67

Figure 4.18: Comparison between estimated $G_r$ values obtained from the proposed Equations 4.4 and average published results as presented in Figure 4.11.

From Figure 4.17, it can be seen that the estimated $G_r$ Equation 4.4 for the healthy population exhibited excellent predictive ability for the first peak, from very slow to very fast, where the error percentage is approximately 0.5% or less. However, the second peak prediction yielded an average estimation with an error percentage less than 10%. Moreover, Figure 4.18 presents the two different forms of Equation 4.4 for all walking speeds published by the researchers compared with the estimated values proposed by the equations.

Similarly, the result of the published data for the sound leg (0.9, 1.2 and 1.5 m/s) [17] has been plotted along with estimated values from the proposed set of equations with corresponding $G_r$ and $V_r$ (0.7, 0.94 and 1.17) values. As shown in Figure 4.19, these values have been chosen to match the first peak of the vGRF for the sound leg. There is a close agreement in the results for $Fz1$ (occurring at about 15% of the gait cycle), $Fz2$ (the trough of the curve) and $Fz3$ (at about 45% of the gait cycle) values. Moreover, the equation has been tested for Slow and Fast speeds, yielding an average prediction for the pattern of the GRF curve. This equation is able to help in optimising the prosthetic feet, as discussed further in Chapter Five. Finally, the parametric equation for the affected leg was tested for different values of $V_r$. The Equation 4.6 yields an excellent $Fz1$ for $V_r$=1 and an average estimation for $Fz3$. Due to the lack of published experimental data on Fast and Very Fast speeds for amputees, this equation is not verified on the complete range of velocities.

Strikingly, as can be seen from Figures 4.20 and 4.21, the difference between the healthy and prosthetic (affected) limbs is small when inspected visually. This indicates that both legs produce approximately the same $G_r$; however, the sound leg is estimated to generate a higher $G_r$ value, as it handles a higher force than the prosthetic leg during the loading phase [147].

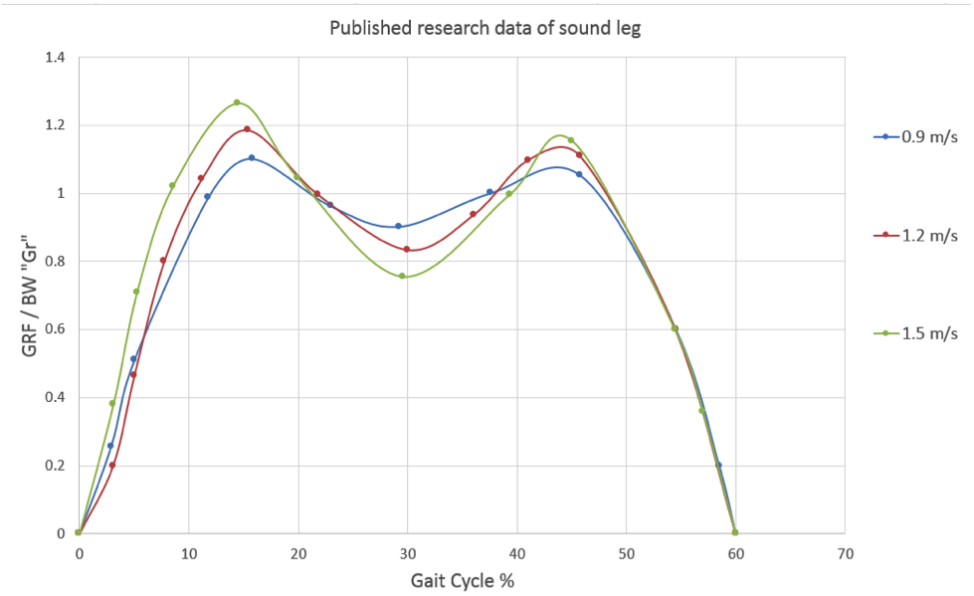


(a) Published experimental results for the sound leg [17].

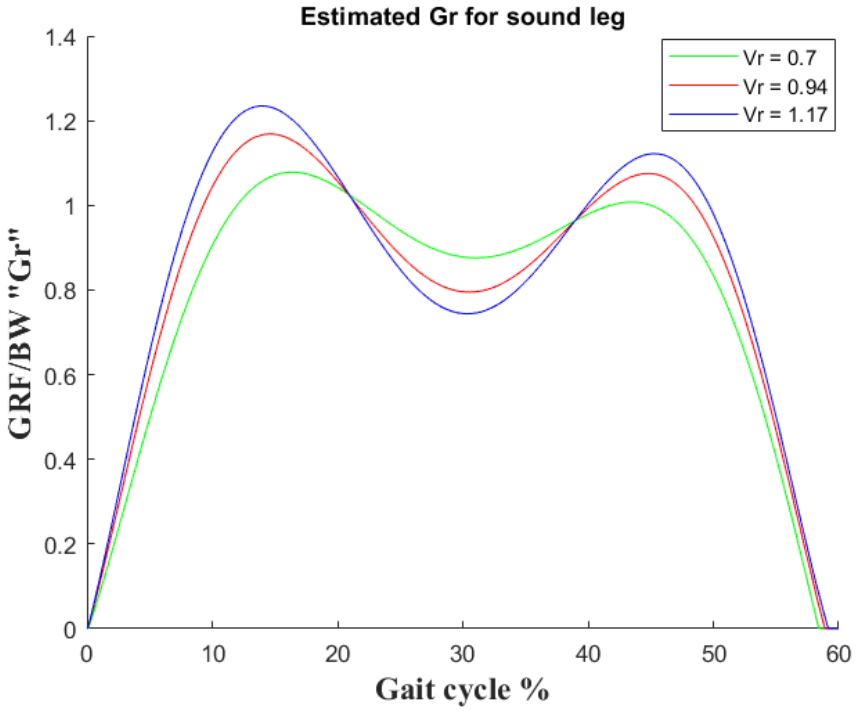


(b) Estimated $G_r$ values for the sound leg at $V_r$=0.7, 0.94, 1.17.

Figure 4.19: $G_r$ values for the sound leg

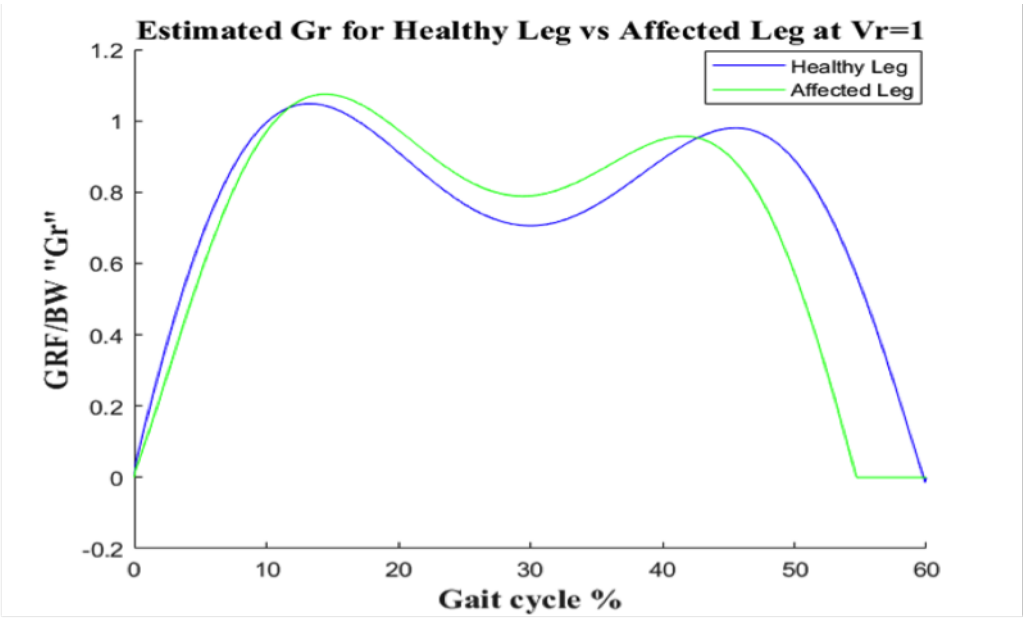


Figure 4.20: Estimated $G_r$ for healthy leg vs affected leg at a velocity ratio equal to 1.

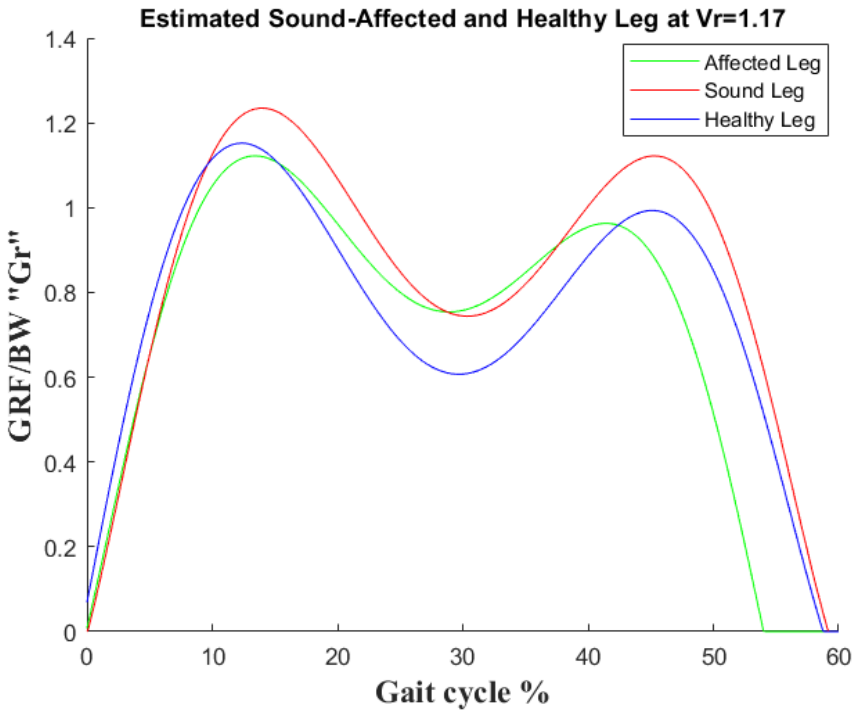


Figure 4.21: Estimated sound-affected and healthy leg at a velocity ratio equal to 1.17.

A new criterion for categorising walking speeds has also been suggested. As shown in Figures 4.15 and 4.16, a best fit $G_r$ curve with the best fit to the experimentally measured GRF curve is determined using the proposed set of Equations 4.4, and the corresponding $V_r$ value is also calculated. The best-fit curve is determined by comparing the $Fz1$ values for $Fz1 \geq 1.15$ and both the $Fz1$ and $Fz2$ values for $Fz1 < 1.15$. A new table (Table 4.9) is suggested in this thesis; specifically, it categorises walking speed as very slow, slow, free, fast and very fast, based on the velocity ratio $V_r$ value rather than using Table 4.4 (based on the actual walking speed value).

Table 4.9: The proposed walking speed categories

| **Velocity Ratio** | **Walking Speed Category** |
|---|---|
| 0.40 | Very Slow (<0.5) |
| 0.63 | Slow |
| 0.80 | Slow |
| 1.00 | Free |
| 1.10 | Free (upper limit < 1.15) |
| 1.17 | Fast |
| 1.20 | Fast |
| 1.25 | Fast |
| 1.30 | Fast (upper limit of Fast >1.3 Very Fast) |
| 1.53 | Very Fast |
| 1.69 | Very Fast (upper limit of Very Fast >1.7 Running) |

### 4.5.3 Validation of the Experimental Data Obtained in the Lab

A novel idea is proposed here; namely, that the walking speed of an individual can be predicted by inspecting the vGRF curve and retrieving the $V_r$ value associated with the vGRF curve with the shape closest to that estimated by the equation. The normal interpretation of the average speed value of $1.85m/s$ is that this speed falls into the Very Fast walking category (Table 4.4). However, as shown in Figure 4.9a, the GRF curves exhibit a pattern corresponding with Free walking velocity ($V_r$ equal to 1). The experimentally determined GRF curves were compared with the curves estimated by the proposed equation. The corresponding $V_r$ values and the resulting walking speed categorisation are tabulated below (Table 4.10).

The walking speed and the resulting GRF curve for an individual is measured (e.g., $1.924m/s$ for Participant 1). This speed is above the level of $0.8m/s$; hence the newly proposed Equation 4.4 is used to match the first peak $Fz1$ (1.0545) value with the experimentally determined $Fz1$ value (1.055). The percentage error in the $Fz1$ value is very small (0.047). The corresponding $V_r$ value (1.01) is calculated from Equation 4.4. A corresponding walking speed category is obtained for this $V_r$ value using Table 4.9. This is a FWS category; hence, the actual walking speed of Participant 1 is classified as FWS. By observing the first peak of GRF ($Fz1$ value), it was concluded that the Participant 2 walked at a fast walking speed, even though it was intended that he walk at a free walking speed (his walking speed was $1.59m/s$). As observed by Hsu et al. [129], it can be inferred that participant lifestyle (sedentary or physically active) can indeed play a role in determining gait response. According to the traditional classification approach, as shown in Table 4.4, all participants, except participant 2, would have been incorrectly classified as walking very fast.

Table 4.10: Recommended FWS

| **Participants** | **Velocity** | $Fz1$ **(Exp.)** | $Fz2$ **(Exp.)** | $Fz3$ **(Exp.)** | $V_r$ **(Eqn.) from** $Fz1$ | $Fz1$ **(Eqn.)** | **%Error** ($Fz1$) | $V_r$ **Classification** | **FW Velocity** |
|---|---|---|---|---|---|---|---|---|---|
| **1** | 1.924 | 1.055 | 0.862 | 1.066 | 1.01 | 1.0545 | 0.047 | Free | 1.90 |
| **2** | 1.590 | 1.147 | 0.818 | 1.172 | 1.16 | 1.1456 | 0.122 | Fast | 1.37 |
| **3** | 1.930 | 1.092 | 0.806 | 1.143 | 1.07 | 1.0931 | 0.101 | Free | 1.80 |
| **4** | 1.760 | 1.107 | 0.800 | 1.120 | 1.10 | 1.1100 | 0.270 | Free | 1.60 |
| **5** | 1.722 | 1.008 | 0.811 | 1.110 | 0.94 | 1.0075 | 0.050 | Free | 1.83 |
| **6** | 1.940 | 1.091 | 0.815 | 1.150 | 1.07 | 1.0930 | 0.183 | Free | 1.81 |

### 4.5.4 The Unhealthy Load (UL) Concept

Stability is a critical factor affecting a prosthetic foot's efficiency. The high vGRF produced on the sound leg relative to the prosthetic foot can occur for various reasons; for example, the amputee might take time to adapt to the new artificial foot, or their confidence in using the prosthetic is low at the beginning, or the amputee exerts more pressure on the sound leg to carry the prosthetic foot because it does not have the same muscle support [64]. This creates an imbalance in vGRF values that results in unhealthy joint loads, or ULs. This imbalance is biomechanically driven; in this thesis, the resulting UL is defined as the difference in peaks between the healthy population's legs and amputees' corresponding legs. This can be calculated using the following formula.

$$UL = |Fz1_s - Fz1_h| + |Fz3_h - Fz3_p| \tag{4.7}$$

Equation 4.7 is normalised by body weight; here, $Fz1_s$ is the first peak of the vGRF of the sound leg, $Fz1_h$ and $Fz3_h$ are the first and second peak of the healthy population vGRF curve, while $Fz3_p$ is the second peak of the prosthetic leg vGRF. The minimum UL value corresponds to a situation when both legs are healthy; this value should be close to zero. Moreover, at very slow walking speeds, it is expected that the UL should have a lower value when compared to very fast walking. Figure 4.22 plots the relationship between the velocity ratio and ULs. The blue line represents the Unhealthy Load value, which is calculated from the estimated $G_r$ equations, as shown in Section 4.5.3. Furthermore, the parametrised equations were able to estimate the UL up to $V_r = 1.08$. This is due to the shortage in the affected leg equation due to the limited availability experimental data on Fast walking with the affected leg. The red line here represents the UL, which has been calculated from the data in the published literature. It is noticeable that the UL variation under low $V_r$ is very small. However, as the velocity ratio increases, the ULs

also begin to increase rapidly. In order to reduce joint, muscle and back pain, the prosthetic foot should be designed to produce a minimum UL value. In the next chapter, a method of optimising the stiffness of the prosthetic foot in order to minimise UL is discussed.

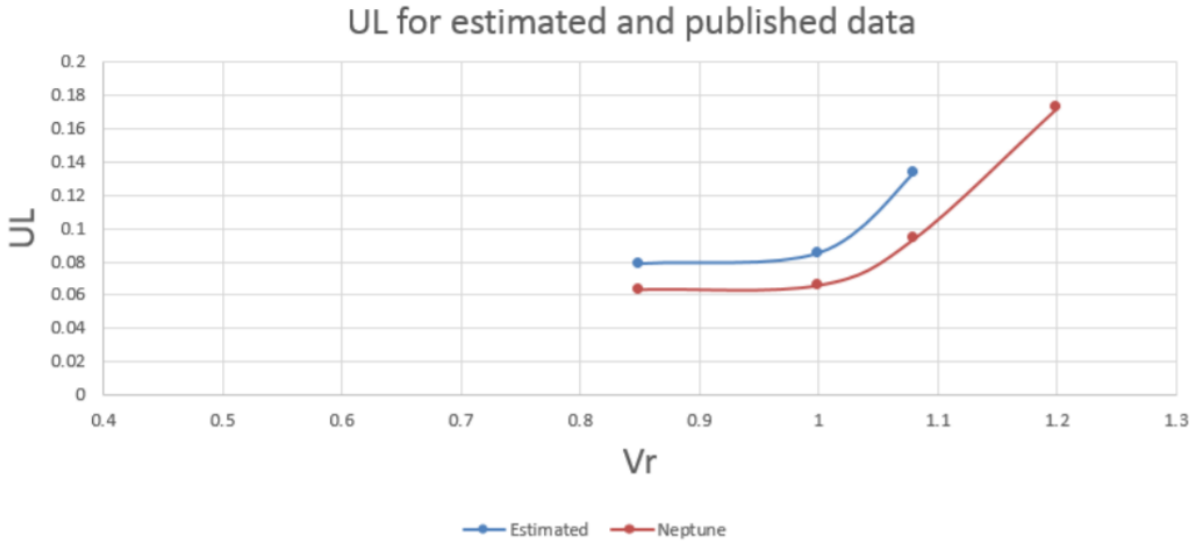


Figure 4.22: Published data [120] vs. estimated UL at various $V_r$

## 4.6 Summary

The dimensionless quantities $G_r$ and $V_r$ , along with the curve-fitting algorithms, are all beneficial, since the required GRF curve can be created from a collection of various chosen walking speeds. Each walking speed requires a unique-order polynomial approximation to yield a $G_r$ during gait. Since only five speed categories (i.e. Very Slow to Very Fast) were explored, an approach that incorporates all walking speeds was developed to help determine a robust GRF curve for any walking speed.

Conversely, an approximated GRF equation for prosthetic and sound legs has been developed in a similar manner, with a sixth-order polynomial curve fit. While the sound leg estimated equation is only valid for the same five ranges of walking speeds, the prosthetic foot GRF

approximated equation is only applicable to the FWS depicted in the chapter, since the amount of existing literature associated with Fast and Very Fast walking speeds for amputees is inadequate.

Data for this study was obtained from results published in reputable journals with participants from across the world, including males and females across various age ranges [56]. Age is a significant factor that must be considered, since some age groups (such as the elderly) are unlikely to attain an adequate walking speed range capable of fitting the data. These factors signify that the overall GRF tendency in each walking speed group is still thought to be typical, consistent and dependable for a healthy population with steady gait. However, the results of this meta-analysis are likely to contain some degree of error, as the outcomes from the primary research papers contained some overlooked nonconformities from the corresponding average values. Moreover, some methodological faults (such as digitisation) reduced overall accuracy.

Plotting the precise point on the graph for the axes and curve was also demanding. Even so, various digitisation trials and reiterations were conducted to help enhance precision, which is sufficiently high for this data to be worked out on an average tendency rather than a stratified or person-explicit inclination. Since the replicated graphs' digitisation into the graph in Figure 4.18 is the second digitisation, it also has a higher error component. Nevertheless, the averages obtained at the $Fz1$, $Fz2$, and $Fz3$ points authenticate the accuracy of the digitisation approach.

Another potential fault could be that the walking velocities computed in Schwartz et al. [80] are likely to be erroneous owing to the approximations made regarding the leg dimension. This study produced GRF data associated with children, who (it may be claimed) possess a walking pattern distinct from that of elderly people or adults; through normalisation, however, it was determined that the walking pattern between the two age groups was similar. One flaw that may occur specifically in the findings of Masani et al. [142] involves the $x$-values of the data not being 100% correct. For instance, the $x$-values initially provided as time (seconds) have been

reduced to scale to enable the past points to appear at 60% of the walk cycle; this was done after considering the tendency of all other outcomes. Even so, the results appear not to shadow the pattern of the previously published findings, which indicates that they are both accurate and dependable. The new parametrised GRF equations, founded on the developed dimensionless quantities, can be utilised to enhance the design of orthoses and prostheses so that they can imitate the performance of a healthy, ordinary foot. This can be achieved by establishing the ideal material properties for orthoses and prostheses capable of reacting differently at various gait speeds to produce a similar GRF profile, thereby providing the user with maximum firmness, steadiness and stability. A more in-depth study of the material properties, using kinematic simulation modelling and the utilisation of the findings shown in the research, may aid in the improvement of the orthotic and prosthetic designs. The proposed set of equations for estimating $G_r$ values are able to discover the free walking speed categories (Very Slow, Slow, Free, Fast and Very Fast) as well as the FWS value for an individual. The measured velocity and GRF values are used along with the proposed set of equations. While more gait experiments are required in future research to verify this claim, it is recommended that this approach be used to classify walking speeds into the above-mentioned categories rather than using Table 4.4.

The idea of UL calculation is presented at the end of this chapter. The correlation between $V_r$ and UL has been created by graphing the outcomes from tests [56] versus the estimated vGRF equations attained.

# Chapter 5

# A Loosely-Coupled Model

## 5.1 Introduction

As medical technology has advanced, there has been a tremendous level of investment in healthcare projects that improve people's quality of life. Researchers focusing on different aspects of health have broken ground on several occasions to reveal transformative tools that set a precedent for a healthier society. For instance, the optimisation of different prosthetic designs relies on a component's structure and ability to function under strain or stress. A parametric analysis utilises a host of resources and tools to develop an appropriate model for the study. Accordingly, researchers often perform a finite element analysis to clarify the operations of different components in a foot model. This type of model is popular when studying the parametric effects resulting from unique materials, alignment, size, shape, and design through the treatment of the resultant variables; this has critical implications for the relationship between a residual limb and the introduced prosthetic. Some scholars, such as Saunders et al. [148], have had some success in examining a design with an articulated and solid heel and ankle interaction. An endeavour of this kind is possible using finite element analysis, which requires

a set of variables relative to a prosthetic action. For instance, Saunders et al. [148] consider the measurements of the surface area of contact between the floor and foot, as well as the force exerted at an instantaneous heel strike. This analysis is extended to include values during a middle stance and full push-off in order to assess a complete gait pattern for below-the-knee amputations. These values were subsequently used to determine the stress and displacement caused to the foot by applying them to a SACH model. Researchers such as Lee and Zhang [149] have opted to use the ISO 10328 maximum loading standards to design a functional prosthetic foot within the FEM. However, other publications by Omasta et al. [93] and Bonnet et al. [150] used the FEM to treat experimental data and compare resultant deflections with values obtained from experiments. Omasta et al. [93] focused on studying stress distribution in the components of a load-bearing prosthetic. This process involved the treatment of force variables during an amputee's reaction to the ground surface. Foot deflections from these results were compared with experimental data. Bonnet et al. [150] performed a controlled analysis by studying an amputee's gait conditions during high walking speeds and a self-selected pace. The relevant GRFs under different conditions were measured using the FEM. This concept was also used to evaluate leg stiffness asymmetry by utilising a spring leg model. Results from this work promise significant insight into gait rehabilitation using physiotherapy and prosthesis devices.

This chapter is structured in the form of steps involved in the journey of a hypothetical amputee walking in the gait lab with the existing prosthetic foot, along with how the proposed loosely coupled model could help redesign the prosthetic foot in a way that would potentially minimise unhealthy joint loads. These steps are laid out in sections as follows. First, Section 5.2 presents the anthropological data and estimated healthy GRF used for the analysis. In Section 5.3, the prediction of healthy stiffness value using PWD simulation is addressed. The finite element analysis for a representative C-shaped prosthetic foot is defined in Section 5.4. This

section consists of the following: an ANSYS foot mesh independency study, material properties, contact definition, boundary conditions, simulation results for a syndiotactic polystyrene (10% carbon fibre) foot, ROS calculation, and analysis for a prosthetic foot. Finally, the discussion and summary are presented in Sections 5.5 and 5.6, respectively.

## 5.2 Anthropological Data and Estimated Healthy GRF

The experiment involves measuring values for the sound and affected leg after exposure to GRF. It is imagined that the hypothetical amputee, with a C-shaped prosthetic foot made of syndiotactic polystyrene (10% carbon fibre), enters the laboratory in order to obtain a customised prosthetic foot. This prosthetic foot has a material property similar to ESAR2 [32]. In some cases, manufacturers determine this stiffness through statically applied loads from strength testing machines [151].

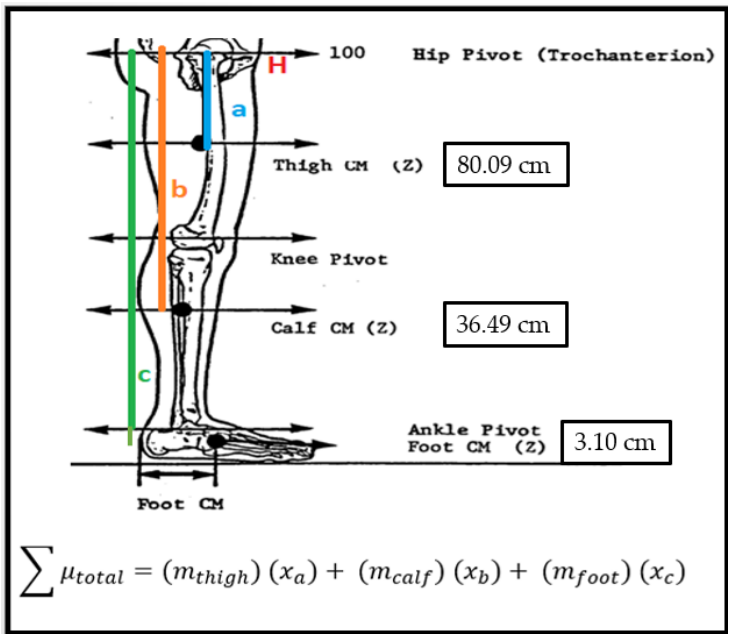


Figure 5.1: COM locations for thigh, calf/shank and foot.

Figure 5.1 illustrates the COM for the healthy population; hip is considered as the pivot point based on the method outlined in [152]. Taking the moment at about point H to produce the total moment on the hip. In order to replace the three COMs with a single centre of mass used for the PWD simulation, the total moment is divided by the leg mass for both the prosthetic and amputee. Table 5.1 presents the anthropological calculations for both a healthy and amputee leg. As an example, the total moment for the healthy population, a value $468.72kg \times cm$, is obtained by multiplying each mass by distance.

Now, in order to find the length ratio (D1,D2: see Figure 5.3), the total moment should be divided by the leg mass ($12.5kg$ see Table 5.3). The value of D1 is $37.5cm$; thus, the value of D2 as 100-37.5 = $62.5cm$. The mass ratio and the length ratio are defined in Section 5.3. Similar steps are applied for calculating corresponding values for the prosthetic leg.

Table 5.1: Anthropological calculations.

| | **Healthy** | | **Prosthetic** | |
|---|---|---|---|---|
| **Parts** | **Mass (kg)** | **Distance (cm)** | **Mass (kg)** | **Distance (cm)** |
| **Thigh (a)** | 8.3 | 19.91 | 8.3 | 19.91 |
| **Calf (b)** | 3.1 | 63.51 | 1.5 | 69.52 |
| **Foot (c)** | 1.1 | 96.90 | 0.9 | 96.90 |

The second step involves the subject practising their walking gait on a pre-installed walking path to ensure that, after a few steps, the whole stance foot surface lands upon a force plate and the swing leg (i.e. sound leg) lands on the next force plate. The GRFs are then measured in a gait lab for both the sound leg (intact leg) and the prosthetic leg. The GRF curves are analysed and the first peak ($Fz1_s$) and second peak ($Fz3_p$) for the sound leg and prosthetic leg are recorded. To ensure more consistency in the present thesis, the values for $Fz1_s$ and $Fz3_p$ will be taken

from the literature review [17] (see Table 5.2). Subsequently, the subject's anthropological data will also be recorded in Table 5.2 [32]. Moreover, the desired ROS is around 30% of the total leg length [100, 113]; thus, the ROS for a healthy leg is assumed to be $0.3m$. Further experiments can be conducted in future to determine the ROS for a corresponding equivalent healthy population to replace the 0.3m value. The proposed model can also be extended to include non-circular-shaped ROS [32].

Table 5.2: Anthropological and sound leg data [17, 32]

| **Foot** | **Healthy Population** |
|---|---|
| **Leg Mass (kg)** | 12.5 |
| **Thigh Mass (kg)** | 8.3 |
| **Calf Mass (kg)** | 3.1 |
| **Foot Mass (kg)** | 1.1 |
| **Leg Length (m)** | 1.0 |
| **Mass Ratio** | 3.6 |
| **Length Ratio** | 0.6 |
| **ROS (m)** | 0.3 |
| **First Peak of Intact Leg** | 1.18 |

Up to this point, the anthropological and kinetic data of the subject has been recorded. Furthermore, the study explains how a loose coupling is proposed between the PWD (see Appendix F) and the finite element-based model. The parametrised GRF equations introduced in Chapter Four are used to determine the subject's velocity ratio. From Table 5.2, the peak value for the sound leg was shown to be 1.18; the values were then compared to the estimated

GRFs for the sound leg in Figure 4.19. These findings indicate that the first peak is almost equal to the estimated first peak at the velocity ratio of 1.17. Figure 5.2 presents the GRF values for healthy walking individuals.

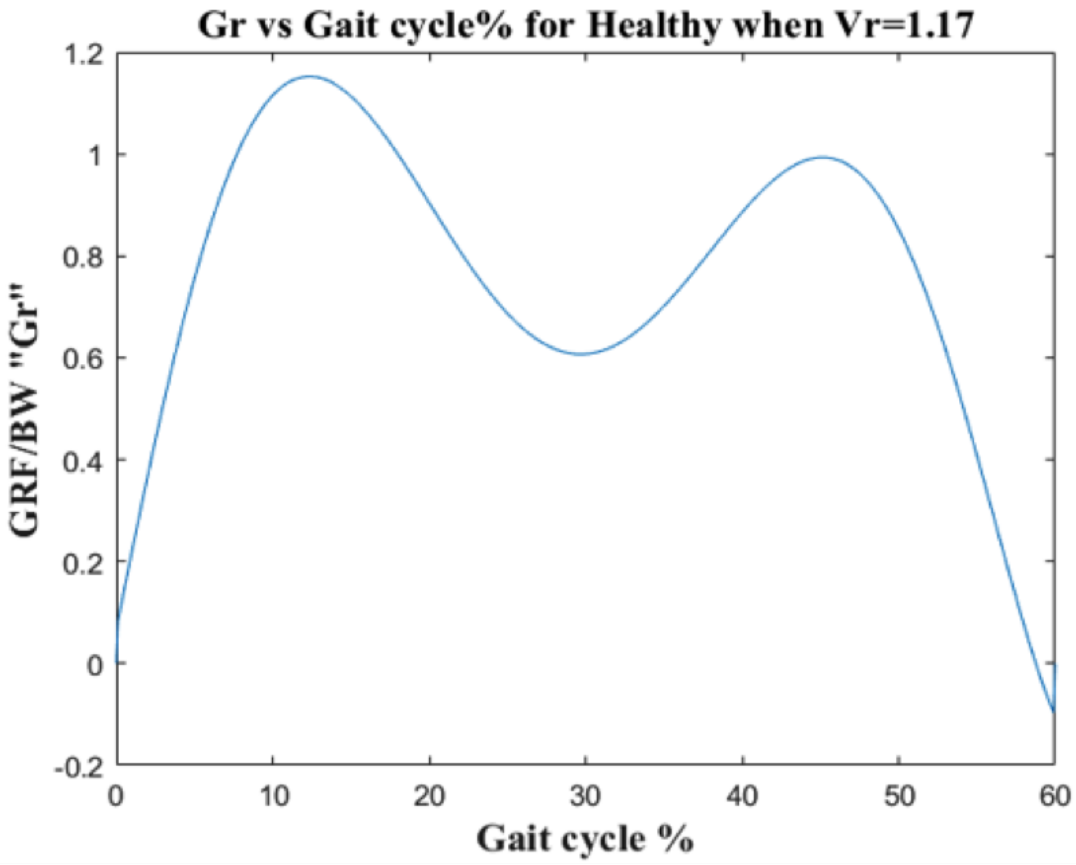


Figure 5.2: $G_r$ graph during the gait cycle for healthy people when the $V_r$ value is 1.17

## 5.3 Predicting the Healthy Stiffness Value for a PWD Model

The following section describes a spring leg model that simulates a contemporary PWD [15]. An assessment of this person's gait patterns using same-leg stiffness values is undertaken. This work reveals the effect of equal mass legs on the model as well as the involved GRFs (Figure 5.3). Legs of equal mass simulate the behaviour of a healthy population.

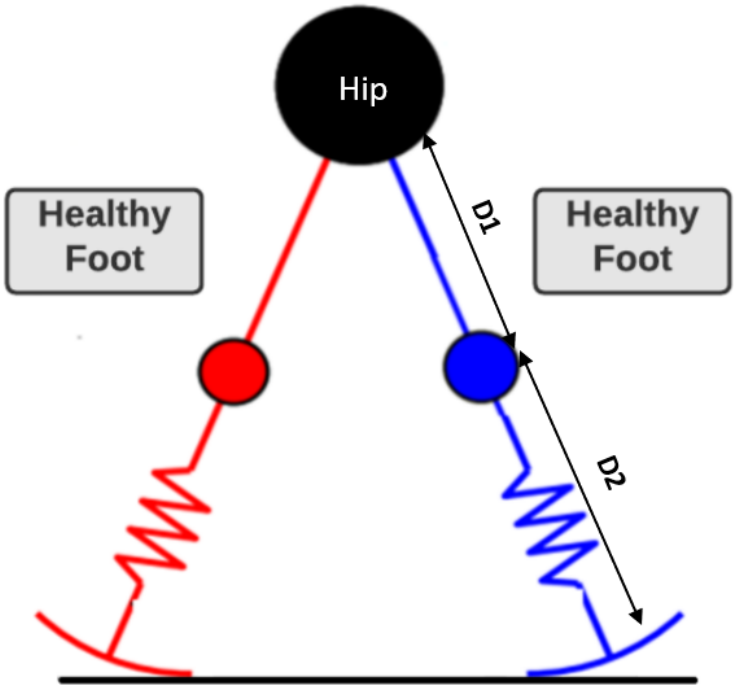


Figure 5.3: Schematic model of a healthy foot, where the blue and red foot represent the healthy leg.

Figure 5.4 represents the procedure for finding the healthy first peak in PWD. The inputs for the PWD model are: ROS value ($0.3m$) for healthy population $[95, 100]$, stiffness, mass ratio [1] and length ratio [2] (see Figure 5.4). Moreover, the initial assumption for the leg stiffness value was selected as $13.5kN/m$ based on the stability region for the PWD model (Appendix F, Figure F-3).

[1] mass of the hip divided by the total mass of the leg

[2] ratio of the upper leg (D1) over the lower leg (D2: see Figure 5.3)

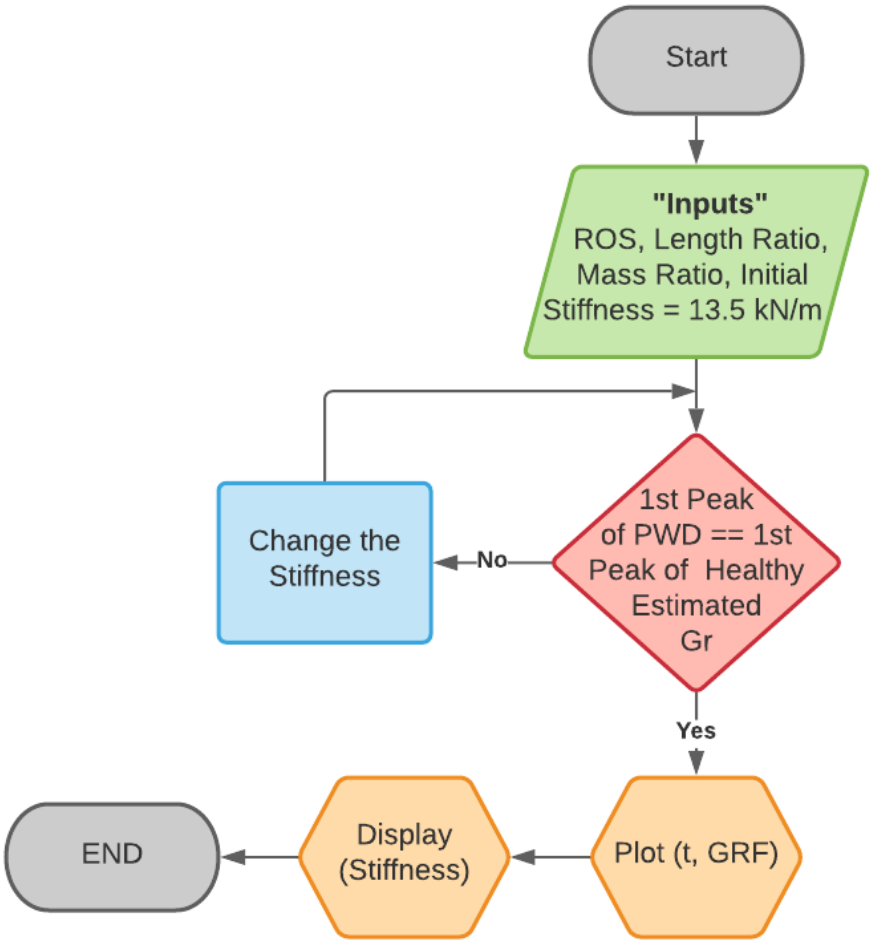


Figure 5.4: Algorithm for finding the healthy first peak in PWD

Table 5.3 displays the values that will be used in model simulation and validation using the MATLAB software employed in this research. The mass is identical for both legs since they are similar and healthy. Similarly, mass ratio, length ratio, and stiffness are equal for both legs, as shown in Figure 5.3. In this figure the right leg is represented in blue while the left is represented in red. The initial input value for leg stiffness for this model is $13.5kN/m$, which was used to check whether the first peak ($Fz1_h$) matches the first peak of the healthy leg's GRF.

Table 5.3: Stiffness of $13.5kN/m$ results. Simulation inputs are leg length = $1m$, total mass = $70kg$, mass ratio = 3.6 (hip mass = $45kg$).

| | **Left Leg (Red)** | **Right Leg (Blue)** |
|---|---|---|
| **Foot** | Healthy | Healthy |
| **Leg Mass (kg)** | 12.5 | 12.5 |
| **Thigh Mass (kg)** | 8.3 | 8.3 |
| **Calf Mass (kg)** | 3.1 | 3.1 |
| **Foot Mass (kg)** | 1.1 | 1.1 |
| **Mass Ratio** | 3.6 | 3.6 |
| **Length Ratio** | 0.6 | 0.6 |
| **ROS (m)** | 0.3 | 0.3 |
| **Stiffness (kN/m)** | 13.5 | 13.5 |

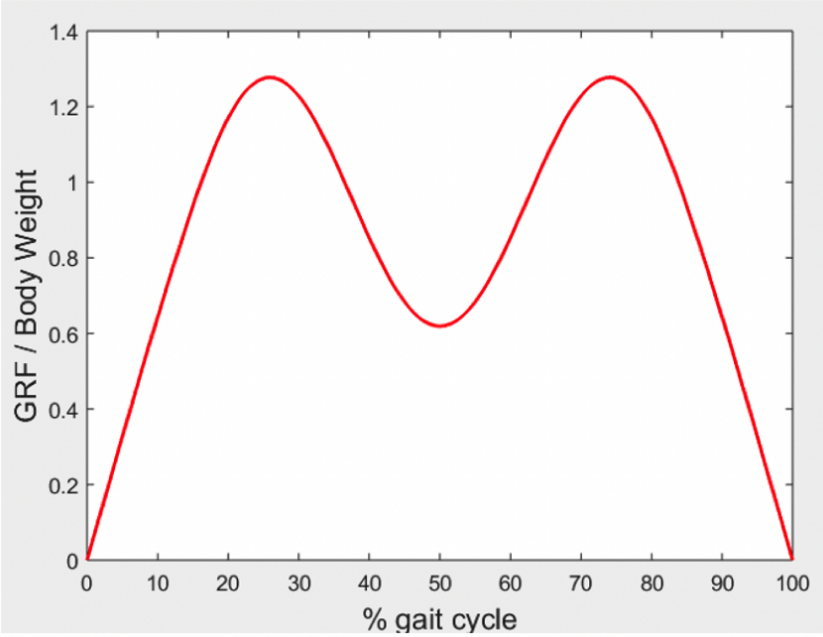


Figure 5.5: $G_r$ results for the tested value of stiffness which is 13.5 kN/m for both legs

A PWD study was carried out and tested to check the model's optimal value of leg stiffness. The initial input value is $13.5kN/m$ and the results are shown in Figure 5.5. The healthy GRF's first peak (shown in Figure 5.2) is approximately 1.16 and the second peak is around 0.99. In Figure 5.5, the first peak resulting from the tested stiffness is 1.28, while the second peak is almost identical. The 1.28 value is far greater than the value of $G_r$ for a healthy population, as shown in Figure 5.2.

As discussed, the PWD first peak (1.28) is higher than the estimated $G_r$ (1.16) first peak. Different cases (a total of six) were tested in order to reach the closest value to the healthy leg that was estimated earlier. The algorithm is presented in Figure 5.4. The cases were studied and tested based on randomly selected vertical stiffness values; these results are shown in Table 5.4, while GRF graphs are presented in Figure 5.6. As can be seen from Figure 5.6, there is a relationship between the leg stiffness and the first peak value, where both are affected in the same manner.

Table 5.4: Tested leg stiffness values for different case results

| **Cases** | **Left Leg Stiffness (kN/m)** | **Right Leg Stiffness (kN/m)** | **Peak GRF Value** |
|---|---|---|---|
| **Case 1** | 10.8 | 10.8 | **1.17** |
| **Case 2** | 13.5 | 13.5 | **1.28** |
| **Case 3** | 16 | 16 | **1.403** |
| **Case 4** | 17 | 17 | **1.42** |
| **Case 5** | 18 | 18 | **1.49** |
| **Case 6** | 19 | 19 | **1.56** |

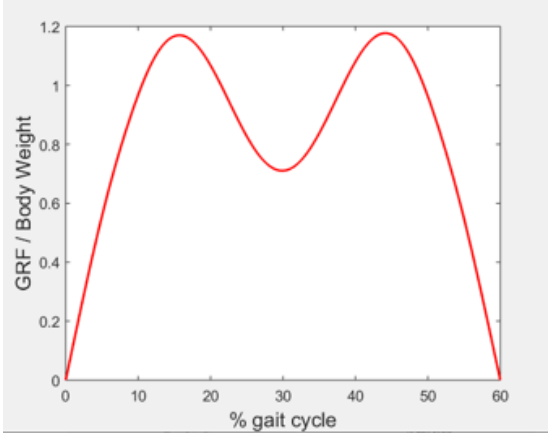


(a) Results for Case 1 with stiffness of 10.8 kN/m and both peaks around 1.17

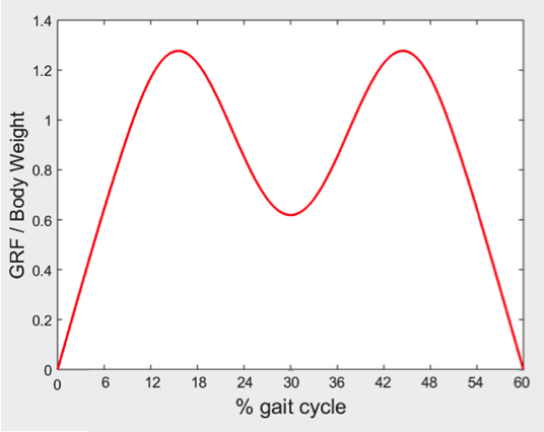


(b) Results for Case 2 with stiffness of 13.5 kN/m and both peaks around 1.28

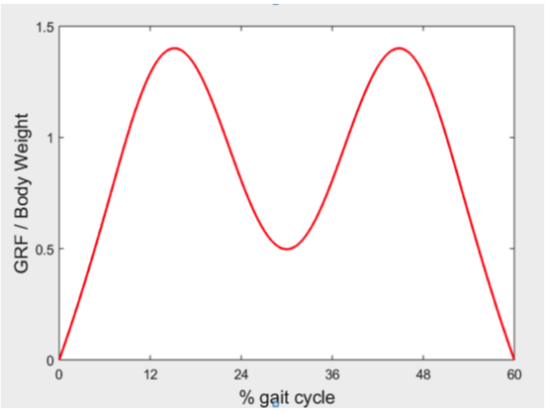


(c) Results for Case 3 with stiffness of 16 kN/m and both peaks around 1.403

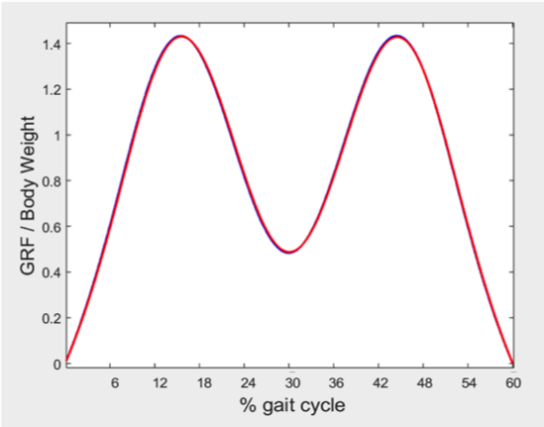


(d) Results for Case 4 with stiffness of 17 kN/m and both peaks around 1.42

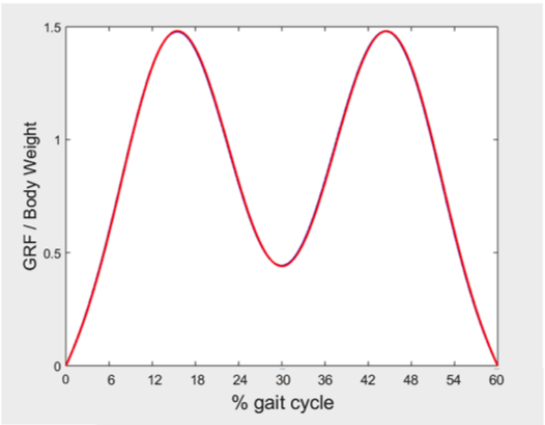


(e) Results for Case 5 with stiffness of 18 kN/m and both peaks around 1.49

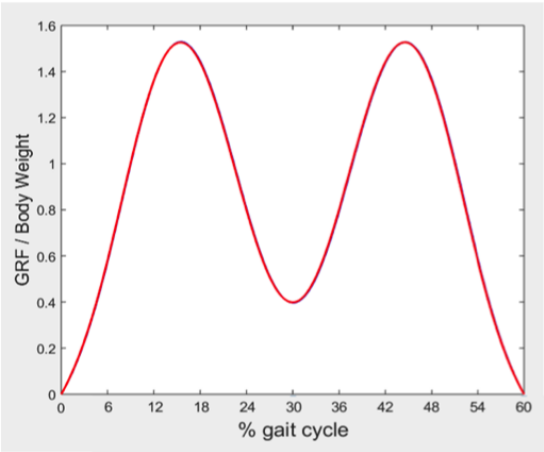


(f) Results for Case 6 with stiffness of 19kN/m and both peaks around 1.56

Figure 5.6: $G_r$ graphs for different stiffness values

The optimal stiffness value, which is closest to the healthy adult first peak shown in Figure 5.2, is represented in Case 1 of Figure 5.6a. The first peak value of Case 1 is approximately 1.17, which is the closest to the healthy estimated $G_r$ values. It can be seen that as the stiffness increases, the peak of GRF values also increases. However, lower values cannot be used because no stable solution can be found for these values. Based on this PWD study; the stiffness of $10.8kN/m$ (Case 1) is considered as the optimal value, for a healthy population and the sound leg of amputees, in order to achieve the desired GRF value that matches the first estimated $G_r$ peak.

**Model Comparison Case Study**

The limitation of the current PWD is that the GRF peaks are almost identical. Experimentally, as the velocity increases, the second peak should be lower than the first peak [56]. The validation of the design criteria achieved by applying the first vGRF peak is discussed below. Yang et al. [120] used a damper in their model to dissipate the energy for the second peak, as shown in Figure 5.7a, which has been digitised using the Web-Plot-Digitizer v3.5 [145] to facilitate clear comparison. While this model was able to dissipate energy, the second peak still shows a higher value than expected (see Table 5.5). The spring-damper model (see Appendix G) also showed the same relationship between vertical stiffness and the first peak value. In order to deduce a valid comparison, the leg stiffness values were chosen to have a first peak between the two models that is almost equal as shown in Figures 5.7a and 5.7b. On the other hand, Figure 5.7c presents the estimated $G_r$ for a healthy adult with respect to the velocity ratio.

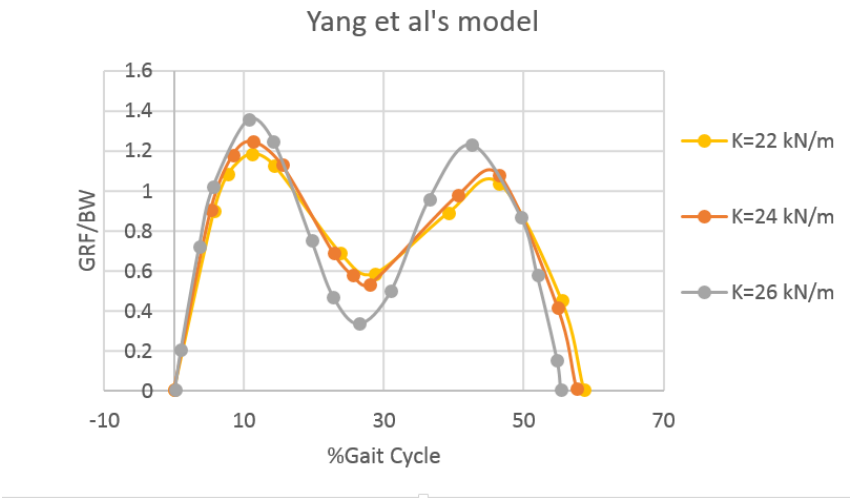


(a) A spring damper model (see Appendix G) [120]

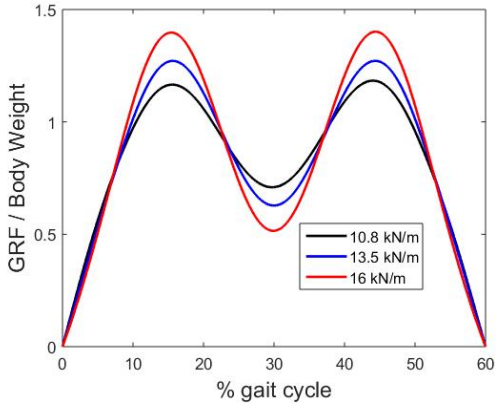


(b) PWD Model

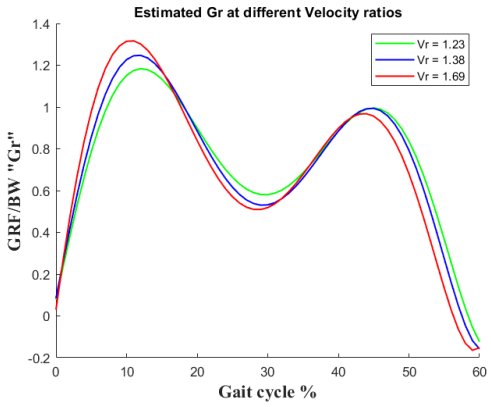


(c) Estimated $G_r$ Equation

Figure 5.7: GRF model comparison

The optimal means of validating the importance of the second peak, with or without a damper, for a healthy foot involves making a comparison between the damper's model [120] and the PWD model with respect to the estimated $G_r$. The percentage difference $(f)$ between both models is measured. From Table 5.5, three different velocity ratios and leg stiffness values are applied in order to check the percentage difference, as shown in Figure 5.8. Furthermore, the difference in percentages will be calculated as shown in Table 5.6.

Table 5.5: Validation process of Fz3 for a healthy foot based on three different case studies

| **Study** | **Case 1** | | | **Case 2** | | | **Case 3** | | |
|---|---|---|---|---|---|---|---|---|---|
| **Models** | **PWD** | **Damper** | **Est.** $G_r$ | **PWD** | **Damper** | **Est.** $G_r$ | **PWD** | **Damper** | **Est.** $G_r$ |
| **Stiffness (kN/m)** | 10.8 | 22 | 1.23 | 13.5 | 24 | 1.38 | 16 | 26 | 1.69 |
| **Fz1** | 1.17 | 1.184 | 1.179 | 1.28 | 1.25 | 1.24 | 1.403 | 1.36 | 1.3 |
| **Fz2** | 0.63 | 0.58 | 0.56 | 0.57 | 0.58 | 0.53 | 0.53 | 0.33 | 0.51 |
| **Fz3** | 1.166 | 1.084 | 0.986 | 1.27 | 1.1 | 0.99 | 1.4 | 1.23 | 0.96 |

Table 5.6: Percentage reduction $(f)$

| | **Stiffness (kN/m)** | **Fz3 Models** | | | $f(\%)$ | | **Models Diff.** | **Stiffness Ratio** |
|---|---|---|---|---|---|---|---|---|
| **Velocity Ratio** | **(PWD, Damper)** | **Estimated** | **PWD** | **Damper** | **PWD** | **Damper** | **(%)** | **(%)** |
| **1.23** | (10.8, 22) | 0.986 | 1.166 | 1.084 | 15.437 | 9.04 | 6.392 | 49.09 |
| **1.38** | (13.5, 24) | 0.99 | 1.27 | 1.1 | 22.04 | 10.00 | 12.04 | 56.25 |
| **1.69** | (16, 26) | 0.96 | 1.4 | 1.23 | 31.42 | 1.95 | 9.47 | 61.5 |

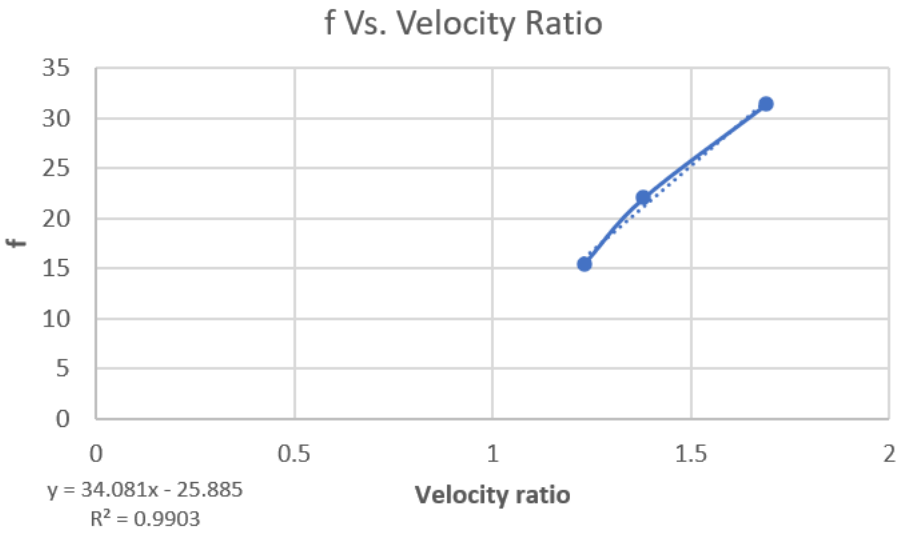


Figure 5.8: Linear correlation between the velocity ratio and reduction difference $f$

From Table 5.6, the percentage difference between the damper model [120] and the estimated $G_r$ is relatively small at low walking speeds, in which it seems that energy dissipates due to damping installation. As the walking speed increases, however, the second peak of the damping model begins to deviate from the estimated $G_r$ value. In addition, the effect of the PWD model with respect to the $G_r$ estimated values has the same effect as the damping model [120] regarding the second peak. This observation suggests that that incorporating damping effects may not have significantly improved the accuracy of the proposed algorithm. As discussed in Chapter Four, the UL is a function of four variables, as follows:

- First peak of healthy leg ($Fz1_h$).
- First peak of sound leg ($Fz1_s$).
- Second peak of prosthetic leg ($Fz3_p$).
- Second peak of healthy leg ($Fz3_h$).

All variables in the UL function can be predicted using the PWD model, except for the healthy second peak. Thus, the following steps are used to estimate the UL:

1. Calculate the $UL_{erroneous}$ by using the PWD peaks or linear interpolation(see Figure 5.28).
2. Based on the $V_r$ value from the healthy estimated $G_r$, use linear interpolation to find the percentage reduction ($f$) of the second peak, as shown in Figure 5.8.
3. Calculate the predicted UL by using,

   $UL_{predicted} = UL_{erroneous} \times (1 - f/100)$.

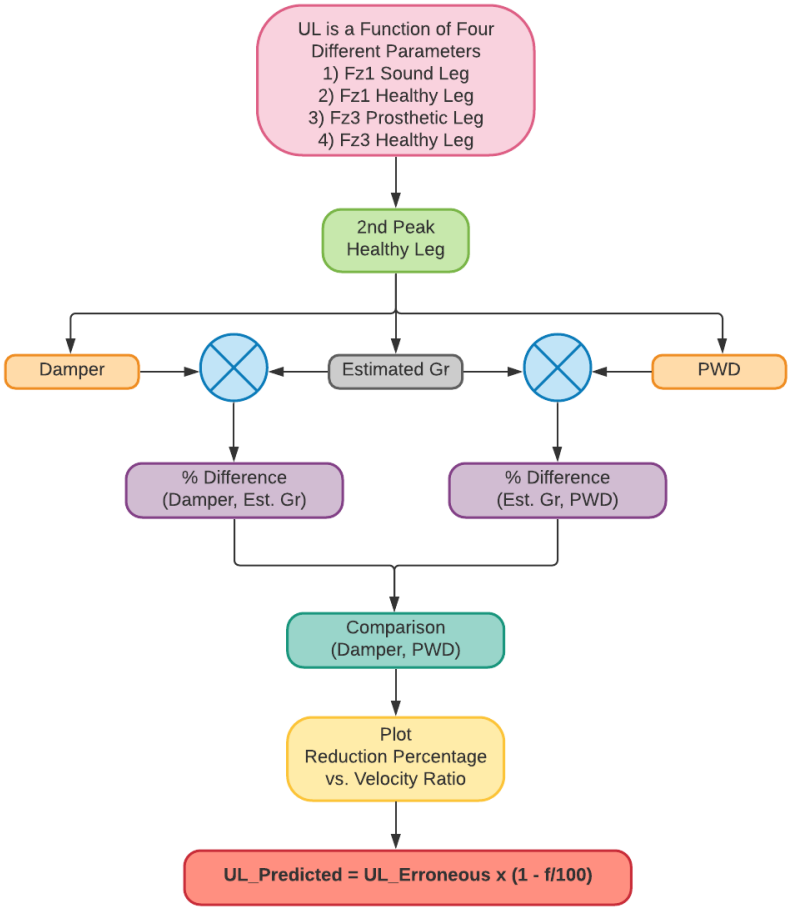


Figure 5.9: Overview of comparison models flowchart

Figure 5.9 illustrates the previous steps for calculating the predicted UL. Based on the study analysis, the author shows that the current PWD model, including the reduction difference ($f$), is sufficient to predict the UL without the need to implement damping effects. To summarise, the damper model [120] can deliver a better estimation of the second peak compared to the PWD model. However, the damper model does not have a rolling contact model, nor does it estimate the effect of prosthetic foot GRF (unbalanced mass), which is necessary for calculating UL. Thus, the PWD model developed by Charles [15] is used to predict the sound and prosthetic GRFs. This will satisfy the aim of choosing the first peak as a design criterion. A change in stiffness leads to a change in the velocity ratio [120]; thus, changing the characteristics of the

GRF pattern can change the stiffness value. Hence, optimising the stiffness value based on the pattern of the GRF is a valid approach. The next section will discuss the estimation of the ROS curve of the prosthetic foot for the hypothetical subject who is imagined to be visiting the laboratory.

## 5.4 Finite Element Analysis for C-Shaped Prosthetic Foot

ANSYS Static Structural Analysis is used to identify the ROS of the prosthetic foot, which was provided by the amputee. The steps involved with analysing the shape and finding the ROS are as follows:

1. The geometry of the foot was designed using the ANSYS design modeller and then used for the FEA simulation.

2. The input of the prosthetic foot was taken from the healthy GRF, which was obtained from the parameterising equation [150].

3. The material properties for high density polystyrene (10% carbon fibre) were used for the foot, as discussed above.

4. The Finite Element Simulation was performed using the contact model developed by Morgan [34].

5. The ROS curve for the prosthetic foot was found.

6. The optimal value of the UL was determined using the results obtained from the simulation.

The next part will discuss the meshing process, the selection of the mesh type, and the size employed.

### 5.4.1 ANSYS Foot Mesh Independency Study

The present study used the ANSYS design modeller to create the CAD model. It also required both 2D and 3D models, as shown in Figure 5.10, to be used in the finite element analysis (FEA). The CAD model consists of common basic components including foot, anchor, secondary keel, platform, and shank. The development of the mesh adhered to a specific methodology that enhanced the balance between speed and quality. The properties of the mesh satisfied the features expected in different locations, including the size, shape, smoothness, and refinement of the mesh. The mesh independence study divided the leg into two parts, namely foot and shank, to accelerate the speed of the simulation. In addition, the shank mesh was not changed in the study because it was not subjected to complex loads and contacts (see Figure 5.11) in comparison to the prosthetic foot. The use of a coarser mesh is computationally efficient, while the finer mesh mesh did not significantly alter the stresses and the deflection in the shank. On the other hand, the foot mesh requires specific refinements and sizing control (as shown in Table 5.7), to accurately measure the changes.

Table 5.7: Selected mesh size for each part of the foot. Size 1 represents the foot end surface mesh size, size 2 represents the foot palm surface mesh size, and size 3 the foot body surface mesh size. Running time for all meshes were 4, 6, 9, and 16 hours, respectively.

| **Mesh Type** | **Size 1** | **Size 2** | **Size 3** |
|---|---|---|---|
| **Coarse** | 4 | 8 | 12 |
| **Medium** | 3 | 6 | 9 |
| **Fine** | 2 | 4 | 6 |
| **Very Fine** | 1 | 2 | 3 |

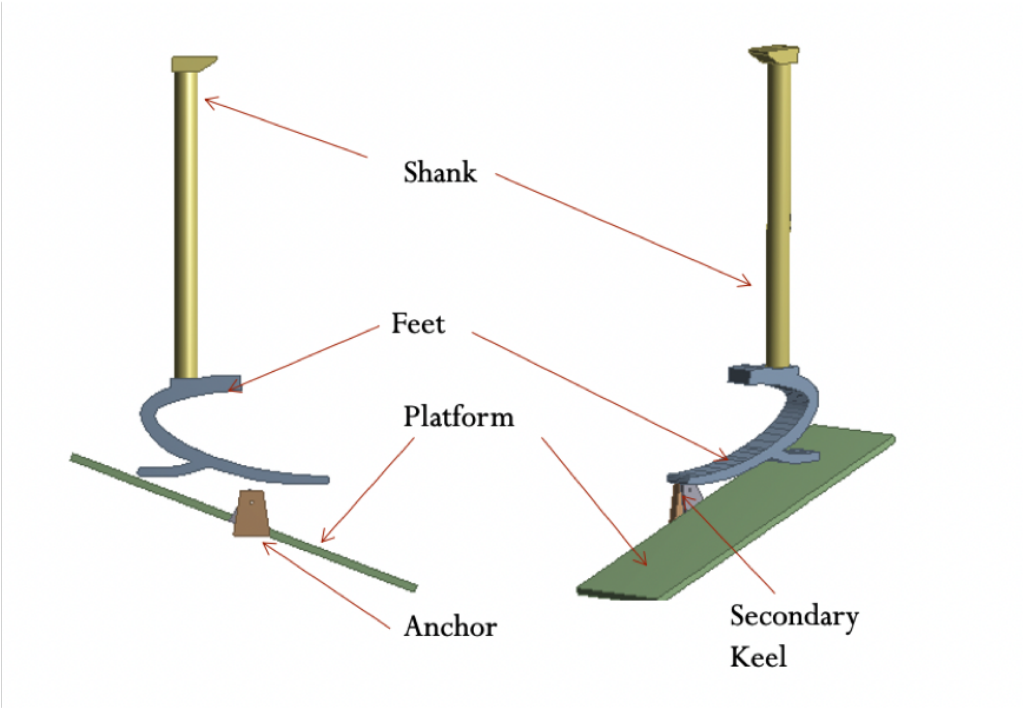


Figure 5.10: Foot CAD model created as both 2D and 3D models

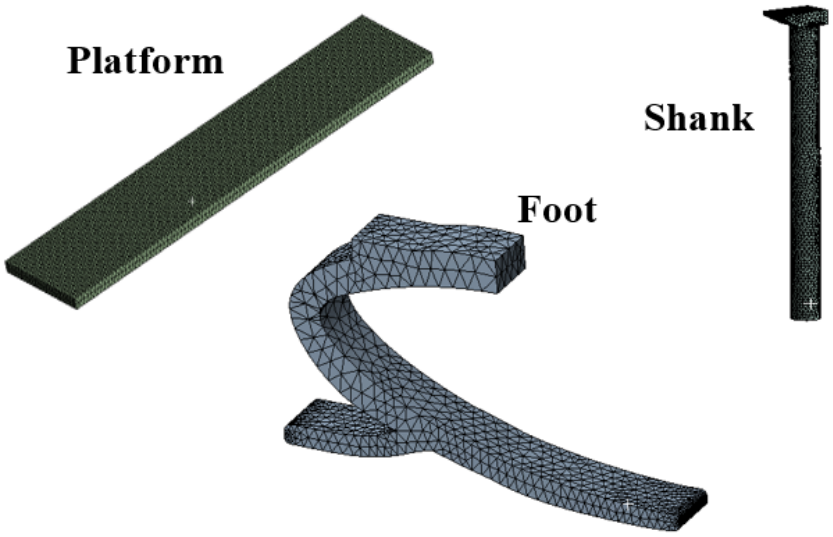


Figure 5.11: Components of the CAD model such as shank, platform, and foot. The shank is defined as a structural component of a prosthesis that connects the socket to the foot ankle system and transfers the body weight to the foot and floor.

A non-conformal mesh was produced for the three different mesh settings. Table 5.8 presents the node and element counts used in the study.

Table 5.8: Foot mesh count

| Mesh Type | Nodes | Element |
|---|---|---|
| **Coarse** | 16547 | 9983 |
| **Medium** | 20292 | 12471 |
| **Fine** | 29930 | 18655 |
| **Very Fine** | 103466 | 65722 |

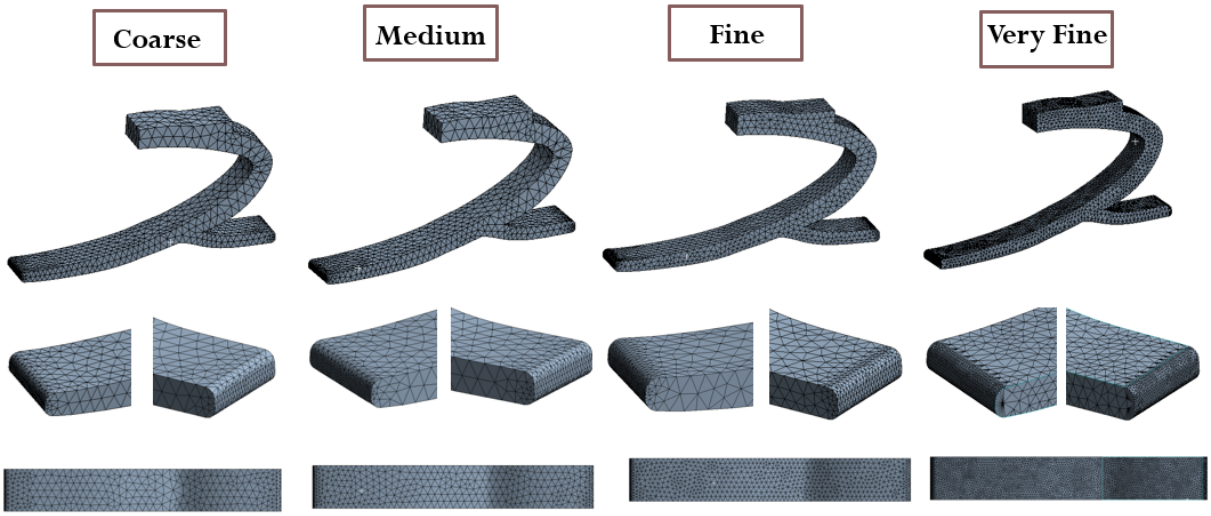


Figure 5.12: Nodes and elements shown in the foot for the different types of mesh study

The simulation involves the use of at least three elements in each region. This strategy reduces the need to approximate, thereby ensuring that the values are sufficiently accurate. This is important due to the large deflections that occur in the simulation, which may lead to shear locking concerns. The study incorporates the minimum four-element limit into the proximity

settings of an ANSYS mesh. Notwithstanding the different faces of the CAD model, a minimum of four elements will be used in a region. Table 5.7 defines the different sizes for the foot (such as coarse, medium and fine mesh) to be used in this study. In addition, the selection of the element type must factor in the geometry and analysis of the problem. The complex features of the foot require specialised options for the mesh; for instance, a tetrahedron-based mesh fits the curved geometry of the foot. The study also adopted a soft global behaviour to minimise the effect of the strict controls of the mesh settings. This approach ensures that the varying sizes will conform to the complex and fine-grained features of the model. Although reducing the size of some of these elements will lead to an increase in the time required for computation, it is also significant in creating a smooth and continuous mesh in the contact regions at the fillets, such as those shown in Figure 5.12. The present study notes that the aspect ratio should be kept low in structural simulations to avoid huge skewing of the elements in cases of large deflections. This approach is sustained by monitoring the aspect ratio through applying other mesh controls, such as size 2 and size 3, on selected faces of the foot. The mesh should be refined around the regions predicted to exhibit the fastest change in variables. The contact areas may affect the accuracy of the measurements. Table 5.7 defines mesh refinement as a foot base by size 2. Moreover, the foot's toe and heel fillets are refined with size 3, as shown in Table 5.7. This approach ensures that the data collected is both accurate and not approximated. This study also used mesh iterations to try and define an accurate mesh for the foot. In designing the simulation, the researcher should select the sizing of the mesh as the first step. Based on the literature survey, this simulation adopts the tetrahedral mesh, as described in Figure 5.11, for the different components of the prosthetic leg. However, in the present mesh independence study, a contact mesh for other parts was used in the simulation presented in Table 5.9. Decreasing the size of the mesh leads to more accurate results, while meshing that is too small is inefficient and

contributes to time loss in the procedures. Figure 5.13 lists the three main settings for the foot mesh sizing, as follows:

- **Size 1**: Foot ends surface mesh size.
- **Size 2**: Foot palm surface mesh size.
- **Size 3**: Foot body surface mesh size.

Table 5.9: Other parts mesh count

| Mesh Type | Nodes | Element |
|---|---|---|
| **Coarse** | 76135 | 51216 |
| **Medium** | 76135 | 51216 |
| **Fine** | 76135 | 51216 |
| **Very Fine** | 76135 | 51216 |

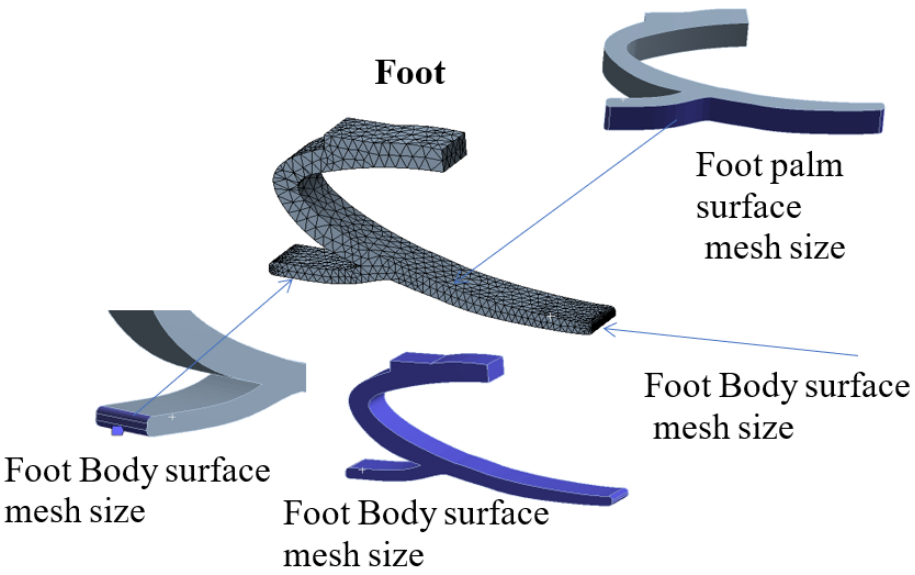


Figure 5.13: The three main settings for foot mesh sizing: foot palm surface mesh size, foot ends surface mesh size, and foot body surface mesh size.

### 5.4.2 Material Properties

The selection of the materials used in the manufacture of a prosthetic foot should guarantee that the foot will be comfortable. It should also be able to withstand force and pressure created during movement. The properties of the material are shown in Table 5.10 [32], while Figure 5.14 outlines the 3D model for the materials used in the present model.

Table 5.10: Materials used in prosthetic foot properties [32]

| **Material Name** | **Syndiotactic Polystyrene** | **Aluminium** | **Structural Steel** |
|---|---|---|---|
| **Density** ($kg/m^3$) | 1069 | 2770 | 7850 |
| **Young's Modulus (MPa)** | 7410 | 71000 | 200000 |
| **Poisson Ratio** | 0.3629 | 0.33 | 0.3 |
| **Yield Tensile Strength (MPa)** | 92-132 | 280 | 250 |
| **Ultimate Tensile Strength (MPa)** | 65.5-175 | 310 | 460 |
| **Yield Compressive Strength (MPa)** | 66 | 280 | 250 |

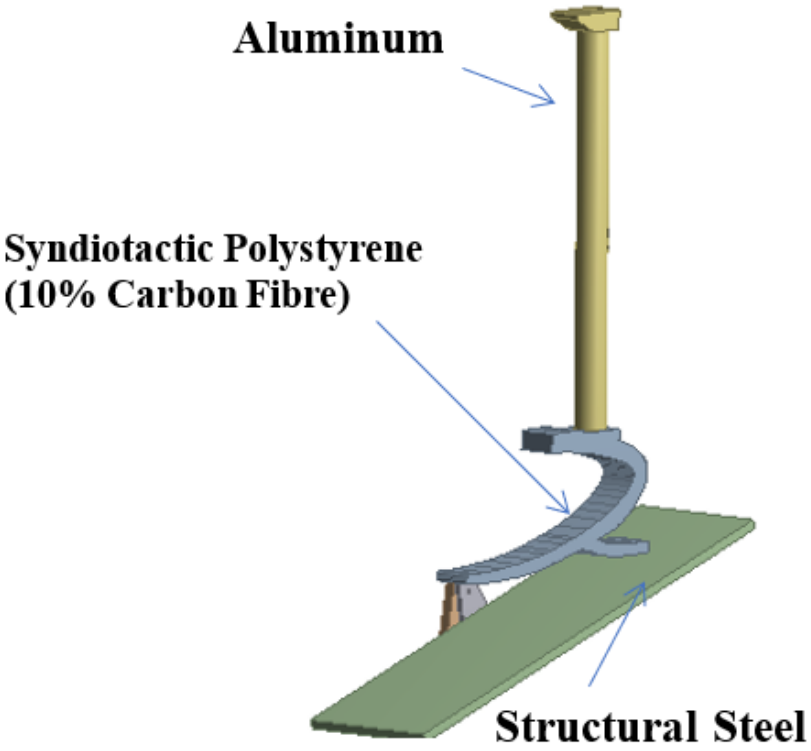


Figure 5.14: 3D model with material selection

### 5.4.3 Contact Definition

In this context, foot contact refers to the interaction of two critical parts, as well as the nature of their connection. The research must treat these connections as central to an experiment and also refer to different load cases. For instance, contact and target surfaces denote specific penetration patterns between bodies, such that the target face is impervious to penetration but can easily penetrate different bodies. Herein, rigid bodies are designated as targets, since they act against the foot as barriers despite their ability to penetrate other bodies. Tables 5.11 and 5.12, along with Figures 5.15 and 5.16, demonstrate the two connection types available in this model - namely contact and joint definitions. In the present simulation setup, the platform is rotating and the leg is only allowed to move in a vertical direction. The platform is in bonded contact with

the secondary kneel; hence they behave as a single part. There are some important definitions in the model simulation which are defined as follows:

- In the contact settings, platform is defined as a target face, while the foot base is defined as a contact face [110].
- The contact between the platform and the foot base is defined as frictionless, while the contact between the shank and the foot is defined as bonded contact [34]. Therefore, the foot and shank act together as a single body in the simulation.
- The contact between the secondary kneel and anchor is defined as a frictionless contact. This contact allows sliding motion between the two surfaces, hence helping the secondary kneel to rotate around the anchor [34].

However, the rotational boundary condition is defined for the platform (see Section 5.4.4). Hence, to both support the platform and simulate real testing conditions, a revolute joint is defined between the secondary kneel and anchor. The anchor is fixed, and is hence defined as a reference body, while the secondary kneel is defined as a mobile body because it rotates with the platform. A contact model proposed by Morgan [34] is used in this study.

Table 5.11: Contact definitions for the foot. The table lists the target face as well as the contact face.

| No. | Contact Type | Target Face | Contact Face |
|---|---|---|---|
| **1** | Frictionless | Platform | Foot Base |
| **2** | Frictionless | Anchor | Secondary Kneel |
| **3** | Bonded | Shank | Foot |

Table 5.12: Types of joint

| Joint Definition | |
|---|---|
| **No.** | 1 |
| **Joint Type** | Revolute |
| **Reference** | Anchor |
| **Mobile** | Secondary Kneel |

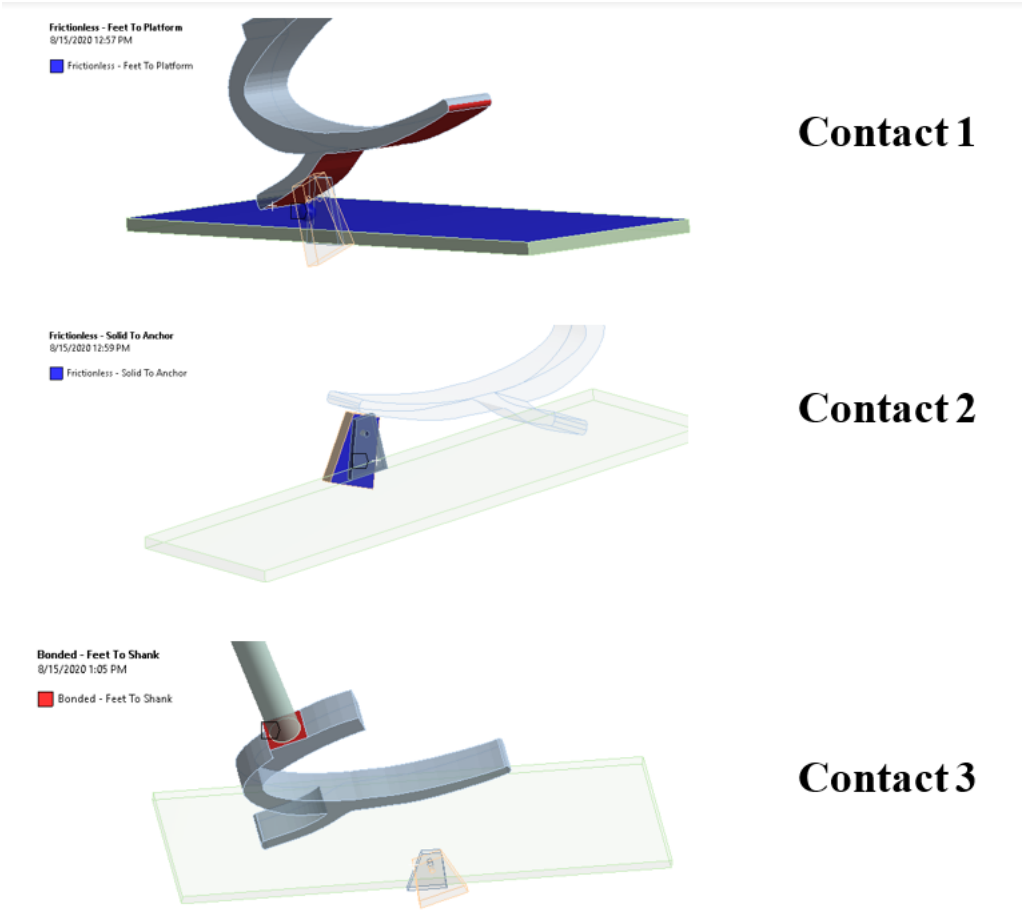


Figure 5.15: Foot contact points in three different faces and locations in the foot

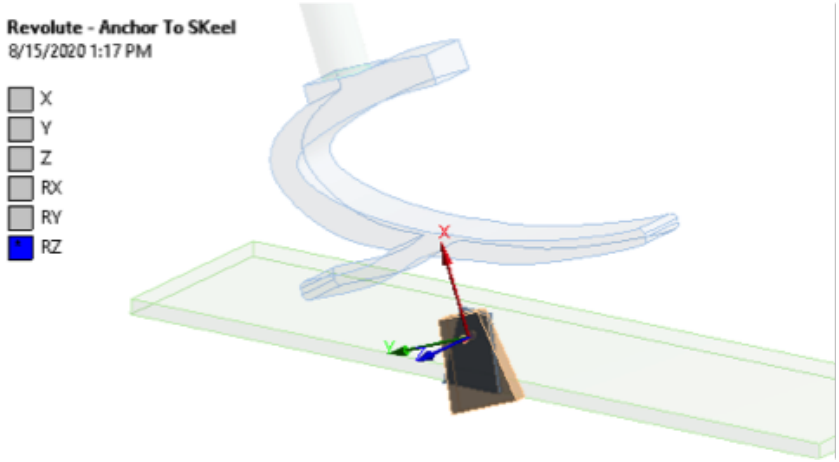


Figure 5.16: Joint definitions

### 5.4.4 Boundary Conditions

In this section, the boundary conditions for the FEA study are described. As this is a transient FEA simulation, the force and platform rotation boundary conditions are specified with time. The objective of the present FEA simulation is to estimate the foot strength and stiffness (based on foot deflection) for the given vGRF. In reality, the ground is stationary and the leg is dynamic; however, to avoid the complex boundary conditions in the simulation, the ground (platform) is made to rotate, while the leg is only allowed to move in a vertical direction. To simulate such a scenario, vGRF values with time are applied over the shank support is indicated by the letter *B*. The vGRF graph and location for the applied force are shown in Figure 5.17. Platform rotation with time is also specified in Figure 5.17 and indicated by the letter *C*. The anchor supports the secondary kneel and platform by means of the revolute joint; hence, the fixed support boundary condition is defined at the base of the Anchor, which is also indicated by the letter *A* in Figure 5.17. As has been discussed, only vertical movement is allowed for the leg; hence, a remote support boundary condition has been defined for the shank and is indicated by the letter *D* in Figure 5.17. Finally, to archive a good convergence in the solver, the remote support boundary

conditions are defined for a platform that is only allowed to rotate and is indicated by the letter *E*.

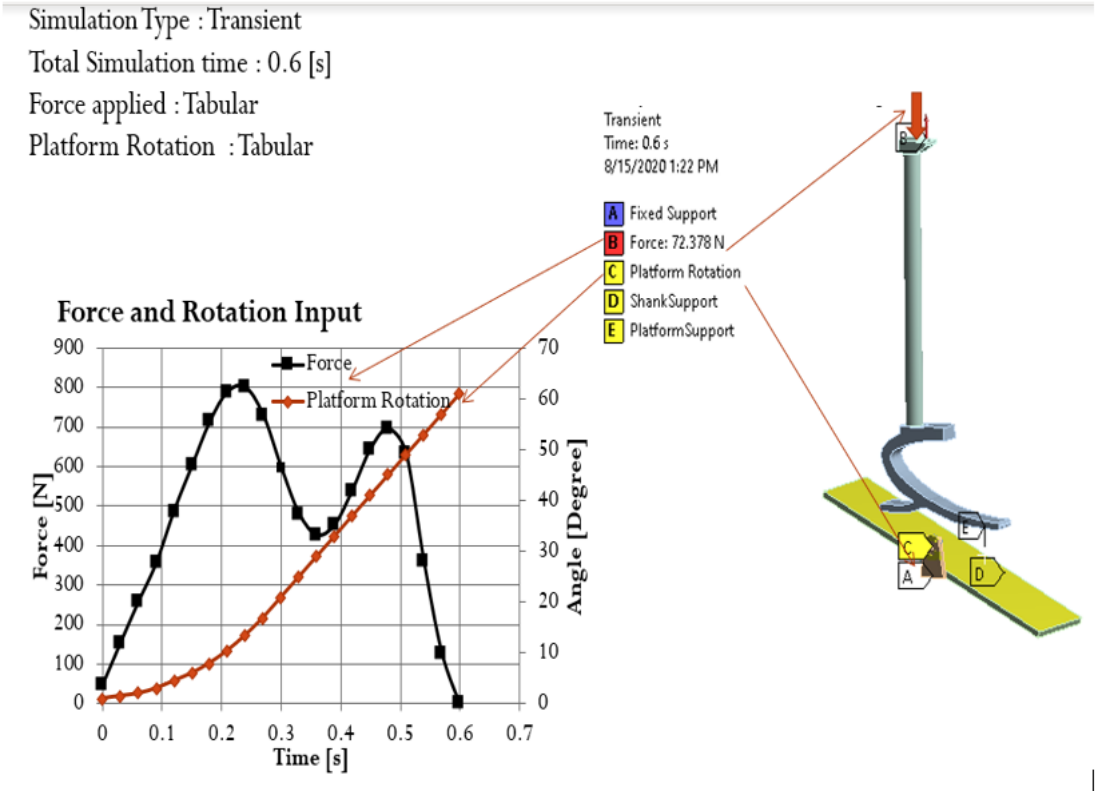


Figure 5.17: Simulation boundary conditions

### 5.4.5 Results for Syndiotactic Polystyrene (10% Carbon Fibre) Foot

In this section, different leg stiffness values from various mesh cases are tested and compared using the model simulation. Results for the three mesh types are plotted in a stiffness versus foot angle graph, as shown in Figures 5.18 and 5.19. As can be seen from the figure, the variation between the three types of mesh is low; however, there is a variation of about 7.4% in terms of average forefoot stiffness value between a coarse and medium mesh. In addition, the variation between a medium and fine mesh is around 0.5%. Through further analysis and study, it is proven that the medium mesh is sufficient to perform future simulation studies.

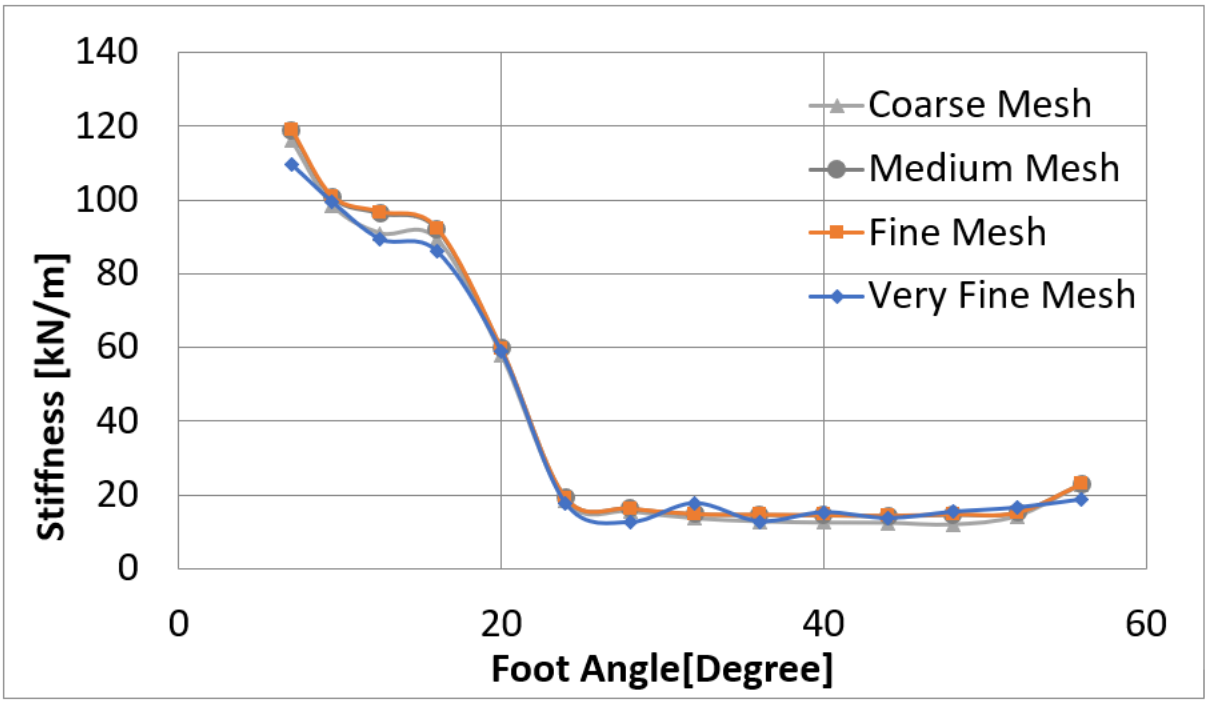


Figure 5.18: Simulation results of syndiotactic polystyrene (10% carbon fibre) foot.

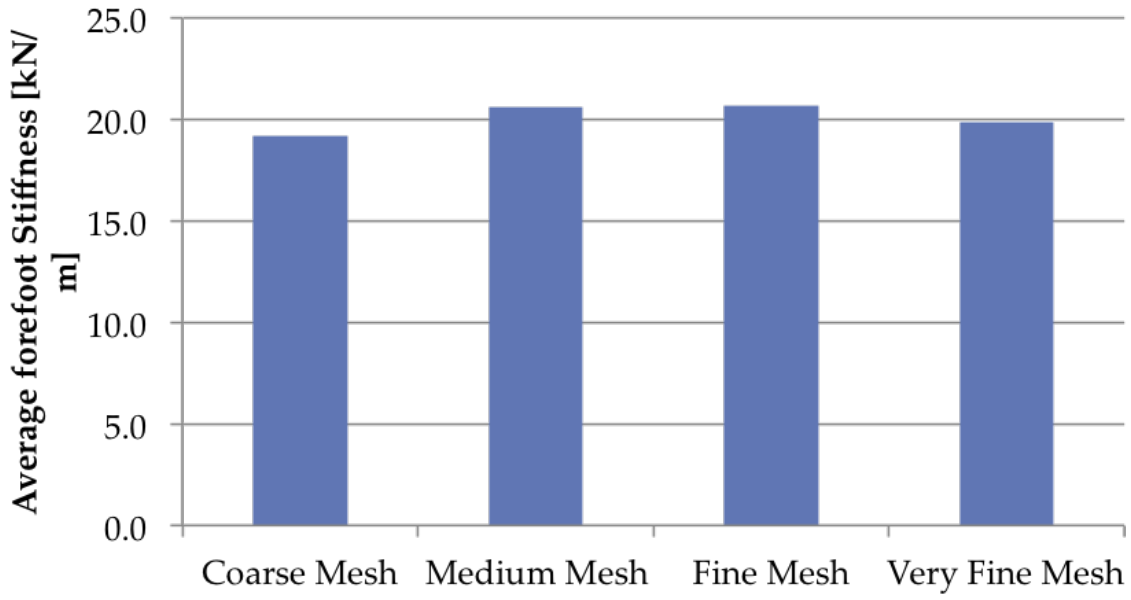


Figure 5.19: Stiffness from various mesh cases are compared. The corresponding results exhibited low variation between the three mesh types.

### 5.4.6 ROS Calculation

The ROS of the ankle is calculated from the data at the COP derived from walking. The foot acquires energy during the stance phase period before the unloading phase of walking. ROSs are integral to the design and alignment of the prosthesis. According to Hansen et al. [153], the ROSs derived from lower limb amputees differ from those derived from able-bodied individuals. An APDL script has been implemented in an ANSYS workbench to extract the COP data in the simulation (see Appendix D). COPx data with foot deflection is used to plot the foot ROS. The calculation of the ROS (see Appendix E) should fit the lower arc of the circle. The shank-based coordinates $(X_0, Z_0)$ of the circular arc correspond to the radius of the circular arc. Regarding the ROS produced by the designed foot, the ROS is a circular arc for the given foot, while the radius of the circular area is estimated to be approximately 0.4m (see Figure 5.20); this radius value will be used for the PWD model optimisation study.

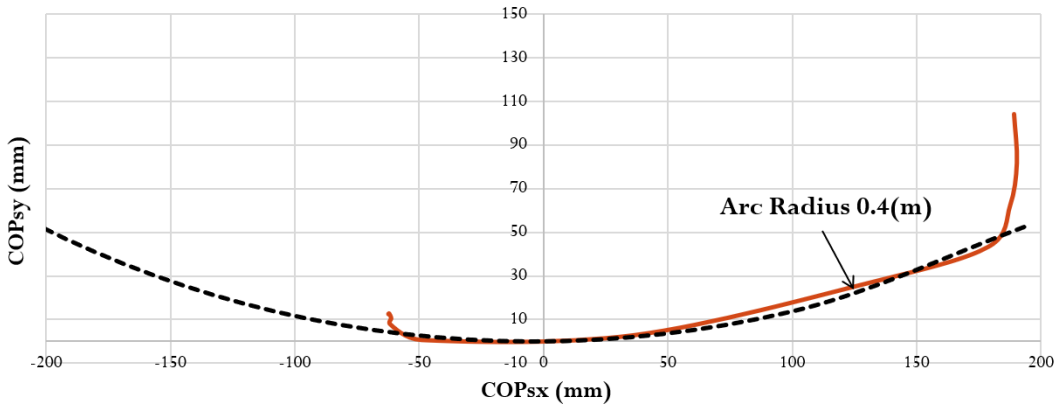


Figure 5.20: ROS syndiotactic polystyrene (10% carbon fibre) foot

The prosthetic foot ROS determined from the FEM is used in the PWD model in order to find the leg stiffness of the prosthetic foot leg.

## 5.5 Analysis for a Prosthetic Foot

This section will discuss and evaluate the leg stiffness of a prosthetic foot based on the finite element ROS calculated in the previous section. The sound leg stiffness was estimated previously as being equal to healthy leg stiffness. In addition, anthropological data for amputees was used [32]. In this step, amputee prosthetic leg stiffness will be used as a variable for minimising UL. Various leg stiffness values for the prosthetic foot are used in the PWD model's iteration to achieve the best fit from simulation data. This parametric study helped to discover the stiffness value that is used as input for the prosthetic model simulation. The aim of this section is to incorporate prosthetic foot settings into the PWD and evaluate the optimised stiffness for the prosthetic foot leg (see Figure 5.21). Model parameters are listed in Table 5.13 and Figure 5.22.

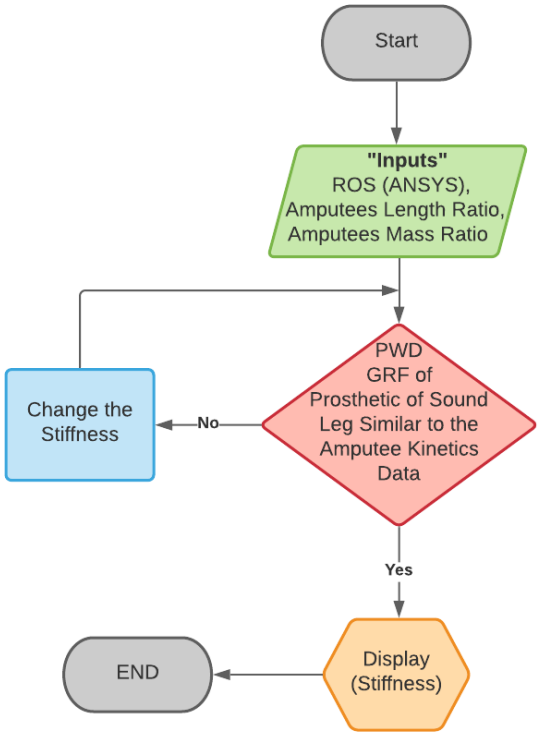


Figure 5.21: Incorporation of the prosthetic foot setting into the PWD model

Table 5.13: Simulation input for the prosthetic foot model. Leg length = $1m$, total tested mass = $70kg$, and mass ratio = 3.6 (hip mass = $45kg$)

| | **Left Leg** | **Right Leg** |
|---|---|---|
| **Foot** | Healthy | Prosthetic |
| **Leg Mass (kg)** | 12.5 | 10.7 |
| **Thigh Mass (kg)** | 8.3 | 8.3 |
| **Calf/Shank Mass (kg)** | 3.1 | 1.5 |
| **Foot Mass (kg)** | 1.1 | 0.9 |
| **Mass Ratio** | 3.6 | 4.2 |
| **Length Ratio** | 0.6 | 0.5 |
| **ROS (m)** | 0.3 | 0.4 |
| **Stiffness (kN/m)** | 10.8 | **Analysed** |

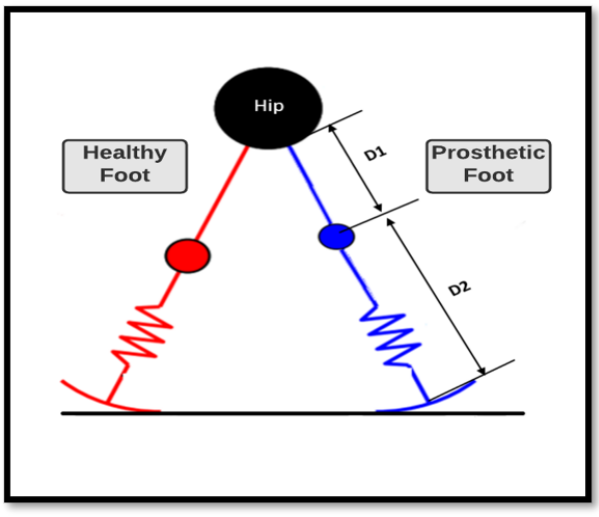


Figure 5.22: Model representing an amputee with a healthy foot (in red) and a prosthetic foot (in blue). The black circle represents the hip mass.

The first step is to determine which case matches the same GRF curve for the amputee data used previously [17]. Comparing the results in Tables 5.14 and 5.15 reveals that the prosthetic foot (C-shape) has a vertical stiffness of $9.8kN/m$ in the PWD while, in ANSYS, the average stiffness for the forefoot is $20.1kN/m$. This indicates how FE and PWD stiffness values compare with each other. However, the UL from this step is 0.115 based on the PWD data, while the UL based on the amputee laboratory data is 0.16 (see Chapter Four, Section 4.5.4, Equation 4.4).

Table 5.14: Sound leg and prosthetic leg data from previous research [17]; healthy leg data obtained from PWD.

| | **First Peak Vertical GRF** | **Second Peak Vertical GRF** |
|---|---|---|
| **Prosthetic Leg** | 1.11 | **1.02** |
| **Sound Leg** | **1.18** | 1.07 |
| **Healthy Leg** | 1.17 | 1.17 |

Table 5.15: Results for the six scenarios tested using the simulation model

| **Cases** | **Prosthetic Foot Stiffness (kN/m)** | **Sound Leg First Leg** | **Prosthetic Leg Second Peak** | **Unhealthy Load** |
|---|---|---|---|---|
| **Case 1** | 9.8 | 1.185 | 1.07 | 0.115 |
| **Case 2** | 9.95 | 1.17 | 1.08 | 0.090 |
| **Case 3** | 10.1 | 1.16 | 1.1 | 0.080 |
| **Case 4** | 10.3 | 1.13 | 1.08 | 0.130 |
| **Case 5** | 10.45 | 1.1 | 1.085 | 0.155 |
| **Case 6** | 10.8 | 1.27 | 1.27 | 0.200 |

For the UL to be reduced, the stiffness value will be changed in order to minimise the ULs (see Figure 5.25). Table 5.15 and Figure 5.23 present the trial cases while Figure 5.24 presents the UL variations with the leg stiffness. The optimum vertical stiffness is $10.1kN/m$; this stiffness value represents the optimum stiffness in the PWD with a corresponding UL of 0.08. To lower the UL, the leg stiffness for the finite element simulation and resulting in the UL can be predicted as follows: $UL_{erroneous}$ = (0.08 × 0.16) / 0.115 = 0.111 (see Figure 5.28).

The above value is the erroneous value of the UL. To evaluate the actual amputee UL at $V_r$=1.17, the value of $(f)$ should be calculated using Figure 5.8.

$UL_{predicted} = 0.111 \times (1 - f/100) = 0.095$, where $f = 13.98$.

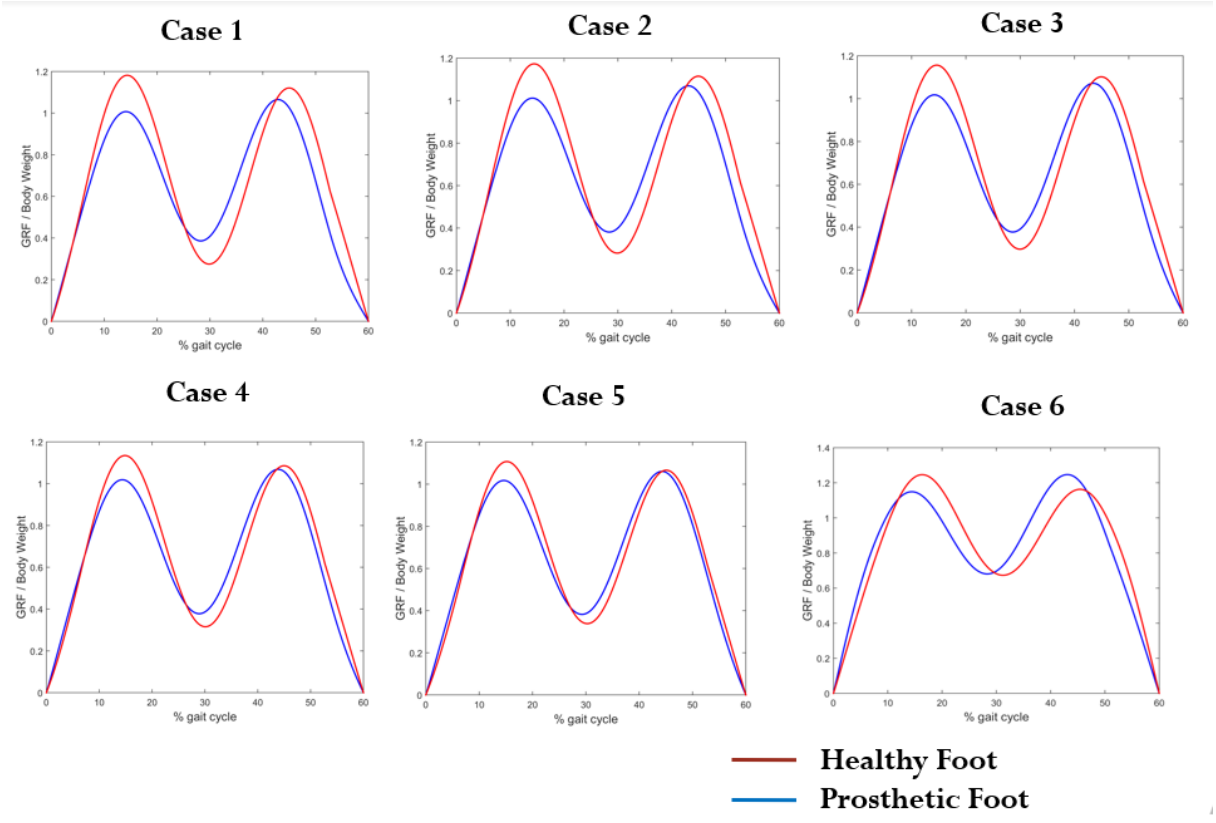


Figure 5.23: Results of different scenarios

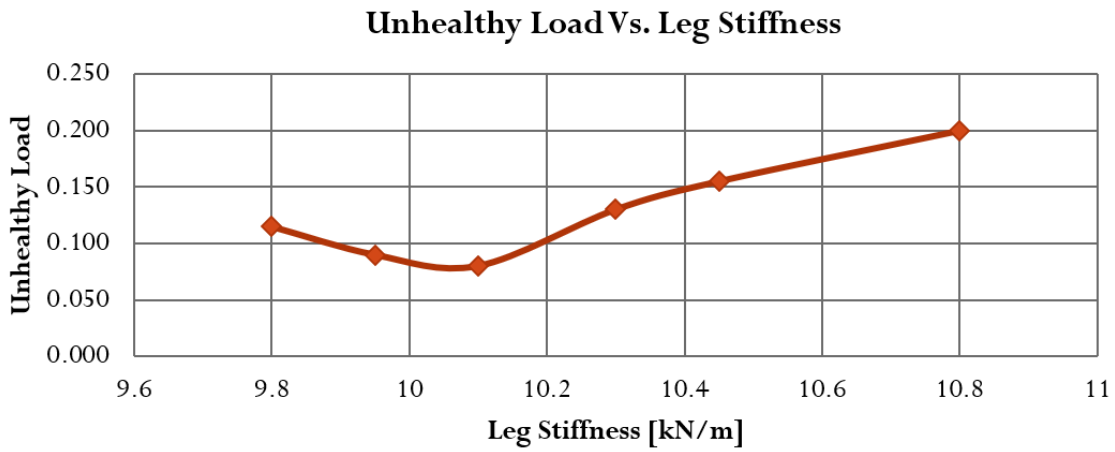


Figure 5.24: UL calculation for selected stiffness values for different cases.

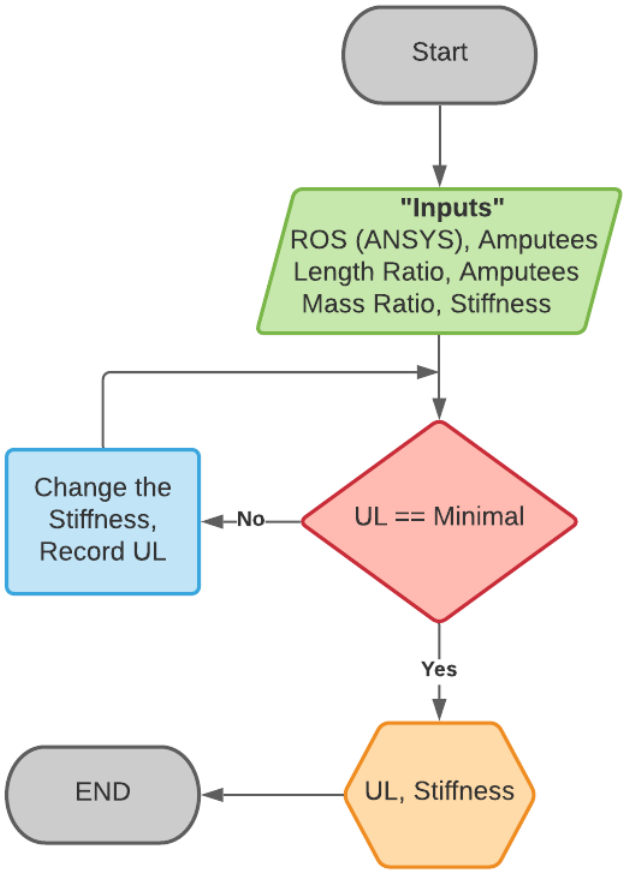


Figure 5.25: Evaluating the minimisation of UL criteria by adjusting the leg stiffness value.

While the UL can be reduced using an optimised stiffness value, the ROS will be the next criterion used to further minimise it, as shown in Table 5.16.

Table 5.16: Simulation input for prosthetic foot model

| | **Left Leg** | **Right Leg** |
|---|---|---|
| **Foot** | Healthy | Prosthetic |
| **Leg Mass (kg)** | 12.5 | 10.7 |
| **Thigh Mass (kg)** | 8.3 | 8.3 |
| **Calf/Shank Mass (kg)** | 3.1 | 1.5 |
| **Foot Mass (kg)** | 1.1 | 0.9 |
| **Mass Ratio** | 3.6 | 4.2 |
| **Length Ratio** | 0.6 | 0.5 |
| **ROS (m)** | 0.3 | **Analysed** |
| **Stiffness (kN/m)** | 10.8 | 10.1 |

**Prosthetic Foot ROS Optimisation Study**

A further investigation is conducted into minimising the UL by preserving the leg stiffness value and changing ROS. Table 5.17 presents the eight tested cases. Figure 5.26 represents the curve between the UL and the different ROS numbers. Note that Case 3 was the case discussed previously when vertical stiffness was the variable; now, Case 4 (see Figure 5.27) is the optimised case, as the UL has been reduced to 0.05.

Table 5.17: Results for the eight tested scenarios using the simulation model for changing ROS

| | ROS | Sound Leg First Peak | Prosthetic Leg Second Peak | UL |
|---|---|---|---|---|
| **Case 1** | 0.36 | 1.184 | 1.08 | 0.104 |
| **Case 2** | 0.39 | 1.18 | 1.09 | 0.090 |
| **Case 3** | 0.40 | 1.16 | 1.1 | 0.080 |
| **Case 4** | 0.41 | 1.17 | 1.12 | 0.050 |
| **Case 5** | 0.42 | 1.183 | 1.115 | 0.068 |
| **Case 6** | 0.44 | 1.176 | 1.11 | 0.066 |
| **Case 7** | 0.47 | 1.165 | 1.08 | 0.095 |
| **Case 8** | 0.51 | 1.161 | 1.05 | 0.129 |

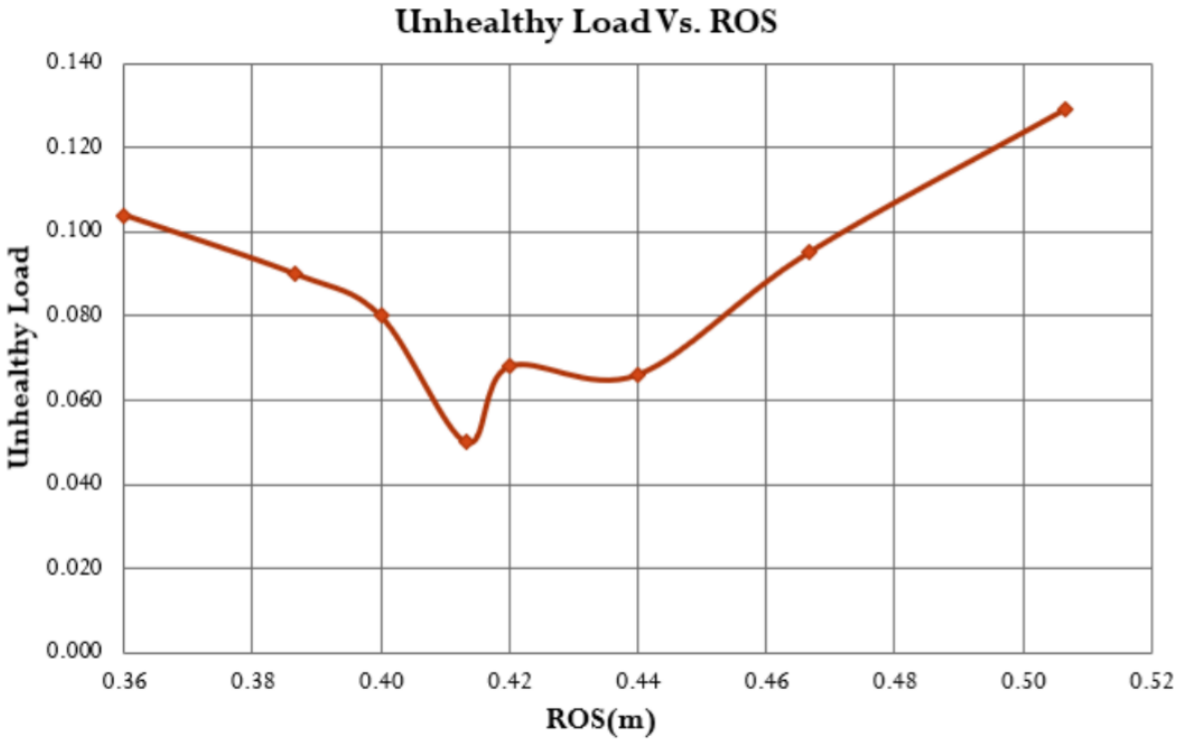


Figure 5.26: UL values for the eight different values of ROS

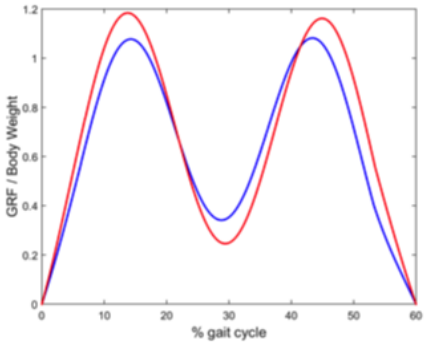


(a) Case 1

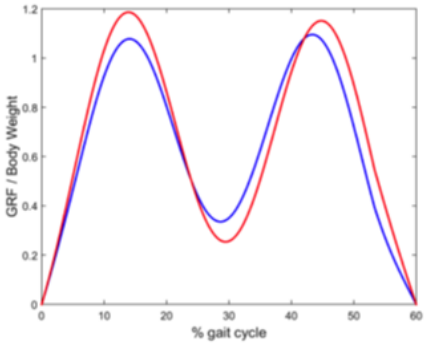


(b) Case 2

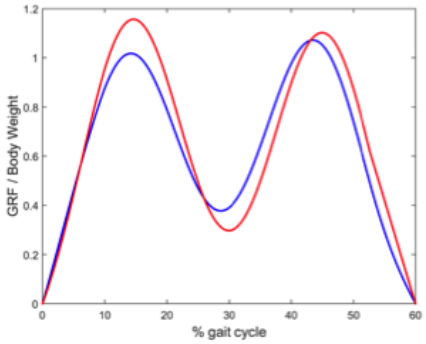


(c) Case 3

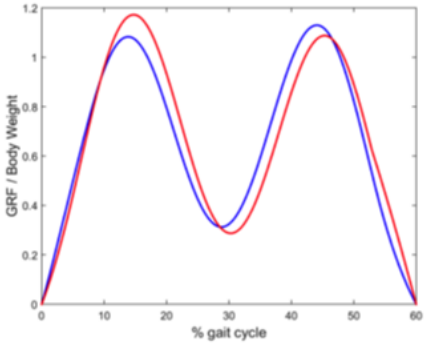


(d) Case 4

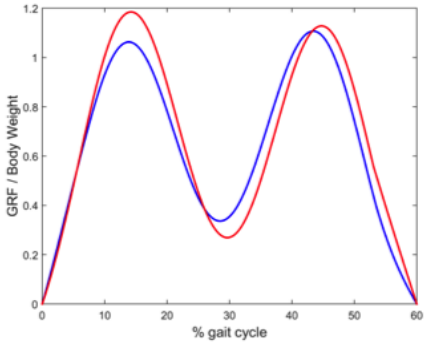


(e) Case 5

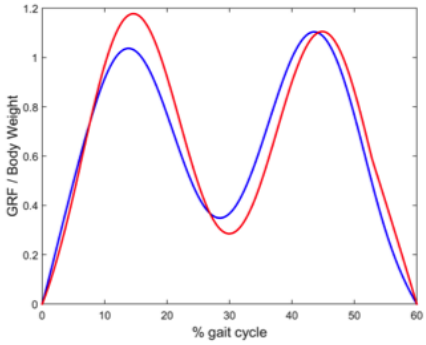


(f) Case 6

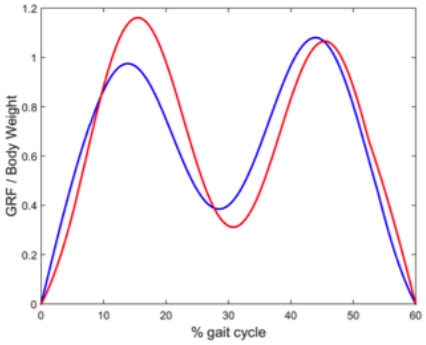


(g) Case 7

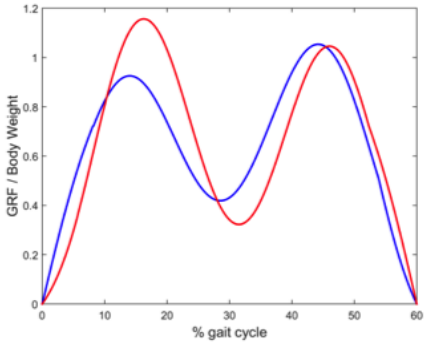


(h) Case 8

Figure 5.27: GRFs for different ROS values (healthy foot: red, prosthetic foot: blue)

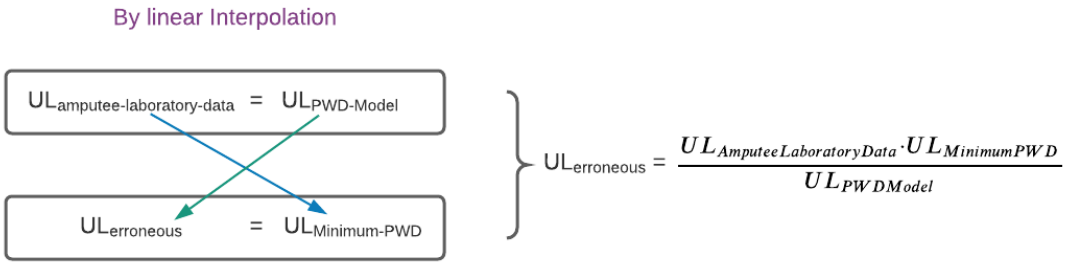


Figure 5.28: Erroneous UL calculation

Up to this point, $UL_{AmputeeLaboratoryData} = 0.16$, $UL_{MinimumPWD} = 0.05$ (Table 5.17, Case 4) and $UL_{PWDModel} = 0.115$. Similarly, the UL from PWD is equal to 0.05, which is the minimum value of UL that can be achieved up to this point. Thus, the minimum erroneous UL for this amputee will be calculated as, $UL_{erroneous} = (0.05 \times 0.16)/0.115 = 0.069$ (see Figure 5.28 for the source of this equation).

Furthermore, $UL_{predicted} = 0.069 \times (1 - f/100) = 0.059$, where $f = 13.98$ (see Figure 5.8). Up to this point, in order to obtain the minimum UL for this amputee, a new prosthetic foot should be designed that produces a ROS with a radius value of $0.41m$ rather than of the existing ROS radius value of 0.4m. This design process is explained in the next chapter.

## 5.6 Discussion

The present study aims to improve design optimisation using PWD simulations of amputee walking and FEM to identify the optimal prosthetic foot design capable of minimising biomechanically driven unhealthy joint loads. The study has hypothesised that optimal forefoot stiffness characteristics have the ability to minimise ULs. Integrating prosthetic foot design optimisation with PWD and FEM, with the help of the experimentally calibrated parameterised GRF equa-

tions proposed in chapter four, enabled not only the examination of the performance of ESAR foot designs, but also an assessment of the interactions among the foot, forward propulsion, and swing leg. The simulation results revealed that there are indeed foot stiffness characteristics for unilateral below-knee amputees that have the potential to minimise ULs. This is explained by the tendency of a stiff forefront to keep more load on the hindfoot, leading to higher energy storage and return (ESAR). Centre-of-mass mechanisms highlight how the whole walking process occurs. Specifically, increasing forefront stiffness will lower the push-off in the prosthetic limb. In addition, walking speeds impact the ankle push-off energy returns. The reduction in vertical GRF is consistent with increasing hindfoot stiffness. In this regard, it is more beneficial to use lower foot stiffness for higher speeds. Measuring the prosthesis' mechanical stiffness will enable prosthesis designers to determine how the loading techniques impact limb stiffness. The design of ESAR prosthetics will benefit from the enhanced measurement of stiffness in prosthetic feet [100]. A stiffer hindfoot results in lower values of returned energy, while a softer hindfoot leads to an increase in the energy returned. Moreover, a softer spring deflects more across all weight classes while providing greater ESAR.

## 5.7 Summary

A novel loosely coupled model between PWD and FEM with the help of a parametrised $G_r$ equation was discussed. The novel model enhances the optimisation of forefoot stiffness and predicts a ROS that is able to minimise ULs. The optimisation process was begun by measuring the gait kinetics of an amputee and was followed by comparing the first peak value of a sound leg with the estimated $G_r$ value in order to predict the velocity ratio. Next, a comparison between various models found a correlation used to help in predicting the actual UL. The FEM study

obtained the ROS of the existing prosthetic foot. This value was used in the PWD model, using purpose-built MATLAB software code [15], to investigate the effect of mass unbalance for amputees. The healthy leg stiffness was calculated in the PWD model with a separate analysis for the equivalent healthy population. Thus, by the end of this process, an optimal value of the ROS is suggested for the prosthetic foot so that the stiffness response of the foot can be redesigned. The next chapter will introduce a new 3D printable prosthetic foot model as one of the options for achieving the optimised ROS. Figures 5.29 and 5.30 summarises the proposed novel loosely coupled model.

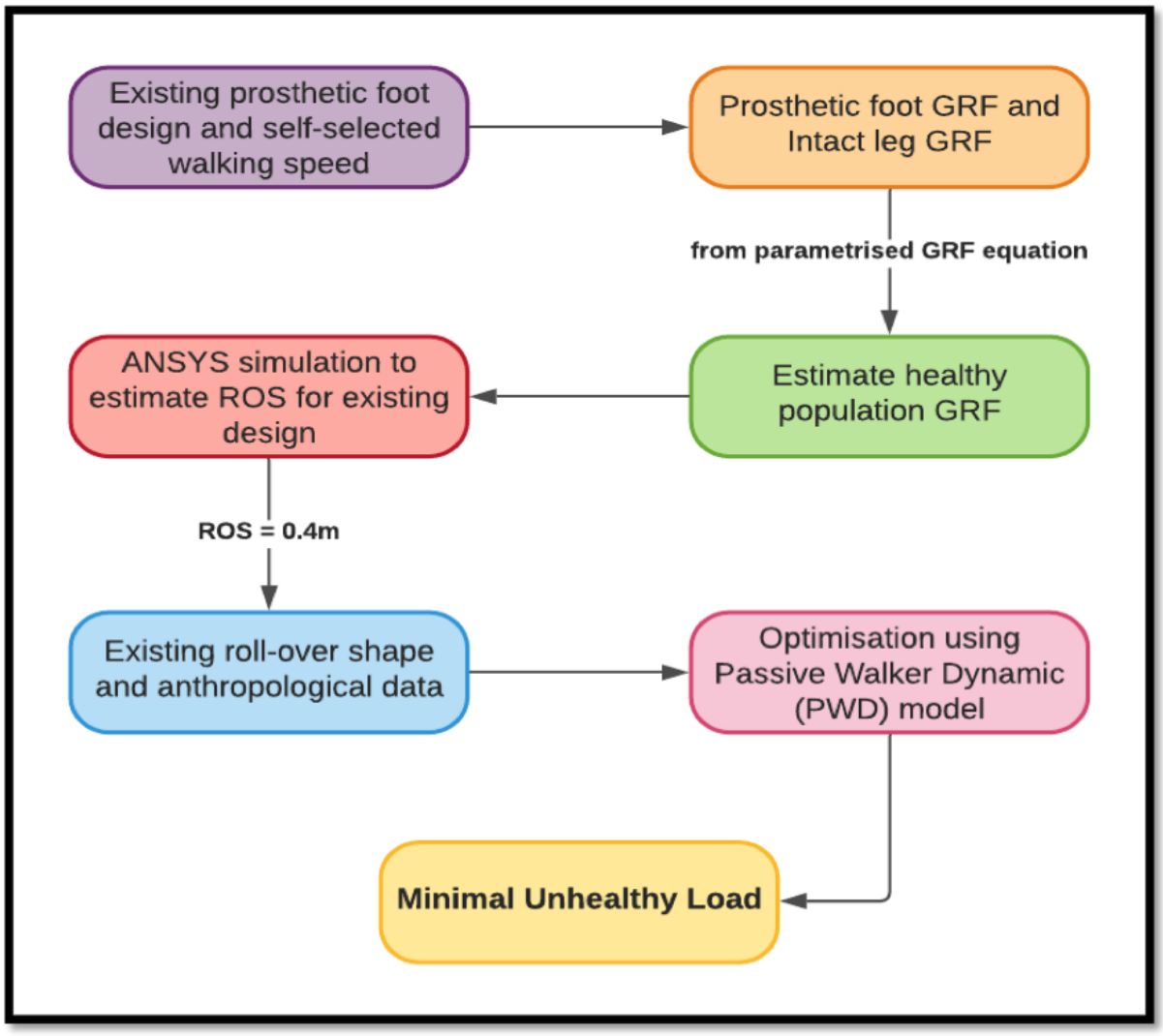


Figure 5.29: The summary of the proposed loosely-coupled model

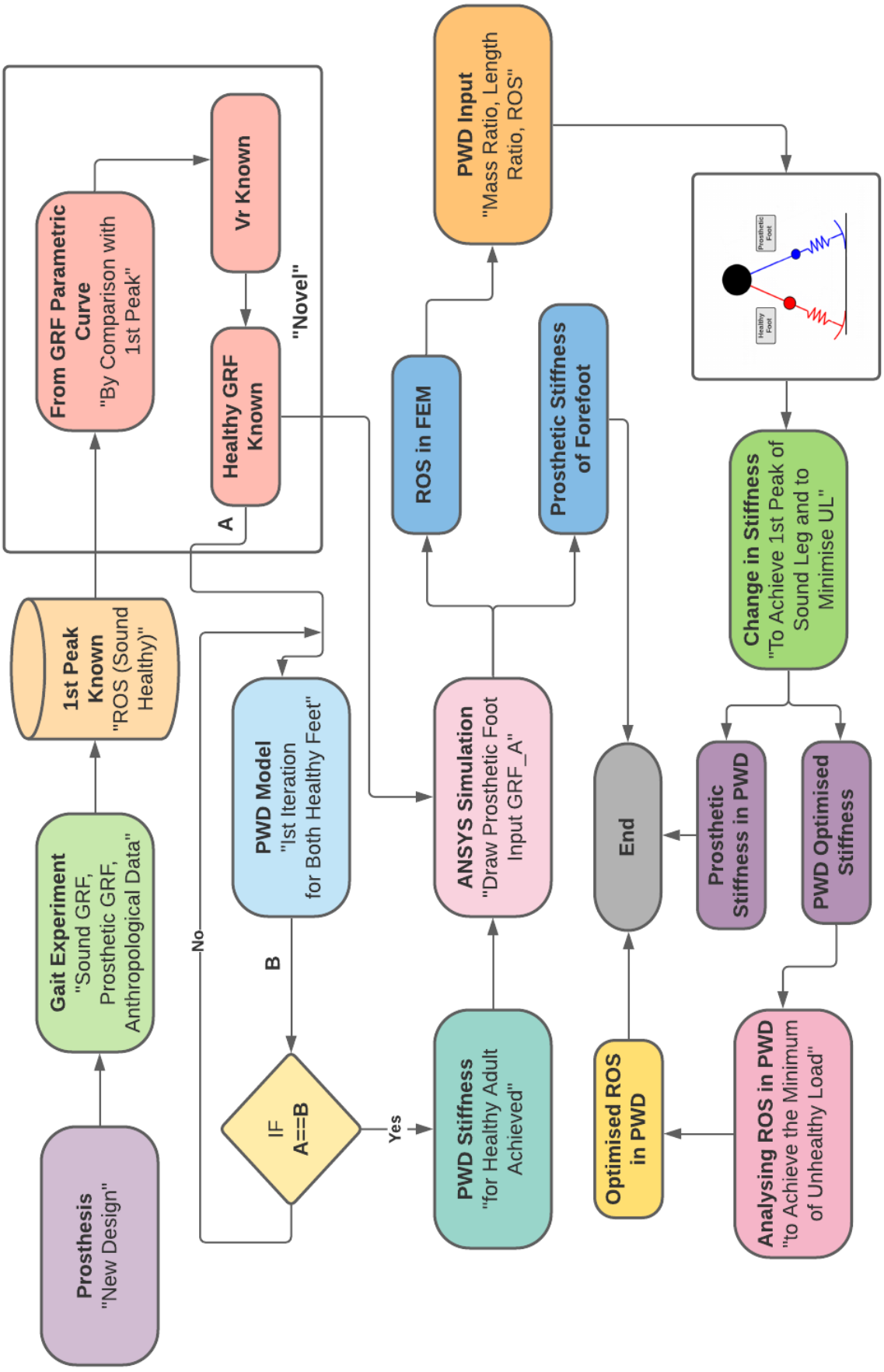


Figure 5.30: Novelty of loosely-coupled model

# Chapter 6

# A 3D-Printable Double-Keel Prosthetic Foot Design

## 6.1 Introduction

Ventura's [154] study determined the energy differences required by the sound leg and prosthetic foot during movement. This research established that existing prosthetic designs had not achieved gait symmetry or high-energy return at toe-off. Lower limb amputees tend to prefer ESAR prosthetics due to their efficacy and energy return. ESAR designs optimise step length symmetry, making it a requirement for all designs that aim to maximise their energy return at toe-off [155]. The efficacy of passive prostheses is reduced due to their lower energy return. Studies in the field aim to optimise prosthetic foot design to enhance performance. For instance, the stiffness of prosthesis in both the forefoot and hindfoot contribute to lower energy return and increased loading on the natural leg [100]. However, there are different types of prosthesis design that use different technologies, leading to differences in the published data. Therefore, the present study attempts to establish the relationship between stiffness and ROS in prostheses with the aim of

improving the design of prosthetic feet. Ventura's [154] research focuses on vGRFs and power output rather than addressing how to improve high energy return. ESAR prosthetics enable lower limb amputees to improve their gait and reduce their energy consumption while walking at different speeds. Many studies have linked the effectiveness of prostheses to the high return of energy into the residual limb, as described by the Pedotti diagram presented in Figure 2.3.

The resulting force vector transfers the energy between the natural and prosthetic foot during movement. Moreover, some studies have examined how the efficacy of prosthetic feet is improved by energy return, along with the loading properties of the sound leg and the subsequent pathological results [21]. Prosthesis design will benefit overall from the effective distribution of energy to and from the prosthetic foot. Existing standards focus primarily on the structural performance of the foot and neglect how energy return affects the body's kinematics. Olesnavage et al. [109] created a design using the 'Lower Leg Trajectory Error' to determine the response of the prosthetic foot. The proposed method offers an effective examination of roll-over geometry, noting that amputees are forced to change their gait due to abnormal movements. Future studies on optimising prosthetic designs should address how the distribution of energy and loading properties affect gait and movement in the lower limb.

The focus of this chapter is to propose a new design for a prosthetic foot that achieves a given ROS and degree of vertical stiffness from the loosely coupled hypothesis based on the design criteria. Section 6.2 presents an overview of the model, which consists of two parts: the design concept of the primary and secondary keel and the geometry details. In Section 6.3, the study outlines the design results simulations for FEM in terms of four criteria: strength testing, boundary conditions, contacts, and a sensitivity study (mesh development). In Section 6.4, the results of the study are discussed. Finally, Section 6.5 summarises how a 3D-printable prosthetic foot should be designed.

## 6.2 The Primary and Secondary Keel Design Concept

This study proposes a new design to minimise the ULs that affect the locomotion of amputees using a prosthetic foot. Further to the observations made in Section 3.4, it was decided to explore a new double keel design option along with a group of final year mechanical engineering students at Swansea University [156]. The proposed concept features a more curved shape in the design to maximise ESAR (see Figure 6.1). The 'C-spring' heel is effective in absorbing the energy created by the heel strike. In addition, the double-keel ensures effective transfer of the energy to the toe. Using ESAR, a cantilever toe introduces elastic mechanisms at toe-off. The force path for the GRF is shortened by the secondary keel, thereby establishing a pivot point. Due to changes in momentum, the contact is detected in the two phases of toe-off and heel-raise, which aids energy return during toe-off. Moreover, the primary keel can efficiently store energy from the heel strike because no contact has taken place. The proposed design also utilises complex geometry to calculate the appropriate stiffness for the amputee, a concept inspired by a Mecuris foot [28]. Mecuris uses technology to produce prostheses that are unique to each individual based on their height, size, and gait characteristics [28]. One of these designs is the 'Comfystep'. This 3D printed prosthetic is optimised for a smooth rollover. The design initiates ROS immediately upon heel-strike and progresses to the stance step without requiring additional energy from the wearer. Although this study's design draws inspiration from the Comfystep, the dimensions of our design are different. The prosthesis has more practical variables, including better stiffness variability and computational time, which support a wide of range of walking speeds. In addition, the foot base curve is modelled using the Bezier curve to increase stiffness variability. The method is applicable to the optimisation of the ROS in prosthesis manufacture [127].

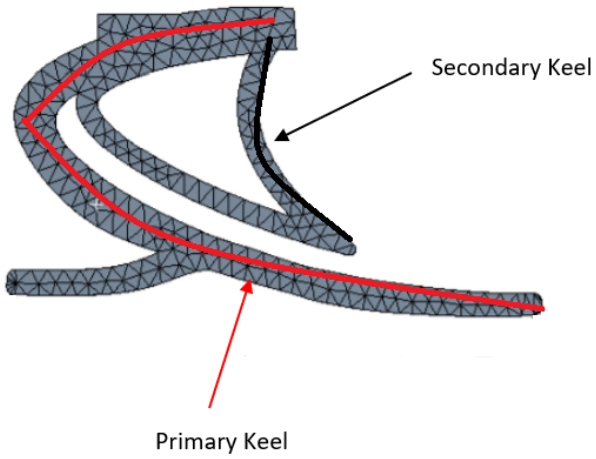


Figure 6.1: Primary and Secondary Keels

The primary keel design is larger at the bend of the C-spring. The configuration maximises the area to increase the yield bending moment, which experiences the highest levels of stress during bending [157]. The primary keel is distinct from the secondary keel. This is evident at the foot base and the gap between the keels is extruded. The secondary keel is thinner because it carries only a smaller portion of the loads and therefore does not require optimisation. More detail about the design is presented in Appendix H.

### Material Selection

3D technology is being increasingly used to create printable prosthetic feet. A majority of commercially available prosthetics are made from composites of carbon fibre and glass, which can store the energy required for propulsion. However, these prosthetics are expensive. Moreover, the cheaper SACH prosthetics fail to return enough energy. Advancements in 3D printing will enable designers to create prosthetics that have ESAR properties, since 3D prosthetics are created using the amputee's gait characteristics, height, and size. As an example, the Mecuris

uses the unique characteristics of every human being as a basis for its prostheses and orthoses. 3D printing expands the geometric freedom in modelling and creating prosthetic feet that meet the different needs of amputees. The functionality of the designs can be further improved by using better materials, including wear-resistant components [25, 26], polymer and metal hybrid microstructures [27] to increase strength. Hence, a 3D-printable foot with high-quality materials has a potential to achieve the required ESAR foot properties.

Polycarbonate materials [158] used in prosthetic engineering are strong and easily thermoformed. The structure of polycarbonates consists of both polymers and carbonate groups. The polymer sheet is often formed through the chemical reaction of carbonic chloride with pyridine. This material is highly hygroscopic; therefore, it is imperative to keep the polymer dry to protect its mechanical structure. According to Hacker et al. [159], polycarbonates degrade incredibly slowly under physiological conditions. Polycarbonates are highly favoured in key industries, including the engineering and medical fields, due to their high scratch resistance [159]. Due to their material strength, the material is integral in the manufacture of foot prosthesis. Wu et al. [160] further note that the key advantage of polycarbonates over other plastics lies in their ultimate strength and their increased transparency level, which is high on the visible spectrum [27]. The 3D printing of prosthetic feet should utilise polycarbonate materials due to their high strength, high scratch resistance, good density, good principal stress rate, and ability to be recycled. Hence, polycarbonate components are suitable for prosthesis manufacture due to their excellent mechanical properties. Grigore [161] notes that polycarbonates have an upper density of $1.24(g/cm^3)$ and a lower density of $1.19(g/cm^3)$. The key material properties of polycarbonates are listed in Table 6.1.

Table 6.1: Material Properties of Polycarbonate [158]

| **Material Name** | **Polycarbonate** |
|---|---|
| **Density** ($kg/m^3$) | 1200 |
| **Young's Modulus (MPa)** | 13500 |
| **Poisson Ratio** | 0.32 |
| **Yield Tensile Strength (MPa)** | 100 |
| **Ultimate Tensile Strength (MPa)** | 112 |

Density is an important measure of the intrinsic strength of construction. Polycarbonates have a higher density strength than most other polymers, meaning that they can produce durable prosthetics that can withstand heavy equipment during the manufacturing process (as such, during the manufacturing process, the 3D prosthetic foot will not experience damage). Furthermore, the high glass temperatures and the low molecular mass grades displayed by polycarbonates mean that they can be easily moulded. This characteristic is vital, since it ensures that prosthetics can be 3D printed in the comfort of a hospital without the risk of the material disintegrating. This trait is important for the first prototype of the 3D prosthetics [158].

Extruded polycarbonates can be used to provide protection for the prosthetic feet. Tensile strength and tensile stimulus are perhaps the most vital factors to consider when choosing products to make prosthetics. Polycarbonates' excellent mechanical properties make them uniquely different from other thermoplastics and polymers. Prosthetic feet require extruded polycarbonates to protect them from environmental factors due to their temperature and impact resistance.

## 6.3 ANSYS Design Results

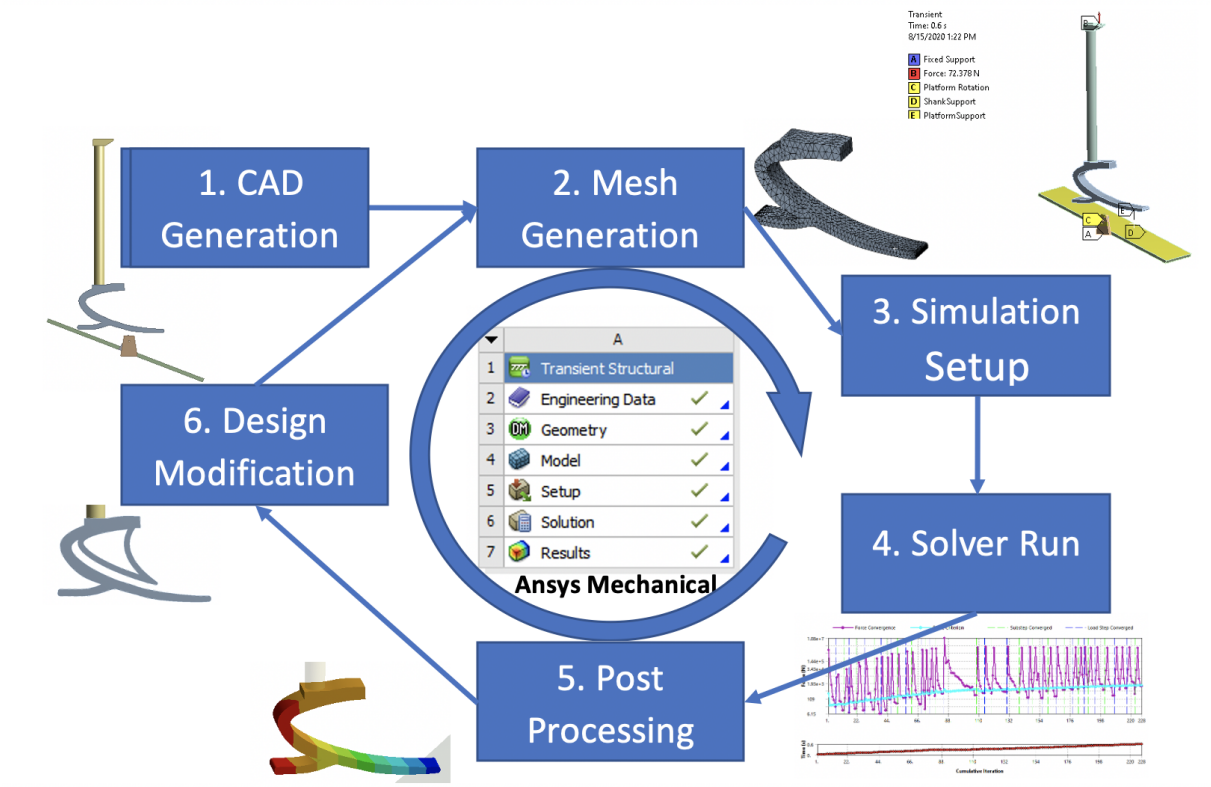


Figure 6.2: ANSYS application flow

This section describes the results of the different experiments performed in chapter five and the criteria employed, including testing, boundary condition, contacts, and the sensitivity study (mesh development). A detailed FEA simulation has been performed to achieve the objectives defined above. The flowchart of the ANSYS simulation presented in Figure 6.2 outlines the procedure employed. The design of the double keel is based on the following steps.

1. The first step is CAD generation. A CAD model of the amputee's prosthetic foot is generated using the ANSYS design modeller and will be used for the FEA study (case study 1). The subsequent case studies will introduce the double keel design.

2. The second step is mesh generation, which involves accurately identifying the mesh setting

for the FEA simulation. As discussed above, mesh sizing is a trade-off between simulation accuracy and machine computation time. A mesh dependency study was performed in the previous chapter to identify the correct mesh size.

3. The third step involves setting up the simulation case in the ANSYS workbench. In this step, the study defines the boundary conditions required to simulate the correct physics. In the present case, the transient behaviour of the foot is simulated.

4. The fourth step involves solving the study problem using the ANSYS workbench. The complex issues involving large deflections and contact movement are solved at this level. Many factors, including mesh, boundary conditions and contact settings, can influence the solver convergence and affect the accuracy of the obtained solution.

5. The fifth step is post-processing, in which the FEA results are analysed and relevant conclusions are derived for design optimisation and change. The built-in post processing of ANSYS allows for plot deflection, forces and stresses to be analysed. An additional script can be added to extract additional post-processing data. In the present FEA study, scripts have been implemented to extract the COP for the foot. Moreover, deflection and COP data are used to estimate the ROS and foot stiffness.

6. The final step in the FEA simulation process is the identification of the design and/or material changes required to achieve the specified objectives.

Once a new design is created, steps 2–6 are repeated to analyse the new design. In this study, the objective of the FEA simulation is to achieve a radius of $0.41m$ for the ROS in order to obtain the minimum UL. Hence, modifications are made to the foot material and thickness so as to achieve the defined objective.

### 6.3.1 Structural Analysis for C-Shaped Prosthetic Foot

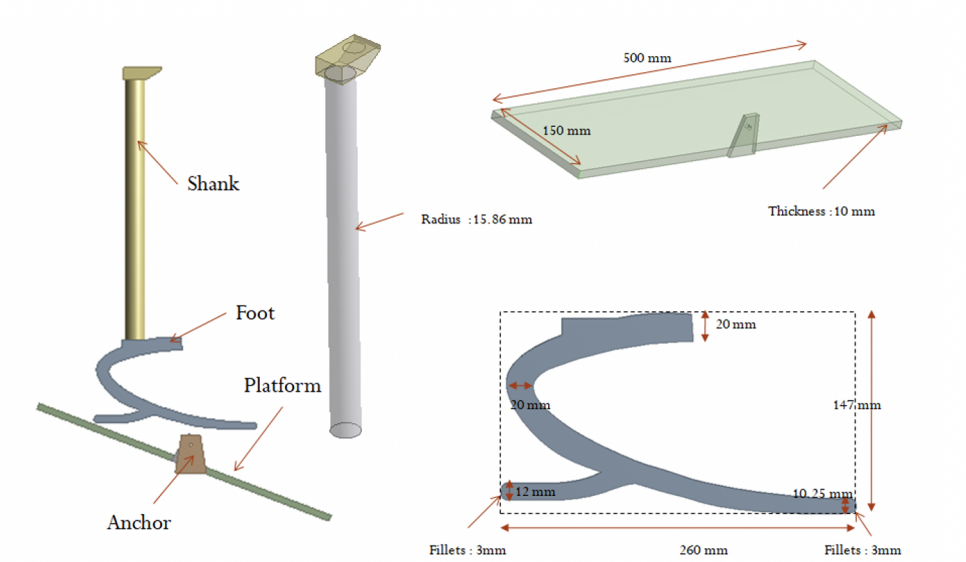


Figure 6.3: The transformation of CAD model into the ANSYS workbench.

While the amputee's prosthetic leg was discussed extensively in chapter five, in this section, the model will be briefly described. Beginning from a prosthetic foot's geometry and investigation of its materials (Single Component Test), the FEM model is developed and the ROS radius compared. A sensitivity analysis was performed earlier to investigate both the robustness of the tool and the response of the overall system to specific variations in parameters. Figure 6.3 presents the CAD model and its transfer into the ANSYS workbench to simulate the results. Mesh generation and boundary conditions have been discussed previously. Figure 6.4 further presents a summary of contact definitions.

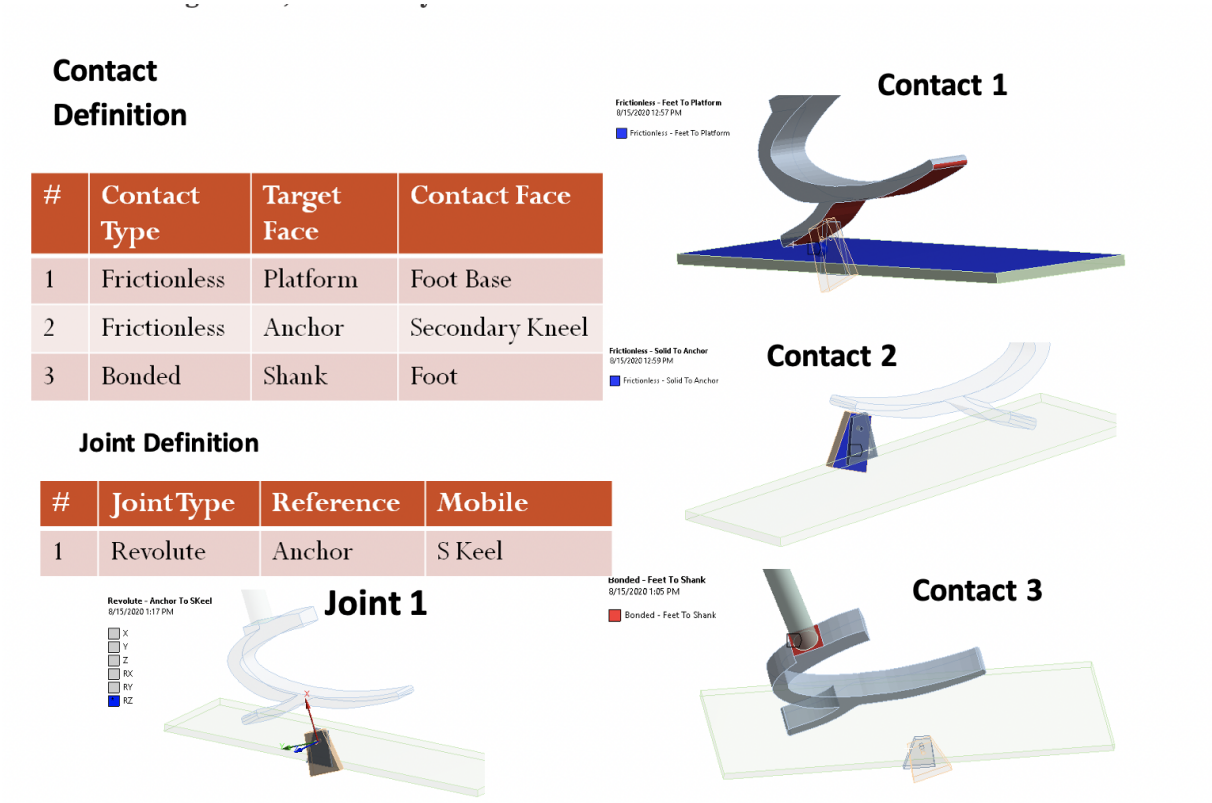


Figure 6.4: Summary of contact definitions

### 6.3.2 C-Shape Simulation Results

The deflection and the von-Mises stresses of the foot are shown in Figures 6.4 and 6.5, respectively. At the heel strike, the stresses begin to increase until they reach $40MPa$ at 15% of the gait cycle. At mid-stance, the stress drops to $21MPa$, while at toe-off (48% of gait cycle), the maximum stress reaches to $90MPa$ (as shown in Figures 6.5 and 6.6). Moreover, Figure 6.7 depicts the deflection curve of the foot during the simulation process and shows that the net deflection of the foot occurring at the toe-off phase is similar to the maximum stress.

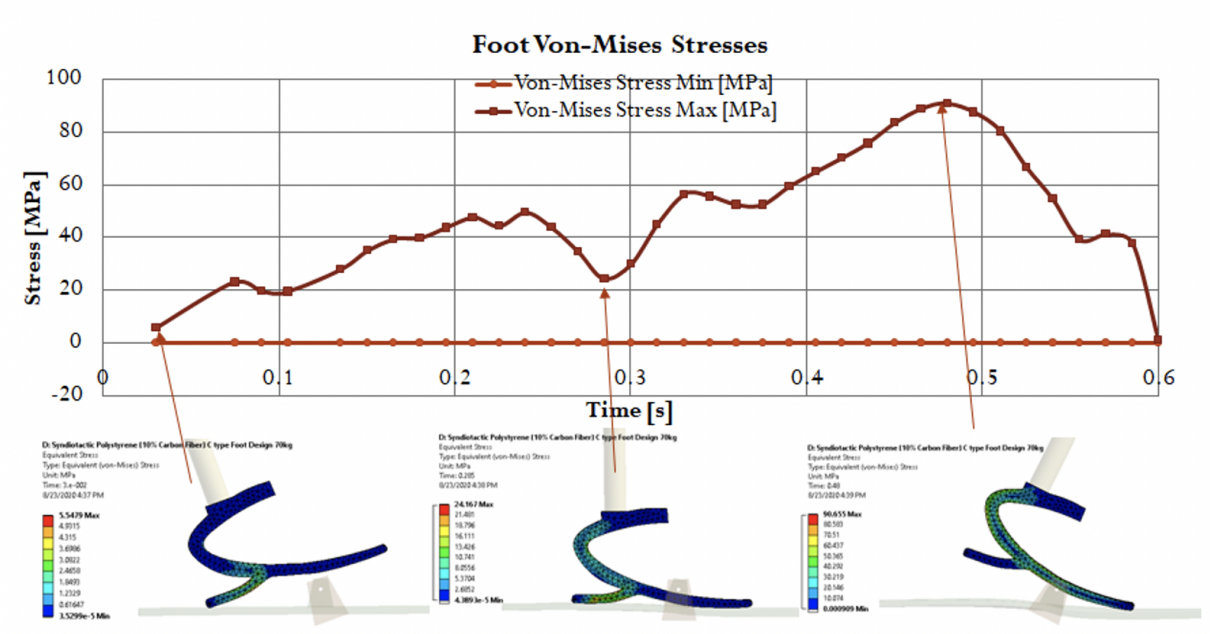


Figure 6.5: von-Mises stresses on the foot for the C-shape case

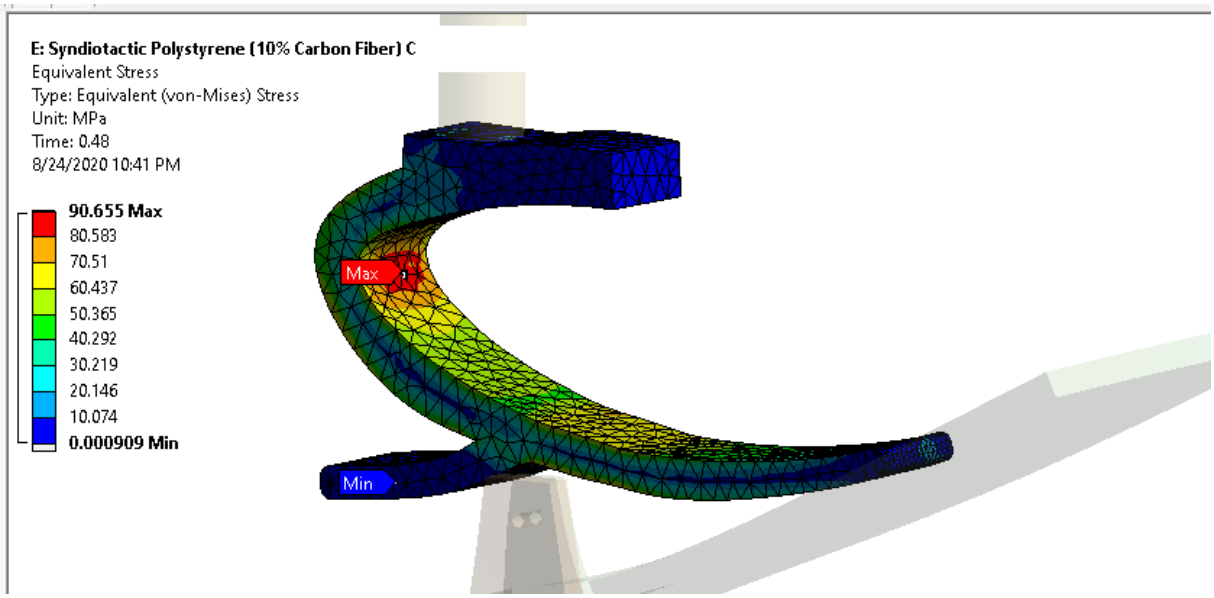


Figure 6.6: Isometric view of von-Mises stresses at 0.48s

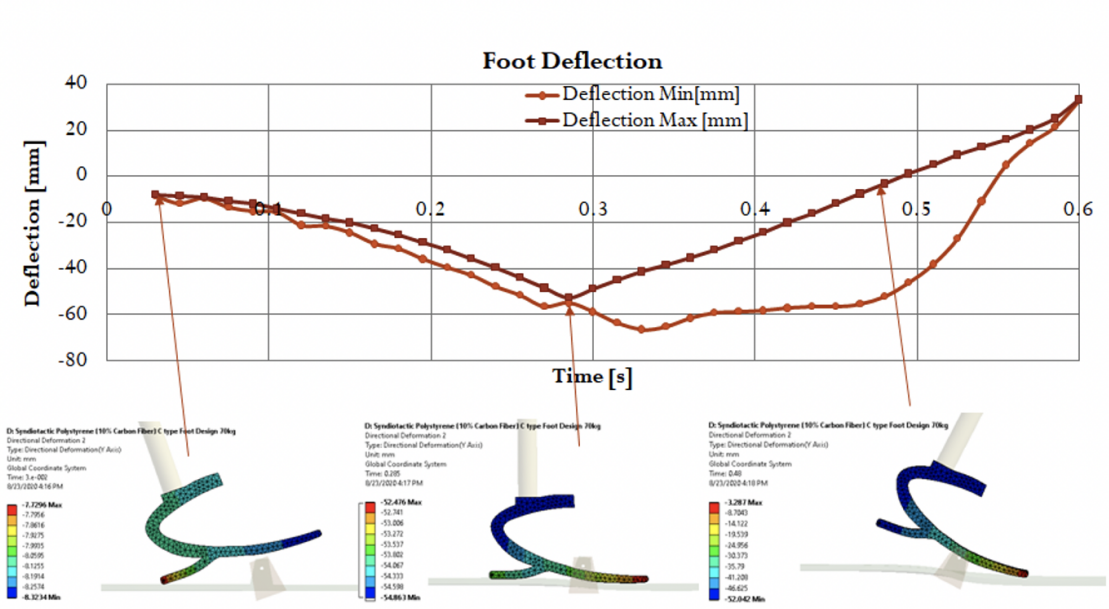


Figure 6.7: C-shape foot deflection

This example reveals high stress on the curve of the primary keel. The next example will introduce the double-keel, which is designed to enhance the stress concentrations and optimise the prosthetic foot to reach the optimum ROS of 0.41$m$ (see Figure 6.8).

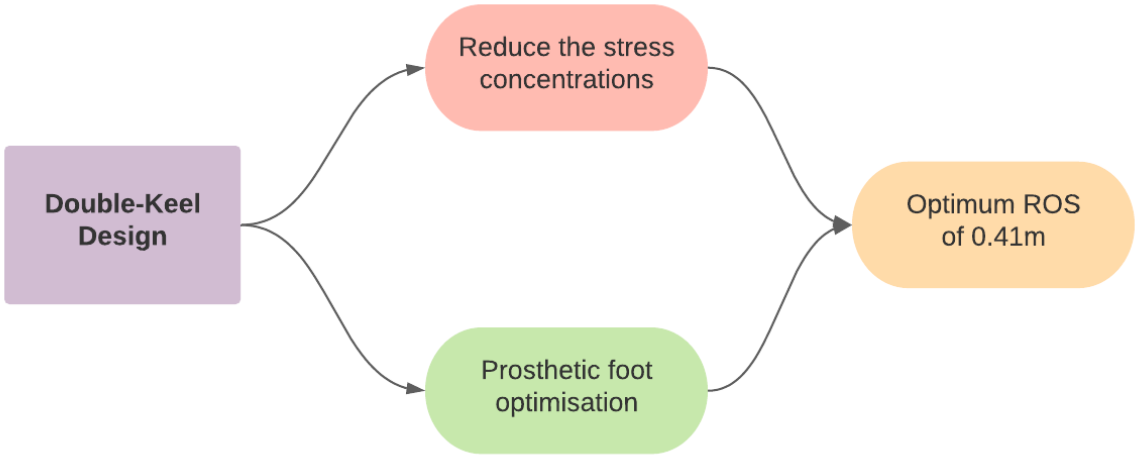


Figure 6.8: Double-keel design optimisation

## 6.4 Introducing the Double-Keel

This section discusses three new case studies to determine the best design.

### 6.4.1 Case Study 1 - Syndiotactic Polystyrene (10% Carbon Fibre)

The C-shaped design produced a high stress level of 0.48$s$ in the gait cycle. This is caused by the large amount of force and the bending that occurs during that moment. In this section, a double-keel design is studied that supports the foot and is suitable for the variable of stiffness. The CAD model, mesh sizing, boundary conditions, and results will be discussed in the next paragraphs.

#### CAD Modelling

The CAD model was developed using the ANSYS design modeller and was based on the dimensions of an amputee's prosthetic foot, as shown in Figures 6.9 and 6.10. Figure 6.10 presents the 3D CAD model in the design modeler workspace.

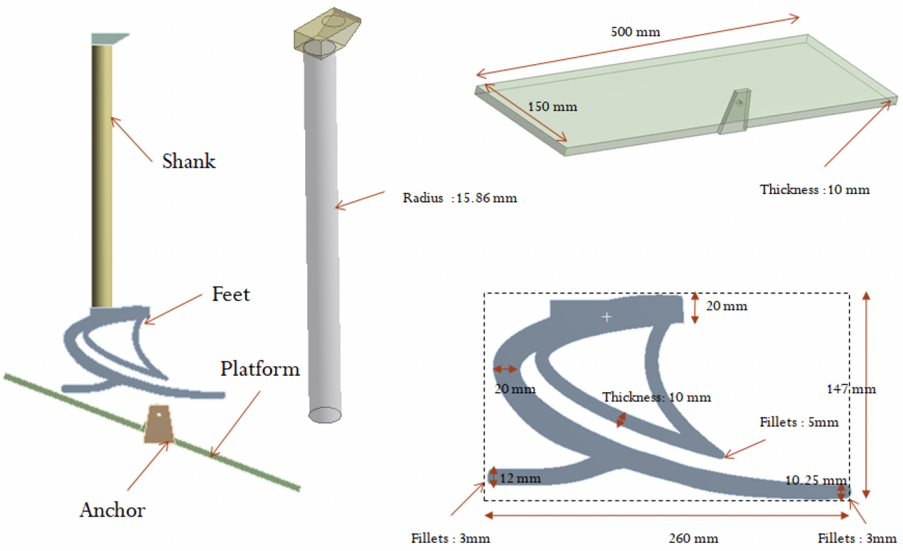


Figure 6.9: Case 1 CAD model

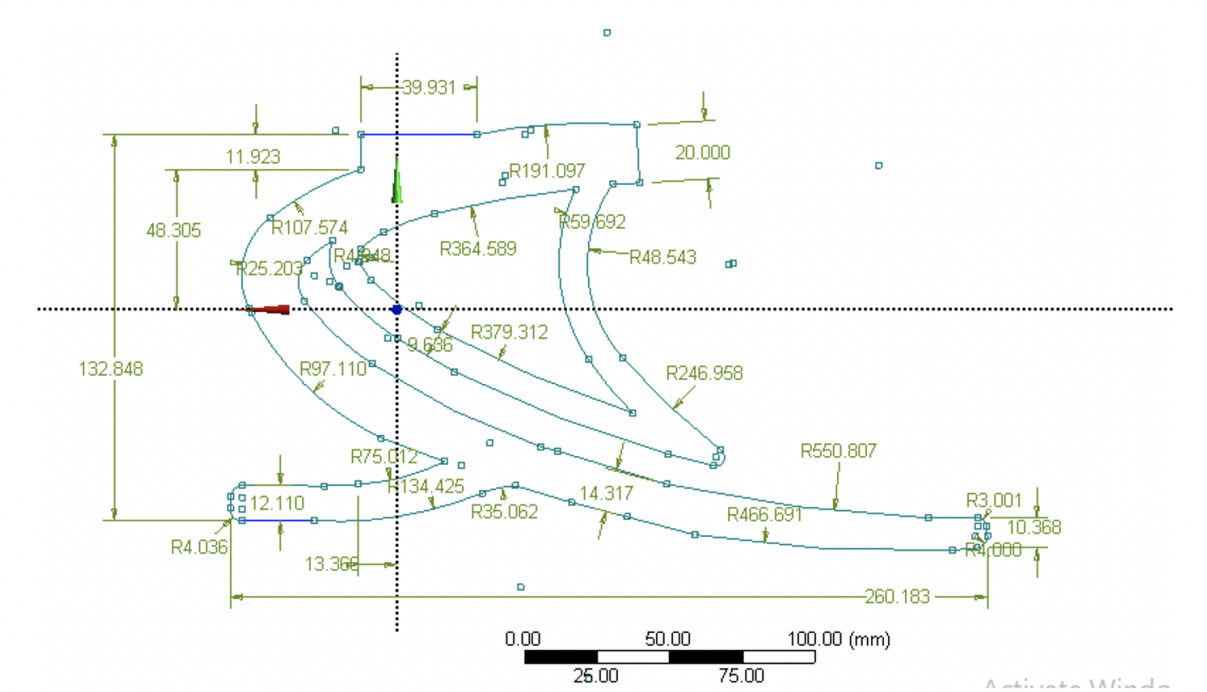


Figure 6.10: Case 1 CAD model dimensions

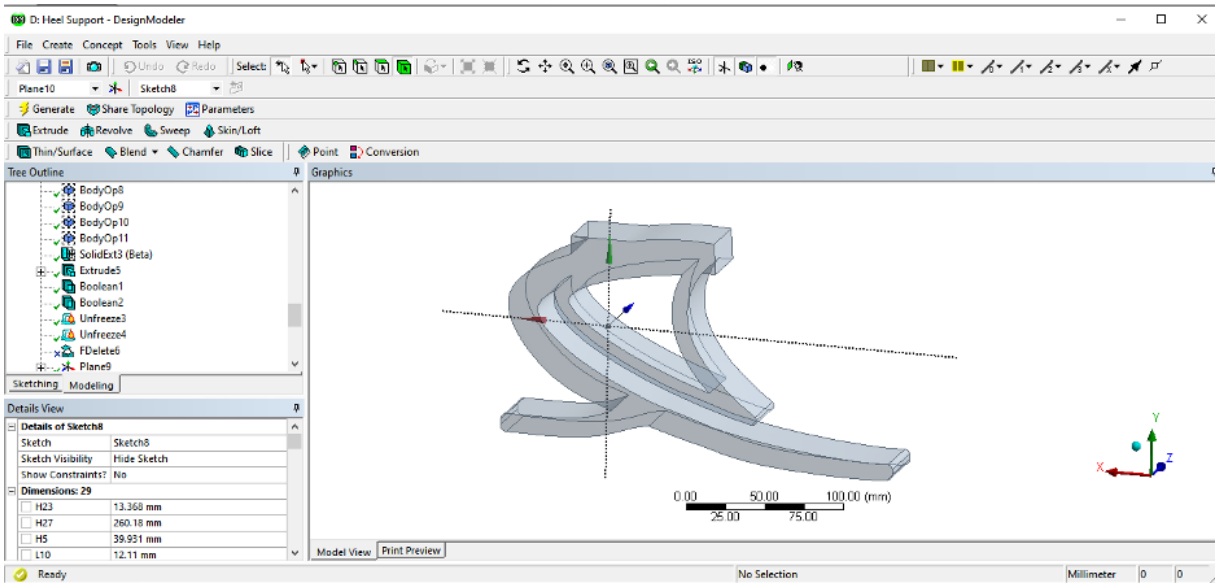


Figure 6.11: 3D Geometry

**Mesh Generation and Boundary Conditions**

In FEA simulation studies, it is important to have consistent mesh for the design experiment. Hence, the mesh setting and/or sizing employed are the same as those used for the C-shaped model in Chapter Five. The previously performed independent mesh study used the same simulation setup for all FEA studies.

Table 6.2: Node and element count for Case 1

| | **Foot Mesh** |
|---|---|
| **Node Count** | 22378 |
| **Element Count** | 13536 |

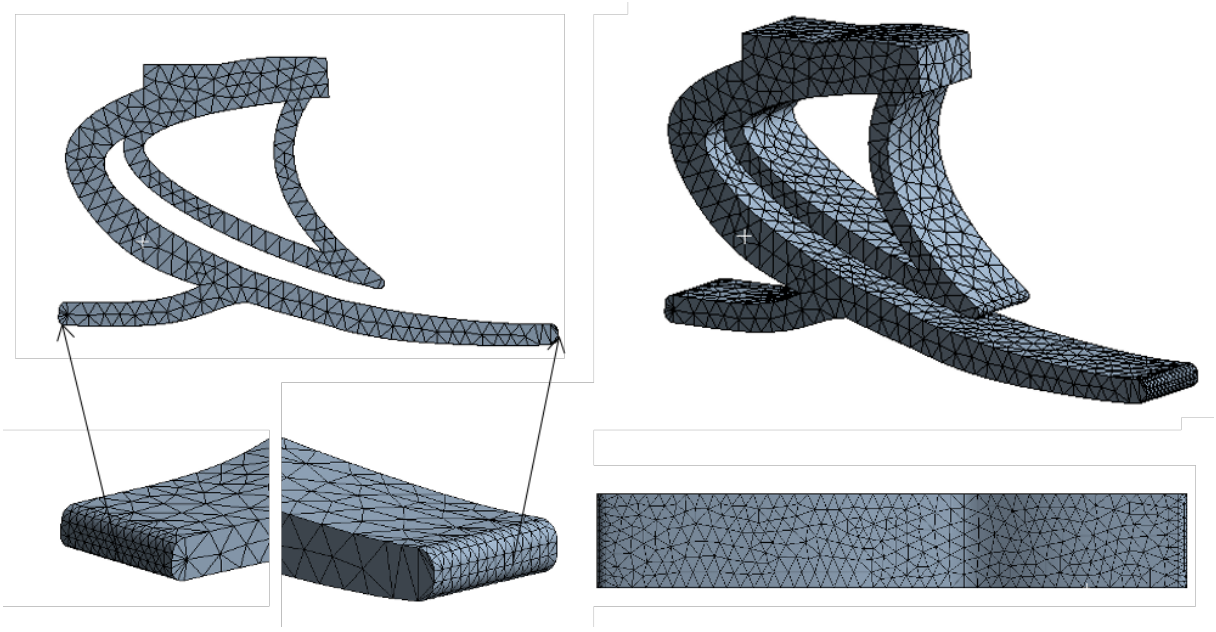

Figure 6.12: Foot mesh for Case 1

**Simulation Results**

This simulation was for the double-keel (DK) foot. The design was tested using the same material properties as for the C-shaped foot (see Table 5.10) in order to accurately observe the results of adding the secondary keel. The leg stiffness was calculated by dividing the vertical GRFs by the net deflection, as shown in Figure 6.13. A forefoot average leg stiffness of $20.4 kN/m$ was observed in the FEA simulation of the DK case, as shown in Figure 6.14. The average leg stiffness had only a small impact on the forefoot due to the new DK design. However, the ROS for the new design was reduced to $0.38m$. Most importantly, the DK design reduced foot stresses by 20% (to $70.3MPa$) compared to the C-shaped foot. The DK design benefitted from a reduction in stress, as shown in Figures 6.15 and 6.16; this will help increase the life of the foot, since maximum stress has been reduced significantly.

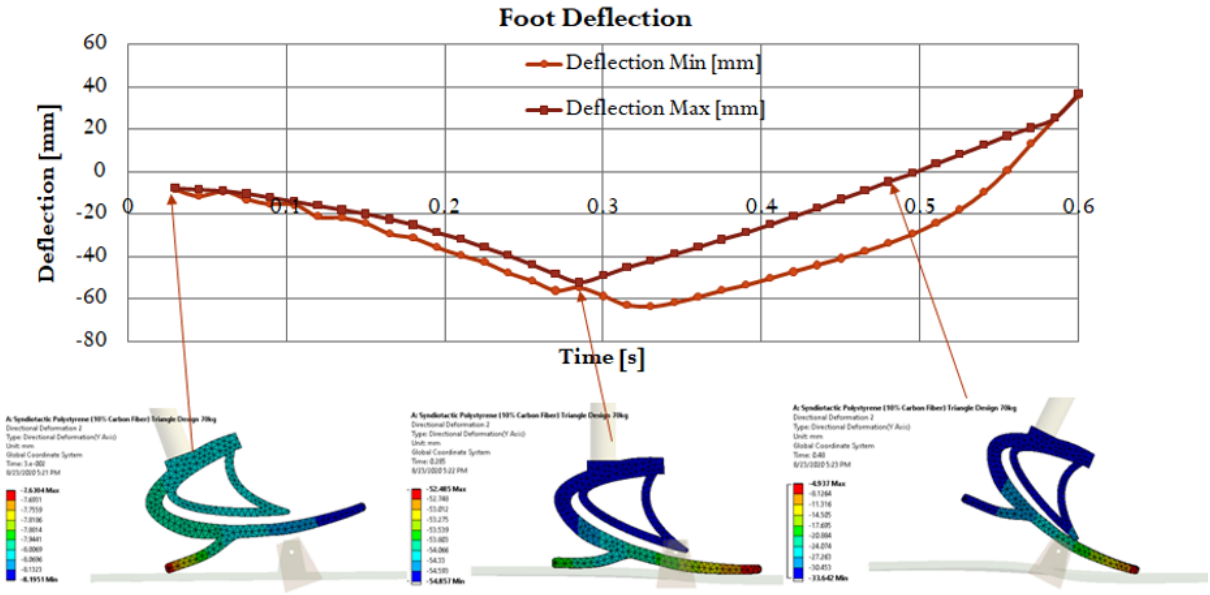


Figure 6.13: Deflection in foot for DK

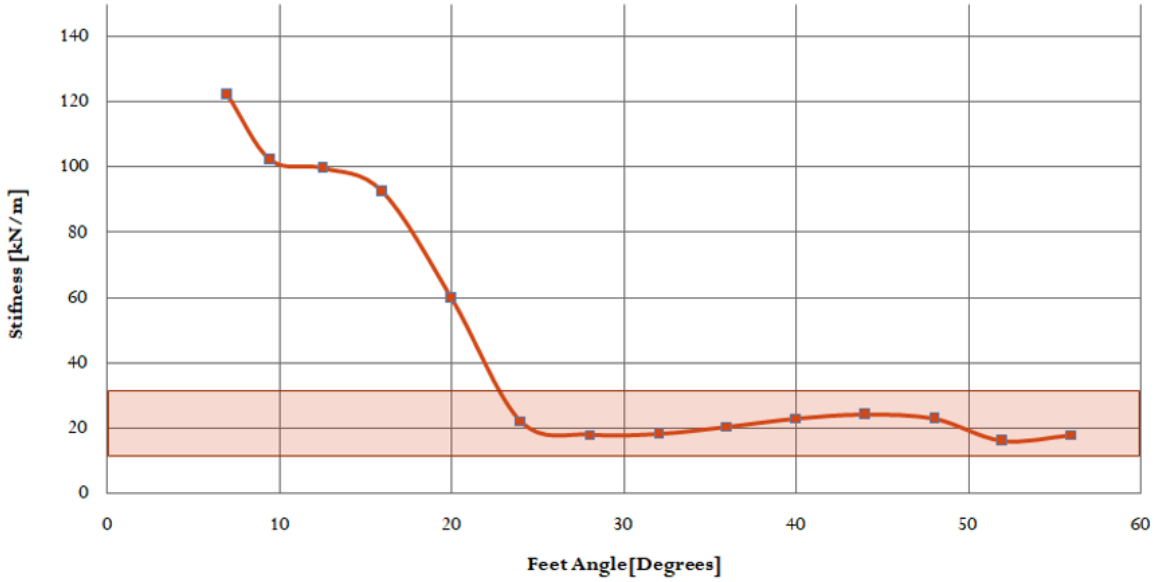


Figure 6.14: Leg stiffness for Case 1

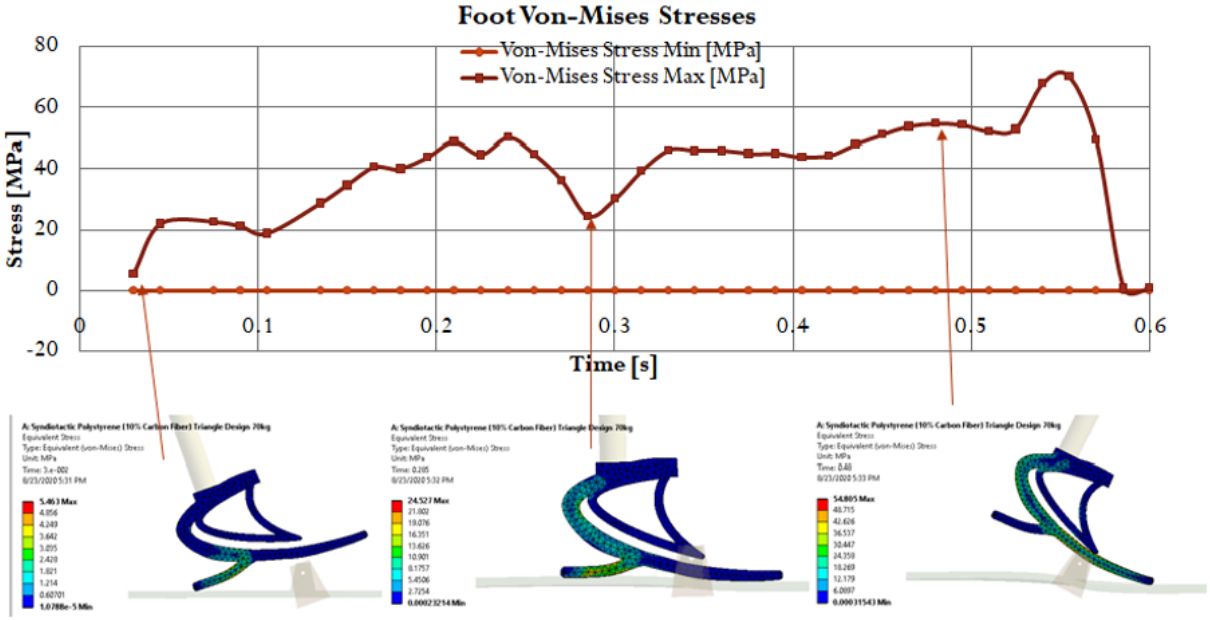


Figure 6.15: von-Mises stress in DK

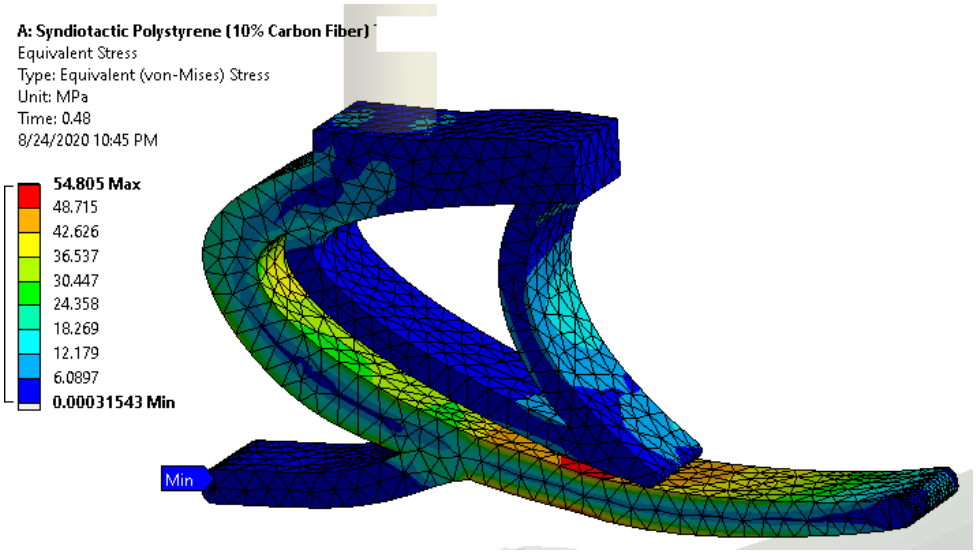


Figure 6.16: Isometric view of von-Mises stresses at 0.48s for Case 1

As discussed in the previous chapter, the calculation of ROS is based on the following:

- APDL script implemented in the ANSYS workbench to extract the COP data in the simulation (see Appendix D).

- Creating the best fit circular radius in the ROS curve, as shown in Figure 6.17 below.

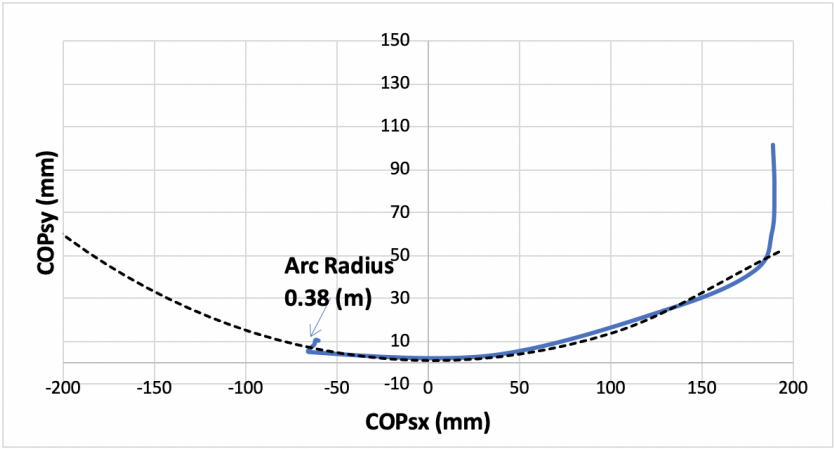


Figure 6.17: Foot ROS of Case 1

From the current model, it can be seen that the results did not satisfy the ROS value and/or the model objectives. As a result, another model will be developed to improve the design further.

The model employed resulted in a ROS value of $0.38m$, which is not sufficiently close to the desired ROS value of $0.41m$ discussed in the previous chapter.

### 6.4.2 Case Study 2 - Polycarbonate

In the present design iteration, the material properties of the foot are changed from the syndiotactic polystyrene (10% carbon fibre) used in Case 1 to polycarbonate.

#### CAD Modelling, Mesh Generation and Boundary Conditions

The CAD model, mesh and boundary conditions for the present study are the same as those described in the previous section, except for the material properties of the foot, which were changed to polycarbonate [158] as shown in Table 6.1.

#### Simulation Results

Figure 6.18 illustrates the deflection for calculating leg stiffness. When the leg stiffness increased, the ROS was almost flat; therefore, the ROS value increased as well [32]. Results from the FEA simulation further indicated an average forefoot leg stiffness of 30.2 kN/m and ROS of 0.5m, as shown in Figures 6.19 and 6.22 respectively. Moreover, the prosthetic foot stresses increased to 90 MPa (see Figures 6.20 and 6.21), which is a side effect of changing the materials used in the prosthetic foot design.

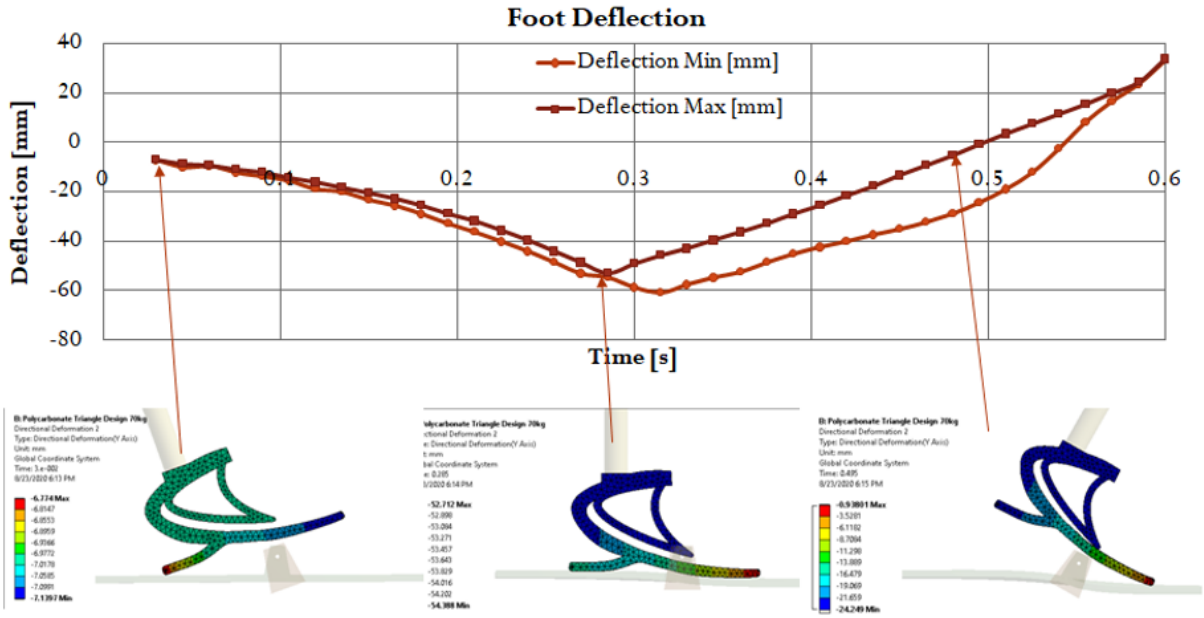


Figure 6.18: Foot deflection in Case 2

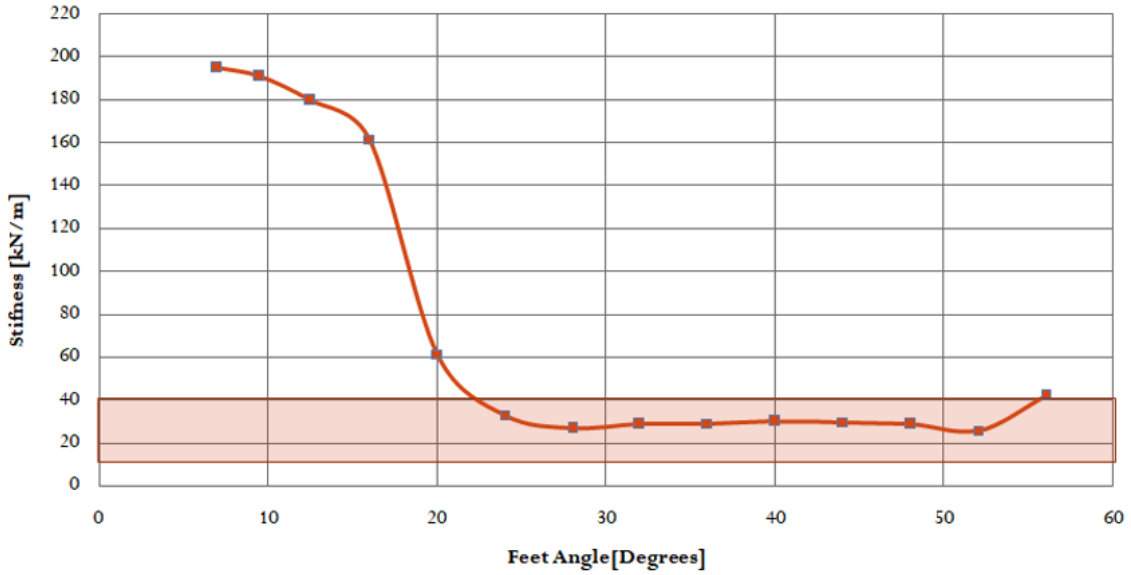


Figure 6.19: Leg stiffness values for Case 2

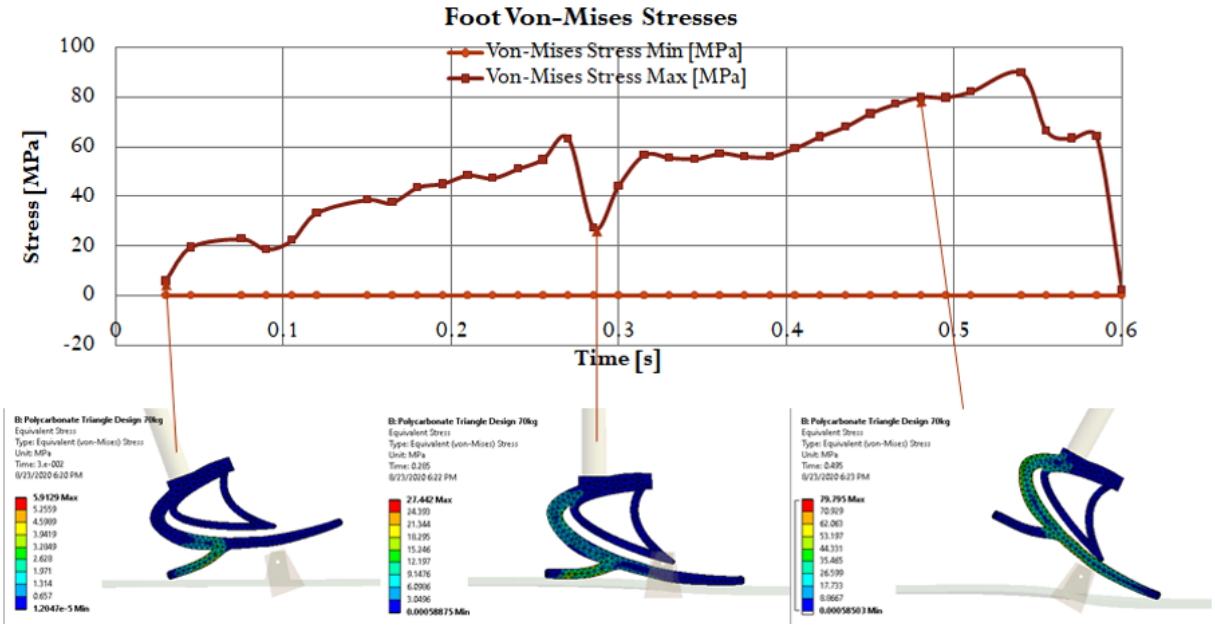


Figure 6.20: von-Mises stresses in Case 2

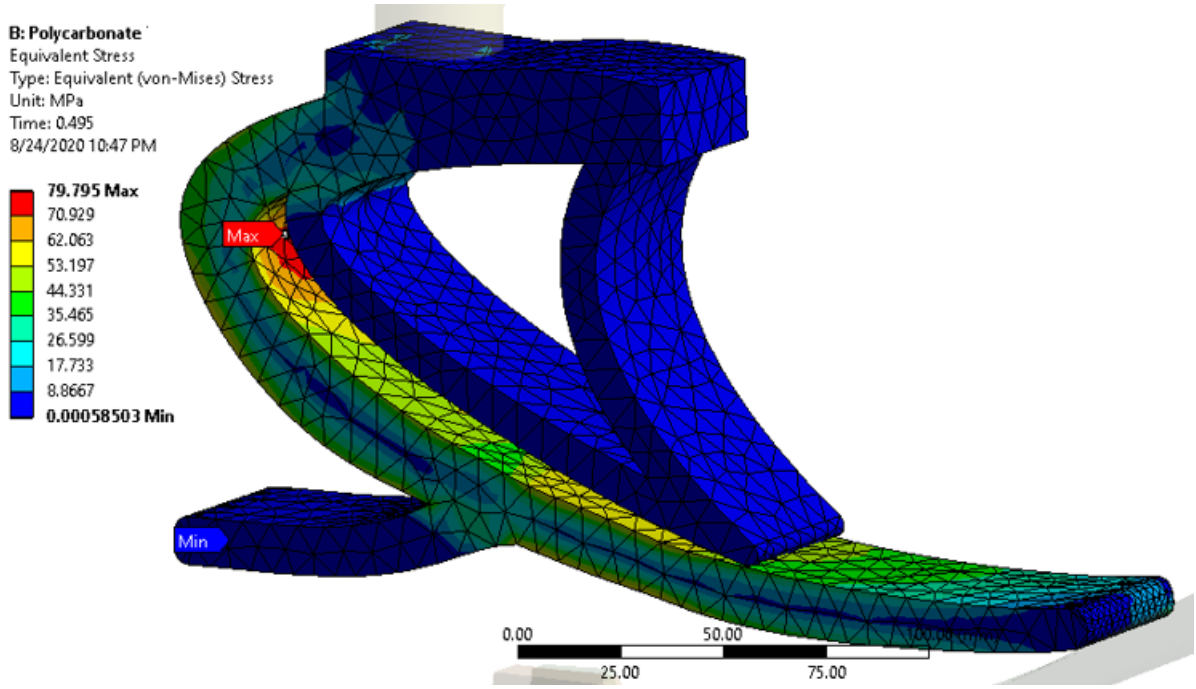


Figure 6.21: Isometric view of von-Mises stresses at 0.48s for Case 2

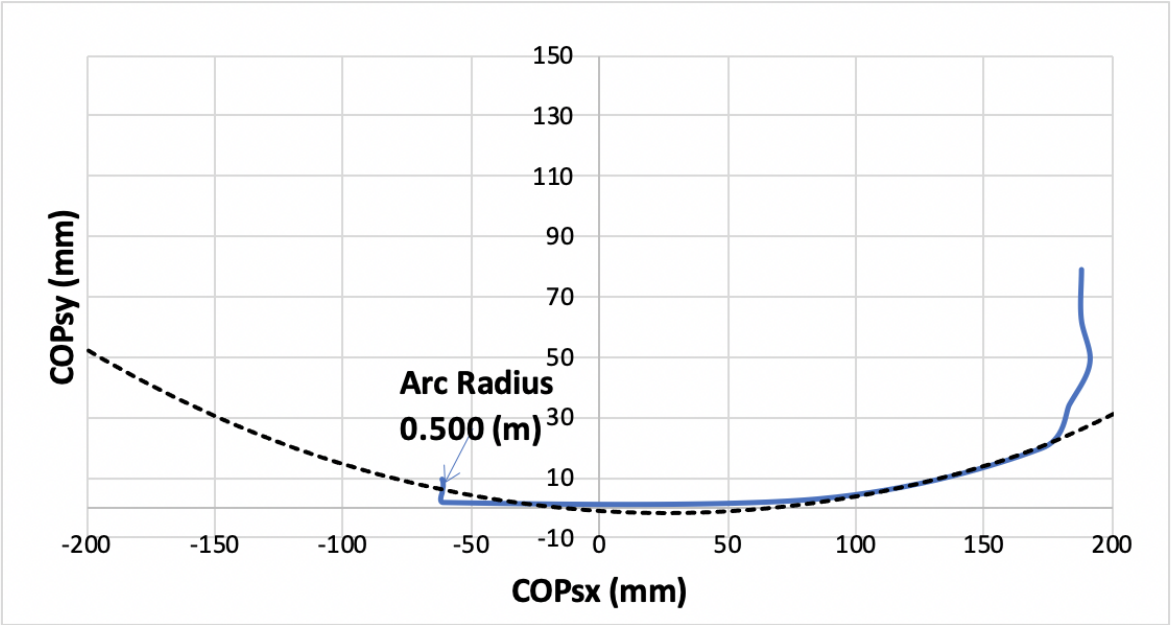


Figure 6.22: Foot ROS for Case 2

As can be seen from these results, the corresponding ROS of the model is about $0.5m$, which is much higher than the desired value of $0.41m$. This increase occurred due to the high stiffness value used in the current model, which increased the effects of ROS for the prosthetic foot. Accordingly, these results reveal that when the material is changed to polycarbonate, the ROS and leg stiffness values also increase.

### 6.4.3 Case Study 3 - Modified Polycarbonate Model

In the previous section (Case 2), when the material was changed to polycarbonate; the average forefoot leg stiffness, stress, and ROS also changed. The ROS value increased to $0.5m$, which differs from the desired ROS. Accordingly, to reduce the ROS, a reduction in the thickness of the primary keel's base will be tested. In the current case, a $3mm$ thickness reduction was chosen and tested. Figure 6.23 presents both the overall design and the thickness reduction.

### CAD Modelling

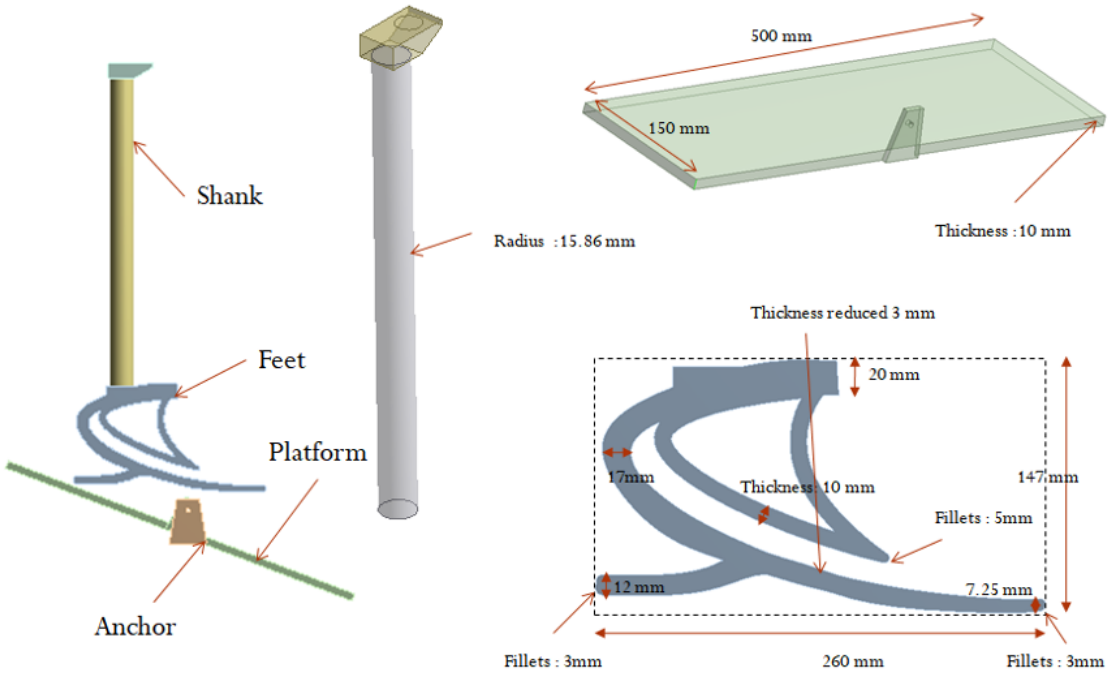


Figure 6.23: Case 3 CAD model and dimensions

### Mesh Generation and Boundary Conditions

In the current simulation, the medium mesh was used (see Table 6.3 and Figure 6.24). The simulation setup for the FEA studies is the same as described earlier in this chapter.

Table 6.3: Node and element count for Case 3

| | **Foot Mesh** |
|---|---|
| **Node Count** | 22298 |
| **Element Count** | 13126 |

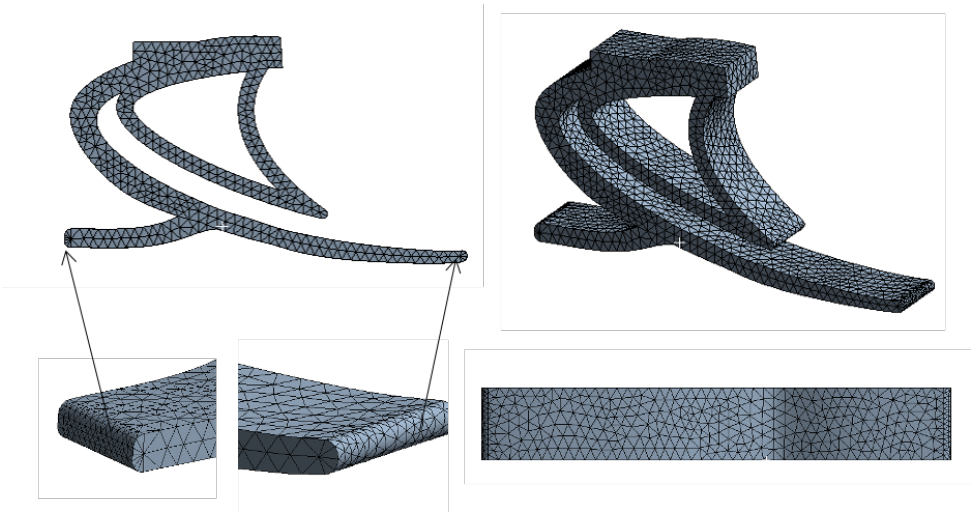

Figure 6.24: Foot mesh for Case 3

### Simulation Results

The FEA simulation yielded leg stiffness of $20.1 kN/m$ and ROS of $0.415m$, as seen in Figures 6.26 and 6.29, respectively. While the ROS was close to the optimised design, the stress increased to $97 MPa$ (see Figures 6.27 and 6.28). The DK design had the advantage of reducing stress and improving the ability to vary stiffness.

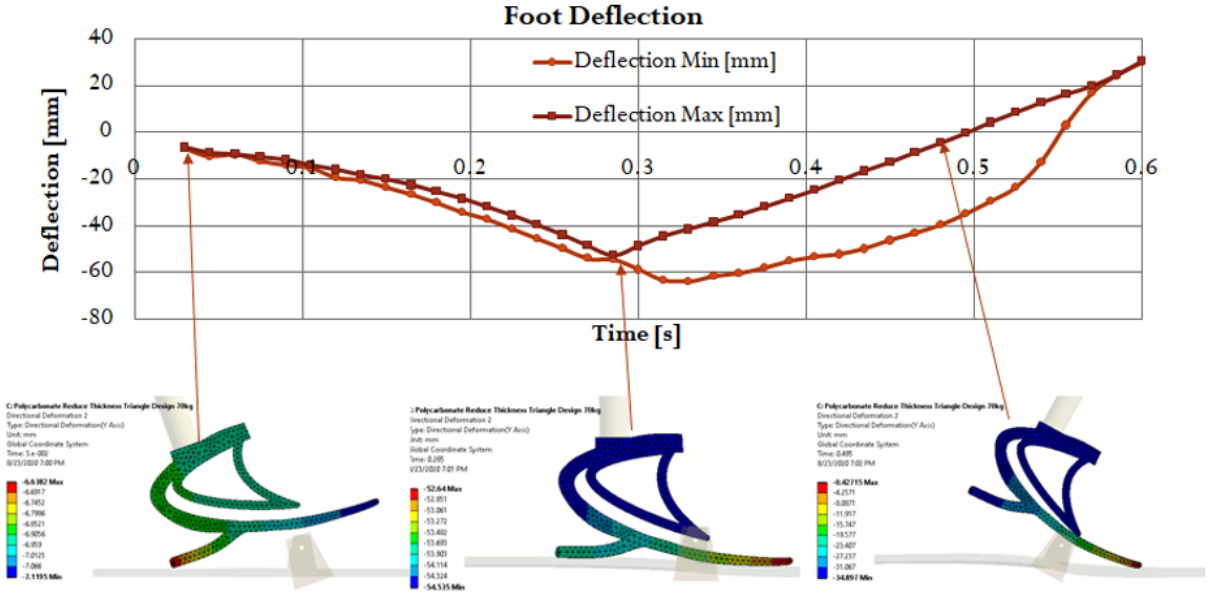


Figure 6.25: Deflection in foot for Case 3

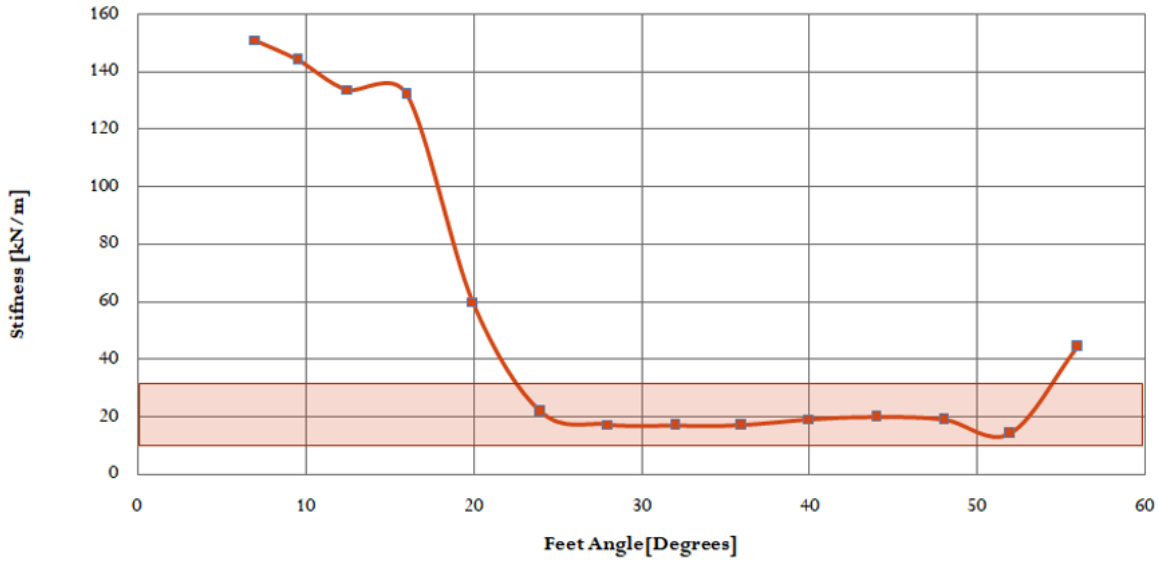


Figure 6.26: Leg stiffness for Case 3

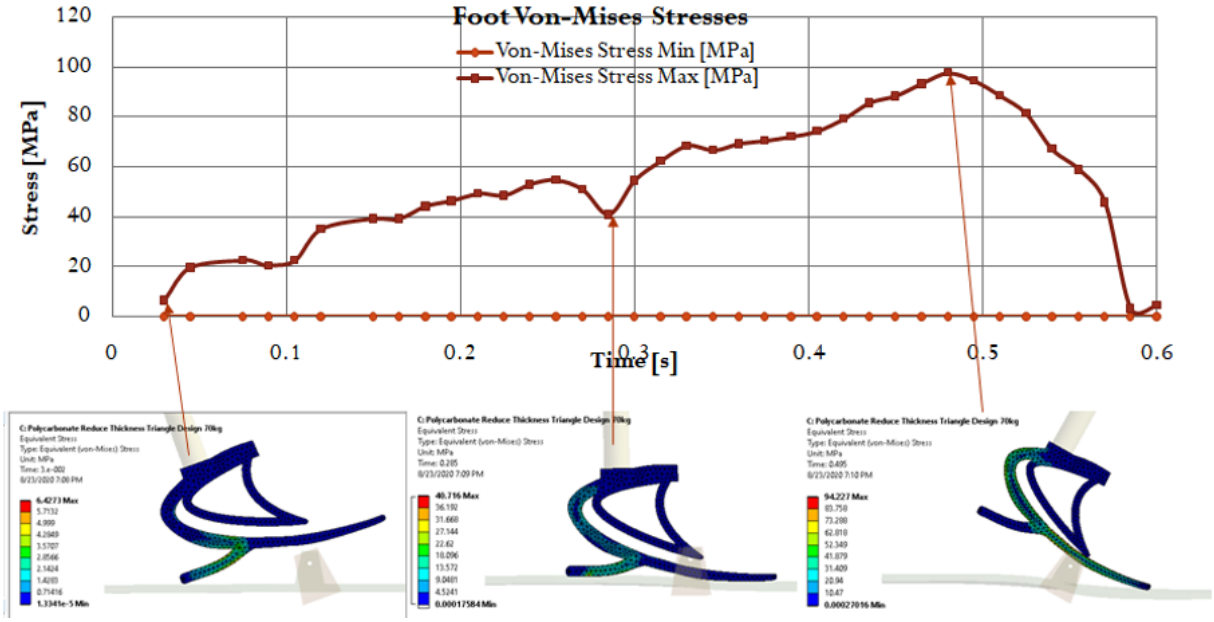


Figure 6.27: von-Mises stresses in foot for Case 3

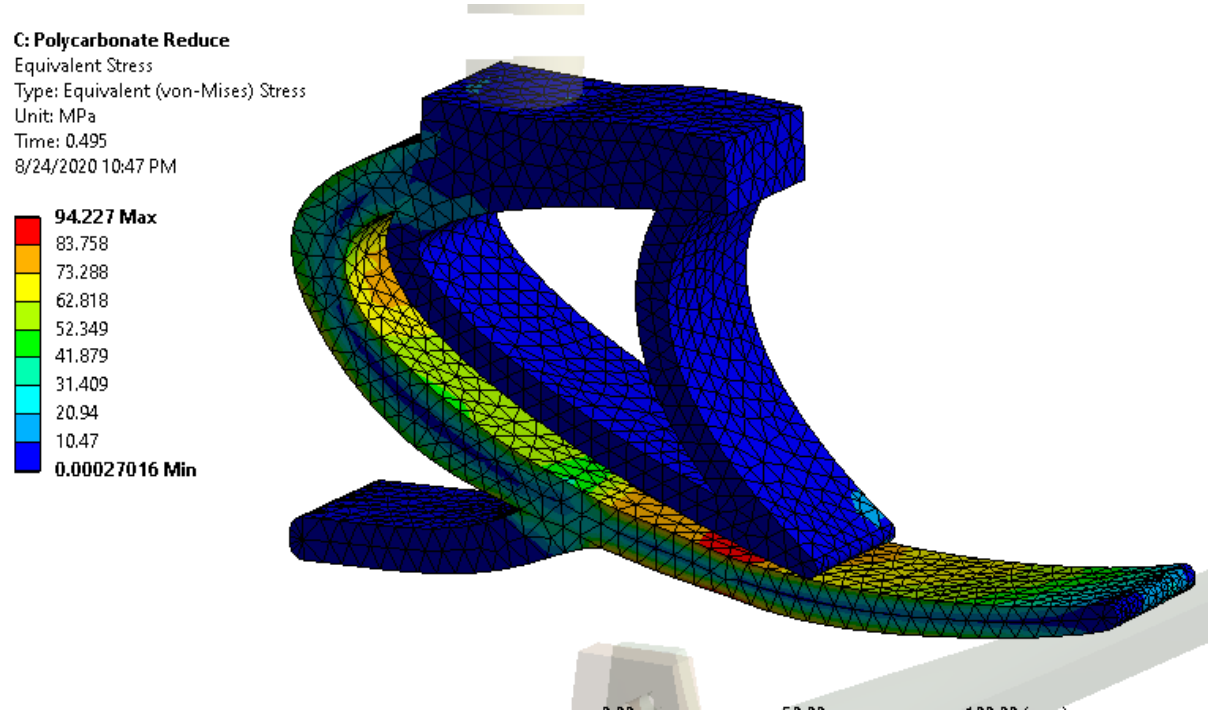


Figure 6.28: Isometric view of von-Mises stresses at 0.48s for Case 3

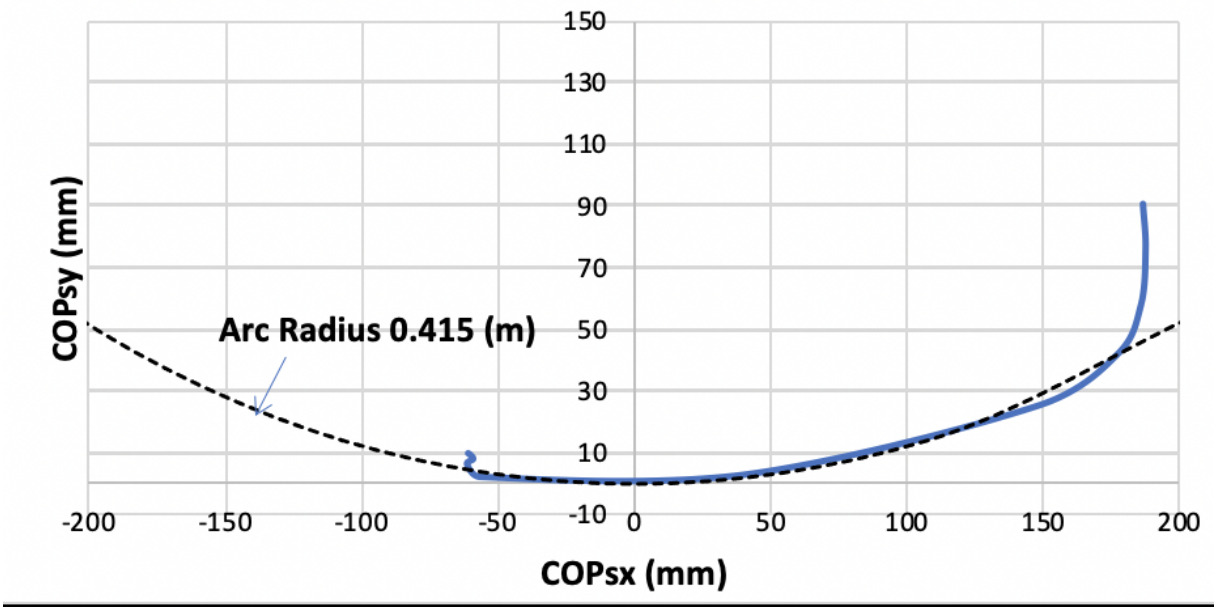


Figure 6.29: Foot ROS for Case 3

The average forefoot leg stiffness from this design was reduced to $20.1 kN/m$, while the ROS recorded is $0.415m$, which is similar to the values in the loosely coupled hypothesis. The

reduced average forefoot leg stiffness is a promising sign, since decreasing the forefoot stiffness will increase the push-off in the prosthetic limb [100]. The amount of energy expended is influenced by the stiffness of the prosthetic: a stiffer hindfoot results in lower values of energy returned, while a softer hindfoot leads to an increase in the returned energy [100]. The following flowchart summarises the choice of the optimal DK design (see Figure 6.30).

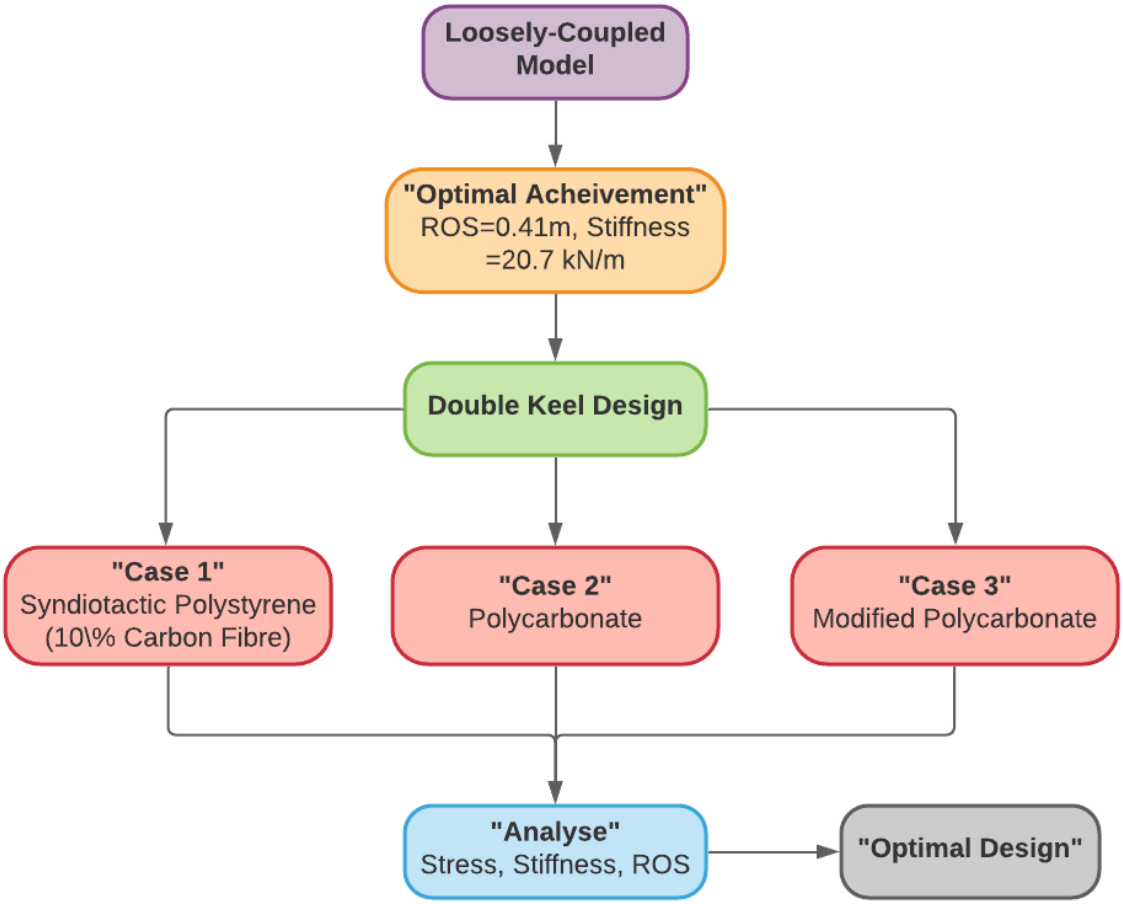


Figure 6.30: The optimal DK design process

## 6.5 Results and Discussion

Table 6.4: Case studies summary; the desired ROS is $0.41m$.

| **Cases** | **C-Shaped Prosthetic Foot** | **Case Study 1** | **Case Study 2** | **Case Study 3** |
|---|---|---|---|---|
| **Material** | Syndiotactic Polystyrene (10% Carbon Fibre) | | Polycarbonate | |
| **Stress (MPa)** | 90 | 70.3 | 90 | 97 |
| **Achieved Stiffness (kN/m)** | - | 20.4 | 30.2 | **20.1** |
| **Achieved ROS (m)** | - | 0.38 | 0.5 | **0.415** |

The ROS from the FEA modelling was $0.415m$, which was closer to the desired value of $0.41m$ obtained in chapter five from the loosely coupled hypothesis. The results from the design were affected by the type of material used in the manufacture of the prosthesis. The study showed that changing from carbon fibre to polycarbonate will improve energy optimisation in prosthetic feet. In addition, the study also achieved forefront stiffness, even though it was reduced to $20.1kN/m$ in this design. The lower energy expenditure will reduce ULs among lower limb amputees. Table 6.4 summarises the results of all case studies.

Table 6.5 and Figure 6.31 present the difference between the proposed DK model and the Mecuris [28] prosthetic foot.

Table 6.5: Prosthetic foot design comparison between Mecuris [66] and Swansea.

| **Mecuris Prosthetic Foot** | **Swansea Prosthetic Foot** |
|---|---|
| Utilises direct force transfer (red arrow). | Utilises in-direct force transfer (red arrow). |
| Removes sections of the foot and adjusts thickness to optimise for patients. | Adjusts curve geometry and thickness to optimise for patients. |
| Main spring deforms over the heel to store energy from heel strike to release at toe-off (blue arrow). | Main spring deforms over the mid-foot to store energy from heel strike to release at toe-off (blue arrow). |
| Utilises a pair of parallel main springs. | Utilises a single main spring. |

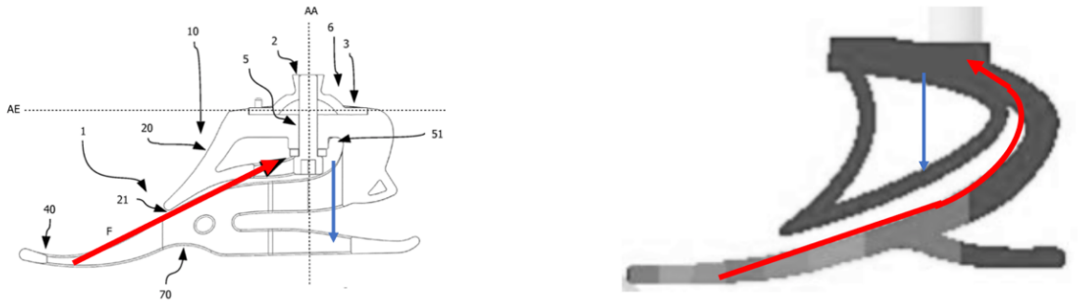


Figure 6.31: The Mecuris [28] transtibial prosthetic foot designs, highlighting the methods used to create push-off power and customisability. This is based on the design 3 concept in Figure 3.12c.

**Design Enhancement**

In running conditions, a higher single peak is observed in the GRF plot. As a result, the heel will experience higher forces and stresses. Further investigations are thus required to estimate the stresses that develop in heel strikes under running conditions. Hence, it is proposed to use an additional heel support, which can support the heel in cases of higher loads such as running speed. The schematic design enhancement is shown in Figure 6.32.

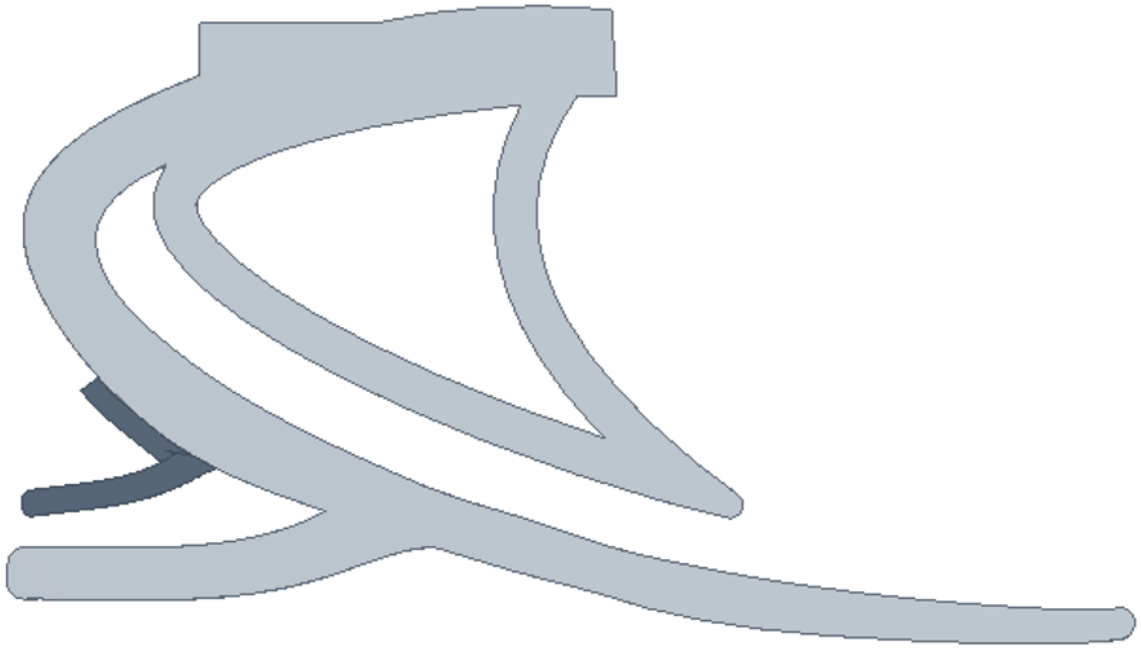

Figure 6.32: Design improvement of Double heel - Double-keel

# Chapter 7

# Conclusion and Future Work

## 7.1 Main Contributions and Conclusion

The prosthetic parts industry has grown and developed over the years due to a worldwide increase in the number of amputees. Amputees usually suffer due to their use of prosthetics, especially artificial feet, which can be uncomfortable and often cause joint pain. This thesis has discussed the way to design comfortable prosthetic feet and find the optimal values for the important parameters that can be used for this purpose. A number of studies regarding prosthetic feet were discussed in the introduction chapter in order to demonstrate the importance of this problem and the objective of the thesis. The aim of this study is to analyse the variation in GRFs during walking at different walking speeds, in addition to calculating the UL that results due to use of the prosthetic foot. Another objective was to use both PWD and FEM models to find the optimal stiffness and ROS values to be used in the model. This yielded an optimal prosthetic foot design that minimises both UL and pain during walking. To analyse the problem, it was first necessary to understand the GRF patterns in healthy people's walking activities. This was done by performing an experiment with six participants, all with different measurements, and

then analysing the results.

The work presented in this thesis contributes to the current research in the field of biomechanics by developing a new data-driven design and related algorithms. A summary of the main contributions of this work concerning the original research objectives is provided in the next paragraphs (see Figure 7.1).

**Objective 1: Develop a model to quantify Unhealthy Loads in order to minimise its value with a parametrised description of ground reaction force (GRF) curves for the healthy population and amputees at a given walking speed.**

Multiple researchers [15, 32, 100, 120] have discussed ways of supporting prosthetic foot enhancement data. These studies helped in developing the parametrised GRF equations found in Chapter Four. The most important results extracted from the experiment were the average walking speed and the corresponding $G_r$ of this speed; this helped with calculating $V_r$ for the next step, which is developing equations. Previous research [15, 32, 100, 120] has showed GRF patterns for different walking speeds, such as Very Slow, Slow, Free, Fast, and Very Fast, using experiments and results analysis. However, in this thesis, Web-Plot-Digitizer v3.5 [145] was used to produce these graphs and analyse the data. Equations for each walking speed range were then established. The author decided that GRF graph characteristics were a more accurate way of defining the ranges and selected the corresponding equation for the FWS for participants in the experiment. It was further proposed that FWS, along with the classification of walking speeds into categories such as Slow, Free and Fast walking for an individual, be estimated by measuring the individual's velocity and the corresponding GRF value curve in a gait lab, along with the proposed set of equations. In addition, UL function was quantified and used further in this thesis.

**Objective 2: Develop a methodology to transfer information associated with walking speed and stiffness values among measurements from experiments, walking dynamics models and FEM-based simulation results.**

The next step was to implement an optimised forefoot stiffness value and ROS by using a loosely coupled passive walker dynamic and FEM-based model. The PWD model was compared to other models [120] to demonstrate the robustness of the design. The model with damper [120] exhibited slightly better ability to predict the second peak of the healthy GRF curve. However, the proposed method generated a reduction ratio '$f$' in order to overcome this problem. At the end of this coupling, the stiffness response of the foot was designed to produce a ROS that minimises unhealthy joint loads. Although the leg stiffness value is embedded inside the GRF patterns, the velocity ratio and the GRF pattern are utilised to transfer the leg stiffness information.

**Objective 3: Develop a coupled walking-dynamics and finite-element-based approach with sufficient complexity to reduce Unhealthy Loads, while retaining the necessary simplicity of models so that they can still be used for the stability analysis.**

A 3D-printable design was introduced to ascertain the stiffness variability information for the stability analysis. The design was tested using FEA to determine the structural ability of the prosthetic foot. Because polycarbonate material is widely used in 3D printing, this material was tested for the prosthetic foot design and also compared with other materials. By the end of the analysis, an optimal design was achieved that met the thesis objective while still retaining the required model simplicity, meaning that the proposed loosely coupled approach could still be used to study the stability region, as suggested by Ruina [30, 31].

**Objective 4: Undertake computational verification of the results from the proposed models when compared to the published state-of-the-art research outputs.**

The proposed parametrised vGRF equation (Equation 4.4, Section 4.4.2, Chapter Four) is based on results compiled from a large number of published papers and has been verified by measuring vGRF data for a group of candidates during an experimental trial in the gait lab (Chapter Four, Section 4.3.4). The results obtained from the ROS calculations (Section 5.4.6), finite element simulation (Section 5.4) and passive dynamics walking models (Section 5.5, Figure 5.7a and Appendix G) [120] were compared with those from published literature.

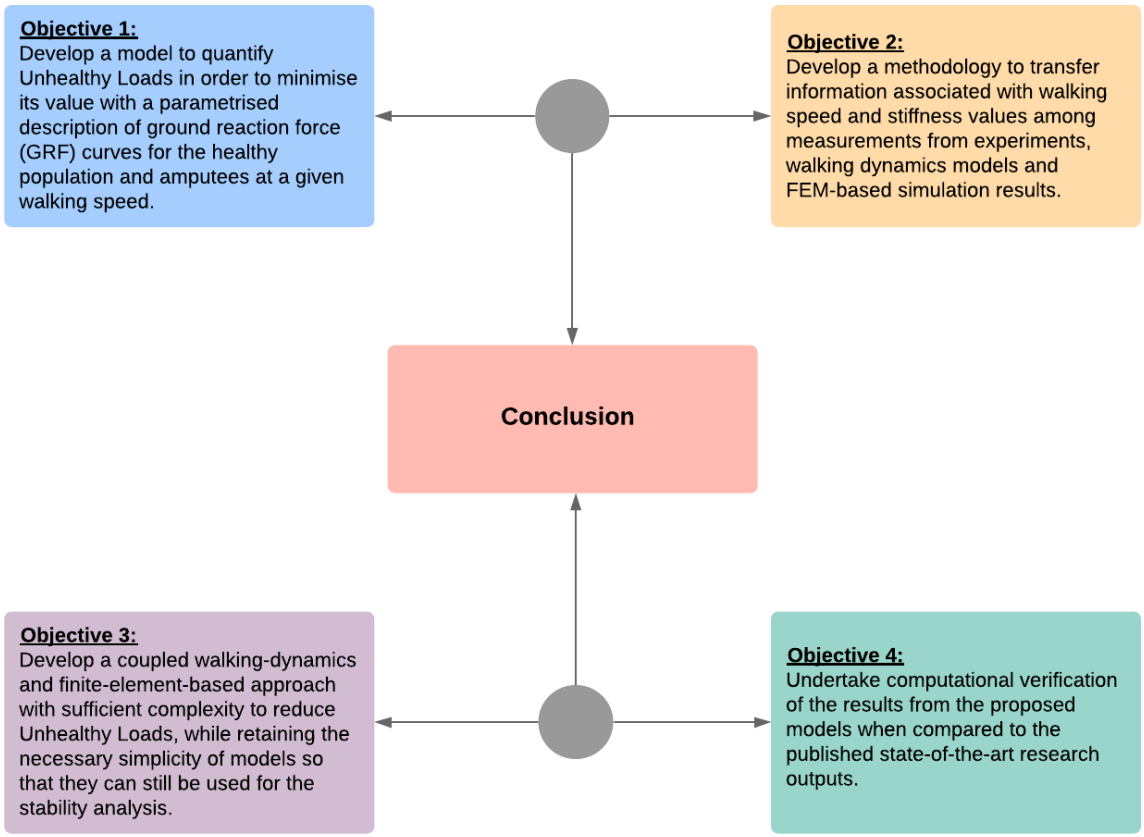


Figure 7.1: Thesis main contribution

## 7.2 Limitations and Future Work

A computational framework is provided in this thesis. A comprehensive experimentation program is necessary to establish the validity of the approach, particularly the use of the concept of optimal ROSs to reduce ULs. The computational models (PWD and FEM) proposed in this thesis are based on linear elastic deformation assumptions. The current PWD model is also limited in its ability to provide stable solutions over a narrow range of walking speeds as determined by the stability regions (Figure F-3 in Appendix F). There is limited published data in the literature on GRFs for amputees at various walking speeds; this may have constrained the proposed GRF estimation equation's ability to relate magnitudes of GRF peaks with walking speeds. Moreover, the foot material proposed in Chapter Six is polycarbonate. It is noted that this material choice may not be well suited for field trials. In addition, while the computational framework is limited to linear assumptions, this approach can be refined in the proposed future work outlined below. This approach also has another benefit, namely that it is extendable to transfemoral as well as double amputees. Research efforts that could potentially extend the current work include the following:

1. Testing the proposed design on real case studies. This will require partnership with prosthetic foot manufacturers, ethics approval and new investment in the gait lab.

2. Enhancing the estimated GRF equations on additional cases, such as running, stair climbing, etc., and conducting new gait experiments to create more evidence that can be used to test the hypothesis that the walking speed categories (Very Slow, Slow, Free, Fast and Very Fast) are based on $G_r$ curves rather than walking velocity.

3. Using the experience gained in point 1 to enhance the current PWD model to active model and embed Ruina's approach [30, 31] to study gait stability regions in order to reduce the

chances of falling, as well as designing actuators to minimise the energy consumption of active feet.

4. Applying other materials that might enhance the double-keel foot design; for example, exploring the use of nature-inspired, ultralight polymer-based structures [27] with carbon fibre reinforcements (see Figure 7.2) on stress lines along with the approach proposed in this thesis to design the next generation of patient-specific prosthetic feet.

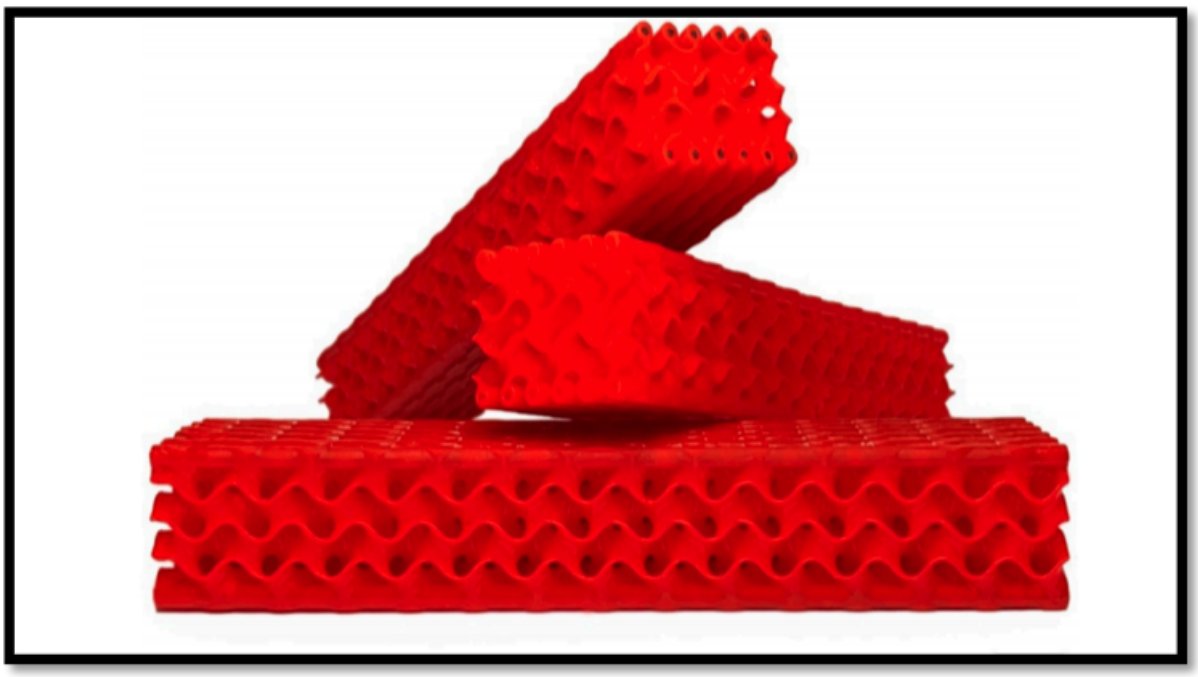

Figure 7.2: Ultralight polymer-based structures with carbon fibre reinforcements [27].

# Bibliography

[1] M. Whittle. Gait analysis an introduction. *Second edition. Oxford, England: Reed Educational and Professional Publishing Ltd*, page 1–20, 1996.

[2] J. Glyde. Upper and lower limb amputations and limb absence. *NHS NSS - NHS Group*, 2014.

[3] F. Davie-Smith, J. Heberton, and H. Scott. A survey of the lower limb amputee population in scotland - full report. *Scottish Physiotherapy Amputee Research Group*, 2015.

[4] S. Whelan. Preventing amputations major concern as diabetes numbers rise. *Press release - Public Health England*, 2019.

[5] P. W. Moxey, D. Hofman, R. J. Hinchliffe, K. Jones, M. M. Thompson, and P. J. Holt. Epidemiological study of lower limb amputation in england between 2003 and 2008. *British Journal of Surgery Society Ltd*, 97:1348–1353, 2010.

[6] L. Donnelly. Record numbers of amputations on nhs amid warnings 1 in 10 will soon suffer type two diabetes. *The Telegraph*, 2019.

[7] P. Russell. 26,378 diabetes-related lower limb amputations in the last three years. *Diabetes UK*, 2018.

[8] I. Singh. Functional asymmetry in the lower limbs. *Cells Tissues Organs*, 77(1):131–8, 1970.

[9] A. Pranav, F. Bhounsule, and A. Zamani. Control based on passive dynamic walking. *Journal of Biomechanics*, 51:123–127, 2017.

[10] J. J. Genin, G. J. Bastien, B. Franck, C. Detrembleur, and P. A. Willems. Effect of speed on the energy cost of walking in unilateral traumatic lower limb amputees. *Eur J Appl Physiol*, 103:655–663, 2008.

[11] E. A. Hedrick, S. J. Stanhope, and K. Z. Takahashi. The foot and ankle structures reveal emergent properties analogous to passive springs during human walking. *An emergent property of the foot and ankle strctures*, 14(6), 2019.

[12] B. M. Thirunindravur, S. Natarajan, and S. Srinivasan. Roll-over shape of a prosthetic foot: a finite element evaluation and experimental validation. *Medical and Biological Engineering and Computing*, pages 1 – 12, 2020.

[13] K. Henry. Amputee patient comfort and compliance. *The O&P EDGE and The Amputee Coalition*, 21(5):1–5, 2011.

[14] S. Park, H. Park, and J. Park. Effect of heel base area and walking speed on the utilized coefficient of friction during high-heeled walking. *Work*, 64:1–9, 09 2019.

[15] W. G. Charles. Dynamic walking models to understand asymmetric gait characteristics. *Swansea University*, 2018.

[16] R. Sheehan, E. Beltran, J. Dingwell, and J. Wilken. Mediolateral angular momentum changes in persons with amputation during perturbed walking. *Gait & Posture*, 41, 02 2015.

[17] A. Silverman and R. Neptune. Differences in whole-body angular momentum between below-knee amputees and non-amputees across walking speeds. *Journal of biomechanics*, 44:379–85, 11 2010.

[18] M. J. Burke, V. Roman, and V. Wright. Bone and joint changes in lower limb amputees. *Annals of the Rheumatic Diseases*, 37(3):252–254, 1978.

[19] Jaipurfoot. Get below knee prosthesis freely? *Jaipur website https://www.jaipurfoot.org/what-we-do/prosthesis/belowkneeprosthesis.html*, 2020.

[20] MIT Media Lab Group. Biomechatronics overview. *Biomechatronic Journal https://www.media.mit.edu/groups/biomechatronics/overview/*, 2020.

[21] L. Childers and K. Takahashi. Increasing prosthetic foot energy return affects whole-body mechanics during walking on level ground and slopes. *Scientific Reports*, 8:5354, 03 2018.

[22] I. Kovac, V. Medved, and L. Ostojic. Ground reaction force analysis in traumatic transtibial amputees' gait. *Collegium antropologicum*, 33 Suppl 2:107–14, 12 2009.

[23] D. Childress. The shape and roll prosthetic foot for use in low-income countries. *Northwestern University Prosthetics-Orthotics Center:School of Medicine*, 2018.

[24] J. Jensen and S. Sexton. A report of the activities under the agreement provided by the united states agency for international development (usaid) to the international society for prosthetics and orthotics. *ISPO Appropriate Prosthetic and Orthotic Technologies in Low Income Countries*, 2010.

[25] T. Neubert and C. Weserland. Functional coating: Atmospheric pressure plasma treatment on 3d printed polymer surfaces. *Polymer Surfaces*

*Journal from https://www.weserland.eu/en/news-events/400-plasma-treatment-on-3d-printed-polymer-surfaces.html*, 2019.

[26] C. Ha, P. Prabhakaran, and Y. Son. 3d-printed polymer/metal hybrid microstructures with ultraprecision for 3d microcoils. 02 2019.

[27] M. Pelanconi and A. Ortona. Nature-inspired, ultra-lightweight structures with gyroid cores produced by additive manufacturing and reinforced by unidirectional carbon fiber ribs. *MDPI*, 12(24):1–14, 2019.

[28] Mecuris. You. create. the digitalization of prosthetics and orthotics. *https://www.mecuris.com/?lang=en*, 2018.

[29] F. Al-Shawwa. 3d printed prosthesis in the uae. *Immensa Additive Manufacturing from https://www.immensalabs.com/3d-printed-prosthesis-in-the-uae/*, 2018.

[30] A. Ruina. Passive dynamics is a good basis for robot design and control, not! *APS Meeting Abstracts*, 2017:X12.013, March 2017.

[31] P. Zaytsev, W. Wolfslag, and A. Ruina. The boundaries of walking stability: Viability and controllability of simple models. *IEEE Transactions on Robotics*, 34(2):336–352, 2018.

[32] P. Mahmoodi. Optimisation of bipedal walking motion with unbalanced masses. *Swansea University*, 2013.

[33] ISO 22675:2006. International organization for standardization, prosthetics-testing of ankle-foot devices and foot units- requirements and test methods. *International Organisation for Standardisation*, 2006.

[34] B. Morgan. Evolution of computational tools and experimental of passive prosthetic feet. *EngD thesis, Swansea University*, To be submitted, 2020.

[35] E. Shahabpoor and A. Pavic. Measurement of walking ground reactions in real-life environments: A systematic review of techniques and technologies. *Sensors*, 17:2085, 09 2017.

[36] E. Simonsen. Contributions to the understanding of gait control. *Danish medical journal*, 61:B4823, 04 2014.

[37] H. Sadeghi, P. Allard, F. Prince, and H. Labelle. Symmetry and limb dominance in able-bodied gait: A review. *Gait & posture*, 12:34–45, 10 2000.

[38] R. W. Selles, J. B. Bussmann, L. M. Klip, B. Speet, A. J. Van Soest, and H. J. Stam. Adaptations to mass perturbations in transtibial amputees: Kinetic or kinematic invariance? *Archives of Physical Medicine and Rehabilitation*, 85:2046–2052, 2004.

[39] A. Kuo and M. Donelan. Dynamic principles of gait and their clinical implications. *Physical therapy*, 90:157–74, 12 2009.

[40] H. Hong, S. Kim, C. Kim, S. Lee, and S. Park. Spring-like gait mechanics observed during walking in both young and older adults. *Journal of biomechanics*, 46, 11 2012.

[41] C. Tudor-Locke, W. Johnson, and P. Katzmarzyk. Accelerometer-determined steps per day in us children and youth. *Medicine and science in sports and exercise*, 42:2244–50, 12 2010.

[42] H. J. Ralston. Energy-speed relation and optimal speed during level walking. *Internationale Zeitschrift fur angewandte Physiologie einschließlich Arbeitsphysiologie*, 17(4):277–283, 1958.

[43] T. Stockel, R. Jacksteit, M. Behrens, R. Skripitz, R. Bader, and A. Mau-Moeller. The mental representation of the human gait in young and older adults. *Frontiers in Psychology*, 6:943, 06 2015.

[44] J. Perry and J. Burnfield. Gait analysis: Normal and pathological function. *Slack Incorporated*, 02 2010.

[45] British Standards Institution. 22675. Testing of ankle-foot devices and foot units—requirements and test methods. *London: BSI*, 2006.

[46] K. Clark, L. Ryan, and P. Weyand. A general relationship links gait mechanics and running ground reaction forces. *The Journal of experimental biology*, 220, 11 2016.

[47] R. Kram and A. Powell. A treadmill-mounted force platform. *Journal of Applied Physiology*, 67:1692–1698, 10 1989.

[48] A. Salah and T. Gevers. Computer analysis of human behavior. 01 2011.

[49] School of health and society. Clinical gait analysis service. *Manchester: University of Salford*, 2017.

[50] A. Muro, B. Zapirain, and A. Mendez-Zorrilla. Gait analysis methods: An overview of wearable and non-wearable systems, highlighting clinical applications. *Sensors (Basel, Switzerland)*, 14:3362–94, 02 2014.

[51] A. Barela, M. L. Celestino, M. Camargo, and J. Barela. Ground reaction forces during level ground walking with body weight unloading. *Revista Brasileira de Fisioterapia*, 18:572–579, 12 2014.

[52] N. Fey, G. Klute, and R. Neptune. Altering prosthetic foot stiffness influences foot and muscle function during below-knee amputee walking: A modeling and simulation analysis. *Journal of biomechanics*, 46, 01 2013.

[53] M. Donelan, R. Kram, and A. Kuo. Mechanical and metabolic determinants of the preferred step width in human walking. *Proceedings. Biological sciences - The Royal Society*, 268:1985–92, 11 2001.

[54] M. Shepherd, A. Azocar, M. Major, and E. Rouse. Amputee perception of prosthetic ankle stiffness during locomotion. *Journal of Neuro-Engineering and Rehabilitation*, 15, 12 2018.

[55] Iso 22523: External limb prostheses and external orthoses — requirements and test methods. *ISO Standards Publication*, pages 1–91, 2018.

[56] T. S. Keller, A. M. Weisberger, J. L. Ray, S. S. Hasan, R. G. Shiavi, and D. M. Spengler. Relationship between vertical ground reaction force and speed during walking, slow jogging, and running. *Clinical biomechanics*, 11(5):253–259, 1996.

[57] At. Hof, R. Bockel, T. Schoppen, and K. Postema. Control of lateral balance in walking. experimental findings in normal subjects and above-knee amputees. *Gait & posture*, 25:250–8, 03 2007.

[58] H. Sadeghi, P. Allard, and M. Duhaime. Functional gait asymmetry in ablebodied subjects. *Human Movement Science*, 16(2-3):243–258, 04 1997.

[59] W. Herzog, B. M. Nigg, L. J. Read, and E. Olsson. Asymmetries in ground reaction force patterns in normal human gait. *Medicine & Science in Sports & Exercise*, 21:110–114, 1989.

[60] N. Vanicek, S. Strike, L. Mcnaughton, and R. Polman. Gait patterns in transtibial amputee fallers vs. non-fallers: Biomechanical differences during level walking. *Gait & posture*, 29:415–20, 04 2009.

[61] W. C. Miller, A. B. Deathe, M. Speechley, and J. Koval. The influence of falling, fear of falling, and balance confidence on prosthetic mobility and social activity among individuals with a lower extremity amputation. *Archives of Physical Medicine and Rehabilitation*, 82(9):1238–1244, 2001.

[62] J. Kulkarni, J. Adams, E. Thomas, and A. Silman. Association between amputation, arthritis and osteopenia in british male war veterans with major lower limb amputations. *Clinical Rehabilitation*, 12:274–279, 09 1998.

[63] P. Ephraim, S. Wegener, E. Mackenzie, T. Dillingham, and L. Pezzin. Phantom pain, residual limb pain, and back pain in amputees: Results of a national survey. *Archives of physical medicine and rehabilitation*, 86:1910–9, 11 2005.

[64] C. Powers, L. Torburn, J. Perry, and E. Ayyappa. Influence of prosthetic foot design on sound limb loading in adults with unilateral below-knee amputations. *Archives of physical medicine and rehabilitation*, 75(7):825–829, 1994.

[65] P. A. Baker and S. R. Hewison. Gait recovery pattern of unilateral lower limb amputees during rehabilitation. *Prosthetics and orthotics international*, 14(2):80–84, 1990.

[66] E. Isakov, H. Burger, J. Krajnik, M. Gregoric, and C. Marincek. Influence of speed on gait parameters and on symmetry in trans-tibial amputees. *Prosthetics and orthotics international*, 20(3):153–158, 1996.

[67] S. J. Mattes, P. E. Martin, and T. D. Royer. Walking symmetry and energy cost in persons with unilateral transtibial amputations: Matching prosthetic and intact limb inertial properties. *Archives of Physical Medicine and Rehabilitation*, 81(5):561–568, 2000.

[68] S. F. Donker and P. J. Beek. Interlimb coordination in prosthetic walking: effects of asymmetry and walking velocity. *Acta psychologica*, 110:265–88, 07 2002.

[69] M. Schaarschmidt, S. W. Lipfert, C. Meier-Gratz, H. C. Scholle, and A. Seyfarth. Functional gait asymmetry of unilateral transfemoral amputees. *Human Movement Science*, 31(4):907–917, 2012.

[70] R. D. Snyder, C. M. Powers, C. Fontaine, and J. Perry. The effect of five prosthetic feet on the gait and loading of the sound limb in dysvascular belowknee amputees. *Journal of rehabilitation research and development*, 49(9):309– 315, 1995.

[71] J. R. Engsberg, A. G. Lee, J. L. Patterson, and J. A. Harder. External loading comparisons between able-bodied and below-knee-amputee children during walking. *Archives of physical medicine and rehabilitation*, 72:657–661, 1991.

[72] G. R. Hurley, R. Mckenney, M. Robinson, M. Zadravec, M. R. Pierrynowski, and G. Hurley. The role of the contralateral limb in below-knee amputee gait. *150 Prosthetics and Orthotics International*, 14(1973):33–42, 1990.

[73] L. Nolan, A. Wit, K. Dudzinski, A. Lees, M. Lake, and M. Wychowanski. Adjustments in gait symmetry with walking speed in trans-femoral and transtibial amputees. *Gait & Posture*, 17(2):142–151, 2003.

[74] J. D. Smith and P. E. Martin. Effects of prosthetic mass distribution on metabolic costs and walking symmetry. *Journal of applied biomechanics*, 29:317–328, 09 2013.

[75] J. F. Lehmann, R. Price, R. Okumura, K. Questad, B. J. De Lateur, and A. N´egretot. Mass and mass distribution of below-knee prostheses: Effect on gait efficacy and self-selected walking speed. *Archives of Physical Medicine and Rehabilitation*, 79(2):162–168, 1998.

[76] R. S. Gailey, M. S. Nash, T. A. Atchley, R. M. Zilmer, G. R. Moline-Little, N. Morris-Cresswell, and L. I. Siebert. The effects of prosthesis mass on metabolic cost of ambulation in non-vascular trans-tibial amputees. *Prosthetics and orthotics international*, 21(1):9–16, 1997.

[77] R. W. Selles, J. B. J. Bussmann, A. J. K. Van Soest, and H. J. Stam. The effect of prosthetic mass properties on the gait of transtibial amputees - a mathematical model. *Disability and Rehabilitation*, 26(12):694–704, 2004.

[78] J. D. Smith and P. E. Martin. Walking patterns change rapidly following asymmetrical lower extremity loading. *Human Movement Science*, 26(3):412–425, 2007.

[79] J. Ventura, G. Klute, and R. Neptune. The effects of prosthetic ankle dorsiflexion and energy return on below-knee amputee leg loading. *Clinical biomechanics (Bristol, Avon)*, 26:298–303, 11 2010.

[80] M. H. Schwartz, A. Rozumalski, and J. P. Trost. The effect of walking speed on the gait of typically developing children. *Journal of biomechanics*, 41:1639–1650, 2008.

[81] M. Chiu and M. Wang. The effect of gait speed and gender on perceived exertion, muscle activity, joint motion of lower extremity, ground reaction force and heart rate during normal walking. *Gait & posture*, 25:385–92, 03 2007.

[82] M. Chung and M. J. Wang. The change of gait parameters during walking at different percentage of preferred walking speed for healthy adults aged 20–60 years. *Gait & posture*, 31:131–135, 2010.

[83] A. D. Koelewijn. Predictive simulations of gait and their application in prosthesis design. *Doctoral dissertation, Cleveland State University*, pages 1–280, 2018.

[84] LaPre. A lower limb prosthesis with active alignment for reduced limb loading. *University of Massachusetts Amherst*, pages 1–142, 2016.

[85] A. G. Cutti, G. Verni, G. L. Migliore, A. Amoresano, and M. Raggi. Reference values for gait temporal and loading symmetry of lower-limb amputees can help in refocusing rehabilitation targets. *Journal of Neuro-Engineering and Rehabilitation*, 15, 09 2018.

[86] K. David. K-levels for amputees. *Kenney Orthopedics, Available from: https://www.kenneyorthopedics.com/about/news/view/444/k-levels-for-amputees*, 2020.

[87] Blatchford. Elite2. *Journal of Blatchford, www.blatchford.co.uk/products/elite2/.*, 2020.

[88] J. Michael. Energy storing feet: A clinical comparison. *Journal of feet energy storing*, 1987.

[89] S. Collins. Dynamic walking principles applied to human gait. *PhD thesis, The University of Michigan*, 2008.

[90] G. A. Cavagna and R. Margaria. Mechanics of walking. *Appl Physiol (J)*, 21(1):271–278, 1966.

[91] S. Mochon and T. A. McMahon. Ballistic walking: an improved model. *Mathematical Biosciences*, 52(3-4):241–260, 1980.

[92] G. A. Cavagna, F. P. Saibene, and R. Margaria. External work in walking. *Journal of applied physiology*, 18:1–9, 02 1963.

[93] M. Omasta, D. Palousek, T. Navrat, and J. Rosicky. Finite element analysis for the evaluation of the structural behaviour, of a prosthesis for trans-tibial amputees. *Medical engineering & physics*, 34:38–45, 07 2011.

[94] A. Hansen and D. Childress. Investigations of roll-over shape: Implications for design, alignment, and evaluation of ankle-foot prostheses and orthoses. *Disability and rehabilitation*, 32:2201–9, 01 2010.

[95] A. Hansen, D. Childress, and E. Knox. Roll-over shapes of human locomotor systems: Effects of walking speed. *Clinical biomechanics (Bristol, Avon)*, 19:407–14, 06 2004.

[96] A. Hansen and D. Childress. Effects of shoe heel height on biologic rollover characteristics during walking. *Journal of rehabilitation research and development*, 41:547–54, 08 2004.

[97] A. Hansen and D. Childress. Effects of adding weight to the torso on roll-over characteristics of walking. *Journal of rehabilitation research and development*, 42:381–90, 05 2005.

[98] A. H. Hansen, D. S. Childress, and S. C. Miff. Roll-over characteristics of human walking on inclined surfaces. *Human movement science*, 23(6):807–21, 2004.

[99] C. Curtze, A. Hof, H. Van Keeken, J. Halbertsma, K. Postema, and E. Otten. Comparative roll-over analysis of prosthetic feet. *Journal of Biomechanics*, 42:1746–53, 06 2009.

[100] P. Adamczyk, M. Roland, and M. Hahn. Sensitivity of biomechanical outcomes to independent variations of hindfoot and forefoot stiffness in foot prostheses. *Human Movement Science*, 54:154–171, 08 2017.

[101] C. C. Wang and A. H. Hansen. Response of able-bodied persons to changes in shoe rocker radius during walking: changes in ankle kinematics to maintain a consistent roll-over shape. *Journal of biomechanics*, 43(12):2288–93, 2010.

[102] K. Olesnavage and A. Winter. Analysis of rollover shape and energy storage and return in cantilever beam-type prosthetic feet. page V05AT08A018, 08 2014.

[103] Northwestern University Prosthetics-Orthotics Center. Effects of prosthetic foot rocker radius on gait of prosthesis users. *Northwestern University*, 2010.

[104] British Standards Institution. 16955: Prosthetics — quantification of physical parameters of ankle foot devices and foot units. *London: BSI*, 2016.

[105] K. Smith. The mechanical response and parametric optimisation of ankle-foot devices. *University of Central Florida*, 2016.

[106] P. Mahmoodi, R. S. Ransing, and M. I. Friswell. Modelling the effect of 'heel to toe' roll-over contact on the walking dynamics of passive biped robots. *Applied Mathematical Modelling*, 37:12–13, 2013.

[107] S. Strike and M. Hillery. The design and testing of a composite lower limb prosthesis. *Proceedings of the Institution of Mechanical Engineers. Part H, Journal of engineering in medicine*, 214:603–14, 02 2000.

[108] K. M. Olesnavage and A. G. Winter. Design and qualitative testing of a prosthetic foot with rotational ankle and metatarsal joints to mimic physiological roll-over shape. page V05AT08A035, 08 2015.

[109] K. Olesnavage, V. Prost, B. Johnson, and V. Winter. Passive prosthetic foot shape and size optimisation using lower leg trajectory error. *Journal of Mechanical Design*, 140, 07 2018.

[110] H. Tryggvason, F. Starker, C. Lecompte, and F. Jónsdóttir. Modeling and simulation in the design process of a prosthetic foot. *In Proceedings of the 58th Conference on Simulation and Modelling (SIMS 58) Reykjavik*, September 25th- 27th:398–405, 2017.

[111] Z. Aftab, T. Robert, P. Bor, and Wieber. Balance recovery prediction with multiple strategies for standing humans. *PLOS ONE*, 11:e0151166, 03 2016.

[112] M. Wisse, A. Schwab, R. Linde, and F. van der Helm. How to keep from falling forward: Elementary swing leg action for passive dynamic walkers. *Robotics, IEEE Transactions on*, 21:393 – 401, 07 2005.

[113] T. McGeer. Passive dynamic walking. *The International Journal of Robotics Research, ISSN 0278-3649.*, 1990.

[114] H. Geyer, A. Seyfarth, and R. Blickhan. Compliant leg behaviour explains basic dynamics of walking and running. proceedings. *Biological sciences - The Royal Society*, 273(1603):2861–7, 2006.

[115] B. Kluitenberg, S. Bredeweg, S. Zijlstra, W. Zijlstra, and I. Buist. Comparison of vertical ground reaction forces during overground and treadmill running. a validation study. *BMC musculoskeletal disorders*, 13:235, 11 2012.

[116] R. Kram, T. M. Griffin, and J. M. Donelan. Force treadmill for measuring vertical and horizontal ground reaction forces. *Journal of Applied Physiology*, 7(9):764–769, 1998.

[117] K. Valenzuela, S. Lynn, L. Mikelson, G. Noffal, and D. Judelson. Effect of acute alterations in foot strike patterns during running on sagittal plane lower limb kinematics and kinetics. *Journal of sports science & medicine*, 14:225–232, 03 2015.

[118] S. W. Lipfert, M. Gunther, D. Renjewski, S. Grimmer, and A. Seyfarth. A model-experiment comparison of system dynamics for human walking and running. *Journal of Theoretical Biology*, 292:11–17, 2012.

[119] S. Lipfert, M. Gunther, D. Renjewski, and A. Seyfarth. Impulsive ankle push-off powers leg swing in human walking. *The Journal of experimental biology*, 217, 12 2013.

[120] Q. Yang, J. W. Qin, and S. Law. A three-dimensional human walking model. *Journal of Sound and Vibration*, 357:437–456, 11 2015.

[121] P. Mahmoodi, S. Aristodemou, R. Ransing, N. Owen, and M. Friswell. Prosthetic foot design optimisation based on roll-over shape and ground reaction force characteristics. *Proceedings of the Institution of Mechanical Engineers, Part C: Journal of Mechanical Engineering Science*, 231(17):3093–3103, 2017.

[122] W. G. Charles, P. Mahmoodi, R.S. Ransing, I. Sazonov, and M.I. Friswell. Comparison of point foot, collisional and smooth rolling contact models on the bifurcations and stability of bipedal walking. *European Journal of Computational Mechanics*, pages 273–293, 2016.

[123] C. Honeycutt, J. Sushko, and K. Reed. Asymmetric passive dynamic walker. *IEEE ... International Conference on Rehabilitation Robotics : [proceedings]*, 2011:5975465, 06 2011.

[124] F. Rasouli, M. Naraghi, and A. Safa. Asymmetric gait analysis based on passive dynamic walking theory. pages 361–366, 10 2016.

[125] E. Boutwell, R. Stine, and S. Gard. Impact testing of the residual limb: System response to changes in prosthetic stiffness. *Journal of Rehabilitation Research and Development*, 53:369–378, 04 2016.

[126] D. Rihs and I. Polizzi. Prosthetic foot design. final year project. *Monash Rehabilitation Technology Research Unit, Monash, Australia*, page 27 – 33, 2001.

[127] N. Holowka and D. Lieberman. Rethinking the evolution of the human foot: Insights from experimental research. *The Journal of Experimental Biology*, 221:jeb174425, 09 2018.

[128] Rehab Technology Team. Super user. rehabtech - home. *Rehabtation Tchnology group from https://Rehabtech.com.au.*, 2020.

[129] M. J. Hsu, D. H. Nielsen, S. J. Lin-Chan, and D. Shurr. The effects of prosthetic foot design on physiologic measurements, self-selected walking velocity, and physical activity in people with transtibial amputation. *Archives of Physical Medicine and Rehabilitation*, 87(1):123–9, 2006.

[130] V. Carli. Design of an active foot for a smart prosthetic leg. *Thesis Dissertation: Vom Fachbereich Maschinenbau an der Technischen Universitat Darmstadt*, 11 2007.

[131] K. Olesnavage and A. Winter. Lower leg trajectory error: A novel optimization parameter for designing passive prosthetic feet. pages 271–276, 08 2015.

[132] International Organisation for Standardisation. Iso 22523:2006. *ISO Standard*, 2011.

[133] H. V. Jaarsveld, H. Grootenboer, J. Vriesand, and H. F. Koopman. Stiffness and hysteresis properties of some prosthetic feet. *Prosthetics and orthotics international*, 14:117–24, 01 1991.

[134] At. Hof, R. Bockel, T. Schoppen, and K. Postema. Control of lateral balance in walking. experimental findings in normal subjects and above-knee amputees. *Gait & posture*, 25:250–8, 03 2007.

[135] A. Merker, J. Rummel, and A. Seyfarth. Stable walking with asymmetric legs. *Bioinspiration & biomimetics*, 6:045004, 12 2011.

[136] R. Waters and S. Mulroy. The energy expenditure of normal and pathologic gait. *Gait & posture*, 9:207–31, 08 1999.

[137] D. Vickers, A. Mcintosh, and K. Beatty. Elderly unilateral transtibial amputee gait on an inclined walkway: a biomechanical analysis. *Gait Posture, 27, 518-529.*, 2008.

[138] J. Markowitz, P. Krishnaswamy, M. Eilenberg, K. Endo, C. Barnhart, and H. Herr. Speed adaptation in a powered transtibial prosthesis controlled with a neuromuscular model. *Philosophical transactions of the Royal Society of London. Series B, Biological sciences*, 366:1621–31, 05 2011.

[139] J. Andrysek. Lower-limb prosthetic technologies in the developing world: A review of literature from 1994–2010. *Prosthetics and orthotics international*, 34:378–98, 12 2010.

[140] M. Q. Liu, F. C. Anderson, M. G. Pandy, and S. L. Delp. Muscle contributions to support and progression over a range of walking speeds. *Journal of biomechanics*, 41:3243–52, 10 2008.

[141] T. P. Andriacchi, J. A. Ogle, and J. O. Galante. Walking speed as a basis for normal and abnormal gait measurements. *Journal of biomechanics*, 10:261–8, 02 1977.

[142] K. Masani, M. Kouzaki, and T. Fukunaga. Variability of ground reaction forces during treadmill walking. *Journal of applied physiology (Bethesda, Md. : 1985)*, 92:1885–90, 06 2002.

[143] B. Stansfield, S. J. Hillman, M. E. Hazlewood, and J. E. Robb. Regression analysis of gait parameters with speed in normal children walking at self-selected speeds. *Gait & posture*, 23:288–94, 05 2006.

[144] N. Stolwijk, K. Koenraadt, J. Louwerens, D. Grim, J. Duysens, and N. Keijsers. Foot lengthening and shortening during gait: A parameter to investigate foot function? *Gait & posture*, 39, 10 2013.

[145] Web Plot Digitizer Software. Extract data from plots, images, and maps. *http://arohatgi.info/WebPlotDigitizer/ (accessed 30 April 2020)*, 2015.

[146] Yellow Springs (Ohio). Anthropology Research Project, United States. Army, United States. Air Force, United States. Navy, and Tri-Service Aeromedical Research Panel. Tri-Service Committee. Anthropometry and mass distribution for human analogues: Military male aviators. *Anthropology Research Project*, 1988.

[147] A. Eshraghi, N. A. Abu Osman, M. Karimi, H. Gholizadeh, E. Soodmand, and W. A. Abas. Gait biomechanics of individuals with transtibial amputation: Effect of suspension system. *PloS one*, 9:e96988, 05 2014.

[148] M. Saunders, E. Schwentker, D. Kay, G. Bennett, C. Jacobs, M. Verstraete, and G. Njus. Finite element analysis as a tool for parametric prosthetic foot design and evaluation.

technique development in the solid ankle cushioned heel (sach) foot. *Computer methods in biomechanics and biomedical engineering*, 6:75–87, 03 2003.

[149] W. C. Lee and M. Zhang. Design of monolimb using finite element modeling and statistics-based taguchi method. *Clinical biomechanics (Bristol, Avon)*, 20:759–66, 09 2005.

[150] X. Bonnet, H. Pillet, P. Fode, F. Lavaste, and W. Skalli. Finite element modelling of an energy-storing prosthetic foot during the stance phase of transtibial amputee gait. *Proceedings of the Institution of Mechanical Engineers. Part H, Journal of engineering in medicine*, 226:70–5, 08 2012.

[151] B. Dyer, P. Sewell, and S. Noroozi. An investigation into the measurement and prediction of mechanical stiffness of lower limb prostheses used for running. *Assistive Technology*, 26, 06 2014.

[152] M. Rabuffetti and G. Baroni. Validation protocol of models for centre of mass estimation. *Journal of Biomechanics*, 32(6):609–613, 1999.

[153] S. C. Miff, A. H. Hansen, D. S. Childress, S. A. Gard, and M. R. Meier. Roll-over shapes of the able-bodied knee-ankle-foot system during gait initiation, steady-state walking, and gait termination. *Gait & posture*, 27:316–22, 03 2008.

[154] J. Ventura, G. Klute, and R. Neptune. The effect of prosthetic ankle energy storage and return properties on muscle activity in below-knee amputee walking. *Gait & posture*, 33:220–6, 02 2011.

[155] H. Houdijk, D. Wezenberg, L. Hak, and A. G. Cutti. Energy storing and return prosthetic feet improve step length symmetry while preserving margins of stability in persons with transtibial amputation. *Journal of NeuroEngineering and Rehabilitation*, 15, 09 2018.

[156] M. Coulson, H. Phillips, T. Wilcox, and J. Morgan. An industry 4.0 approach to patient specific trans-tibial prostheses. *Group design report, College of Engineering, Swansea University*, 05 2020.

[157] W. F. Hosford. Solid mechanics. *Cambridge University Press*, 2010.

[158] MatWeb technical group. The online materials information resource. (2020). retrieved 31 april 2020, from http://www.matweb.com/search/datasheet. *The MatWeb journal*, 2020.

[159] M. Hacker, J. Krieghoff, and A. Mikos. Synthetic polymers. pages 559–590, 01 2019.

[160] W. I. Wu, P. Rezai, L. Hsu, and P. R. Selvaganapathy. Materials and methods for the microfabrication of microfluidic biomedical devices. *Microfluidic Devices for Biomedical Applications*, pages 3–62, 10 2013.

[161] M. E. Grigore. Methods of recycling, properties and applications of recycled thermoplastic polymers. *Recycling*, 2:24, 11 2017.

# Appendices

# Appendix A: Swansea University Ethics

The below figure represent the ethics document in Swansea University conducted to the author.

**APPLICATION FOR ETHICAL COMMITTEE APPROVAL OF A RESEARCH PROJECT**

All research with human participants, or on data derived from research with human participants that is not publicly available, undertaken by staff or students linked with A-STEM or in the College of Engineering more widely must be approved by the College of Engineering Research Ethics Committee.

**RESEARCH MAY ONLY COMMENCE ONCE ETHICAL APPROVAL HAS BEEN OBTAINED**

The researcher(s) should complete the form in consultation with the project supervisor. After completing and signing the form students should ask their supervisor to sign it. The form should be submitted electronically to coe-researchethics@swansea.ac.uk.

Applicants will be informed of the Committee's decision via email to the project leader/supervisor.

| **1. TITLE OF PROJECT** |
| --- |
| An investigation to quantify the power generating ability in healthy adults at the push-off stage of the gait cycle. |

| **2. DATE OF PROJECT COMMENCEMENT AND PROPOSED DURATION OF THE STUDY** |
| --- |
| Proposed commencement and completion dates for the study are 1st April 2019 - 18th June 2019.<br>The study will last roughly 3-4 months |

| **3. NAMES AND STATUS OF THE RESEARCH TEAM** |
| --- |
| Ben Morgan, EngD Student<br>Dr Rajesh Ransing, Associate Professor in College of Engineering<br>Nick Owen, Senior Lecturer in Sports Science<br>Turki Alqemlas, PhD Student |

| **4. RATIONALE AND REFERENCES** |
| --- |
| For able-bodied persons, the power at the push off stage is generated via muscles and tendons found in lower leg. Amputees using a prosthetic foot do not have this muscle and tendon support. The push off power is given by the energy return mechanism found in commonly used passive Energy Storing and Return (ESR) prosthetics.<br>The research team believes that the passive ESR prosthetics currently available to amputees globally are less efficient and their energy return ability can be improved. It has been suggested that a lack of power supplied at push-off is linked to increased effort and joint overloading, which will lead to health complications later in life (Morgenroth et al., 2011; Powers, Torburn, Perry, & Ayyappa, 1994). Powered prosthetics can significantly improve these conditions, however they come with a higher cost (Hill & Herr, 2013). |

Figure A-1: Ethics for amplifying the experiment on real case studies

# Appendix B: Experiment and Average Walking Speed in terms of %FWS

## B1. Experiment

## B2. Average Walking Speed in terms of %FWS

# B1. Experiment

The figure below shows the pointers formed while walking, which are colour-coded from the hip, femoral *LC*, tibial *LC*, malleolus, and fifth meta.

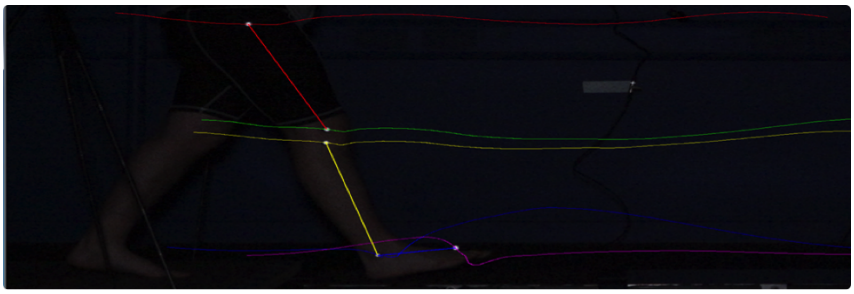

Figure B-1: Foot reflectors

# B2. Walking Speed Average in terms of %FWS

| | % of free walking speed Avg (Min – Max) | % gait cycle at which $Fz_1$ occurs Avg (Min – Max) | $Fz_1$ Avg (Min – Max) (GRF/BW) | $Fz_1$ as % of free $Fz_1$ Avg (Min – Max) | % gait cycle at which $Fz_2$ occurs Avg (Min – Max) | $Fz_2$ Avg (Min – Max) (GRF/BW) | $Fz_2$ as % of free $Fz_2$ Avg (Min – Max) | % gait cycle at which $Fz_3$ occurs Avg (Min – Max) | $Fz_3$ Avg (Min – Max) (GRF/BW) | $Fz_2$ as % of free $Fz_2$ Avg (Min – Max) |
|---|---|---|---|---|---|---|---|---|---|---|
| **Very Slow** | 37.3 (29.3 - 47.0) | 17 (15.6 - 18.4) | 0.973 (0.956 - 0.990) | 85.4 (77.7 - 97.1) | 30.8 (30.3 - 31.3) | 0.967 (0.967 - 0.967) | 136.0 (124.3 - 149.9) | 45.2 (44.4 - 45.9) | 1.01 (1.00 - 1.01) | 92.7 (88.5 - 98.1) |
| **Slow** | 64.4 (50.0 - 87.0) | 15.8 (15.0 - 16.3) | 0.977 (0.967 - 1.00) | 85.7 (78.6 – 98.0) | 29.8 (28.7 - 31.2) | 0.903 (0.882 - 0.945) | 127.0 (113.4 - 146.5) | 44.1 (41.1 - 46.1) | 1.01 (0.989 - 1.04) | 92.7 (87.5 - 101.0) |
| **Free** | 100 (76.7 - 130.4) | 14.4 (13.3 - 15.5) | 1.14 (1.02 - 1.23) | 100 (82.9 - 120.6) | 29.1 (27.7 - 31.3) | 0.711 (0.645 - 0.778) | 100 (82.9 - 120.6) | 45.6 (44.9 - 47.4) | 1.09 (1.03 - 1.13) | 100 (91.2 - 109.7) |
| **Fast** | 120.8 (100.0 - 154.8) | 12.7 (11.9 - 13.3) | 1.23 (1.20 - 1.27) | 107.9 (97.6 - 124.5) | 28.8 (27.2 - 29.6) | 0.618 (0.558 - 0.675) | 86.9 (71.7 - 104.7) | 45.0 (43.5 - 46.6) | 1.12 (1.07 - 1.17) | 102.8 (94.7 - 113.6) |
| **Very Fast** | 162.3 (130.0 - 217.4) | 12.3 (11.7 - 13.7) | 1.35 (1.26 - 1.45) | 118.4 (102.4 - 142.2) | 30.4 (27.8 - 33.6) | 0.499 (0.349 - 0.588) | 70.2 (44.9 - 91.2) | 43.3 (42.5 - 44.1) | 0.963 (0.783 - 1.14) | 88.3 (69.3 - 110.7) |

Figure B-2: The average of walking speed as %FWS

# Appendix C: Kovac and Silverman Experimental Data

## C1. Experimental Data by Kovac

## C2. Experimental Data by Silverman and Neptune

# C1. Kovac Experimental Data

The below table presents the data of the experimental study conducted by Kovac [22] for the sound, prosthetic and control group.

| Variable | Leg | Number of measurements | $\overline{X}$ force N/kg | Standard deviation |
|---|---|---|---|---|
| Fz 1 | R PRO A | 14 | 1.04 | 0.07 |
| Fz 1 | R L C | 13 | 1.08 | 0.11 |
| Fz 1 | L L A | 14 | 1.17 | 0.10 |
| Fz 1 | L L C | 13 | 1.06 | 0.10 |
| Fz 2 | R PRO A | 14 | 0.81 | 0.05 |
| Fz 2 | R L C | 13 | 0.75 | 0.08 |
| Fz 2 | L L A | 14 | 0.76 | 0.07 |
| Fz 2 | L L C | 13 | 0.72 | 0.08 |
| Fz 3 | R PRO A | 14 | 0.99 | 0.04 |
| Fz 3 | R L C | 13 | 1.07 | 0.06 |
| Fz 3 | L L A | 14 | 1.06 | 0.06 |
| Fz 3 | L L C | 13 | 1.07 | 0.05 |

R PRO A – right leg (prosthesis) of amputees, L L A – left leg of amputees, R L C – right leg of able bodied persons, L L C – left leg of able bodied persons

Figure C-1: $Fz1$, $Fz2$ and $Fz3$ values for the prosthetic, sound and control group [22].

# C2. Silverman and Neptune's Experimental Data

The below figure presents the data from the work of Silverman and Neptune [17] for the non-amputee, amputee and sound leg groups.

| Speed (m/s) | 0.6 | 0.9 | 1.2 | 1.5 |
|---|---|---|---|---|
| ***Residual leg*** | | | | |
| Peak propulsive GRF | 6.478 (1.833)* | 10.060 (1.736)* | 12.661 (2.374)* | 15.368 (3.364)* |
| Peak braking GRF | −7.122 (1.143)* | −10.102 (1.541)* | −13.839 (2.550)* | −17.534 (3.199)* |
| First peak vertical GRF | 99.652 (4.028) | 102.772 (4.546) | 106.265 (4.267)* | 110.883 (6.194) |
| Second peak vertical GRF | 100.160 (3.074)* | 99.255 (3.637)* | 100.762 (3.517)* | 101.847 (4.247)* |
| First peak M/L GRF | 6.077 (1.495) | 4.829 (1.071) | 5.146 (1.210) | 5.587 (1.127) |
| Second peak ML GRF | 5.859 (1.148) | 4.737 (0.737) | 4.670 (0.937) | 4.462 (0.742) |
| ***Intact leg*** | | | | |
| Peak propulsive GRF | 8.144 (1.150)* | 13.158 (1.368)* | 18.601 (1.299) | 23.452 (1.983) |
| Peak braking GRF | −8.723 (1.463) | −13.485 (1.893) | −17.274 (2.361) | −21.672 (2.641) |
| First peak vertical GRF | 103.312 (3.003) | 104.062 (4.855) | 110.856 (5.249) | 118.366 (5.392) |
| Second peak vertical GRF | 98.595 (1.583)* | 99.495 (2.325)* | 103.003 (2.514)* | 106.772 (3.819)* |
| First peak M/L GRF | 6.702 (1.345) | 5.390 (1.332) | 5.745 (1.192) | 5.949 (1.206) |
| Second peak ML GRF | 6.392 (1.188) | 5.394 (1.298) | 5.556 (1.158) | 5.558 (1.449) |
| ***Non-amputee average leg*** | | | | |
| Peak propulsive GRF | 9.981 (0.946) | 14.948 (1.400) | 19.527 (2.417) | 25.722 (2.712) |
| Peak braking GRF | −8.441 (0.804) | −13.105 (1.374) | −18.504 (1.689) | −23.993 (1.978) |
| First peak vertical GRF | 102.810 (3.674) | 105.045 (4.036) | 108.592 (6.300) | 114.679 (6.041) |
| Second peak vertical GRF | 106.007 (4.796) | 106.841 (5.188) | 109.293 (4.975) | 113.950 (3.894) |
| First peak M/L GRF | 5.542 (0.767) | 4.668 (0.741) | 5.127 (0.617) | 5.453 (0.600) |
| Second peak ML GRF | 5.535 (0.700) | 4.655 (0.550) | 4.676 (0.856) | 4.558 (0.826) |

* Significant differences with the non-amputee average leg.

Figure C-2: $Fz1$, $Fz2$ and $Fz3$ values for residual leg, intact leg and non-amputee at different walking speeds [17].

# Appendix D: APDL Script

## D1. ANSYS Parametric Design Language (APDL)

## D2. APDL Full Annotated Script

# D1. ANSYS Parametric Design Language (APDL)

The below figure represent the APDL script to extract COPs.

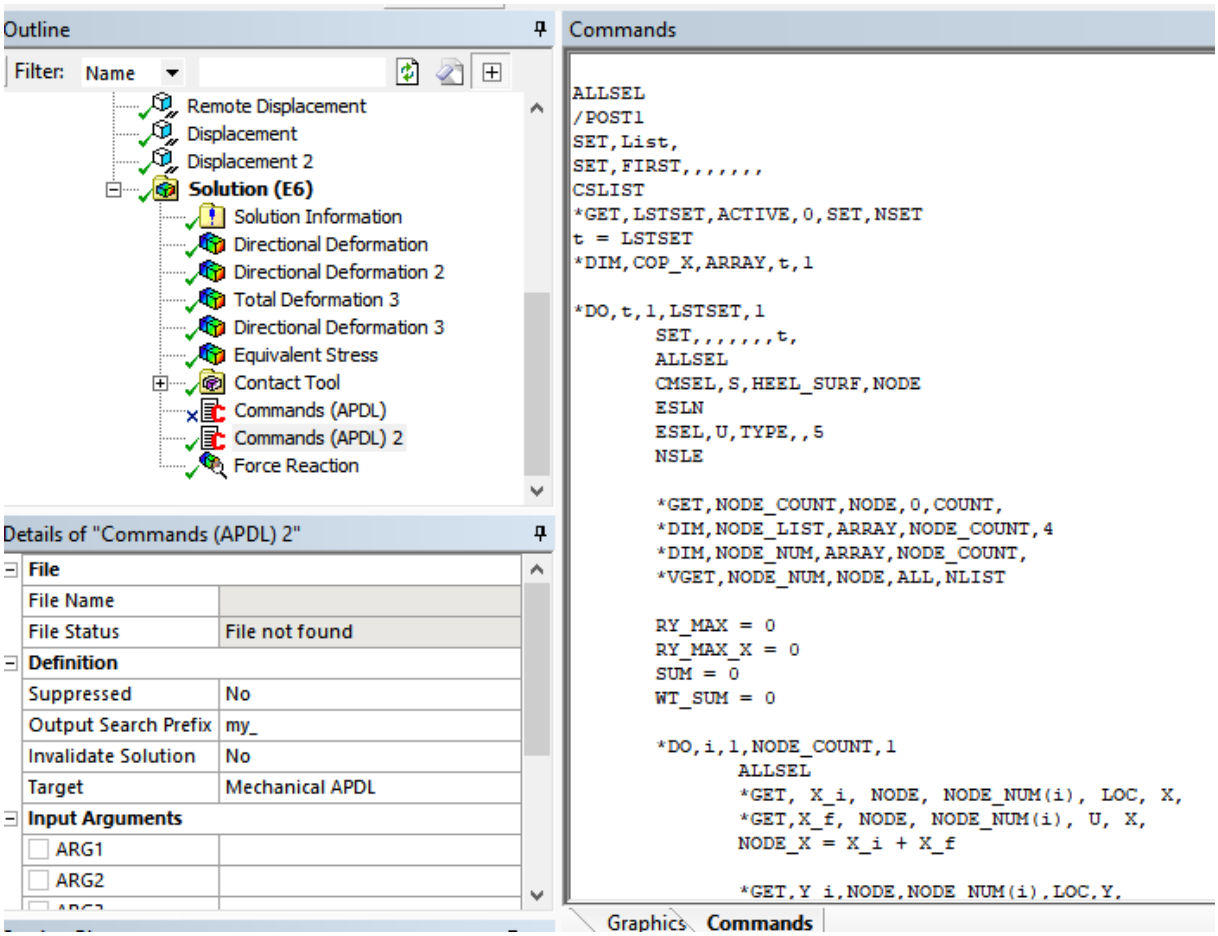


Figure D-1: COPs extraction in APDL Script

# D2. APDL Full Annotated Script

```
ALLSEL

/POST1

SET,List,

SET,FIRST,,,,,,,

CSLIST

*GET,LSTSET,ACTIVE,0,SET,NSET

t = LSTSET

\\Defining variable to store data

*DIM,COP_X,ARRAY,t,1

\\Loop start from 1 to last time step

*DO,t,1,LSTSET,1

SET,,,,,,,t,

ALLSEL

\\Select surface with name HEEL_SURF

CMSEL,S,HEEL_SURF,NODE

ESLN

ESEL,U,TYPE,,5

NSLE

\\Extract node count, node coordinates

*GET,NODE_COUNT,NODE,0,COUNT,

*DIM,NODE_LIST,ARRAY,NODE_COUNT,4

*DIM,NODE_NUM,ARRAY,NODE_COUNT,
```

```
*VGET,NODE_NUM,NODE,ALL,NLIST

\\Initialise variable

RY_MAX = 0

RY_MAX_X = 0

SUM = 0

WT_SUM = 0

\\Second Loop start for each node over Heel surface

*DO,i,1,NODE_COUNT,1

ALLSEL

\\Extract individual node x co-ordinate and deflection in X direction,

and store it in X_i,X_f variable

*GET, X_i, NODE, NODE_NUM(i), LOC, X,

*GET,X_f, NODE, NODE_NUM(i), U, X,

NODE_X = X_i + X_f

\\Extract individual node y co-ordinate and deflection in Y direction,

and store it in Y_i,Y_f variable

*GET,Y_i,NODE,NODE_NUM(i),LOC,Y,

*GET,Y_f,NODE,NODE_NUM(i),U,Y,

NODE_Y = Y_i - Y_f

NSEL,S,NODE, , NODE_NUM(i)

ESLN

FSUM,

\\Extract Force value in Y direction and store it in variable SIGNED_LOAD

*GET, SIGNED_LOAD, FSUM, 0, ITEM, FY,
```

```
NODE_LOAD = SIGNED_LOAD

NODE_LIST(i,1) = NODE_NUM(i)

NODE_LIST(i,2) = NODE_X

NODE_LIST(i,3) = NODE_LOAD

NODE_LIST(i,4) = NODE_Y

\\Calculate Total Force and Moment for individual nodes

SUM = SUM + NODE_LOAD

WT_SUM = WT_SUM + NODE_LOAD*NODE_X

\\If condition to estimate maximum force on certain node point

*IF,RY_MAX,LT,NODE_LOAD,THEN

RY_MAX = NODE_LOAD

RY_MAX_X = NODE_X

RY_MAX_Y = NODE_Y

*ENDIF

*ENDDO               \\End loop 1

\\ Calculate Center of Pressure (COP_X) based on Total Moment

and Total Force for individual time step

COP_X(t,1) = WT_SUM/SUM

*ENDDO          \\End loop 2

\\Write COP_X value for all times steps in a text file

*MWRITE,COP_X,C:/Users/Turki/Desktop/COP_X,txt

%7.2F
```

# Appendix E: Roll-Over Shape

The procedure ROS calculations is described by Mahmoodi [32] and the text has been reproduced in this appendix for clarity. To capture the walking step motion using a motion camera, retro-reflective spherical markers are attached at three locations: the force plate corner, knee joint and ankle joint. Quintic software is used to analyse the marker angular displacement for a gait cycle. Yellow and green colours are used to represent the knee joint and ankle joint respectively in the Quintic software. The force plate corner is used to indicate the origin of the global coordinate system [32]. The kinematic data starts to be captured at a different time from the force plate. To indicate the time at which the force plate begins to capture data, light-emitting diode (LED) illumination – shown in Figure E-1 as a red light – is used.

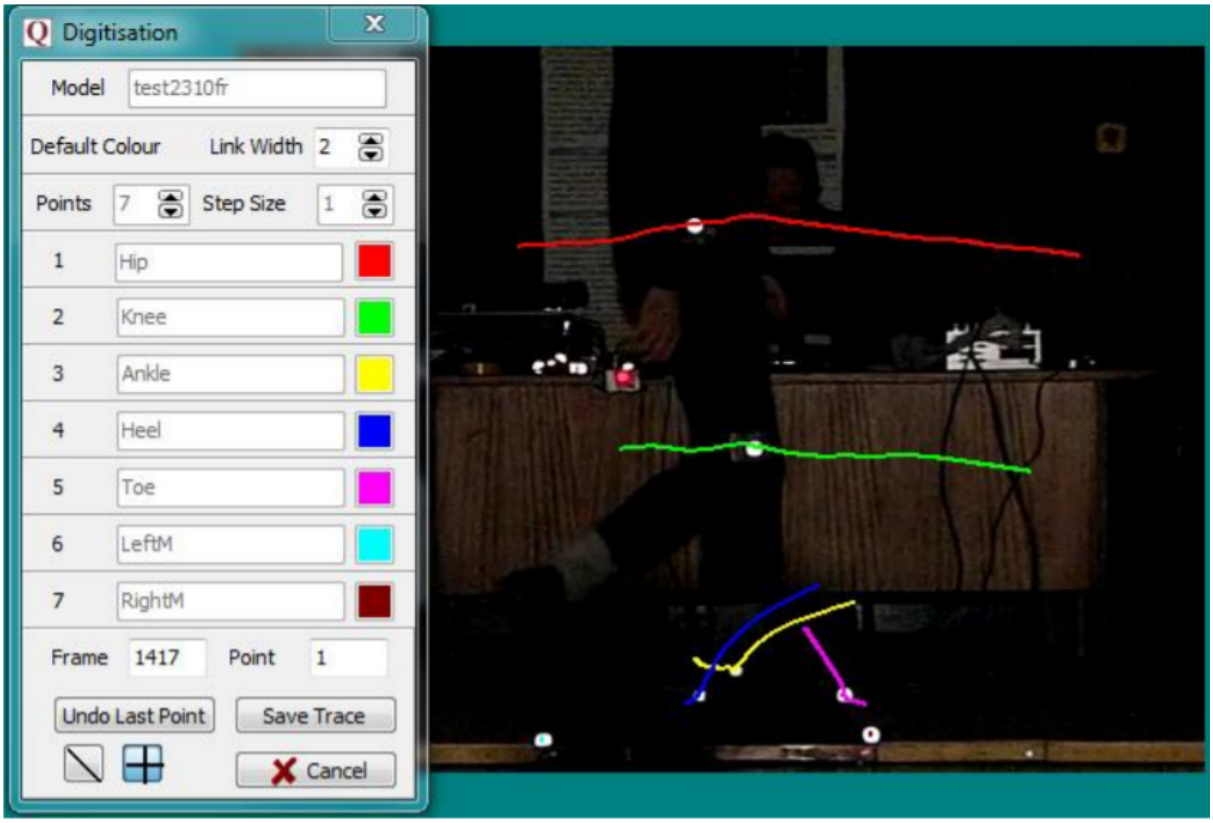


Figure E-1: Walking step trajectory of the ankle (yellow line) and the knee (green line) joint. The global coordinate system origin is located on the left side of the force plate [32].

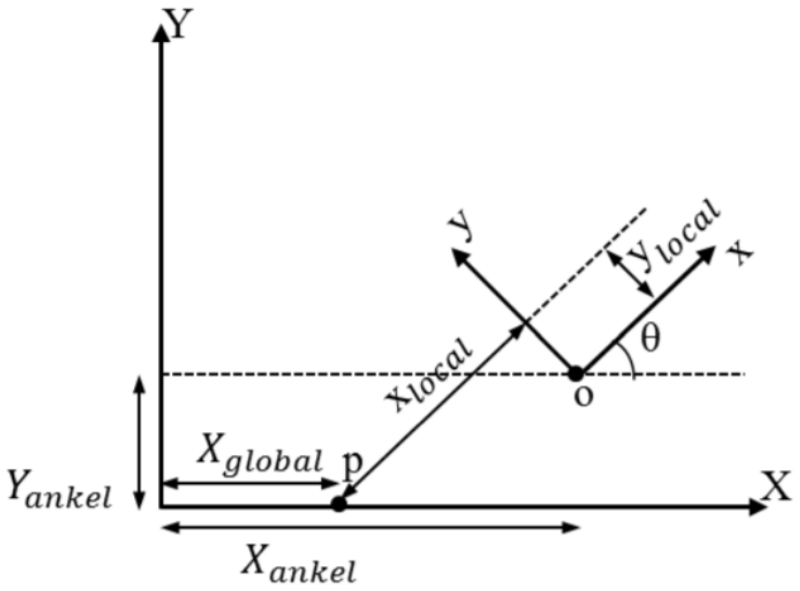


Figure E-2: The coordinate system of both global (X-Y) and local (x-y) [32].

Illumination is also used in the temporal synchronisation of the video camera and the force plate. Using the local coordinate system, the COP position is determined using the transformation presented in Equation 1. The relationship between the local and global coordinate systems is shown in Figure E-2.

$$\begin{bmatrix} X^i_{local} \\ Y^i_{local} \end{bmatrix} = \begin{bmatrix} \cos(\theta^i_{ankle}) & (\sin\theta^i_{ankle}) \\ -(\sin\theta^i_{ankle}) & (\cos\theta^i_{ankle}) \end{bmatrix} \begin{bmatrix} X^i_{global} - X_{ankle} \\ Y^i_{global} - Y_{ankle} \end{bmatrix} \quad (1)$$

In the transformation, $i$ represents the pivot point, $(X, Y)$ and $(x, y)$ are the global and local coordinate systems respectively – represents the COP position, $\theta$ indicates the angle between global and local coordinate systems and $(X_{ankle}, Y_{ankle})$ represents the ankle joint.

In reference to the global coordinate system, the COP position, knee joint and ankle joint are used [32]. Similarly, the ROS/COP position in reference to the local coordinate system is shown in Mahmoodi [32]. Thick lines are used to connect the knee joint and the ankle joint for a single walking step. A single line, on the other hand, describes the knee joint-ankle joint connection for a single walking step [32].

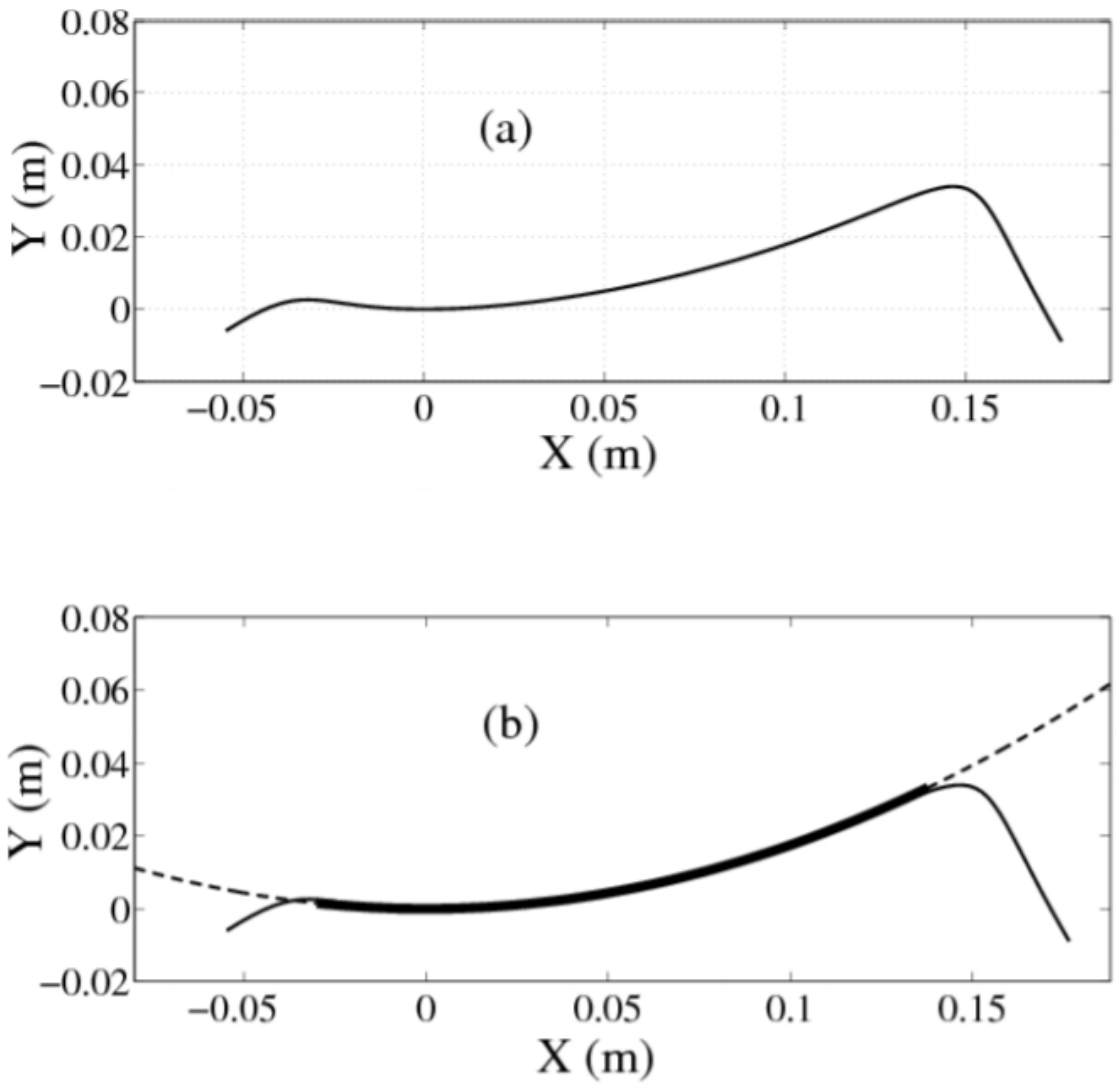


Figure E-3: Figure (a) represents the computational model, while Figure (b) represent the experimentally determined ROS (indicated by dashed line) [32].

In summary, four steps are used in the measurement of the ROS:

1. The Bioware and the force plate are used to determine the body's COP location in a single walking step using the global coordinate system [32].

2. The Quantic video analysis software and markers are used to determine the positions of the ankle and knee joints (figure E-1).

3. The force plate is identified using a red light. Before the force plate recording begins, the video camera is started with the time difference calculated and synchronised using a MATLAB script.

4. Using Equation 5.1, the ROS/COP position is calculated using the data collected in the first three steps in reference to the local coordinate system (Figure E-2).

Applying the four stages, the ROS/COP position retains the stages of the gait cycle – power plantarflexion (toe-off), controlled dorsiflexion (middle phase) and controlled plantarflexion (heel-strike). To perform the required computations, the ROS [32] is used to produce Figure E-3a. The experimental ROS – the dashed curve shown in Figure E-3b – is modelled using the polynomial function presented in Chapter Three. The computational model – indicated by the thick solid line – is developed from the experimental ROS [32].

# Appendix F: PWD Description and Equations

In this section, the PWD model (described in Chapters Three and Five) is used to develop a comprehensive spring-loaded passive walker (SLPW) model. Investigation of the gait characteristics – with asymmetric leg stiffness or unbalanced masses – is conducted using the PWD model, which includes masses for each leg. The ultimate goal of this section is to provide an in-depth definition of the PWD model. The equations and Figures F-1 and F-3 have been reproduced from Charles [15].

**PWD Equations of Motion**

The PWD equations of motion are derived from the compass model presented by Charles [15]. However, the model is adjusted to include compliant springs in order to provide information regarding the double-support phase of human walking and match the GRFs. The configuration of the model is described by the extension of the leg $\left(r = [r_1, r_2]^T\right)$ and leg angles $\left(\theta = [\theta_1, \theta_2]^T\right)$ as shown in Figure F-1 below. In these equations, $\theta_1$ represents the angle between normal to the ground and the support leg while $\theta_2$ represents the angle between the swinging leg and the support leg. The extension of the swinging leg and the stance leg is given by $r_1$ and $r_2$ respectively.

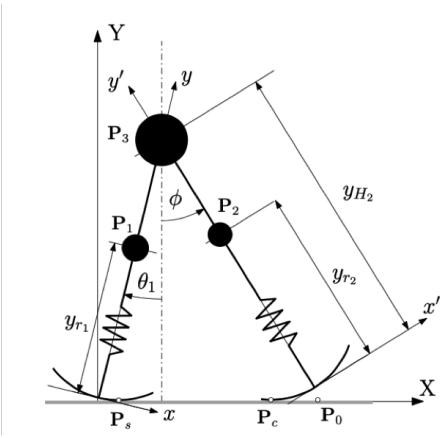


Figure F-1: PWD model for a single-support stance phase [15].

Combining the two parameters, the state model of the PWD is given by Equation 2 below.

$$q = [\theta, r]^T = [\theta_1, \theta_2, r_1, r_2]^T \tag{2}$$

The PWD model is configured with three masses - $m_1, m_2$ and $m_3$ - for two legs (position $P_1$ and $P_2$) and the hip position ($P_3$). The position of the masses of the two legs are defined using the local coordinate system, as shown in Equation 3.

$$y_{ri} = L_i + r_i \tag{3}$$

Here, $L_i$ represents the original position of an unloaded leg and $i = 1, 2$. The position and total length of each hip mass for each leg is given by:

$$y_{Hi} = L_H + r_i \tag{4}$$

In Equation 4, $L_H$ represents the original length of the leg. In the global coordinate system, each mass is represented by Equations 5 and 6 below.

$$\begin{aligned} X_1(\theta_1, r_1) &= -x_\theta(\theta_1)\cos\theta_1 + (y_{r1}(r_1) - y_\theta(\theta_1))\sin\theta_1 + s(\theta_1) \\ Y_1(\theta_1, r_1) &= x_\theta(\theta_1)\sin\theta_1 + (y_{r1}(r_1) - y_\theta(\theta_1))\cos\theta_1 \end{aligned} \tag{5}$$

$$\begin{aligned} X_3(\theta_1, r_1) &= -x_\theta(\theta_1)\cos\theta_1 + (y_{H1}(r_1) - y_\theta(\theta_1))\sin\theta_1 + s(\theta_1) \\ Y_3(\theta_1, r_1) &= x_\theta(\theta_1)\sin\theta_1 + (y_{H1}(r_1) - y_\theta(\theta_1))\cos\theta_1 \end{aligned} \tag{6}$$

In Equation 6, $y_\theta(\theta_1)$ and $x_\theta(\theta_1)$ represent the COP location described by the rollover function given in equations ($y_\theta(\theta_1) = -Rcos(\theta_1) + R$) and ($x_\theta(\theta_1) = Rsin(\theta_1)$). Equation 7 is used to describe the swinging leg.

$$\begin{aligned} X_2(\theta_1, \theta_2, r_1) &= \left(x_{p2}(\theta_2) - x_\theta(\theta_1)\right)\cos\theta_1 + \left(y_{p_2}(\theta_2, r_1) - y_\theta(\theta_1)\right)\sin\theta_1 + s(\theta_1) \\ Y_2(\theta_1, \theta_2, r_1) &= -\left(x_{p2}(\theta_2) - x_\theta(\theta_1)\right)\sin\theta_1 + \left(y_{p2}(\theta_2, r_1) - y_\theta(\theta_1)\right)\cos\theta_1 \end{aligned} \tag{7}$$

In Equation 7, $\left[x_{p2} \text{ and } y_{p2}\right]$ represent the position of point $P_2$ in the local coordinate system $\{x_1, y_1\}$. The coordinates $-x_{p2}$ and $y_{p2}-$ can be calculated as follows:

$$\begin{aligned} x_{p2}\left(\theta_2\right) &= \left(y_{r2} - y_{H2}\right)\sin\theta_2 \\ y_{p2}\left(\theta_2, r_1\right) &= \left(y_{r2} - y_{H2}\right)\cos\theta_2 + y_{H2}\left(r_1\right) \end{aligned} \tag{8}$$

**Derivation of the PWD Equations of Motion**

To derive the PWD equations of motion, the Euler-Lagrange equation is used as follows:

$$\frac{d}{dt}\left(\frac{\partial \mathcal{L}(q,\dot{q})}{\partial \dot{q}}\right) - \frac{\partial \mathcal{L}(q,\dot{q})}{\partial \dot{q}} = 0 \tag{9}$$

In Equation 9, $\mathcal{L}(q,\dot{q})$ is the Lagrangian term, which represents the difference between the potential and kinetic energy ($\mathcal{L}(q,\dot{q}) = K(q,\dot{q}) - V(q)$). This potential and kinetic energy can be calculated as follows:

$$\begin{aligned} K(\boldsymbol{q},\dot{\boldsymbol{q}}) &= \tfrac{1}{2}m_1\left|\overrightarrow{\boldsymbol{v}}_1\right|^2 + \tfrac{1}{2}m_2\left|\overrightarrow{\boldsymbol{v}}_2\right|^2 + \tfrac{1}{2}m_3\left|\overrightarrow{\boldsymbol{v}}_3\right|^2 \\ V(\boldsymbol{q}) &= m_1 g Y_1 + m_2 g Y_2 + m_3 g Y_3 + \tfrac{1}{2}k_1 r_1^2 + \tfrac{1}{2}k_2 r_2^2 \end{aligned} \tag{10}$$

For each mass, the vectors of the velocity are defined as follows:

$$\overrightarrow{\boldsymbol{v}}_m = \dot{X}_m\vec{\imath} + \dot{Y}_m\vec{\jmath} \tag{11}$$

The velocity is then calculated for each mass, as follows:

$$\begin{aligned} \dot{X}_m &= \frac{\partial X_m}{\partial \theta_1}\dot{\theta}_1 + \frac{\partial X_m}{\partial r_1}\dot{r}_1 + \frac{\partial X_m}{\partial \theta_2}\dot{\theta}_2 + \frac{\partial X_m}{\partial r_2}\dot{r}_2 \\ \dot{Y}_m &= \frac{\partial Y_m}{\partial \theta_1}\dot{\theta}_1 + \frac{\partial Y_m}{\partial r_1}\dot{r}_1 + \frac{\partial Y_m}{\partial \theta_2}\dot{\theta}_2 + \frac{\partial Y_m}{\partial r_2}\dot{r}_2 \end{aligned} \tag{12}$$

The kinetic energy Equation 10 can be rewritten by separating out the state vector variables as follows: In this equation, the values of $M_{ij}$ are calculated using Equation 13, as follows.

$$M_{ij} = \sum_{m=1}^{3} m_m\left(\frac{\partial X_m}{\partial q_i}\frac{\partial X_m}{\partial q_j} + \frac{\partial Y_m}{\partial q_i}\frac{\partial Y_m}{\partial q_j}\right) \tag{13}$$

By rewriting the Euler-Lagrange Equations 9 into the state-space form, we obtain:

$$\boldsymbol{M}(\boldsymbol{q})\ddot{\boldsymbol{q}} + \boldsymbol{N}(\boldsymbol{q}, \dot{\boldsymbol{q}})\dot{\boldsymbol{q}} + \boldsymbol{V}'(\boldsymbol{q}) = 0 \tag{14}$$

The matrices N and $V'$ are calculated as follows:

$$N_{ij} = \sum_{n=1}^{4} \frac{\partial M_{in}}{\partial q_j}\dot{q}_n - \frac{1}{2}\sum_{n=1}^{4} \frac{\partial M_{jn}}{\partial q_i}\dot{q}_n \tag{15}$$

and

$$\boldsymbol{V}'(\boldsymbol{q}) = \begin{pmatrix} \frac{\partial V}{\partial \theta_1} & \frac{\partial V}{\partial \theta_2} & \frac{\partial V}{\partial r_1} & \frac{\partial V}{\partial r_2} \end{pmatrix}^T \tag{16}$$

In the stance phase (single support), there is no swing leg extension, implying that $r_2 = 0$. As such,

$$\boldsymbol{q} = [\theta_1, \theta_2, r_1] \tag{17}$$

Using Equation 17, it can be seen that V′ is a $3 \times 1$ matrix while M and N are $3 \times 3$ matrices for the single-support stance phase. The PWD does not move down the slope because no energy is lost during collision [15]. For the PWD to move, adaptations are required to include a damper (for each leg) and a slanting ground.

**Numerical Implementation of the PWD Model**

The PWD includes both single-support and double-support phases. The model operates in the single-support system when the PWD extends the rear leg, resulting in loss of floor contact ($r_1 = 0$) [15]. A touchdown event occurs when the swinging leg makes floor contact, resulting in the transfer of momentum. This transfer of momentum is essential to ensuring that the angular momentum and mechanical energy are not altered due to foot slipping. Furthermore, momentum transfer ensures that the dynamics of the model change to the double-support phase when the next step starts.

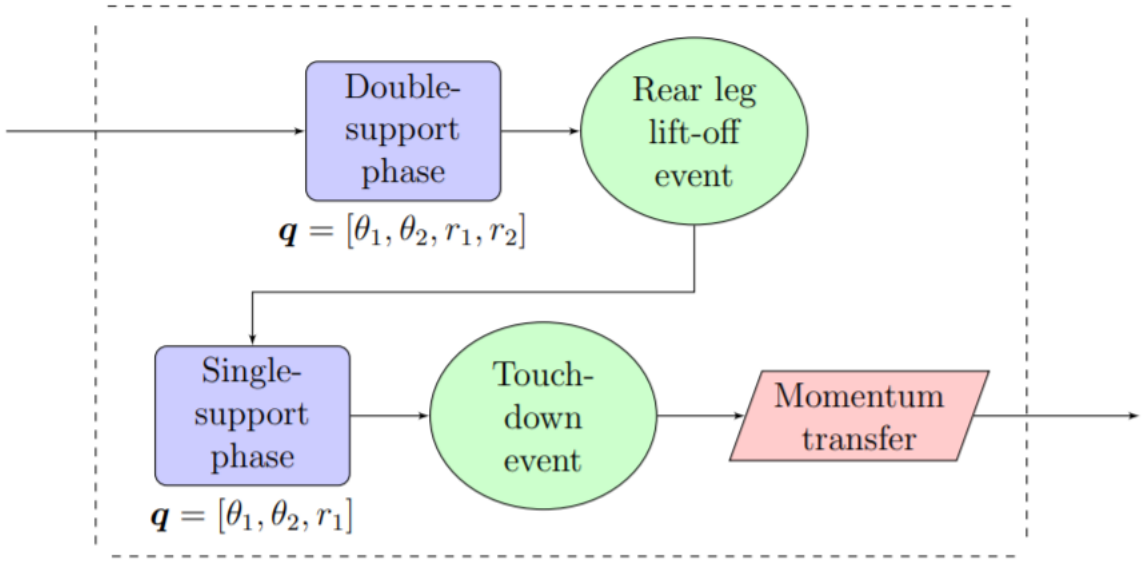


Figure F-2: Flowchart of the PWD model for a complete walking step.

**PWD Model Parameter Domain**

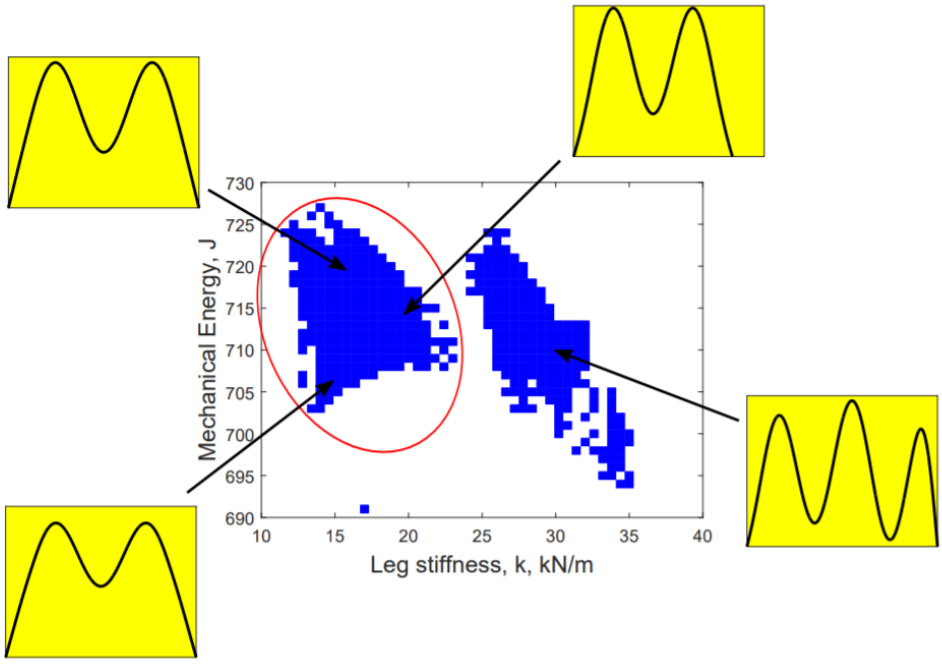


Figure F-3: Stable walking conditions parameter domain combining effective mechanical energy and leg stiffness. Here, the red ellipsoid represents the double peak region [15].

For a walking individual, parameters such as leg length and body mass are fixed, while effective stiffness and mechanical energy vary with the walking speed. The parameter domain of the model can be divided into peaks using the GRF. As a result, the GRF curve is M-shaped with two defined peaks [15]. In this work, only results with two peaks are considered. The plots (Figure F-3) shown outside the graph represent the GRF pattern with more than two peaks.

**Model parameters**

Similar to existing models, the PWD model developed in this work is derived from the human walking parameters. Anthropomorphic data from Ohio is used to extract the values for leg mass ratio, total body mass, and leg length ratio [146]. The force-length curves are then studied to estimate the effective stiffness of the leg from human gait data [118]; the effective stiffness data can also be derived from approximation of the walking speed. A rocking contact (30% of the leg length) is used to replicate the ROS [95]. The extracted standard parameters - listed in Table 5.3 - are used in this thesis. Some variables are changed to investigate asymmetry, as specified in the table.

# Appendix G: Yang's Model

## G1. Spring Damper Model

## G2. Stiffness Results

# G1. Spring Damper Model

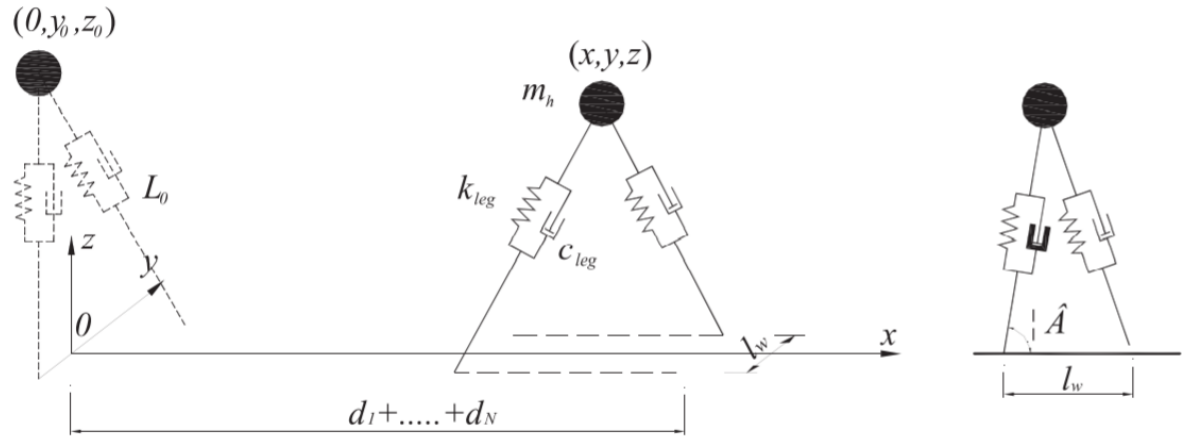


Figure G-1: Mass spring damper model [120]

# G2. Stiffness Results

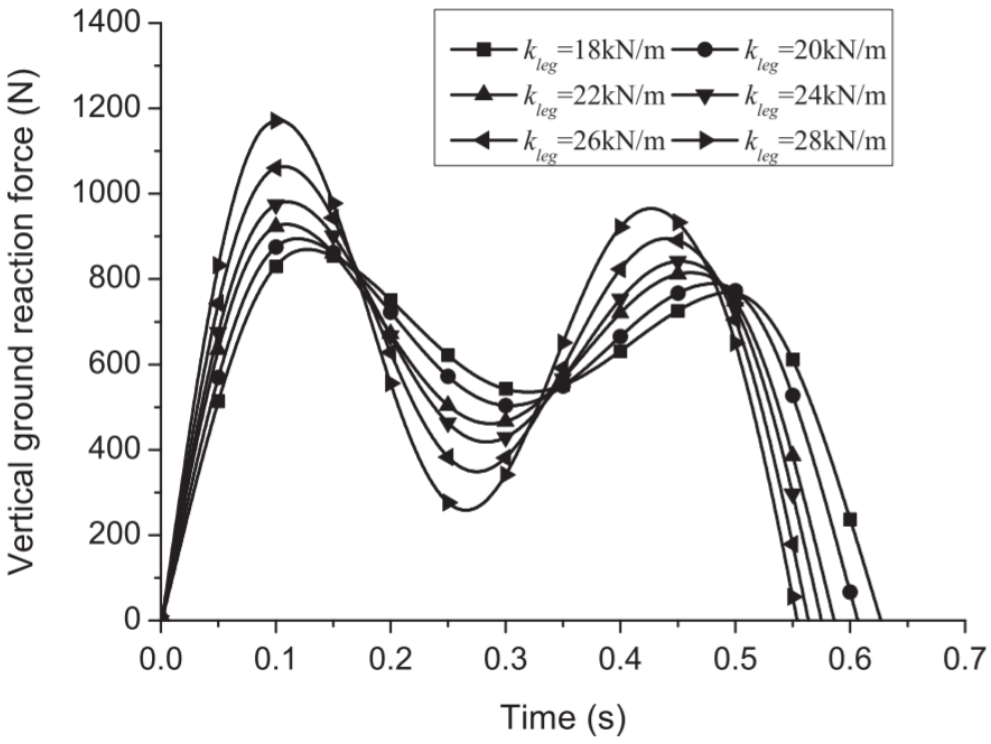


Figure G-2: Stiffness results by [120]

# Appendix H: Configuration of Double-Keel Design

Geometrical constructions are integral to the optimisation of prosthetics. As shown in the Figure H-1, the current design utilises Bezier curves constructed out of 14 points to establish a clear connection between the geometry and stiffness profile of the prosthetic. The parametric curves have both $x$ and $y$ co-ordinates at the centre line of the foot. The aggregate value of the loft is 11 points. These points of the model are delineated at the cross-over point linking the curves to the perpendicular line that runs through one of the construction points. This design effectively lowers the number of variables in the curves by eliminating the defined points on the $x$ and $y$ co-ordinates. The construction points on the axis depend on the construction points of the curves. The loft points of the curve are used to form the primary keel and foot base [156]. The prosthetics are sketched perpendicular to the curve with clearly defined breadth and width. Moreover, each construction point is denoted by a rectangle. To begin with, the breadth is kept constant, while the depth diminishes along the plane towards the ends of the keel and foot base curves. The uniform values of the width allow the simulations to be validated with simplicity and ease. Conversely, tapering the depth to create a cantilever provides elasticity for energy storage and return.The designers must validate the model behaviour in order to enhance the accurate determination of the load case. Both the depth and breadth of the primary keel are thickest at the curve of the 'C-spring,' which maximises the second moment of the area to enhance its bend yield, since it is the most stressed part during movement [157]. Conversely, the design of the secondary keel is different from the specifications of the primary keel and foot base. The variance is offset by $10mm$, which is the initial value, and the gap is extruded. The primary keel is thicker than the secondary keel because it supports the overall load, while the secondary keel also has a less robust optimisation route. The current construction of the prosthetic involves a toe and heel split along the centre line of the design: the gap is $1mm$, the toe length is $85mm$, and the heel length is $50mm$. However, these values are not optimised.

The initial figures were derived from competitor analysis, and the design allows for at least a 10 degree eversion. The designing involves filleting the internal angles of the toe, heel, and top edges by 5, 6, 6, and 10*mm* respectively. Filleting minimises sharp changes in geometry to manage stress concentration along the edges and eliminate hazardous edges [156].

(a) Foot Base Geometry

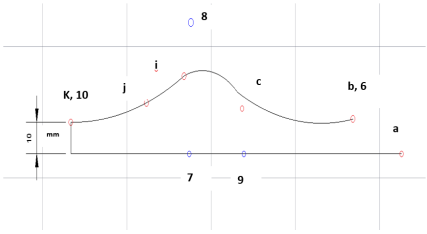


(b) Foot Base Construction Curve

(c) Primary Keel Geometry

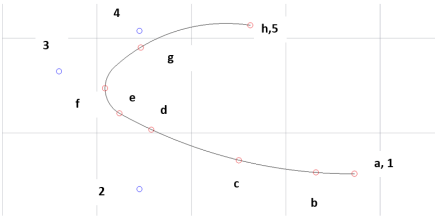


(d) Primary Keel Construction Curve

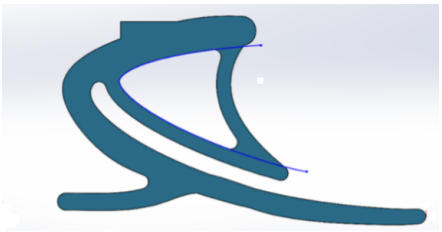

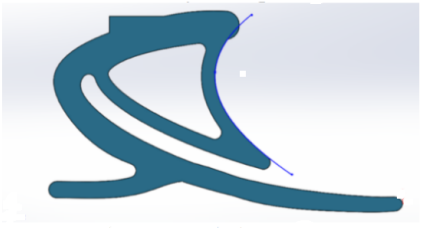

(e) Secondary Keel Geometry

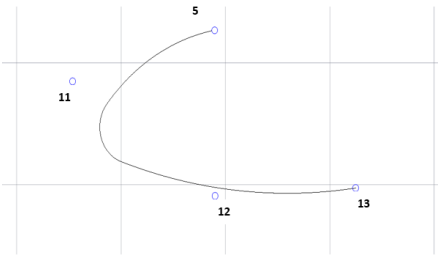


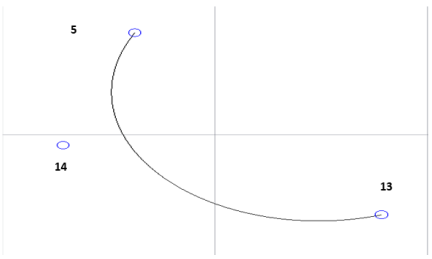


(f) Secondary Keel Construction Curve

Figure H-1: Design Configuration [156].

# Appendix I: MATLAB Curve Fitting Software

The below figures show the MATLAB curve fitting for both exponential and linear fitting.

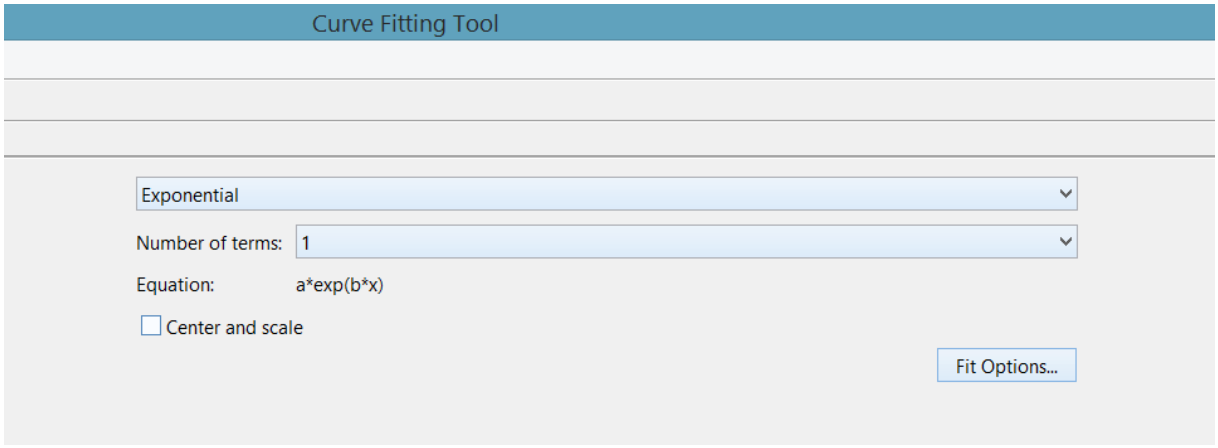


Figure I-1: MATLAB Exponential curve fitting

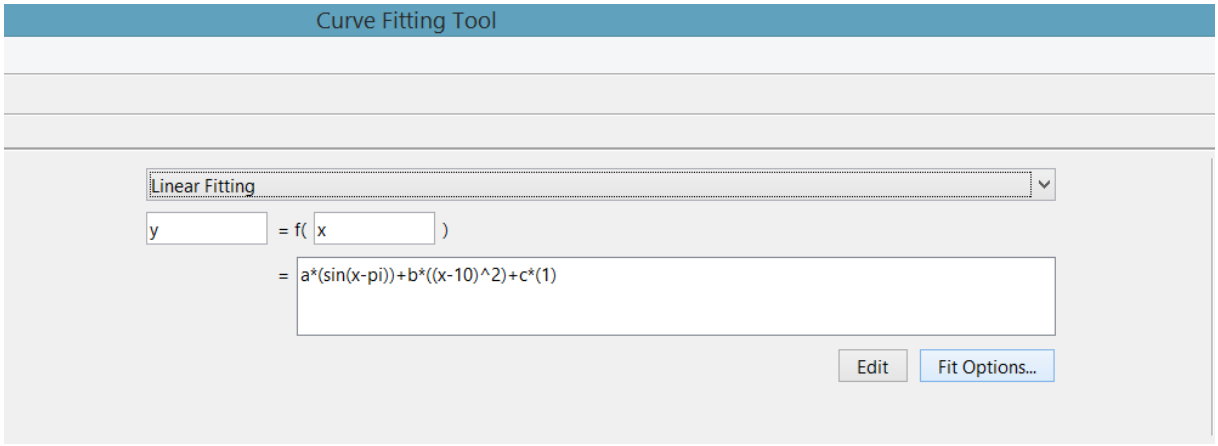


Figure I-2: MATLAB Linear curve fitting